Electronic Theses and Dissertations   Theses, Dissertations, and Major Papers

2012

Determination of the Deformation State of a Ti-6Al-4V Alloy Subjected to Orthogonal Cutting Using Experimental and Numerical Methods

Md Aquidul Islam
University of Windsor

Follow this and additional works at: https://scholar.uwindsor.ca/etd

Determination of the Deformation State of a Ti-6Al-4V Alloy Subjected to Orthogonal Cutting Using Experimental and Numerical Methods

By

Md. Aquidul Islam

A Thesis

Submitted to the Faculty of Graduate Studies

through Engineering Materials

in Partial Fulfillment of the Requirements for

the Degree of Master of Applied Science at the

University of Windsor

Windsor, Ontario, Canada

2012

© 2012 Md. Aquidul Islam

Determination of the Deformation State of a Ti-6Al-4V Alloy Subjected to Orthogonal Cutting Using Experimental and Numerical Methods

By

Md. Aquidul Islam

APPROVED BY:

_____

Dr. A. T. Alpas, Co-advisor

Department of Mechanical, Automotive, and Materials Engineering

_____

Dr. W. J. Altenhof, Co-advisor

Department of Mechanical, Automotive, and Materials Engineering

_____

Dr. R. Riahi

Department of Mechanical, Automotive, and Materials Engineering

_____

Dr. S. Das

Department of Civil and Environmental Engineering

_____

Dr. H. Hu, Chair of Defense

Department of Mechanical, Automotive, and Materials Engineering

17 May 2012

AUTHOR'S DECLARATION OF ORIGINALITY

I hereby certify that I am the sole author of this thesis and that no part of this thesis has been published or submitted for publication.

I certify that, to the best of my knowledge, my thesis does not infringe upon anyone's copyright nor violate any proprietary rights and that any ideas, techniques, quotations, or any other material from the work of other people included in my thesis, published or otherwise, are fully acknowledged in accordance with the standard referencing practices. Furthermore, to the extent that I have included copyrighted material that surpasses the bounds of fair dealing within the meaning of the Canada Copyright Act, I certify that I have obtained a written permission from the copyright owner(s) to include such material(s) in my thesis and have included copies of such copyright clearances to my appendix.

I declare that this is a true copy of my thesis, including any final revisions, as approved by my thesis committee and the Graduate Studies office, and that this thesis has not been submitted for a higher degree to any other University or Institution.

ABSTRACT

Orthogonal cutting of Ti-6Al-4V alloy was studied. Surface roughness, chip thickness and shear band frequency increased with the feed rate and cutting speed. Serrated chips were formed due to shear band. Strain and flow stress distributions in the material ahead of the tool tip were estimated from shear angle measurements and microhardness measurements respectively. The stress-strain data obtained in this way was used in numerical models. Two numerical models were developed by using two-dimensional Lagrangian element formulation and Smoothed-particle hydrodynamics formulations employing the Johnson-Cook constitutive relationship that utilised the experimental data generated from the machined material with the damage criteria. The Lagrangian element formulation predicted the strain and temperature generated in the material ahead of the tool tip as 1.65 and 1222 K respectively, which were in agreement with the experimental strain (1.65) and temperature (1217 K). The predicted results using Lagrangian element formulation correlated well with the experimental findings.

To my parents,

Dr. Md. Atiqul Islam and Mrs. Monju Ara Begum,

and to my brother and sister

for their love, endless support and encouragement

ACKNOWLEDGEMENTS

TABLE OF CONTENTS

LIST OF TABLES

LIST OF FIGURES

xv

CHAPTER 1: INTRODUCTION

1.1. Background of this Research

Metal cutting methods are manufacturing processes in which metal parts are shaped to the required dimensions and finish by removal of unwanted metal. It is important to understand the machining process to have better control over the product dimensions and surface finish, power consumption, and tool life.

During orthogonal cutting of metals and alloys, large strains and strain gradients are generated in the workpiece material ahead of the tool tip, and the deformation microstructures of the workpiece material need to be studied carefully in order to obtain a thorough understanding of the chip formation mechanisms. Previous researchers have adopted various means to investigate energy expenditure processes in the workpiece ahead of the tool tip. Merchant [1] proposed a model to predict the orientation of the primary shear plane with respect to the cutting direction using the principle of minimization of plastic deformation work. Lee and Shaffer [2] applied the slip line field analysis to the material ahead of the tool tip to predict shear angles and shear strain distributions. Stevenson and Oxley [3] used aluminum sample on which a fine scale grid was imprinted and estimated the distribution of shear strains and strain rate fields in the material ahead of the tool tip. Ramalingam and Black [4], using scanning and transmission electron microscopy of the plastically deformed zone at the root of the chips, shed light on the role of microstructure of the work material on the machinability.

Ti-6Al-4V is an α-β titanium alloy which is known as a difficult to machine material. This alloy is chemically reactive and therefore has a tendency to weld to the cutting tool during machining, thus leading to tool failure [5]. Its low thermal conductivity increases the temperature at the tool-workpiece interface, which affects the tool life adversely [6]. Serrated chip formation is obtained during orthogonal cutting of Ti–6Al–4V alloy under conventional cutting conditions and even at low cutting speeds due to the thermoplastic instability, which results in shear localization or adiabatic shear band formation [7]. This adiabatic shear band is formed as the combined effects of strain and strain rate hardening are outweighed by the thermal softening caused by adiabatic deformation in the primary shear zone [8].

The modeling of machining processes using the finite-element method (FEM) provides an effective alternative to reduce the machining costs and analysis time. The FEA method can account for the large deformation, strain rate effect, tool-chip contacts and friction, local heating and temperature effect, the different boundary and loading conditions, and other phenomena associated with the metal cutting operation. Numerical modeling for high strain (and strain rate) typical of metal cutting processes consists of three major element formulation implementations, namely, Lagrangian, Eulerian, and Arbitrary Lagrangian-Eulerian (ALE) [9]. Recently, researchers have implemented smooth particle hydrodynamic (SPH) particle formulations [10] to investigate workpiece deformation during cutting. Most studies dealing with FE modeling of orthogonal cutting has implemented a Lagrangian FE formulation, in which the finite-element mesh of the workpiece that consists of material elements are attached to the material and allowed to deform together. Commonly two groups of methods were used to simulate serrated chip

formation: either damage or material failure model [11] or material model for temperature-dependent flow softening based adiabatic shearing [12]. Smoothed-particle hydrodynamics (SPH) formulation was also used to model the serrated chip formation during machining of AISI 4340 steel [13]. Benson and Okazawa [14] studied application of the Eulerian finite-element formulation in machining and simulated serrated chip formation during high-speed machining.

1.2. Thesis Objective

The objective of this research was to perform dry orthogonal cutting experiments on Ti-6Al-4V alloy at different cutting conditions to observe their effects on the deformation behaviour of Ti-6Al-4V alloy as well as to understand the mechanism of chip formation or shear band formation using metallographic methods and numerical analysis. The effective plastic strains were calculated on the basis of shear angle measurements. Local flow stress values were determined from the microhardness measurements. The shear band properties in terms of hardness and shear strain were also determined. Another challenge of this research was to develop a numerical model that formed serrated chips during cutting. Numerical simulations were performed using the explicit nonlinear FE code, LS-DYNA with Lagrangian element formulation and smoothed-particle hydrodynamics formulations. The boundary conditions and geometry of the workpiece and tool were defined from the experimental observation. These models integrated the material models based on the microstructural data with the dynamics of strain localization. The capabilities of different FEA formulations were evaluated to include complexities of strain localization exhibited during machining. Another aim of

this research was to conduct the comparison between the numerical results and the experimental findings with respect to strain, stress and temperature distributions and cutting force, in order to validate the models and find the most suitable model that could represent the machining operation more accurately including phase transformation.

CHAPTER 2: LITERATURE REVIEW

The metal cutting process is an industrial process in which a metal part is shaped by removal of unwanted material. The machining process is one of the most important manufacturing processes due to the value added to the finished product. Most titanium parts used in aerospace industries are still manufactured by conventional machining methods such as turning, milling, drilling, reaming, grinding, and tapping. In this chapter the previous research work on the machining of Ti-6Al-4V alloy is introduced to better understand the mechanism of serrated chip formation. A summary of previous attempts made on the finite-element modeling of metal cutting is also included in this chapter.

2.1. Basics of Machining Process

2.1.1. Principle of Cutting Operations

The three most widely used cutting operations are: 1. Turning, 2. Milling, and 3. Drilling [15]. Turning is a process using a single point tool that removes unwanted material to produce a desired product. In turning a cutting tool is fed into a rotating workpiece to generate an external or internal surface concentric with the axis of rotation. Turning is carried out using a lathe, one of the oldest and most versatile conventional machine tools [16].

2.1.1.1. Orthogonal Cutting: A Type of Turning Operation

Depending on the way the cutting tool makes contact with the workpiece material, the turning processes are normally identified as (1) orthogonal cutting and (2) oblique

cutting [15]. The term orthogonal cutting has been pointed to cover the case where the cutting tool generates a plane surface parallel to an original plane surface of the material being cut and is set with its cutting edge perpendicular to the direction of relative motion of tool and work piece [15,16] (Fig. 2.1). If the cutting direction and tool edges are not perpendicular to each other or the contacting edge of the cutting tool with the workpiece is not a straight line, the oblique cutting results [16,17]. The orthogonal cutting process and oblique cutting process are considered as two-dimensional and three-dimensional problems, respectively.

2.1.2. Deformation Zones in the Workpiece

Three deformation zones are present during metal cutting and chip formation, namely, primary deformation zone (PDZ), secondary deformation zone (SDZ), and tertiary deformation zone (or machined surface) shown in Fig. 2.2. The primary deformation zone is formed as the tool advances and penetrates through the workpiece, and the material directly in front of the tool tip undergoes shearing and heavy plastic deformation. According to early assumptions [1,18,19], the workpiece shearing takes place along a fixed plane, called the primary shear plane, which passes through the primary deformation zone. The angle between the cutting direction and the primary shear plane is called the shear angle, φ shown in Fig. 2.2. The secondary deformation zone is formed as the chip produced at the tool tip undergoes further sliding against the rake face of the tool, thus undergoing further deformation due to friction between the two surfaces. Finally, the tertiary deformation zone is formed due to the friction between the newly machined surface and the flank of the tool.

6

2.1.3. Chips Formation and Classification

The unwanted material removed during orthogonal cutting is in the form of chips that can be classified into the following four main classes [16]:

2.1.3.1. Continuous Chip

The continuous chip is an ideal type of chip for analysis because it is relatively stable and simple to analyze. Continuous chips are long, ribbon-like chips (Fig. 2.3a) formed during machining of soft, ductile material such as aluminum [20], or copper [21]. The favourable conditions for the generation of continuous chips are: high speeds, small feeds and small depths of cut [15,16,22]. However, the continuous chip often interferes with the machining process, wraps around the workpiece and machine spindle and may cause some unpredictable flaws and damage on the machined surface, cutting tool or machine tool; it may even cause injuries to the operator.

2.1.3.2. Discontinuous Chip

Discontinuous chips or fragmented chips are generally formed during machining of brittle materials such as cast iron due to cyclic fracturing (Fig. 2.3b). Fracture occurs as the material is unable to undergo a large amount of plastic deformation. Factors such as low cutting speed or high tool-chip friction and large feed and depth of cut favour the formation of discontinuous chips [15,16].

2.1.3.3. Continuous Chip with Built-up Edge

During machining, when the temperature at the chip-tool interface is relatively low, fracture may happen within the chip along a plane approximately at right angle to the shear plane, leaving behind a portion of the chip attached to the tool face, which acts as the cutting edge and is called a built-up edge (BUE) (Fig. 2.3c). BUE formation leads to modification of effective tool geometry, thus leading to irregularities in the machined surface. BUE formation is undesirable in a machining operation and can be avoided by increasing the cutting speed, using positive rake tools, or by application of a coolant [15,22].

2.1.3.4. Serrated Chip

Serrated chips (or saw-tooth chips), are formed due to thermoplastic instability which results in shear localization or adiabatic shear band formation [7]. This catastrophic shear or adiabatic shear band is formed as the combined effects of strain and strain rate hardening are outweighed by the thermal softening caused by effectively adiabatic plastic deformation in the primary shear zone [7,23]. This type of chip (Fig. 2.3d) is likely to form during machining of titanium alloys or hardened and stainless steels at high cutting speed [24-26].

2.1.4. Forces and Stresses during Orthogonal Cutting

Merchant assumed that the force between the tool face and the chip, and the force between the work piece and the chip along the shear plane are equal in equilibrium

condition, and the relationships between the various forces on the basis of the force diagram (Fig. 2.4) are as follows [15,18]:

$$F_s = F_c \cos \varphi - F_t \sin \varphi \qquad (2.1)$$

$$N_s = F_c \sin \varphi + F_t \cos \varphi \qquad (2.2)$$

$$F_p = F_c \sin \alpha + F_t \cos \alpha \qquad (2.3)$$

$$N_p = F_c \cos \alpha - F_t \sin \alpha \qquad (2.4)$$

where, F_c is cutting force, F_t is thrust force, F_s is the shear force on the shear plane, N_s is the normal force on the shear plane, F_p is shear force on rake face and N_p is the normal force on the rake face.

The components of the forces on the rake face can be used to find the coefficient of friction on the tool face (μ):

$$\mu = F_p/N_p = (F_c \sin \alpha + F_t \cos \alpha)/(F_c \cos \alpha - F_t \sin \alpha)$$

$$\mu = (F_t + F_c \tan \alpha)/(F_c - F_t \tan \alpha) \qquad (2.5)$$

The shear model or card model is a simplified and useful method to predict the stresses on the shear plane and rake face of an orthogonally cut sample. It is assumed that the distribution of shear and normal forces on the shear plane and on the shear rake face is uniform. From this assumption, the shear stress on the shear plane τ_s can be calculated as follows [18,22]:

$$\tau_s = \frac{\text{Shear force on shear plane}}{\text{Area of shear plane}}$$

$$\tau_s = \frac{F_c \cos \varphi - F_t \sin \varphi}{\left[\frac{w.f}{\sin \varphi}\right]} \tag{2.6}$$

where, f is the uncut chip thickness which is equal to the feed rate and w is the depth of cut during orthogonal cutting.

The normal stress on the shear plane σ_s can similarly be computed as:

$$\sigma_s = \frac{\text{Normal force on shear plane}}{\text{Area of shear plane}}$$

$$\sigma_s = \frac{F_c \sin \varphi + F_t \cos \varphi}{\left[\frac{w.f}{\sin \varphi}\right]} \tag{2.7}$$

Similarly, the shear stress τ_f on the chip contact with the rake face is equal to:

$$\tau_f = \frac{F_c \sin \alpha + N_s \cos \alpha}{[w.l]} \tag{2.8}$$

And the normal stress on the rake face σ_f can be written as:

$$\sigma_f = \frac{F_c \cos \alpha - N_s \sin \alpha}{[w.l]} \tag{2.9}$$

where, l is the length of sliding contact.

2.1.5. Deformation Microstructures of the Workpiece Subjected to Orthogonal Cutting

Machining operations generate large strains and strain gradients in the work material. It is important to understand the development of the deformation microstructures in the workpiece material in order to rationalize the energy expenditure

10

process during machining operations, and thus to have better control of the machining parameters. Ramalingam and Black [4,27] used SEM (Scanning electron microscopy) and TEM (Transmission electron microscopy) to analyze the plastic deformation zone at the root of the chip in steel and concluded that the dynamic equilibrium is established between strain hardening and recovery during the chip formation, and that plastic flow in machining is a microscopically heterogeneous deformation process dependent upon the prior deformation history of the workpiece, both before and during machining. Zhang and Alpas [20] observed the deformation microstructure of aluminum alloy (Fig. 2.5) subjected to orthogonal cutting to quantify the plastic strain gradients. Ni et al. used TEM to investigate the deformation microstructure generated in copper [21] and aluminum [28] ahead of the tool tip during machining. It was observed that the microstructure of the primary deformation zone (PDZ) was characterized by the formation of elongated dislocation cell structures composed of heavily tangled dislocation walls, and that dynamic recrystallization occurred in the microstructure of the machined chips of copper.

2.1.5.1. Shear Angle Estimation

To measure the shear angle, Zhang and Alpas [20] considered the orientation change of the deformed grains, which behave like flow lines, on the cross-sectional plane (Fig 2.5) and generated a schematic diagram (Fig. 2.6a). The values of shear angle, φ, were computed from the slopes of the flow lines (Fig. 2.6b) bending in the direction of plastic deformation as follows:

$$\varphi = \tan^{-1}\left(\frac{\Delta y}{\Delta x}\right) \tag{2.10}$$

11

2.1.5.2. Strain Estimation

Plastic deformation occurs in the workpiece material during metal cutting, and it is important to measure the amount of plastic deformation. Dautzenberg and Zaat [29] explained the method of measuring the equivalent or effective plastic strain more clearly. They considered an ideal spherical crystal (ABC in Fig. 2.7) deforming under the influence of true shearing, where the shear strain component was $d\gamma_{yx} \neq 0$. It was assumed that the normal strain components and the rest shear components were zero, that is:

$$d\varepsilon_x = d\varepsilon_y = d\varepsilon_z = d\gamma_{zy} = d\gamma_{zx} = 0 \qquad (2.11)$$

where, $d\varepsilon_{x,y,z}$ is the normal incremental normal strain components and $d\gamma_{ij}$ is the shear strain components.

The incremental effective plastic strain $d\bar{\varepsilon}$ is defined as [30]:

$$\frac{9}{4}(d\bar{\varepsilon})^2 = \frac{1}{2}[(d\varepsilon_x - d\varepsilon_y)^2 + (d\varepsilon_y - d\varepsilon_z)^2 + (d\varepsilon_z - d\varepsilon_x)^2] + \frac{3}{4}[d\gamma_{yx}^2 + d\gamma_{zy}^2 + d\gamma_{xz}^2]$$
$$(2.12)$$

From Eq. 2.11 and Eq. 2.12, it follows that:

$$d\bar{\varepsilon} = \frac{d\gamma_{yx}}{\sqrt{(3)}} = \frac{\sqrt{(3)}}{3}\frac{dl_x}{l_y} \qquad (2.13)$$

Integration of Eq. 2.13 leads to:

$$\bar{\varepsilon} = \frac{\sqrt{(3)}}{3}\frac{1}{l_y}\int_0^{l_x} dl_x = \frac{\sqrt{(3)}}{3}\frac{l_x}{l_y} \qquad (2.14)$$

$$\bar{\varepsilon} = \frac{\sqrt{(3)}}{3} \tan \theta \tag{2.15}$$

where θ is the deformation angle which can be written as: $\theta = 90° - \varphi$. Here, φ is the shear angle.

This method of equivalent strain estimation has been found to be applicable and has been used for investigating the plastic strain generated due to high deformation which occurred during machining. Zhang and Alpas [20] have used Eq. 2.15 to estimate the equivalent strains from the orientation change of the extrusion lines or flow lines (Fig.2.6a) during orthogonal cutting of 6061 Al. The same method has been used successfully by Elmadagli et al. to estimate the strains during dry machining of commercial purity copper [31] and Al 1100 [28]. Fig. 2.8 depicts the strain distribution diagram in Al 1100 ahead of the tool tip. The maximum strain value was 2.52 generated in the material ahead of the tool tip and the depth of deformed zone 1300 μm.

2.1.5.3. Flow Stress Estimation

The microhardness of the material ahead of the tool tip and below the machined surface varies from one location to another. Flow stress value can be estimated from the measured microhardness value, which was explained clearly by Tabor [32].

In [32], Tabor attempted to correlate the hardness of a metal with its elastic limit and with the way in which the elastic limit varies with the amount of deformation to which the metal has been subjected. If σ_1, σ_2, σ_3 are the principal stresses in a solid body (Fig.2.9), the criterion for plastic flow or effective stress is [33]:

$$\sigma_0 = \frac{1}{\sqrt{2}}[(\sigma_1 - \sigma_2)^2 + (\sigma_2 - \sigma_3)^2 + (\sigma_3 - \sigma_1)^2]^{1/2}$$

Or, $2\sigma_0{}^2 = (\sigma_1 - \sigma_2)^2 + (\sigma_2 - \sigma_3)^2 + (\sigma_3 - \sigma_1)^2$ \hfill (2.16)

where σ_0 is the effective stress of the material as found by pure tension (of frictionless compression) experiments. The Eq. 2.16 has been solved by Hill et al. [34], and they suggested that the plastic yielding would occur when the mean pressure, was:

$$\sigma_m = 3\sigma_0 \tag{2.17}$$

For Eq. 2.17, the assumptions are:

- The deformed area is not too large compared with the size of the specimen
- σ_m is independent of the applied load and size of the indentation.
- Frictionless compression is performed.

It was proposed by Marsh [35] that the Vickers hardness number, H, of the fully work-hardened material could be related to the corresponding flow stress σ, as:

$$\sigma = \frac{H}{3} \tag{2.18}$$

This approximate equation is commonly used to estimate the flow stress of the materials ahead of the tool tip after performing cutting operation [21,28].

2.1.5.4. Energy Expended and Temperature Rise during Plastic Deformation

To measure the energy expended during the deformation of the material ahead of the tool tip, a relationship between the equivalent stresses and strains was developed by

plotting the corresponding stress and strain values determined at each point in the material ahead of the tool tip [31]. From the regression analysis, the relationship between the flow stress and the equivalent strain (Fig. 2.10) in the case of copper was described in the formalism of the Voce equation [36].

$$\bar{\sigma} = \overline{\sigma_s} - (\overline{\sigma_s} - \bar{\sigma}_o)\exp(-\frac{\bar{\varepsilon}}{\bar{\varepsilon}_c}) \tag{2.19}$$

In this equation σ is the value of the equivalent flow stress, $\bar{\varepsilon}$ is the corresponding equivalent strain, $\overline{\sigma}_s$ is the saturation stress or the stress at which the work hardening rate becomes zero, $\overline{\sigma}_o$ is the value of the yield flow strength of the material, and $\bar{\varepsilon}_c$ is a constant. Fig 2.10 depicts the saturation stress and flow strength of copper as 422.2 MPa and 199.3 MPa respectively. However, in the case of 1100 Aluminum, the saturation stress and flow strength are 299.0 MPa and 138.8 MPa respectively, which are lower in value compared to copper. Because, copper is a low stacking fault energy material, work hardens at a faster rate during machining [28].

The energy expended during the deformation of the material ahead of the tool tip can be calculated from the area under the stress/strain curve in Fig. 2.10. For each increment of strain, the work of plastic deformation, W, (per unit volume) is given as [31]:

$$W = \int_{\bar{\varepsilon}_n}^{\bar{\varepsilon}_{n+1}} (\overline{\sigma_s} - (\overline{\sigma_s} - \bar{\sigma}_o)\exp(-\frac{\bar{\varepsilon}}{\bar{\varepsilon}_c}))d\bar{\varepsilon} \tag{2.20}$$

A large portion of the work done during the plastic deformation of the workpiece is transformed into heat to produce a temperature increase (ΔT) in the work material which can be expressed (Fig. 2.11) as [28]:

$$\Delta T = \frac{\beta}{\rho C} \int_{\bar{\varepsilon}_n}^{\bar{\varepsilon}_{n+1}} (\overline{\sigma_s} - (\overline{\sigma_s} - \overline{\sigma}_o)\exp(-\frac{\bar{\varepsilon}}{\bar{\varepsilon}_c}))d\bar{\varepsilon} \qquad (2.21)$$

where β is the fraction of plastic work converted into heat. It is generally assumed that $\beta = 0.95$ [18], ρ is the density, and C is the specific heat capacity of the workpiece.

For 1100 Aluminum the local temperature increments calculated according to Eq. 2.21 are presented in the form of a temperature distribution diagram in Fig. 2.11. The maximum temperature is 244 °C generated in the material ahead of the tool tip [28].

2.2. Machining of Titanium Alloy

Titanium and its alloys are used extensively in the aerospace industry because of their excellent combination of high specific strength (strength-to-weight ratio) which is maintained at elevated temperature, fracture resistant, and corrosion resistant characteristics. They are also being used in other industrial and commercial applications such as petroleum refining, chemical processing, surgical implantation, pulp and paper, pollution control, nuclear waste storage, food processing, electrochemical (including cathodic protection and extractive metallurgy), and marine applications [37,38].

Most titanium parts are still manufactured by conventional machining methods. Virtually all types of machining operations such as turning, milling, drilling, reaming, tapping, sawing, and grinding, are employed in producing aerospace components [5]. For

the manufacture of gas turbine engines, turning and drilling are the major machining operations, whereas in airframe production, end milling and drilling are among the most important machining operations.

2.2.1. Ti-6Al-4V Alloy

Titanium alloys may be divided into four main groups according to their basic metallurgical characteristics: α alloys, near α alloys, α − β alloys, and β alloys [39,40]. Among these four types of alloy, the Ti-6AI-4V (α − β) alloy is known as the workhorse of the titanium industry because it is by far the most common titanium alloy, accounting for more than 50% of the total titanium production. Table 2.1 gives the comparisons among the important properties of Ti-6AI-4V alloy, AISI 1045 steel, Aluminum 1100, and ETP copper.

Table 2.1. Important properties of different metals [40-45]**.**

Properties	Ti-6Al-4V	AISI-1045 Steel	Aluminum 1100	ETP Copper
Yield Strength, MPa	880	505	103	76
Modulus of Elasticity, GPa	110	205	68.9	125
Density, g/cc	4.43	7.84	2.71	8.89
Thermal conductivity, W/m k	7.3	49.8	220	388

It is interesting to note the Ti-6Al-4V alloy has lower density and higher yield strength compared to AISI-1045 steel and lower thermal conductivity compared to all other metals such as AISI-1045, Aluminum 1100, and ETP copper.

2.2.1.1. Microstructure of Ti-6Al-4V Alloy

At room temperature, the microstructure of Ti-6Al-4V alloy is composed of equiaxed α grains, along with a lamellar, α + β bimodal microstructure as shown in Fig. 2.12. The α phase (hexagonal close-packed structure) is the stable phase and the β phase (body centred cubic structure) is the metastable phase at room temperature. For this alloy, allotropic phase transformation from α-phase to β-phase occurs at 995±15 ˚C [46].

2.2.2. Research into Machining of Ti-6Al-4V Alloy

Pioneering studies on the mechanics of chip during machining of titanium alloy or Ti-6Al-4V alloy have been conducted since the early 1950s by Shaw and his coworkers [47,48] and Boston et al. [49]. Komanduri et al. [6,50] explained the mechanism of chip formation during the machining of titanium alloy more clearly. Previous studies on the machinability of Ti-6Al-4V alloy, microstructural changes, and mechanism of chip formation are explained below.

2.2.2.1. Machinability of Ti-6Al-4V Alloy

Machinability is the characteristic of a material that make it easier to cut, drill, grind, shape, and so on. In general, there are three main aspects of machinability [15]: product surface finish, tool life, and power required to cut. Materials with good machinability can be cut quickly, easily obtain a good finish, require little power to cut,

and do not wear the tool significantly. The factors that typically improve the performance or mechanical properties of a material often degrade its machinability. Therefore, to manufacture components economically, engineers are challenged to find ways to improve machinability without harming performance.

Ti-6Al-4V alloy is a very interesting material for industrial applications because of their high strength-to-weight ratio, combined with ductility and fracture resistance properties. Despite these features, the utilization of titanium alloys is still limited due to their poor machinability or high machining cost. Many researchers [5,6,49,51-55] claim individually some of the following points as the reasons for the poor machinability of titanium.

1. Due to the poor thermal conductivity of Ti-6Al-4V alloy (Table 2.1), high cutting temperatures are generated during machining of this alloy and a large proportion of the generated heat is conducted into the tool as it cannot be removed with the fast flowing chip. Investigation of the distribution of the cutting temperature has shown that the temperature gradients are much steeper and the heat-affected zone much smaller and much closer to the cutting edge when machining titanium alloy compared to steel, which causes high tool-tip temperatures of up to about 1100 ˚C. As illustrated in Fig. 2.13, a large proportion (about 80%) of the heat generated when machining titanium alloy Ti-6AI-4V is conducted into the tool because it cannot be removed with the fast flowing chip due to the low thermal conductivity of titanium alloys, which is about 1/6 that of steels [56]. About 50% of the heat generated is absorbed into the tool when machining steel. As a result, tool failure occurs due to the thermal fatigue.

2. The chip of titanium is very thin with an unusually small contact area with the tool ($1/_3$ to $1/_2$ of that for turning steel) which causes high stresses on the tip of the tool. The combination of high stress and high temperature at the tool tip promote tool wear and increase production cost.

3. The high strength of Ti-6Al-4V alloy is maintained to elevate temperatures (Fig. 2.14) that are generated during machining and this opposes the plastic deformation needed to form a chip and causes high cutting force to cut.

4. There is strong chemical reactivity of titanium at the cutting temperature (which is greater than 500 ˚C) with almost all tool materials available. The freshly generated hot shear-failed surface in contact with the tool face can cause rapid chemical reaction and tool wear.

5. Chatter is another main problem to be overcome when machining titanium alloys, especially for finish machining, the low modulus of elasticity of titanium alloys (Table 2.1) being a principle cause of the chatter during machining. When subjected to cutting pressure, titanium deflects nearly twice as much as carbon steel, and the greater spring-back behind the cutting edge results in premature flank wear, vibration and higher cutting temperature. In effect, there is a bouncing action as the cutting edge enters the cut. The appearance of chatter may also be partly associated with the high dynamic cutting forces in the machining of titanium. This force can be up to 30% of the static force due to the adiabatic or catastrophic thermoplastic shear process by which titanium chips are formed.

These problems may be minimized by employing very rigid machines, using proper cutting tools and set-ups, minimizing cutting pressures, providing copious coolant flow and designing special tools or non-conventional cutting methods.

2.2.2.2. Machined Surface and Subsurface

During machining of titanium alloys, many forms of surface defects on the machined surface are reported in the literature. Main surface defects observed during machining are surface drag, material pull-out/cracking, feed marks, adhered material particles, tearing surface, chip layer formation, debris of microchips, surface plucking, deformed grains, surface cavities, slip zones, laps (material folded onto the surface), and lay patterns [57-59]. Surface defects mainly depend on the cutting conditions and the tool materials. Surface roughness increases with the cutting speed (Fig. 2.15a) and cutting time (Fig. 2.15b) [60,61]. However, the presence of lubricant reduces the amount of surface damage in the workpiece during machining [58].

During machining operations, the thermal, mechanical, and chemical effects on the workpiece material can lead to strain aging or recrystallization of the material. Due to the strain aging process, the material might become harder but less ductile, and recrystallization might cause the material to become less hard but more ductile. These thermal (high temperature and rapid quenching) and mechanical (high stress and strain) effects are the main reasons for the microstructural alterations in the material, as well as for phase transformations and plastic deformations [62].

During machining of Ti-6Al-4V alloy, grains below the machined surface were observed to deform along the machined direction due to the thermal and mechanical

effects [59,63]. The depth of the deformed zone mainly depends on the cutting conditions. Velasquez et al. [63] observed that the deformed zone increased with the cutting speed. It is reported that an overheated white layer can be formed when titanium alloy is machined in an abusive manner (such as using a dull tool). This white layer may be harder or softer than the base metal depending on the cutting conditions [64,65]. The white layer is also formed during machining of hardened steel and this white layer is harder compared to the bulk metal [66].

2.2.2.3. Mechanism of Chip Formation in Ti6Al-4V Alloy

Under conventional cutting conditions and even at low cutting speeds, formation of saw-tooth (or serrated) chips (Fig. 2.16) is a fundamental characteristic of the machined Ti–6Al– 4V alloy [67]. Two different mechanisms have been adopted to describe saw-tooth chip formation during machining under different machining conditions, namely (i) the initiation and propagation of cracks inside the primary shear zone of the workpiece material and (ii) the thermoplastic instability.

Cook et al. [68], Nakayama et al. [69], Elbestawi et al. [70], Vyas and Shaw [71] and Poulachonand Moisan [72] have suggested that a crack initiates periodically at the free surface of the workpiece ahead of the tool and propagates towards the tool tip. Thus the periodic cracks originated at the free surface are the root of saw-tooth chip formation. Discontinuous chips are formed during orthogonal cutting of aluminum 6% silicon alloy (319 Al) due to the crack formation [73]. According to Hua and Shivpuri [74], serrated or saw-tooth chips are formed during machining of Ti-6Al-4V alloy due to crack initiation and propagation.

R. F. Recht [7], Komanduri et al. [24], Semiatin and Rao [75], Xia et al. [76-78] and Hou and Komanduri [79] have proposed thermoplastic instability as the root cause of saw-tooth chip formation during machining of titanium alloy. This mechanism is often referred to as the formation of adiabatic shear band.

Recent publications tend to support the thermoplastic shear instability theory rather than the periodic theory. Gente and Hoffmeister [80] introduced a new quick stop method to obtain partially formed chip during machining of Ti-6Al-4V alloy at extremely high cutting speed and found that the serrated chips are formed due to the localized shear. Puerta Velásquez et al. [81] performed metallurgical analyses on chips obtained from high speed machining of Ti6Al4V alloy and found that the saw-tooth chips were formed due to the catastrophic thermoplastic shear, instead of the periodic crack initiation. Cotterell and Byrne [82] recorded the saw-tooth chip formation cycle of Ti6Al4V by high-speed imaging system and found that the thermoplastic shear instability or adiabatic shear band resulted in saw-tooth chip formation during machining of titanium alloy Ti6Al4V. Barry and Byrne [83] studied the mechanism of chip formation in machining hardened steels and concluded that the saw-tooth chip is formed due to the adiabatic shear.

2.2.2.4. Adiabatic Shear Band

Adiabatic shear band (ASB) was observed for the first time by Zener and Hollomon [84] in 1944. ASB is a region where plastic deformation in the material is highly concentrated. Adiabatic shear results from plastic instability arising when the combined effects of strain and strain rate hardening are outweighed by the thermal

softening caused by effectively adiabatic plastic deformation [8,23]. ASB usually manifests as zones of intense shear deformation and/or microstructural modification of the original material up to hundreds of micrometres wide, interspersed between regions of relatively homogeneous deformation. The maximum temperature attained within the developing shear bands may be up to several hundred degrees above that of the surrounding matrix [85].

Adiabatic shear deformation is a term used to describe the localization of plastic flow that occurs in many metals when they are deformed at high strain rates to large plastic strains [86]. The titanium alloy Ti-6Al-4V is very susceptible to adiabatic shear localization which dominates its deformation behaviour at large plastic strains under conditions of rapid deformation, for example in ballistic impact [8], machining [50], high strain rate compression [87], and dynamic torsion [88]. This is an important mode of deformation as the shear zones often become the sites later on for eventual failure of the material.

2.2.2.4.1. Criteria of Forming Adiabatic Shear Band

It has been reported that an adiabatic shear band is observed in discrete zones of intense shear deformation, and large shear strains are a prominent feature of the band. Depending on the alloy, various combinations of process variables such as tool and workpiece geometry, deformation rate, preheat temperature, die temperature and lubrication, as well as material parameters such as strain-rate sensitivity and temperature dependence of the flow stress, strain hardening rate, thermal conductivity, specific heat,

and the phase transformation kinetic have been observed to lead to the development of bands [89].

According to Recht [7], the criteria for catastrophic slip can be written as:

$$0 \leq \frac{\frac{\delta \tau}{\delta \varepsilon}}{-\frac{\delta \tau}{\delta T} \frac{dT}{d\varepsilon}} \leq 1 \tag{2.22}$$

In Eq. 2.22, if the ratio between the strain hardening and thermal softening is between zero and 1, the material will shear catastrophically and shear band will be formed. Negative value of the ratio indicates that the material actually becomes stronger with an increase in temperature and that shear deformation will distribute. High positive values above the unity indicate that strain-hardening is predominant, and shear deformation will distribute throughout the material.

According to Lemaire and Backofen [23], the criterion for instability can be expressed as:

$$\left(\frac{\partial \tau}{\partial T}\right) \cdot \left(\frac{\partial T}{\partial \gamma}\right) < -\frac{C_{m_R} \cdot b}{A} \tag{2.23}$$

Where C_{m_R} = machine stiffness in the direction of the resultant force, b = shear zone thickness, A = area of the sheared plane.

Culver [90] and Timothy and Hutchings [8] suggested that the shear localization is imminent once a critical shear strain has been exceeded and the critical instability strain, γ_i, is given by:

$$\gamma_i = \frac{n\rho C}{\beta(\frac{\delta\tau}{\delta T})_{\gamma,\dot{\gamma}}} \qquad (2.24)$$

where ρ is the density of the material, n is the strain hardening exponent, C is the specific heat capacity, β is the fraction of plastic work that appears as heat (generally $0.9 \leq \beta \leq 1.0$), and $\delta\tau/\delta T$, is the slope slop of the temperature dependence of flow stress taken at constant strain and strain rate.

Bayaumi and Xie [91] suggested that the shear band formation during machining depends on the chip load factor = Vf. Here, V is the cutting speed and f is the feed rate. In the case of Ti-6Al-4V alloy and AISI 4340 steel, the critical cutting load value is 0.004 and 0.006 respectively. According to Komanduri and Hou [92], a critical cutting condition is necessary for the shear band formation (Fig. 2.17).

2.2.2.4.2. Types of Adiabatic Shear Band

Shear bands can be classified depending upon whether or not they are accompanied by a phase change in the material and also upon the extent of adiabatic strain localization [8]. Backman and Finnegan [93] originally proposed that shear bands in different metals could be broadly classified as either deformed or transformed depending on the temperature at the shear band. The temperature within the shear zone, T_{sz}, can be measured by [23]:

$$T_{sz} = \frac{\tau\gamma_{sb}}{\rho C} \left[\frac{1}{1+1.328\sqrt{\frac{K\gamma_{sb}}{V_c d}}} \right] + T_{amb} \qquad (2.25)$$

where ρ is the density, C is the specific heat capacity, τ is the shear stress, K is the thermal diffusivity of the alloy, T_{amb} is the ambient temperature, V_c is the cutting speed, d is depth of cut which is equal to the feed rate, and γ_{sb} is the shear strain within the shear band. According to [94], the shear strain, γ_{sb}, within the shear band can be estimated by the shear displacement within the shear band, d_s, divided by the thickness of the shear band, t_s (Fig. 2.16):

$$\gamma_{sb} = \frac{d_s}{t_s} \tag{2.26}$$

A. Deformed Shear Bands: The deformed adiabatic shear zone is not accompanied by any phase change in the material, even though the grains present in the band show an extremely high amount of distortion. Fig. 2.18 depicts that the deformed shear band is formed in 7039 aluminum alloy during the ballistic impact test [95].

B. Transformed Shear Bands: The term transformed is associated primarily with a phase transformation in the shear band, hence restricting number of alloy systems in which it can form. A permanent change in structure is associated with the transformed shear band, and the relative larger temperature rise within developing transformed shear zones is therefore assumed by definition (Fig. 2.19). Metals of low thermal diffusivity and of low resistance to adiabatic shear localization were found to be more susceptible to the formation of transformed shear bands. In general, the formation of a transformed shear band appeared to correspond to an advanced stage of adiabatic strain localization in a given metal, with a deformed shear band representing an earlier stage in this process [85].

It is claimed that during orthogonal cutting of Ti–6Al–4V alloy, the temperature rises rapidly to above allotropic phase transformation temperature (995±15 °C), and the lattice structure of Ti–6Al–4V changes from hcp (α-phase) with fewer slip planes into bcc (β-phase) with more slip planes [96,97]. New slip planes accelerate localized deformations, cause further instability and complexity in the plastic deformation process, and result in formation of serrated chips [6]. However, Velasquez et al. [81] used electron backscatter diffraction or EBSD measurements and claimed that deformed shear band was formed because no phase transformation occurred within the shear band during machining of Ti-6Al-4V alloy.

2.2.2.4.3. Hardness of the Shear Band

Shahan and Taheri [98] report that the shear zone hardness depends on the alloy forming conditions and the widths of the adiabatic shear zone could be either harder or softer than the surrounding regions. The hardness may change by as much as 100 HV in the banded microstructure. For steels, transformed shear bands are usually much harder than the surrounding material [99]. Figure 2.20a shows the microhardness traverse for an AISI 4340 steel. The hardness inside a shear band in Ti-6AI-4V alloy was not substantially different from the surrounding region [25,100,101] (Fig. 2.20b). It was claimed that the α' martensite formed in the transformed shear band was up to ∼ 10% softer than the adjacent deformed matrix [8].

2.2.2.4.4. Effect of Cutting Conditions on Adiabatic Shear Bands

The adiabatic shear banding phenomenon in the metal cutting process is mainly affected by cutting conditions and material properties. The effects of cutting conditions

on chip formation can be understood by the effect of those on the cutting temperature and hence the work hardening/softening rate. It was concluded by Bayoumi and Xie [91] that the cutting speed and feed rate are the dominant factors to influence the onset point at which the shear localized chips can be initiated. The shear banding frequency is defined as the average distance between the centre-line of two consecutive shear bands (L_c value in Fig. 2.16), which can be used to depict how frequently the shear bands are generated during the chip formation process. This is a useful parameter for the purpose of chip control and/or disposal in automatic machining operations.

Shear band frequency or the average distance between the centre-line of two consecutive shear bands increases with the cutting speed and the feed rate due to the increment of cutting temperature or thermal gradient [102]. However, Bayoumi and Xie [91] and Molinari et al. [97] claimed that the shear banding frequency increases with decrease of the cutting speed.

Wright and Ockendon [103] and Molinari [97] have determined the characteristic distance, L_c, between adiabatic shear bands obtained in a shear test at high strain rates, and the L_c is given by:

$$L_c = 2\pi \left(\frac{m^2 kc(1-a)^2 \theta_0^2}{\left(1+\frac{1}{m}\right)\beta^2 (\dot{\gamma})^3 \hat{\tau}_0 a^2} \right)^{\frac{1}{4}} \tag{2.27}$$

where m is the strain rate sensitivity, k is the heat conductivity, c is the heat capacity per unit mass, β is the Taylor Quinney coefficient characterizing the part of plastic work

transformed into heat, a is the thermal softening parameter, θ_0 is the initial temperature, $\hat{\tau}_0$ is the stress which can be written as:

$$\hat{\tau}_0 = \tau_0(1 - a)\left(\frac{\dot{\gamma}}{\dot{\gamma}_0}\right)^m \tag{2.28}$$

where τ_0 is the shear flow resistance, $\dot{\gamma}$ is the shear strain rate and $\dot{\gamma}_0$ is the reference strain rate. Eq. 2.27 shows that the distance between two shear bands, L_c, decreases with increase in the strain rate as well as the cutting speed. However, the recent publication [104] shows that the distance between the shear band or the value of L_c (Fig. 2.21) and the thickness of the shear band increases with the cutting speed and feed rate due to the increment of thermal gradient.

2.2.2.5. Tool Materials for Machining of Ti-6Al-4V Alloy

Major improvements in the rate at which workpieces are machined usually result from the development and application of new tool materials. However, none of these developments in cutting tool materials has had successful application in improving the machinability of titanium alloys. The requirements of the tool material for machining titanium alloy, are: (i) high hardness to resist the high stresses involved; (ii) good thermal conductivity to minimize thermal gradients and thermal shock; (iii) good chemical inertness to depress the tendency to react with titanium; (iv) toughness and fatigue resistance to withstand the chip segmentation process; and (v) high compressive, tensile, and shear strength.

Dearnley and Grearson [105] carried out many trials involving various tool materials in the continuous turning of Ti-6AI-4V and confirmed that the K grade carbides

were the best choice. They suggested that those WC/Co alloys with Co content of 6 wt% and a medium WC grain size (about 0.8 and 1.4 μm) provided the optimum performance. It has been proven that steel cutting grades (P grades of ISO codes) of cemented carbides are not suitable for machining titanium alloys because of the greater wear rate of the mixed carbide grains compared that of the WC grains [54,56,105,106].

All coated carbide tools tested (cemented carbides coated with TiC, TiCN, TiN-TiC, Al_2O_3-TiC, TiN-Ti(C,N)-TiC, Al_2O_3, HfN, and TiB_2) also show greater wear rates than those of straight grade cemented carbides [105,106]. Bhattacharyya et al. [107] observed the performance of triple coated cemented carbide tools when machining Ti-6Al-4V alloy and showed that chemical interactions between coating materials and workpiece occurred, and the coating thus was rapidly removed, resulting in the substrate acting as the cutting edge over most of the tool life.

The super-hard cutting tool materials (cubic boron nitride and polycrystalline diamond) have also shown good performance in terms of wear rate in the machining of titanium [105,108]. However, their applications are limited due to their high price.

2.2.2.6. Tool Wear during Machining of Ti-6Al-4V Alloy

Some specific studies on tool failure modes and wear mechanisms when machining titanium alloys have been conducted [56,60,105,106]. Notching, flank wear, crater wear, chipping, and catastrophic failure are the prominent failure modes when machining titanium alloys, these being caused by a combination of high temperature and high cutting stresses developed at the cutting edge of the tool, the strong chemical reactivity of titanium, the formation process of catastrophic shear or serrated chips, and

so on. Figure 2.22 depicts the different types of wear formed during machining of Ti-6Al-4V alloy.

Tool life can be expressed as the time or volume of material removed before a cutting tool becomes worn out or fractures. In machining titanium alloys, small changes in cutting speed cause extremely high changes in tool life. Flank wear, rake wear and tool life are significantly affected by the cutting speeds [60,109,110]. Increase in cutting speed caused the bigger increment in cutting temperature at the cutting edge of the tool. High temperature plays an important role to reduce the strength of the tool as well as to promote the reactivity of different wear mechanisms [60,110]. Tool life in machining titanium alloys, however, is also sensitive to changes in feed [5]. Fig. 2.23 reveals the effect of cutting speed and feed on tool life in turning Ti-6AI-4V.

2.2.2.7. Temperature at the Tool Tip

The combination of a small contact area and the low thermal conductivity of Ti-6Al-4V alloy results in very high cutting temperatures at the tool tip. The analysis of the microstructure suggests that the maximum temperature rise during formation of the shear band occurs at the centre of the zones [98,101]. The thin chips, a thin secondary shear zone and a short chip-tool contact length cause high tool-tip temperatures of up to about 1100°C [54,55,105].

2.3. Finite Element Modeling

2.3.1. Introduction

Modeling of the metal cutting process using the finite element method is effective to reduce the machining costs and analysis time. This numerical method takes into account not only the large deformation, strain rate effect, tool-chip contacts and friction, local heating and temperature effect but also the different boundary and loading conditions, and other phenomena encountered in the metal cutting processes. These operations are dynamic in nature, and this method is also able to analyze the dynamic deformation behaviour that occurs over a short time interval within which the loads and boundary conditions are highly time dependent.

A commercially available FE code, LS-DYNA was used in the present work. LS-DYNA is an explicit FE program, developed by Livermore Software Technology Corporation (LSTC), and capable of performing non-linear dynamic analyses of both two-dimensional and three-dimensional structures [9].

2.3.2. Types of Element Formulations in LS-DYNA

Numerical modeling for high strain (and strain rate) typical of metal cutting processes consists of three major element formulation implementations, namely, Lagrangian, Eulerian and Arbitrary Lagrangian-Eulerian (ALE). Comparisons of Lagrangian, Eulerian and Arbitrary Lagrangian-Eulerian (ALE) element formulations from Livermore Software Technology Corporation's tutorial [111] are discussed below.

In the Lagrangian element formulation, the FE mesh consists of material elements that cover the region of analysis exactly. These elements are attached to the material and are deformed with the deformation of the workpiece (Fig. 2.24a). This approach is very convenient, particularly, when unconstrained flow of material is involved, because the FE mesh will accurately represent the material boundaries during the course of the analysis.

Another approach in modeling of metal cutting is to apply an Eulerian FE formulation method where the overall mesh can be considered as two overlapping meshes consisting of a background spatial mesh, which is fixed in space, and material, which can flow through the fixed mesh (Fig. 2.24b). Because the mesh is fixed in space, the numerical difficulties associated with the distortion of the elements are eliminated. Eulerian FE formulation methods have two main steps: the Lagrangian step and the Eulerian advection step. The Lagrangian step, performed first, advances the solution in time, whereas the Eulerian step accounts for the transport between the elements. The Lagrangian step in the Eulerian element formulation is very similar to the time step in Lagrangian element formulations. After the Lagrangian step, the mesh is remapped to its original spatial coordinates, referred to as advection step or the Eulerian step.

The Arbitrary Lagrangian-Eulerian formulation is a hybrid of the Eulerian and Lagrangian formulation. ALE and purely Eulerian formulations are the same in their Lagrangian step but differ in the advection step. However, the Eulerian mesh is always remapped back to its original position during the advection step, the ALE mesh is remapped to an entirely new mesh smoothed only to a level that eliminates excessive distortion (Fig. 2.24c). Meshes can be smoothed by using smoothing weight factors such as: 1) simple average, 2) volume weighting, 3) equipotential, and 4) equilibrium. Each of

the smoothing factors has a unique approach to determine the coordinates of nodes in the advection step [112].

In both the Eulerian and ALE formulation methods, the advection step can be either a first-order donor cell where the properties are assumed constant throughout the element or a second-order Van Leer to allow the interpolation of properties within an element into a piecewise function [113,114].

2.3.3. Studies on Metal Cutting Using Finite Element Modeling

2.3.3.1. Lagrangian Element Formulation

One of the earliest FE models for metal cutting was developed by Klamecki [115], who simulated the cutting process from the incipient state using three-dimensional FEM modeling. The model did not thrive largely due to significant modeling shortcuts, such as modeling the workpiece as a perfectly plastic material and disregarding friction. Usui and Shirakashi [116] treated steady-state metal cutting based on empirical data and assuming rate-independent deformation behaviour. A later study by Iwata et al. [117] considered the effect of friction between the chip and the tool rake face but was limited to very low cutting speeds and strain rates and assumed rigid-plastic deformation. Strenkowski and Carroll [118] and Carroll and Strenkowski [119] used the FE method applying Lagrangian formulation to model the orthogonal metal cutting process, developed a technique for element separation in front of the tool tip, and proposed an element-separation criterion based on the magnitude of plastic strains. The chip-tool interaction was accounted for using several methods, including defining a constant coefficient of friction at the interface [118] and defining a distinct coefficient of friction

35

for the two regions of contact (sticking and sliding) [120]. Ceretti et al. [121] considered the effect of friction and temperature increase in orthogonal cutting and compared the simulated results with the experimental results; the simulated results were in good agreement with experiments in terms of estimating chip geometry, tool workpiece contact length, and chip and tool temperatures (Fig. 2.25). Shih and Yang [122] and Shih [123,124] conducted a combined experimental and numerical investigation of the orthogonal metal cutting process to consider the effects of large strain, high strain-rate, and temperature.

Most studies dealing with FE modeling of orthogonal cutting hava implemented a Lagrangian FE formulation due to accurate representation of the material boundaries during the analysis. However, due to the high strains on the order of 2 to 8 [125] and high strain rates of 10^3 to 10^7 s^{-1} [3] associated with the machining process, application of a Lagrangian FE mesh often degrades the accuracy of the simulation due to severe mesh distortion. Because of chip separation/breakage criterion or application of a failure criterion along a predetermined line lying parallel to the cutting direction at the level of the tool tip [126-129], adaptive meshing or continuous re-meshing [121,130-132] are commonly used techniques to compensate for mesh distortion and disintegration. In the geometrical and physical criteria, separation occurs at a critical distance from the tool tip and when a critical shear stress is reached, respectively. In the combined geometrical and physical criterion, separation is prompted by either critical distance or critical shear stress, whichever occurs first [133,134]. Lin and Lo [135] applied the geometry criterion to simulate ultra-precision orthogonal cutting for oxygen-free high-conductive copper, with validation by numerical-experimental comparison in terms of cutting force. In Fig.

36

2.26, it was shown that the chip and the workpiece were connected by twin nodes along a predefined separation path OB. The chip was separated when the distance D between the leading node and the tool edge was equal to or smaller than the given value D_c. Ceretti and Marusich [130,131] have used mesh adaptivity and proved that the use of mesh adaptivity is equivalent but costly in computational time. In addition, inappropriate application of mesh adaptivity criteria may decrease the error yet still give rise to excessive processing times.

2.3.3.1.1. Lagrangian Element Formulation in Serrated Chips Formation

Most of the researchers used the Lagrangian Element Formulation to obtain the serrated chips in numerical simulations. Often there are approaches that are utilized to simulate serrated chip formation: (a) using damage or material failure models [11,136-140] or (b) using modified material models for temperature-dependent flow softening based adiabatic shearing [12,141-145]. Using the material failure criteria, Xie et al. [146] developed a numerical model of machining of Ti-6Al-4V alloy and calculated the effective plastic strain and effective shear stress distributions ahead of the tool tip (Fig. 2.27). Ceretti et al. [147] also used the damage criteria to obtain the serrated chips during machining of steel AISI 1045 and observed the temperature and stress distributions ahead of the tool tip (Fig. 2.28) and also the variation of cutting force with cutting speed. They predicted the maximum temperature and stress were generated in the material at the tool tip. Hua and Shivpuri [138] also used damage criteria to predict the chip morphology and segmentation during machining of Ti-6Al-4V alloy. Their predicted cutting forces at different cutting conditions were in agreement with the experimental results (Fig. 2.29).

Rhim and Oh [148] integrated the effect of flow softening due to dynamic recrystallization initiating after a critical strain value at temperatures higher than half of the melting temperature in the material model. Calamaz et al. [143,144] considered the adiabatic shear band formation without material failure in the primary shear zone and developed a new material model that takes into account the influence of strain, strain rate, and temperature on the flow stress and also considers the strain softening effect. Chip morphology, cutting and feed forces predicted by numerical simulations are compared with experimental results (Fig. 2.30).

2.3.3.2. Eulerian Element Formulation

Another alternative method in the modeling of the metal cutting process is to apply an Eulerian element formulation for the workpiece. Application of the Eulerian FE formulation for the simulation of the metal cutting process provides two significant advantages. First, the magnitude of strains observed in the machining process (2 to 8) can be simulated without application of mesh adaptivity or simulation results influenced by computational error due to severe mesh distortion. Second, the use of an Eulerian FE formulation eliminates the need for any element separation criterion (either physical or geometrical). Material deformation behaviour is determined based upon established material properties and is not dependent upon element separation criteria, which is potentially dependent upon the FE mesh and the problem being studied [149]. However, the Eulerian FE approach has limited applications in modelling solid mechanics problems compared with the Lagrangian element formulation [150,151].

Caroll and Strenkowski [119] used both Lagrangian and Eulerian element formulations to investigate the cutting process of aluminum 2024-T361 and suggested that the Eulerian method is more accurate and computationally less intensive than the Lagrangian formulation. The disadvantage is that the final shape of the chip cannot be easily predicted. Strenkowski and Moon [152] proposed a steady-state metal cutting technique based on an Eulerian formulation. They used the technique to predict chip geometry and temperature distribution. A good correlation between model predictions and metal cutting measurements was found.

The Eulerian formulation was also successfully employed by Raczy et al. [149] to predict the stress and strain distributions in the material (copper) subjected to orthogonal cutting. Material behaviour of the workpiece was studied using an elastic plastic hydrodynamic material model incorporated with a Voce-type stress- strain relationship. An alternative material model was based on the Johnson-Cook constitutive equation. Both of the simulation results were validated by experimental results of strain (Fig. 2.45) and stress distributions. Numerical and experimental stress and strain distributions correlated well in terms of both magnitudes and distributions. By using the Johnson-Cook constitutive equation, the predicted strain distribution ahead of the tool tip was fairly accurate, whereas the predicted tool tip stresses were higher than those from the hydrodynamic material model due to the power-law nature of the Johnson-Cook equation. Benson and Okazawa [14,153] studied application of the Eulerian finite-element formulation in machining and simulated discontinuous chip formation of AISI 4340 steel during high-speed machining.

2.3.3.3. Arbitrary Lagrangian-Eulerian (ALE) Element Formulation

An Arbitrary Lagrangian-Eulerian (ALE) formulation, which combines the advantage of both Lagrangian and Eulerian formulations in a single description, has been developed and applied to model high deformation problems such as metal forming and machining. Benson [154] was one of the first researchers to introduce the concept of the ALE element formulation and discuss its strengths and weaknesses. Many researchers have used the ALE formulation to predict chip formation, strain, strain rate and temperature, as well as chip-tool contact length, chip thickness and cutting forces. Movahhedy et al. [155,156] and Olovsson et al. [157] developed and studied the efficiency of ALE models for two-dimensional metal cutting processes. They concluded that there was no need for chip separation criteria, and the ALE formulation eliminated mesh distortions because the mesh was not obligated to follow the material flow, while enabling an approximate initial chip shape to smoothly evolve into a reasonable chip shape. Nasr et al. [158] used an ALE finite-element model to study the effects of cutting edge radius on residual stresses during orthogonal dry cutting of an austenitic stainless steel. Miguelez et al. [159] investigated the influence of geometric parameters and cutting speed during orthogonal cutting using an ALE formulation.

Pantale et al. [160] presented a two-dimensional and three-dimensional finite element model of unsteady state metal cutting performed with the Abaqus/Explicit finite element code. The yield stress was taken as a function of strain, strain rate and temperature. Instead of using one of the separation criteria, a Johnson-Cook damage law, which took into account strain, strain rate, temperature and pressure, was used in the model to better represent reality. Cutting force results agreed with experimental result

very well. von Mises stresses and distributions are shown at different stages of the cutting process (Figure 2.46).

2.3.4. Smooth Particle Hydrodynamic (SPH) Formulation

Smoothed-particle hydrodynamics (SPH) is a Lagrangian numerical technique and has found application in the study of certain problems in which large mesh deformations leading to significant numerical problems are an important concern [161,162] due to its mesh-free characteristic, that is, there is no connectivity between the particles. From the computational point of view, in the SPH formulation the workpiece is represented as a set of moving particles evolving/displacing during machining process. Each SPH particle represents an interpolation point on which all the properties of the material are known. The solution of the entire problem is calculated on all the particles with a regular interpolation function, the so-called smoothing function, over the smoothing length. The equations of conservation (mass, momentum, and energy) are then equivalent to terms expressing fluxes or inter-particular forces. The details about the mathematical basis of the SPH formulation can be found in references [161] and [163].

Over the past three decades, the SPH formulation has been improved and extends to continuum mechanics scales. Bonet and Kulasegaram [164] developed an SPH formulation for metal-forming simulations including plane strain upsetting, plane strain forging, and axis-symmetric forging. However, Buyuk et al. [165] reported that the SPH formulation is not as successful as the Lagrangian and Eulerian methods in a simulation of ballistic impact. Limido et al. [10,13] have utilized the SPH technique in two-dimensional modeling of orthogonal cutting, to simulate continuous (Fig. 2.47a) and

shear localized chip (2.47b) formation. Akarca et al. [151,166] implemented the SPH formulation for modeling of orthogonal cutting of aluminum alloy, and the numerically obtained stress-strain distribution was in a good agreement with the experimental work. Calamaz et at. [167] used the SPH formulation in modelling of orthogonal cutting of Ti-6Al-4V alloy to observe the effect of tool wear. The predicted chip morphology and the cutting force evolution with respect to the tool wear are qualitatively compared with experimental trends. Very recently, Bagci [168] and Limido et al. [169] have used the SPH formulation in two-dimensional modeling of orthogonal cutting and calculated the cutting force, and good agreement between predicted and experimental cutting forces was observed.

2.3.5. Material Models and Properties

In finite element models, an accurate material model is the key requirement for a successful process simulation. Generally the material data used to assign the material behaviour are obtained from experimental testing such as uniaxial tension test, torsion test, Taylor bar tests, and so on. Over 100 material models are available in the LS-DYNA code, including models designed to replicate the behaviour of composites, ceramics, polymers, metals, and fluids, including specialized types of materials such as foams, glass, fabric, hydrodynamic materials, plastics, rubber, soil, wood, and heart and human tissue. Each of the material models has its distinct characteristics, and the details of the material models and their applicability to the analysis are discussed in LS-DYNA Keyword User's Manual Volume I [170] and Theoretical Manual [112]. In some cases, thermal analysis is also needed to be considered. In that situation, the behaviour of the material is defined by a material model (*MAT_OPTION) and a thermal material model

42

(*MAT_THERMAL_OPTION). Again, when a material model is used in modeling hydro materials or fluids, it must be accompanied by an equation of state (*EOS_OPTION), which accounts for resistance to hydrostatic compression [103].

During the selection of a material model for high rate sensitive materials such as steel and titanium alloy, some important aspects such as the levels of strain rate and temperature dependent strain rate effects should always be taken into account. Xie et al. [146] suggested that the material behaviour during the formation of the shear localized chip or the serrated chip is very complicated and there has been no confirmed model to describe the behaviour of workpiece material during machining process. The majority of the energy dissipated in cutting is converted into heat in a very small zone, which makes the temperature distribution in the deformation zone complex. They assumed the workpiece material as an elastoplastic material and predicted the force, strain, and stress distributions (Fig. 2.41) in the material ahead of the tool tip. Hua and Shivpuri [74] used a rigid-viscoplastic material model with von Mises yield criterion to model the workpiece of titanium alloy and predicted the forces at different cutting conditions.

2.3.5.1. Johnson-Cook Constitutive Material Model

In finite element models, a constitutive material model is required to relate the flow stress to strain, strain rate, and temperature. The Johnson-Cook equation [171] is a well-known constitutive relation widely used in numerical and theoretical modeling of materials subjected to deformation in a broad range of strains, strain rates, and temperatures [172-174]. The general form of the Johnson-Cook equation is as follows:

$$\sigma = (\sigma_y + B\bar{\varepsilon}^{p^n})(1 + c\ln \dot{\varepsilon}^*)(1 - T^{*^m}) \qquad (2.29)$$

where σ_y is the yield strength, B is the strength coefficient, n is the plastic strain-hardening exponent, $\bar{\varepsilon}^p$ is the equivalent plastic strain, $\dot{\varepsilon}^* = \dot{\varepsilon}/\dot{\varepsilon}_0$ is the normalized equivalent plastic strain rate for $\dot{\varepsilon}_0 = 1.0\ \text{s}^{-1}$, m is thermal softening exponent (= 0.577 for Ti-6Al-4V alloy), and T^* is the homologous temperature and can be defined as:

$$T^* = \frac{T - T_{room}}{T_{melt} - T_{room}} \tag{2.30}$$

c is the strain rate sensitivity which can be expressed by [33]:

$$c = \frac{\dot{\varepsilon}}{\sigma}\left(\frac{\delta\sigma}{\delta\dot{\varepsilon}}\right)_{\varepsilon,T} = \frac{\log(\sigma_2/\sigma_1)}{\log(\dot{\varepsilon}_2/\dot{\varepsilon}_1)} \tag{2.31}$$

Here, $\dot{\varepsilon}_1$ and $\dot{\varepsilon}_2$ are different strain rates, and σ_1 and σ_2 are the corresponding flow stresses respectively.

Failure accumulation in the Johnson-Cook model does not directly degrade the yield surface. The model defines the strain at fracture as:

$$\varepsilon_f = [D_1 + D_2 \exp(D_3\sigma^*)][1 + D_4\ln(\dot{\varepsilon}^*)][1 + D_5 T^*] \tag{2.32}$$

where the five constants D_1, D_2, D_3, D_4 and D_5 are Johnson-Cook failure parameter, σ^* is the ratio of the pressure to the effective stress, that is:

$$\sigma^* = \frac{\text{Pressure}}{\bar{\sigma}} \tag{2.33}$$

Fracture occurs in the Johnson-Cook model when the damage parameter D exceeds 1.0. The evolution of D is given by the accumulated incremental effective plastic strains divided by the current strain at fracture as:

$$D = \sum \frac{\Delta \bar{\varepsilon}^P}{\varepsilon_f} \tag{2.34}$$

However, some authors [143,175] affirmed that the Johnson-Cook model cannot predict the adiabatic phenomenon responsible for the saw-tooth chip formation, which is common in machining processes because the strain softening is not taken into account. In order to achieve the adiabatic phenomenon, Calamaz et al. [143,144] developed a new material constitutive law, which takes into account the influence strain, strain rate, and temperature on the flow stress and also introduces a strain softening effect; and the new material flow stress is expressed by the following equation:

$$\sigma = \left(\sigma_y + B\varepsilon^n \left(\frac{1}{\exp(\varepsilon^a)} \right) \right) \left(1 + c \ln \frac{\dot{\varepsilon}}{\dot{\varepsilon}_0} \right) \left(1 - \left(\frac{T - T_r}{T_m - T_r} \right)^m \right) \left(D + (1 - D) \tanh \left(\frac{1}{(\varepsilon + S)^c} \right) \right)$$

$$\tag{2.35}$$

Sima and Ozel et al. [12], Karpat [145] also improved the Johnson-Cook model by considering the temperature-dependent flow softening, to obtain the serrated chip formation.

2.4. Research Focus

It can be concluded from the literature survey that the machining operation is an extremely complex process. This is a very important process as most titanium parts used in aerospace industries are still manufactured by conventional machining methods. Machining parameters, workpiece material property, tool material property, and lubricants or coolants play the most important roles in the machining process.

In this research the effect of feed rate and cutting speed on the machinability of the Ti-6Al-4V alloy that includes the surface quality and the forces, is analyzed. In this literature survey it was shown that the subsurface microstructure below the machined surface deformed in the cutting direction. Under this project, the depth of the subsurface deformed zone and the strain gradient are also examined. Serrated chips are formed during machining of Ti-6Al-4V alloy, and it is important to understand the mechanism of the chip formation. This work also studies the plastic deformation in the workpiece ahead of the tool tip where the chip formation starts and also the effect of feed rate and cutting speed on the chip morphology.

Under this project, numerical models that include localized strain information and take into account the deformation behaviour of the Ti-6Al-4V alloy are developed and the predicted results are compared to the experimental findings in order to validate the model and find out a most suitable model that can represent the machining operation more accurately.

FIGURES- CHAPTER 2
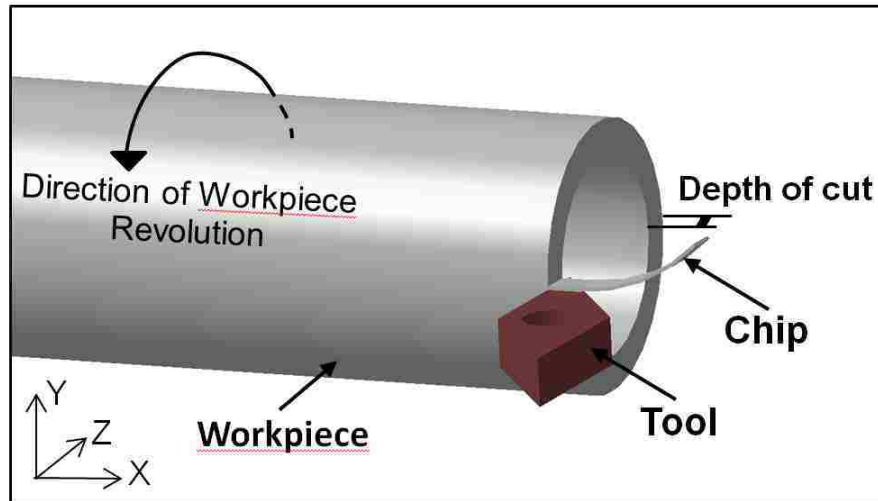
Fig.2.1. Schematic diagram showing the chip formation during the orthogonal cutting.
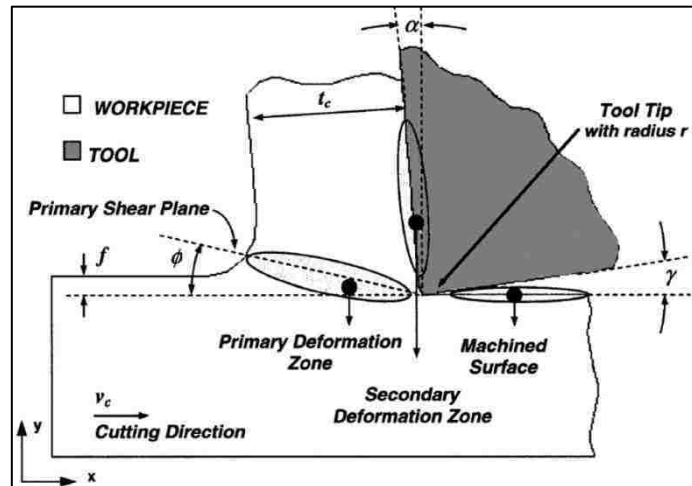
Fig. 2.2. Schematic diagram of sectioned orthogonally cut sample showing deformation zones and cutting parameters, where, α is the rake angle, γ is the clearance angle, f is the feed, V_c is the cutting speed, and φ is the primary shear plane angle, t_c is the chip thickness [149].
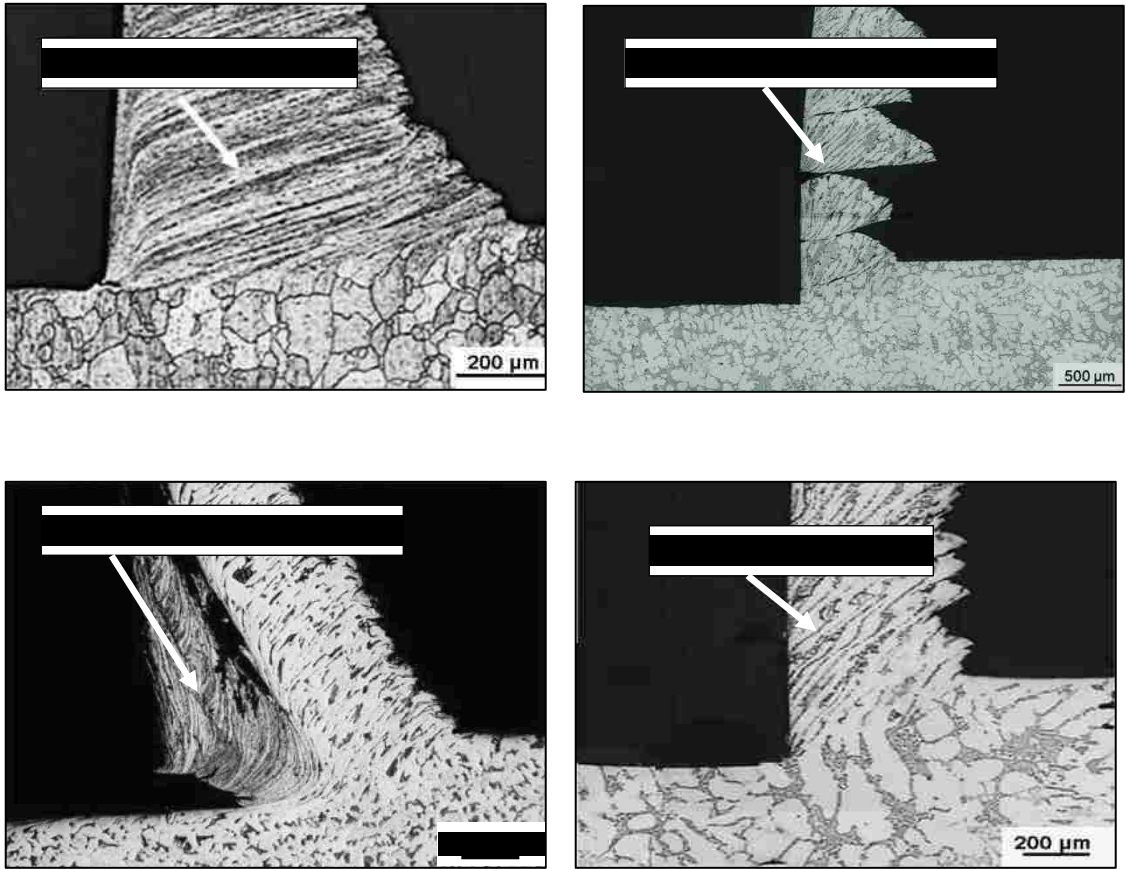
Fig. 2.3. Various types of chips produced during orthogonal machining: (a) Continuous chip formed during machining of 6061 Al at 36 m/min cutting speed and 0.30 mm/rev feed rate [20], (b) Discontinuous chip formed during machining of Al 319 at 50 m/min cutting speed and 0.35 mm/rev feed rate [73], (c) Chip with BUE formed during machining of low carbon steel at 0.24 m/s cutting speed and 0.13 mm/rev feed rate [176], (d) Serrated chip formed during machining of Al 319 at 115 m/min cutting speed and 0.25 mm/rev feed rate [73].
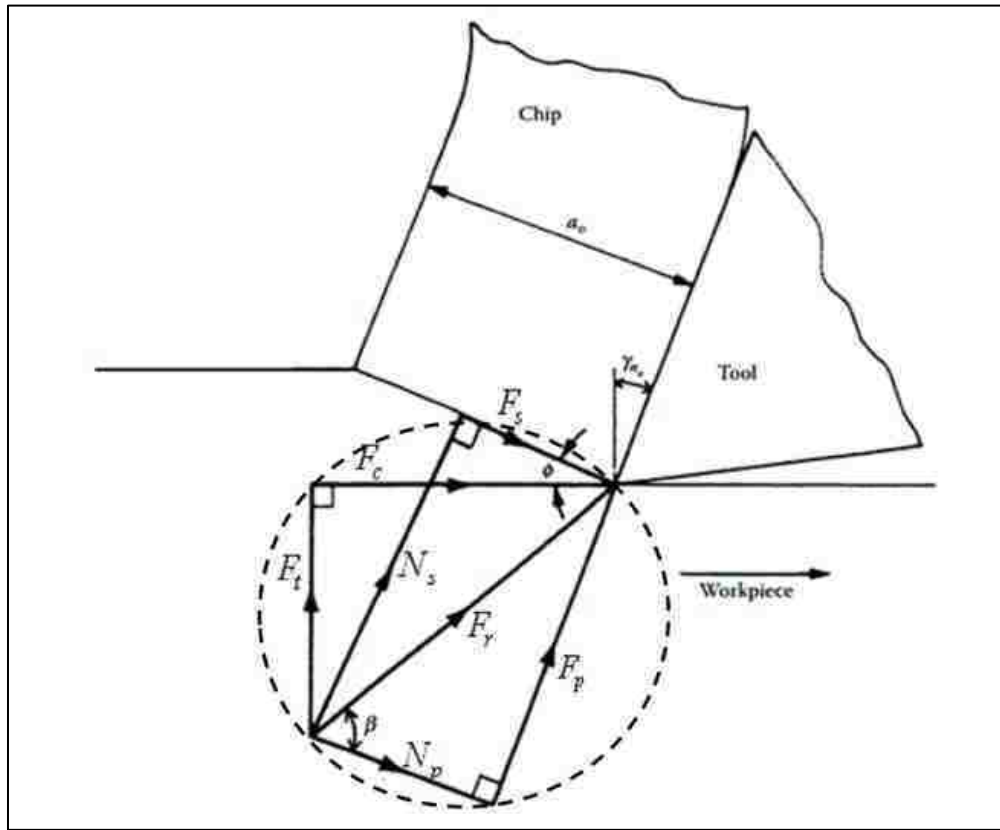
Fig. 2.4. Force diagram for orthogonal cutting where F_c is cutting force, F_t is thrust force, F_s is the shear force on the shear plane, N_s is the normal force on the shear plane, F_p is shear force on rake face and N_p is the normal force on the rake face [15].
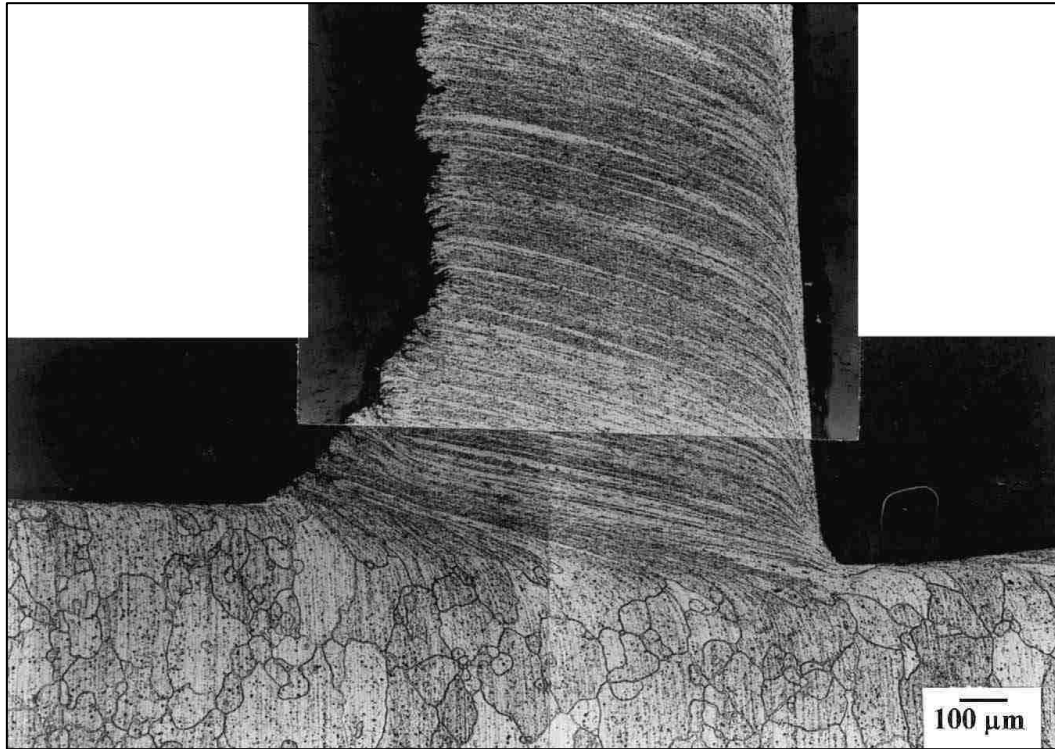
Fig. 2.5. Optical micrograph of a section through a machined chip of 6061 Al attached to the work piece. Cutting speed = 0.6 m/s, feed = 0.30 mm, rake angle = −5° [20].
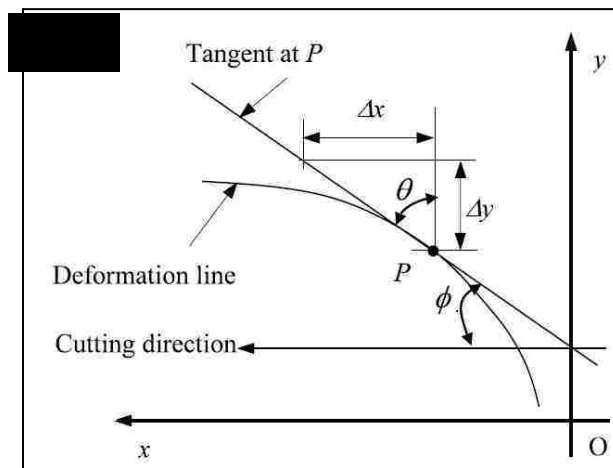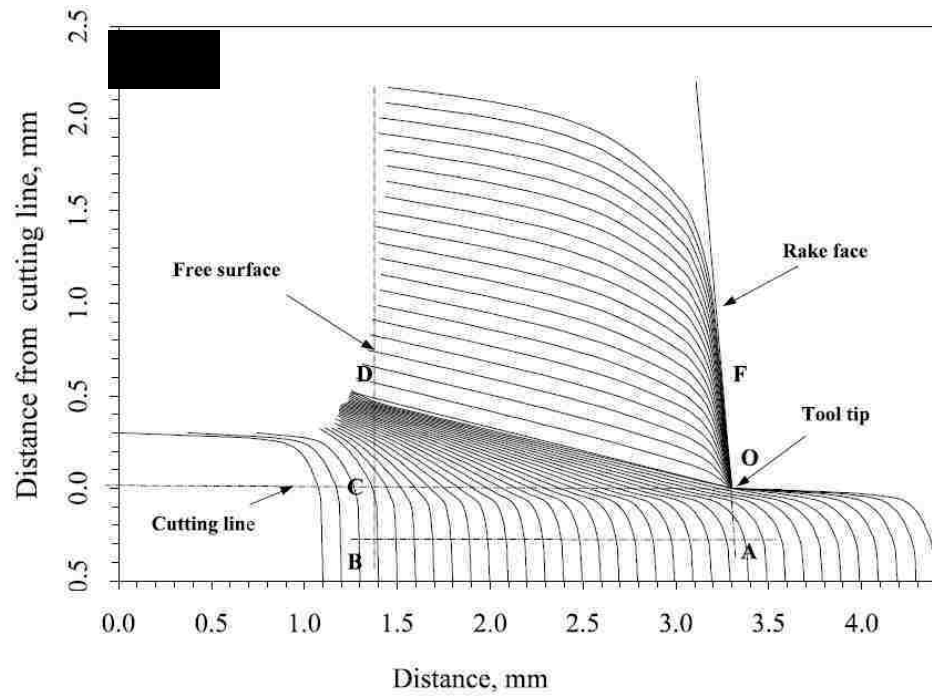
Fig. 2.6. (a) A computer-generated image of the cross-section of the machined work piece with the chip still attached. The image was obtained by determining the location of each point on the deformation lines and these were plotted to actual scale shown on the diagram, (b) Schematic diagram showing the measurement of shear angles from the slopes of the deformation lines [20].
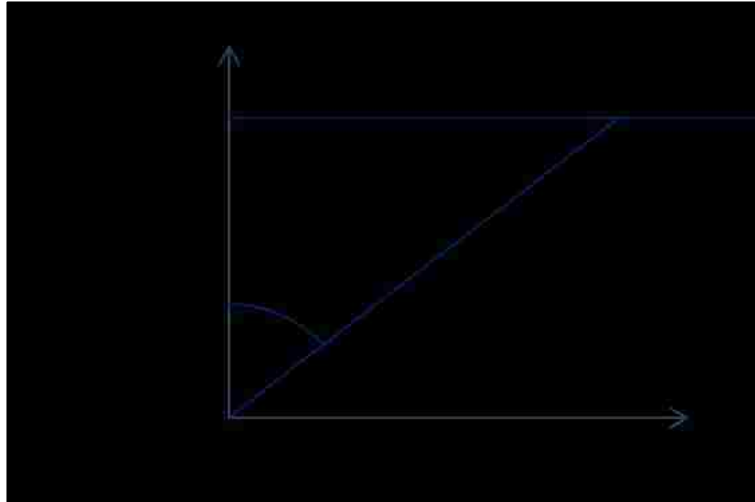
Fig. 2.7. Model for true shearing of a sphere [29]. Here ABC is an ideal sphrical crystals and after shearing it becomes A'B'C. l_x and l_y are the distances at the X and Y directions respectively and θ is the deformation angle.
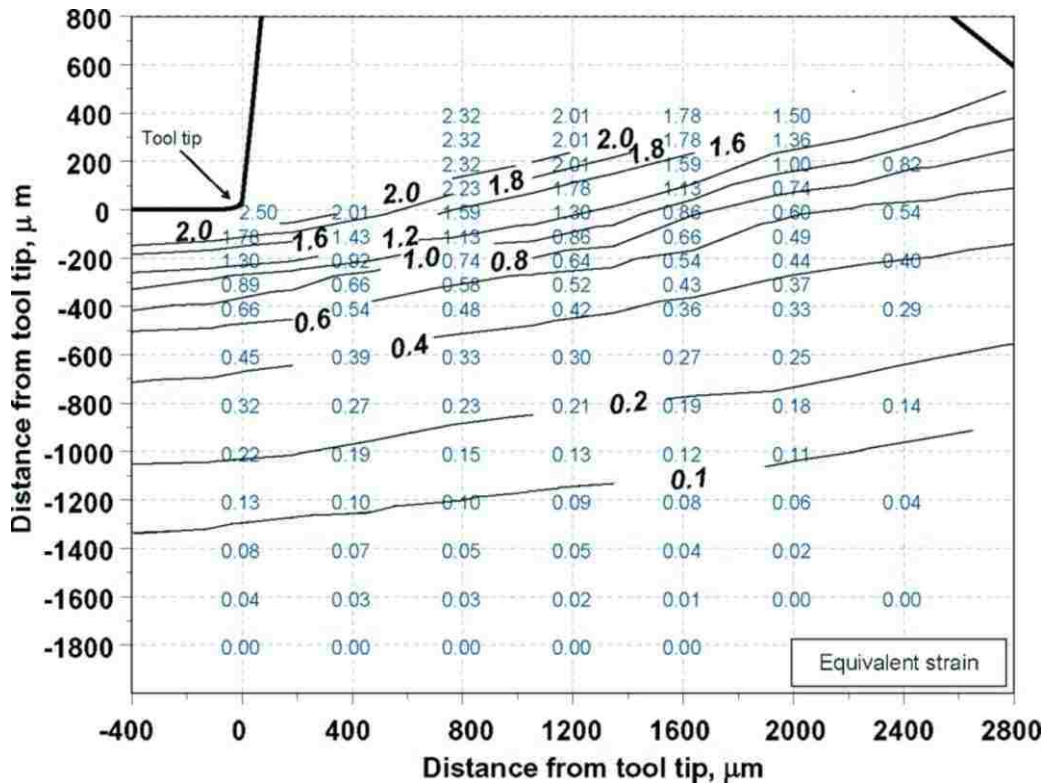
Fig. 2.8. Strain distribution diagram showing the values of equivalent shear strains, $\bar{\varepsilon}$, in the material (Al 1100) ahead of the tool tip. Equivalent strains were estimated from the local shear angle values (φ) using Eq. (2.15). The iso-strain contours are also shown [28].

52

Fig. 2.9. Plastic deformation of a flat surface by a harder spherical surface. (a) This onset of plasticity occurs at the point Z below the surface when the mean stress, $\sigma_m \approx 1.1\ \sigma_0$, (b) At a later stage the whole of the material around the indentation flows plastically; at this stage $\sigma_m \approx 3\ \sigma_0$ [177].
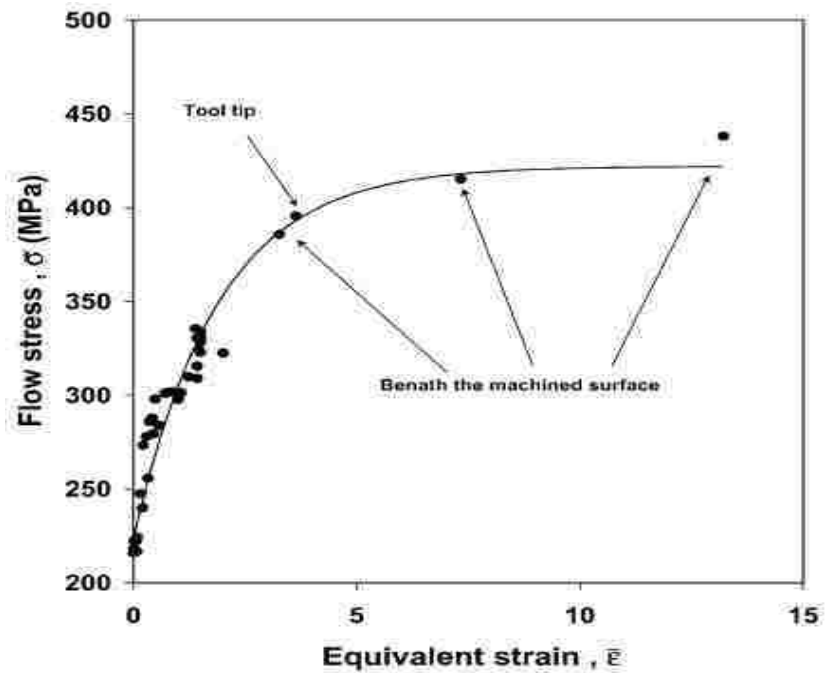
Fig. 2.10. The cumulative stress-strain curve of commercial purity copper subjected to orthogonal cutting [31].
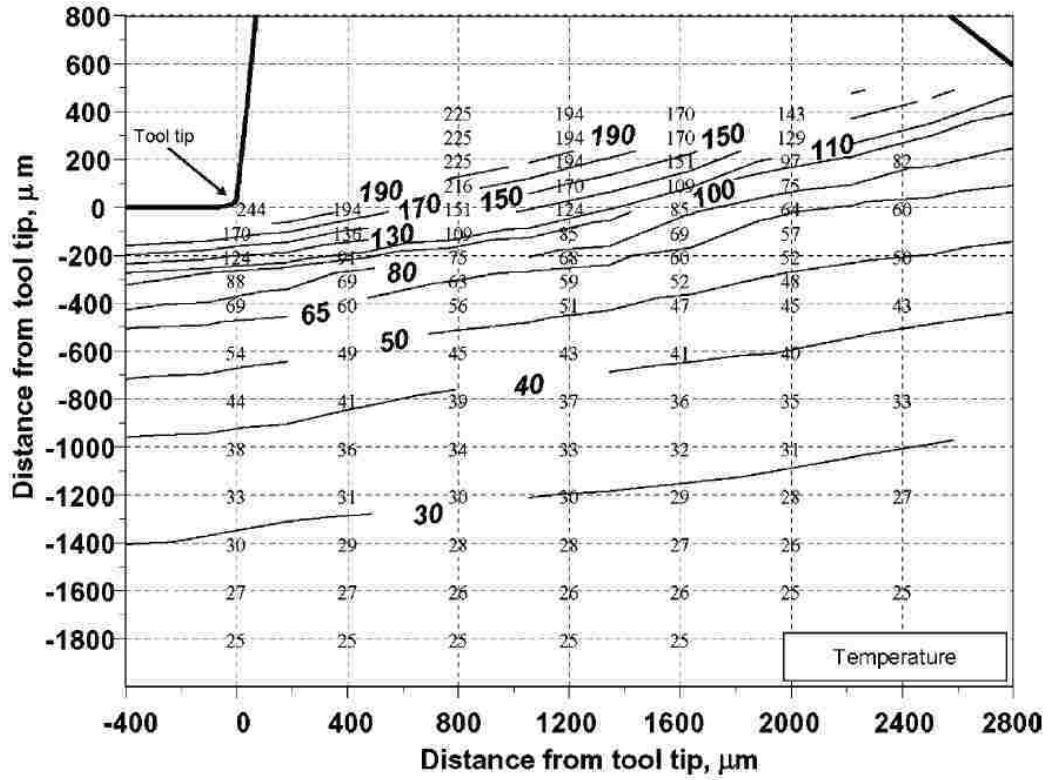
Fig. 2.11. Temperature map showing local increases in temperature as a result of transformation of the work done during plastic deformation into heat [28].
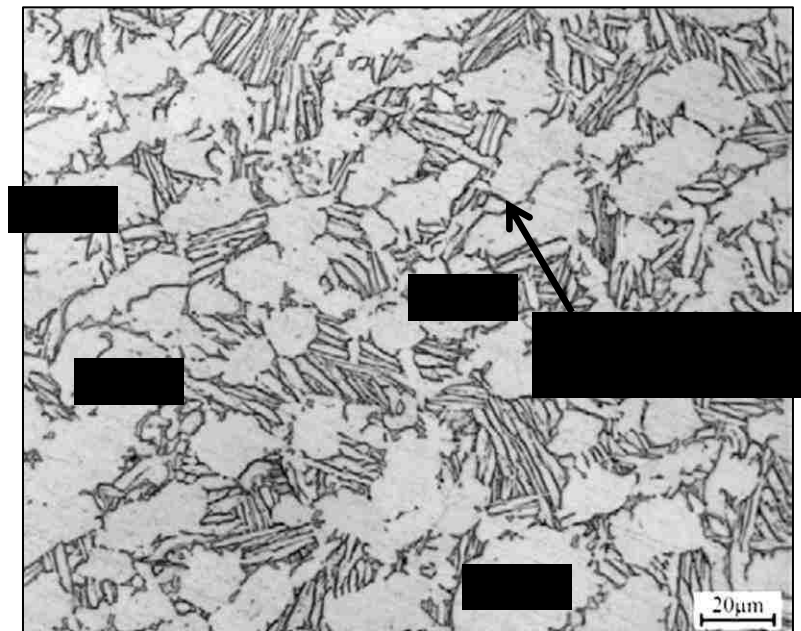
Fig. 2.12. Optical image of Ti-6A1-4V microstructure [178].
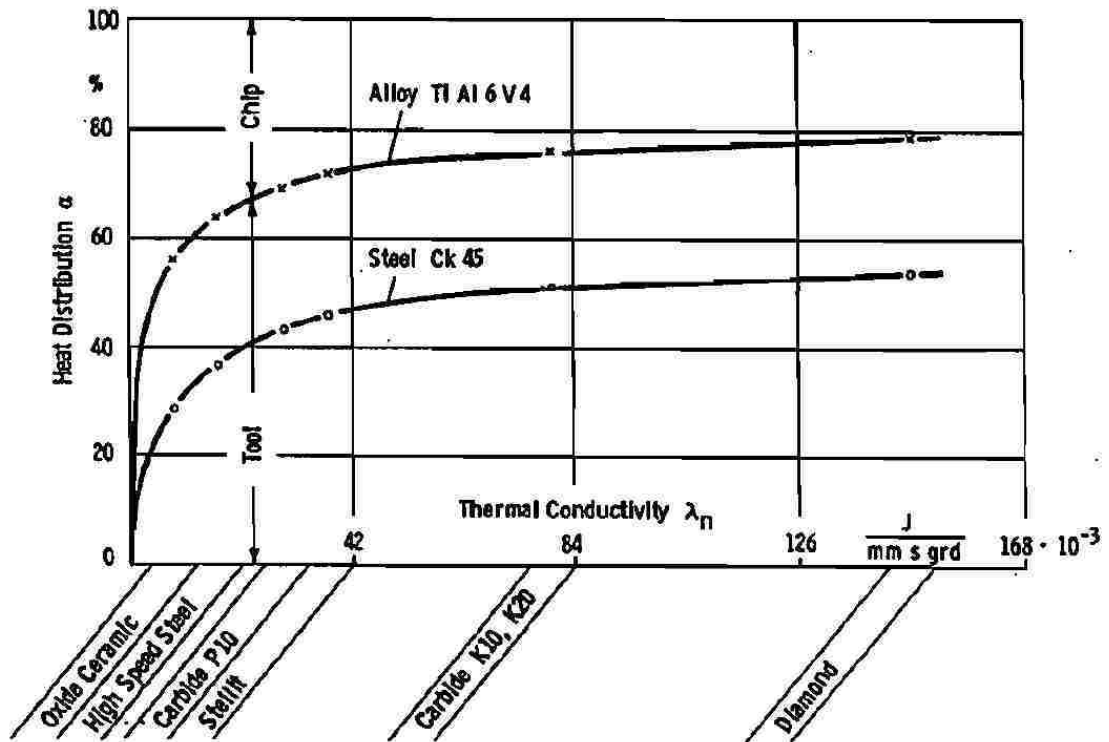
Fig. 2.13. Distribution of heat when machining titanium and steel [56] with different conductive tool materials. A large proportion of the heat generated during the machining of Ti-6Al-4V alloy is conducted into the tool due to the low thermal conductivity of the alloy.
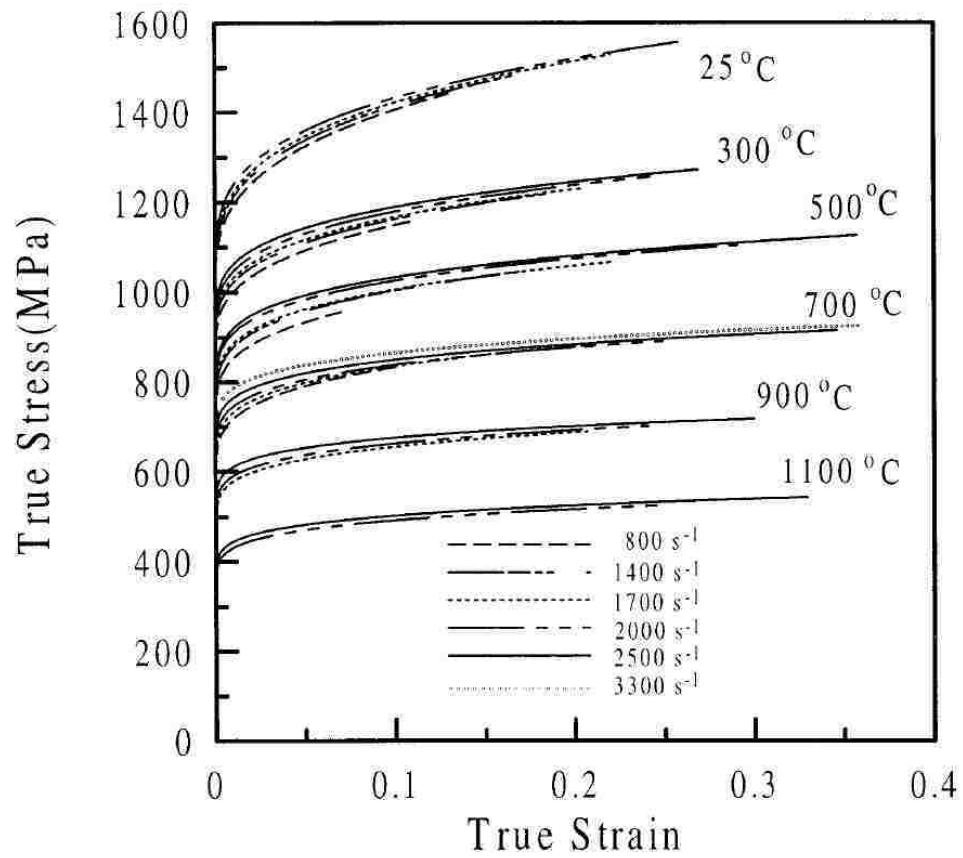
Fig. 2.14. True stress–strain curves of Ti–6Al–4V alloy deformed (compression) at different strain rates and temperature conditions [179].
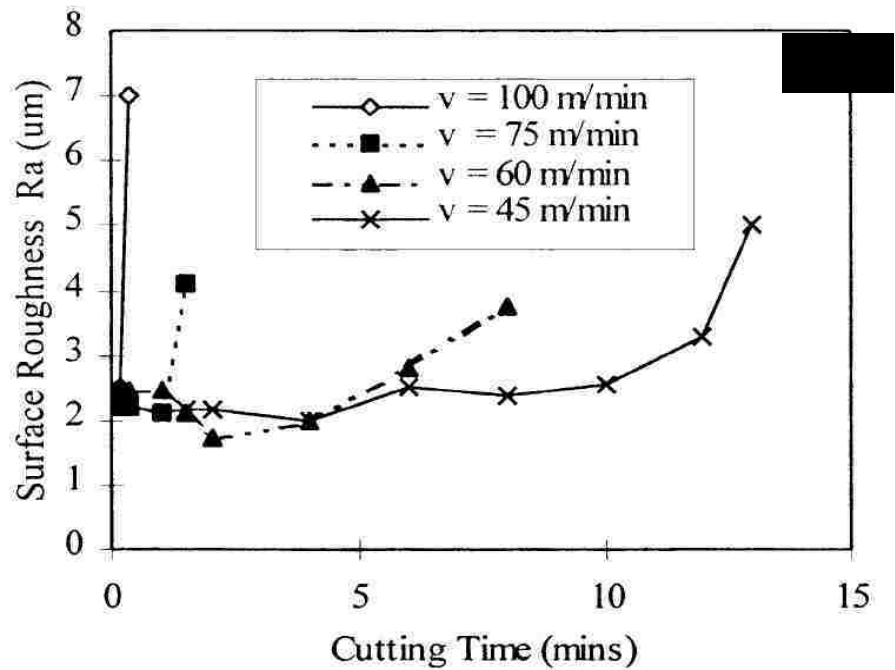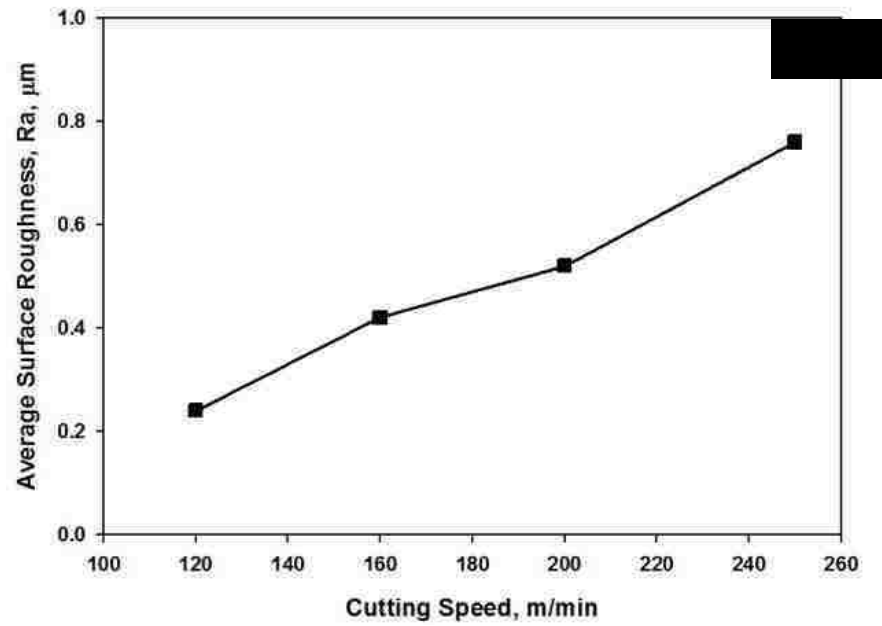
Fig. 2.15. Diagram showing the (a) variation of average surface roughness value with cutting speed for milling of Ti-64 alloy at feed = 0.1 mm/tooth and depth of cut = 1 mm [61] and (b) typical surface roughness when machining of alpha-beta titanium alloy with tungsten carbide tool (CNMG 120408-MR3-890) at feed rate of 0.25 mm/rev [60].
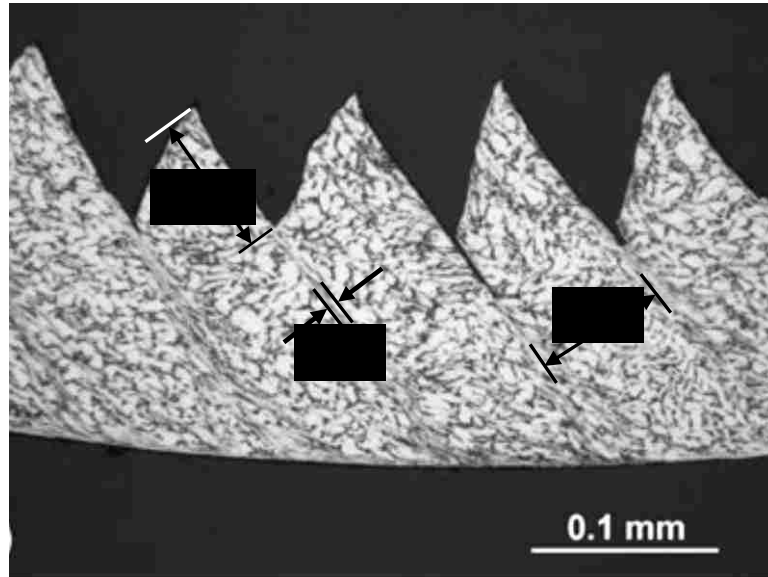
Fig. 2.16. Serrated chips are formed during machining of Ti-64 alloy where d_s is the shear displacement within the shear band, t_s is the thickness of the shear band and L_c is the distance between two consecutive shear bands (Cutting condition: feed 0.214mm and cutting speed 80 m/min) [180].
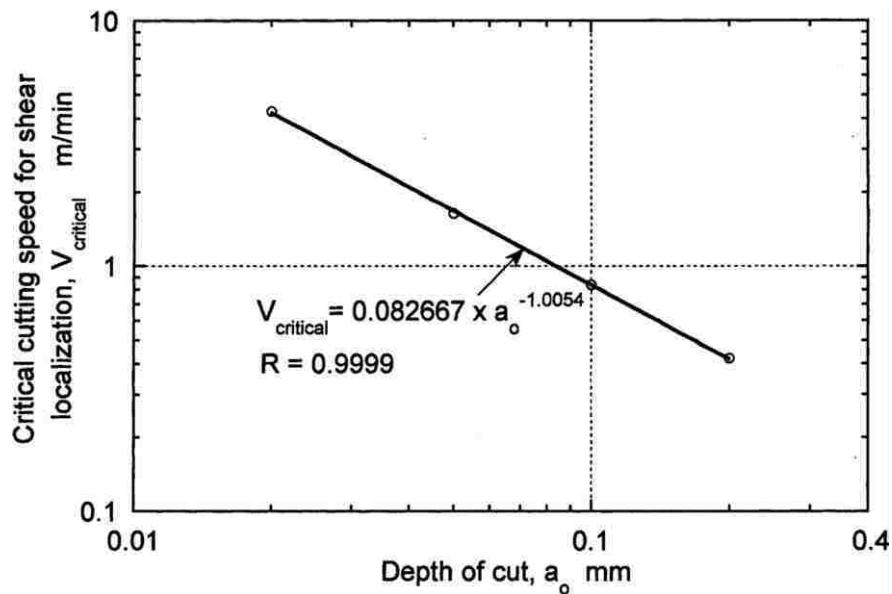
Fig. 2.17. Variation of the critical cutting velocity for shear localization with the depth of cut or feed rate [92].

Fig. 2.18. Adiabatic deformed shear band in 7039 aluminum alloy at impact velocity
311 m/s [95].
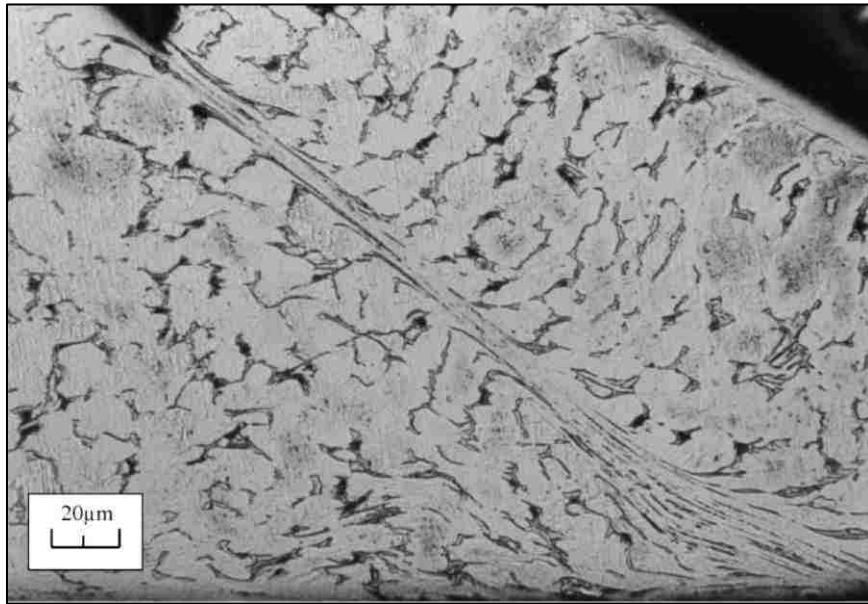
Fig. 2.19. Adiabatic transformed shear band in a chip of titanium alloy Ti-6Al-4V,
obtained by orthogonal cutting at the velocity 13 m/s [97].
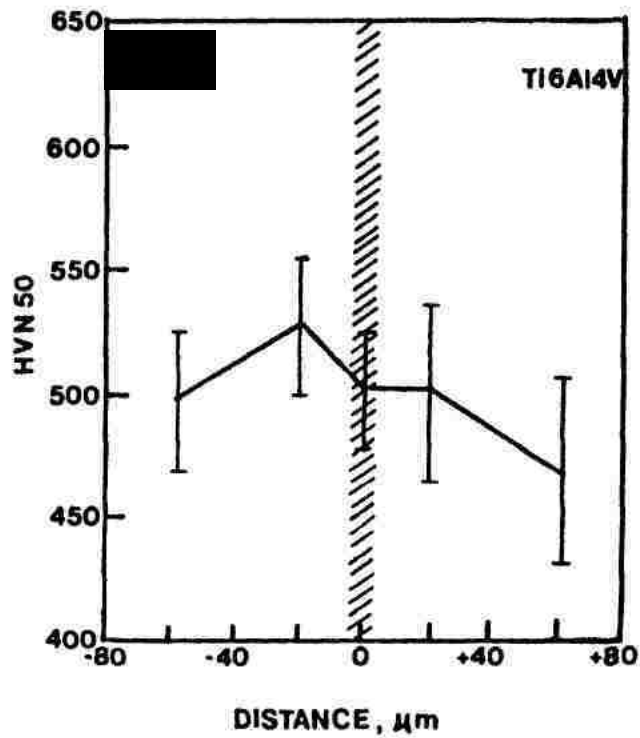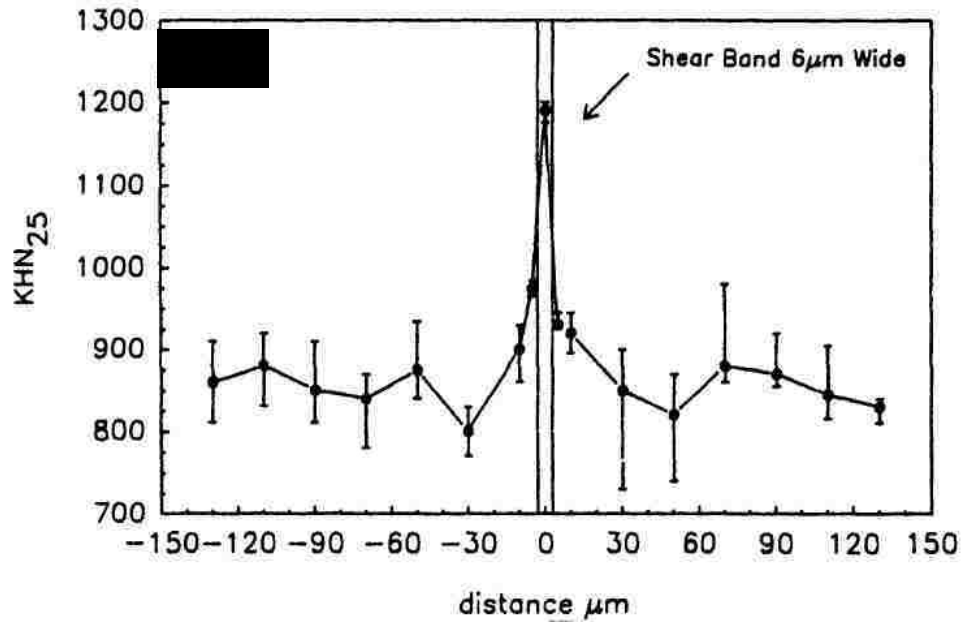
Fig. 2.20. Microhardness traverses encompassing shear bands for (a) AlSI 4340 quenched and tempered steel [99] (b) Ti-6Al-4V alloy [25].
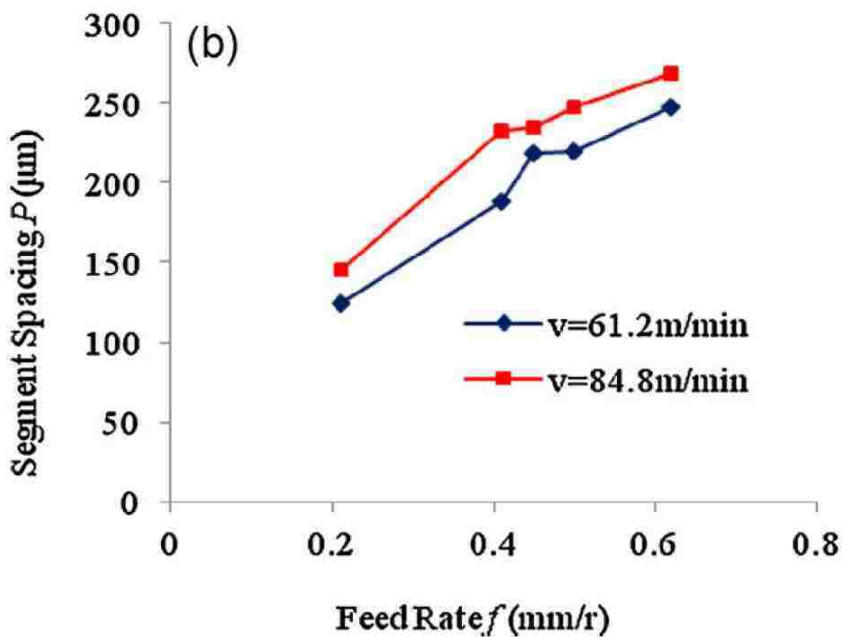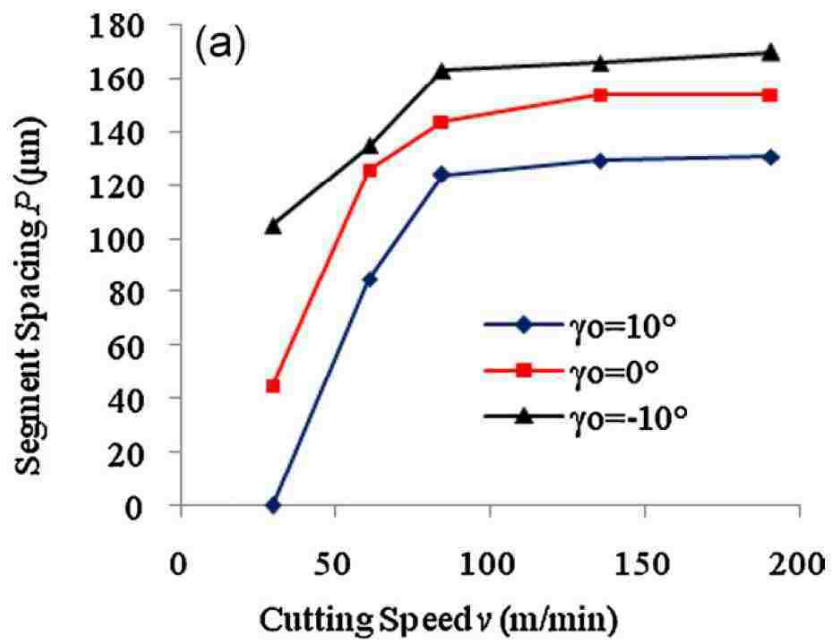
Fig. 2.21. Diagram showing the variation of segment spacing or shear band frequency in case of Ti-6Al-4V alloy, with the (a) cutting speed and (b) feed rate. Here γo is the rake angle [104].
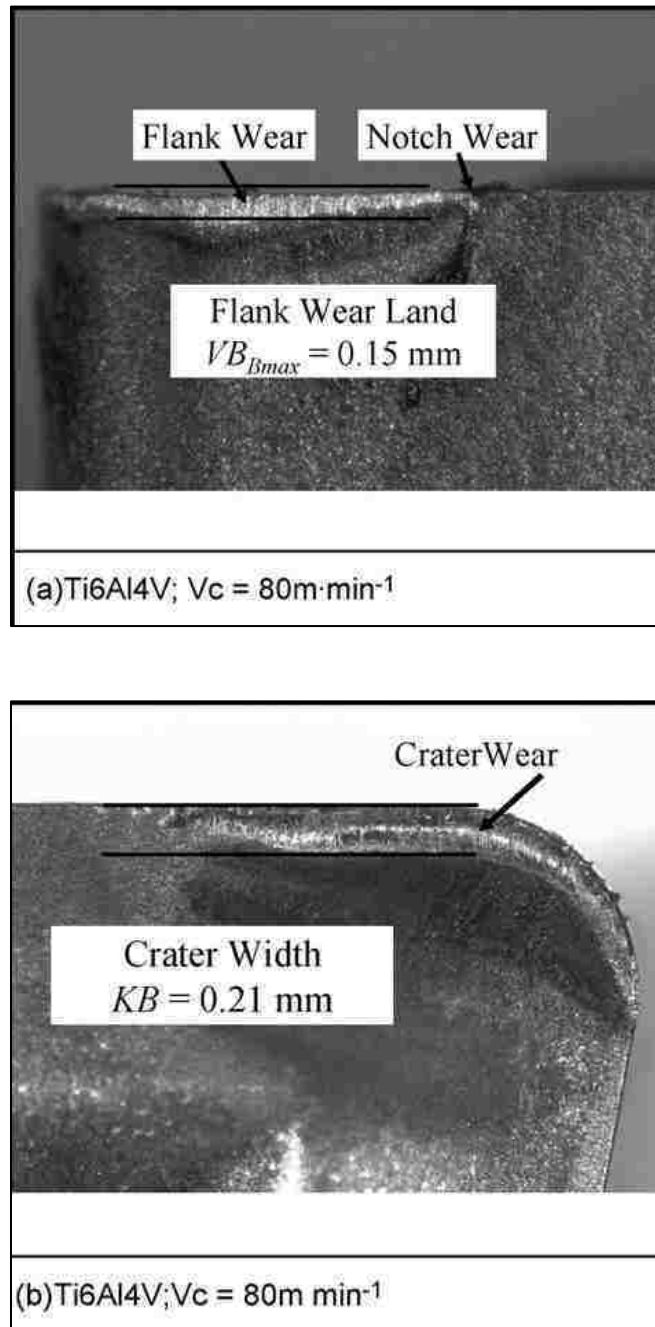
Fig. 2.22. Flank and rake face wear patterns (T = 15min) [109]. The tool material was uncoated cemented carbide (grade K15 micrograin).
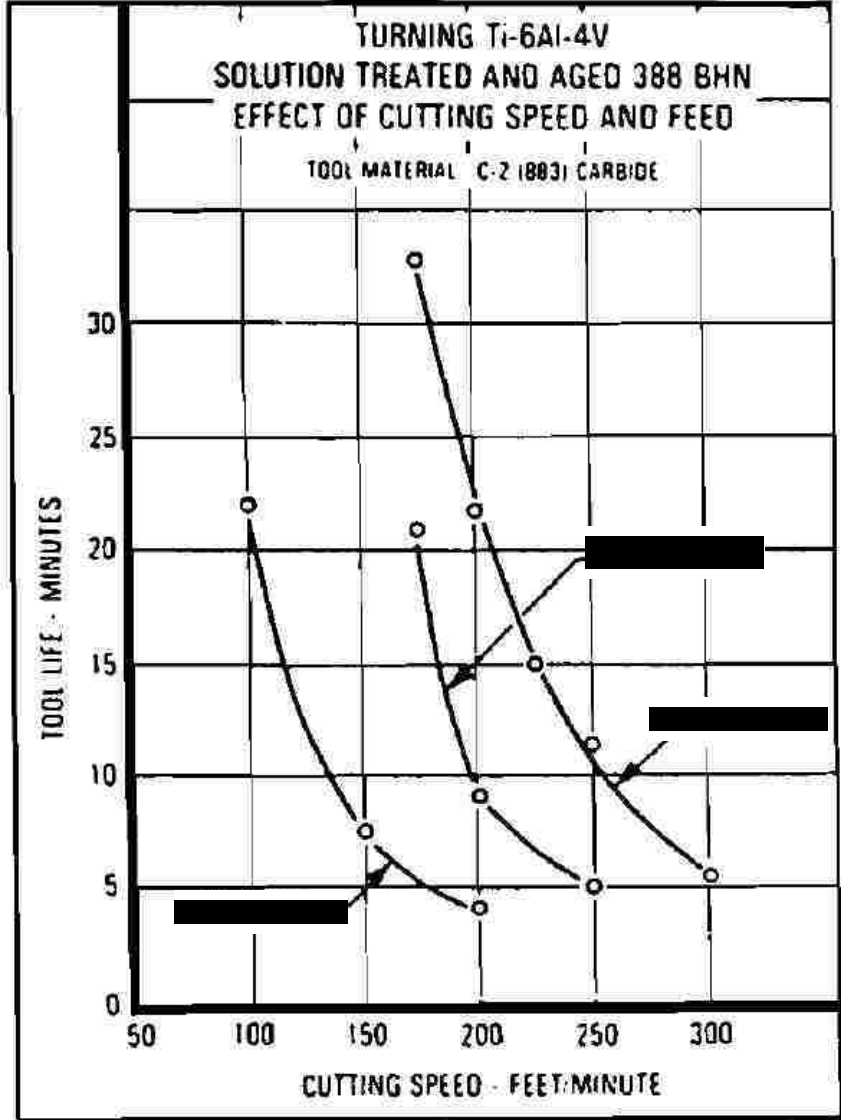
Fig. 2.23. Effect of cutting speed and feed on tool life in turning Ti-6AI-4V [5].
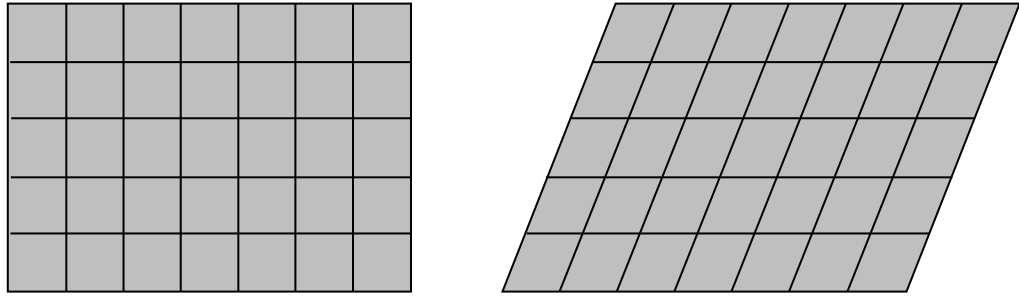
(a) Lagrangian mesh behaviour
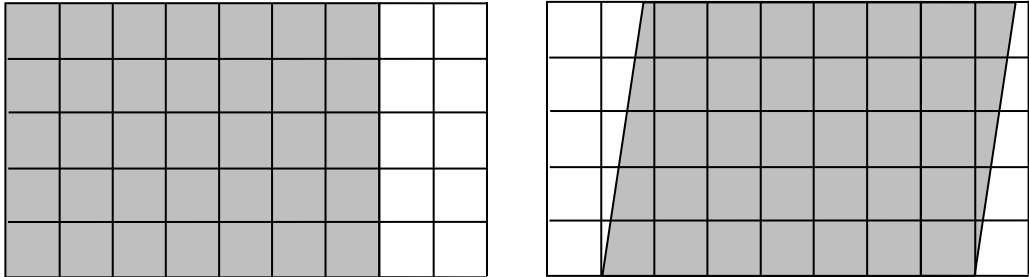
(b) Eulerian mesh behaviour
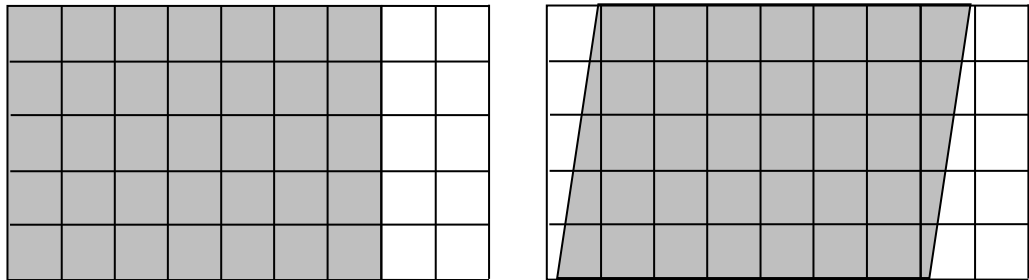
(c) ALE mesh behaviour

Fig. 2.24. Comparison of Lagangian, Eulerian and ALE mesh behaviour Eulerian Approach [111].
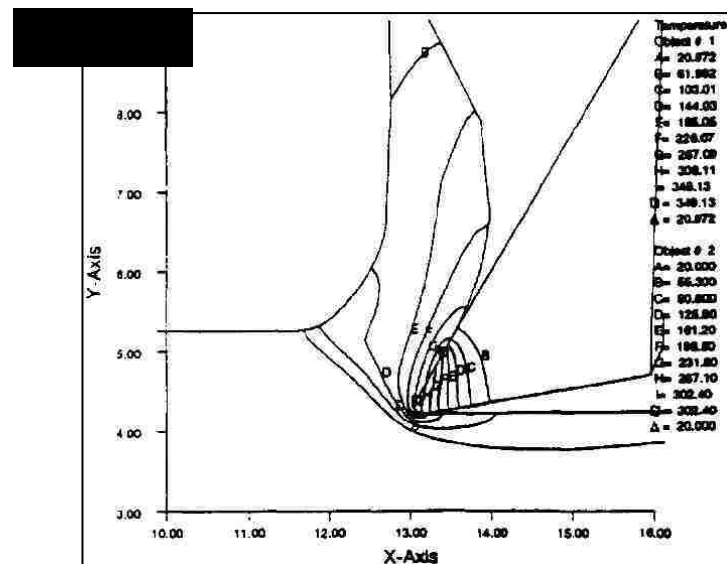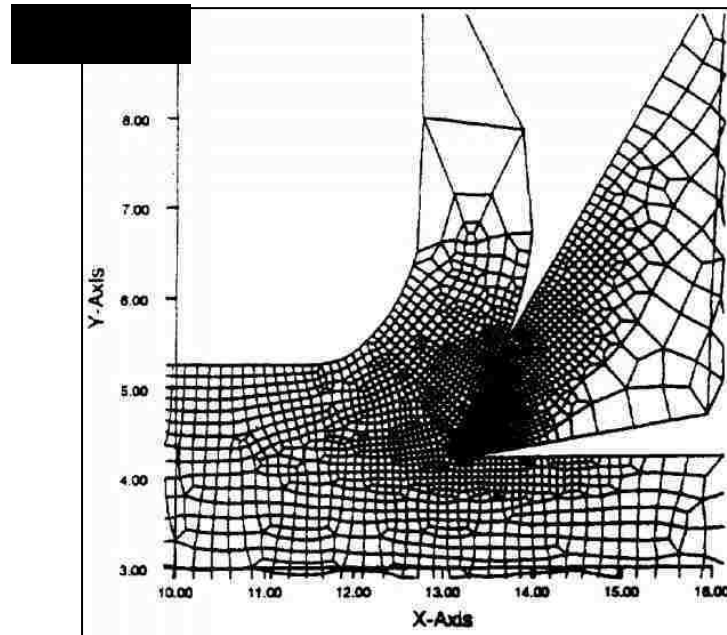
Fig. 2.25. Diagram showing the (a) chip geometry and (b) temperature distribution after a tool path of 7 mm. (Cutting speed 250 mm/s, feed rate 0.1 mm/rev, depth of cut 1 mm, rake angle 10˚ and coefficient of friction 0.5) [121].
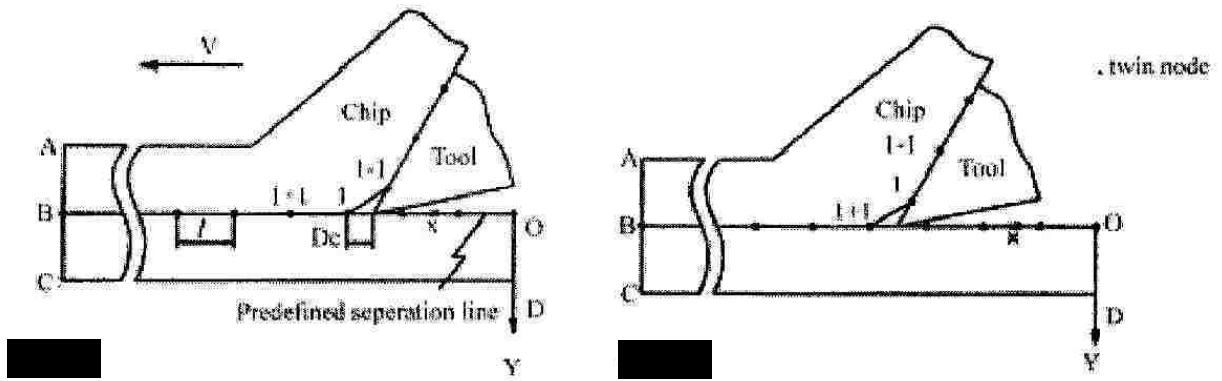
Fig. 2.26. Diagram showing the geometrical separation method: (a) before node separation, (b) after node separation [135].
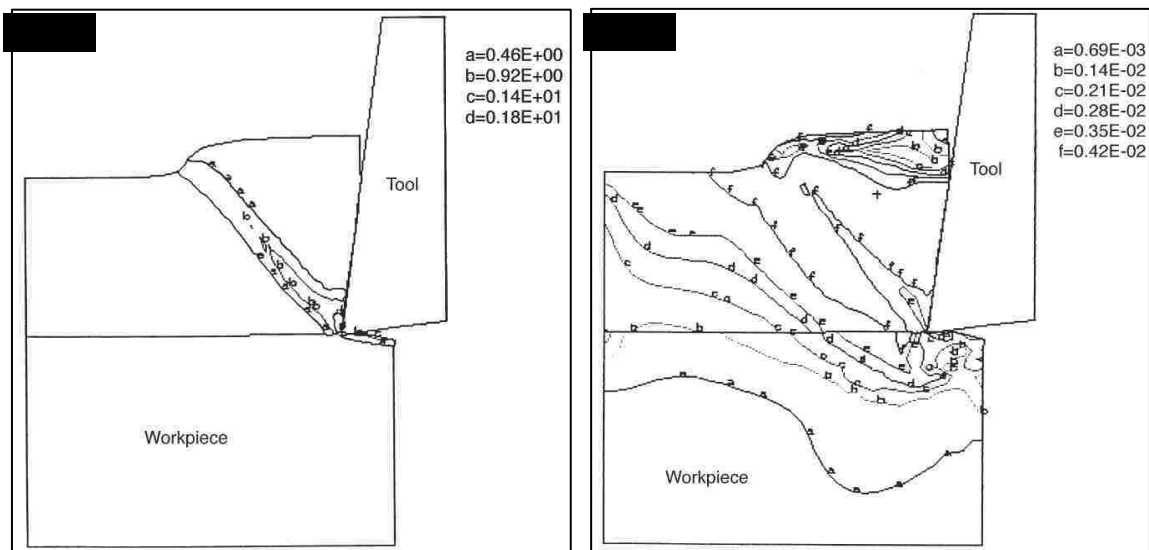
Fig. 2.27. Diagram showing the (a) contours of effective plastic strain when the shear band is fully formed, (b) contours of effective shear stress (10^5 N/mm^2) at the indication of the shear banding initiation [146].
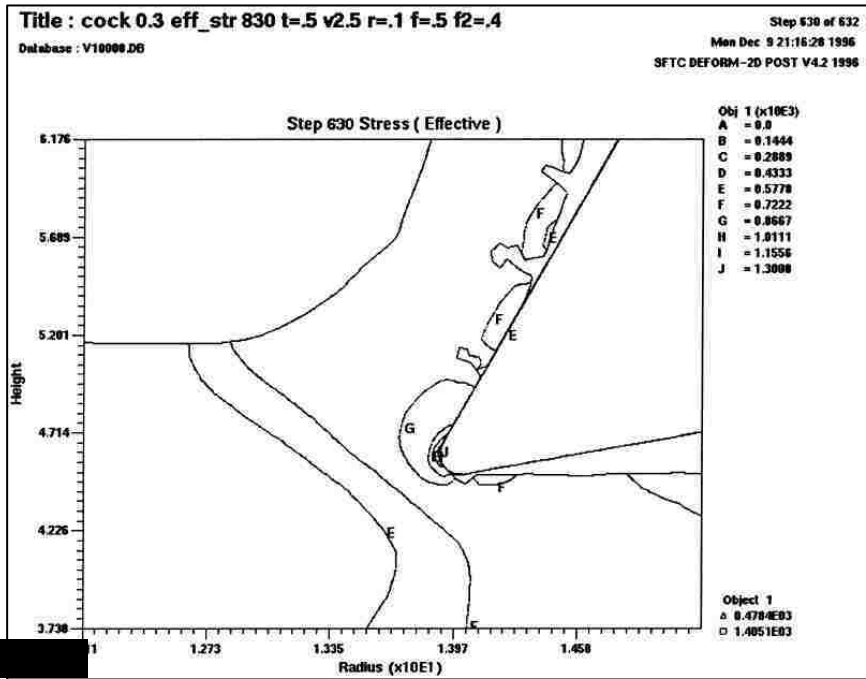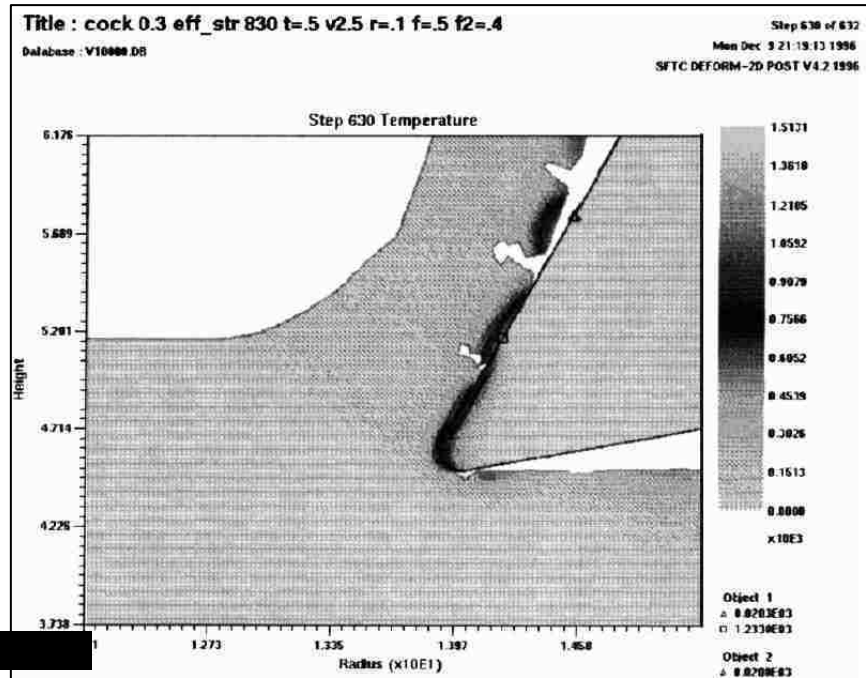
Fig. 2.28. Diagrams showing the (a) temperature distribution and (b) stress distribution ahead of the tool tip of AISI 1045 steel (cutting speed = 600 m/min, feed rate = 0.1 mm/rev) [147].
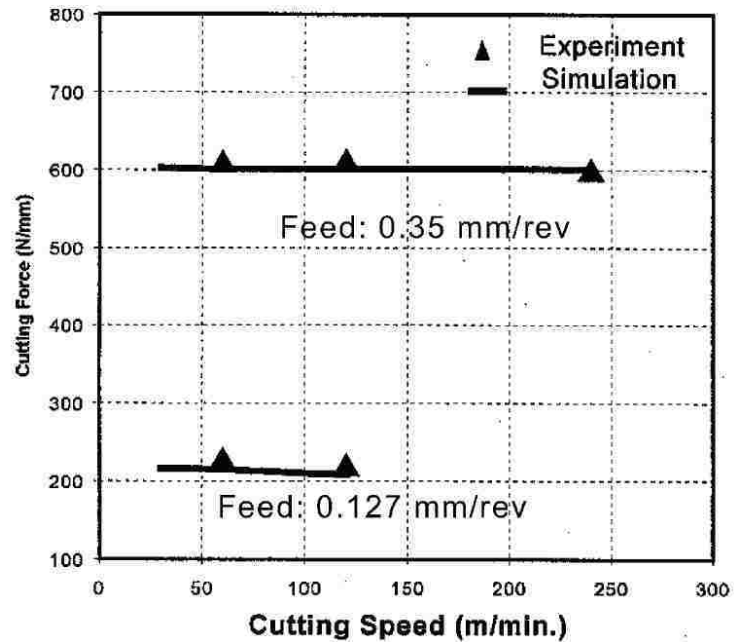
Fig. 2.29. Diagram showing the comparison of force data for turning of Ti-6Al-4V alloy experiments and model predictions [74].
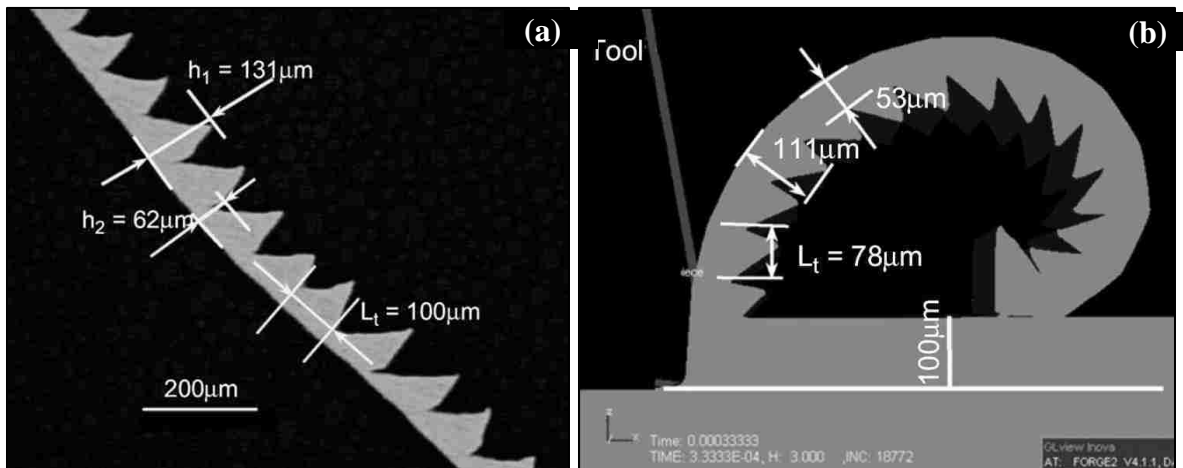
Fig. 2.30. (a) Experimental chip obtained when machining with a cutting speed of 180 m/min and a feed of 0.1 mm, (b) Simulated chips at a cutting speed of 180 m/min and a feed of 0.1 mm: using modified material model [143].

68
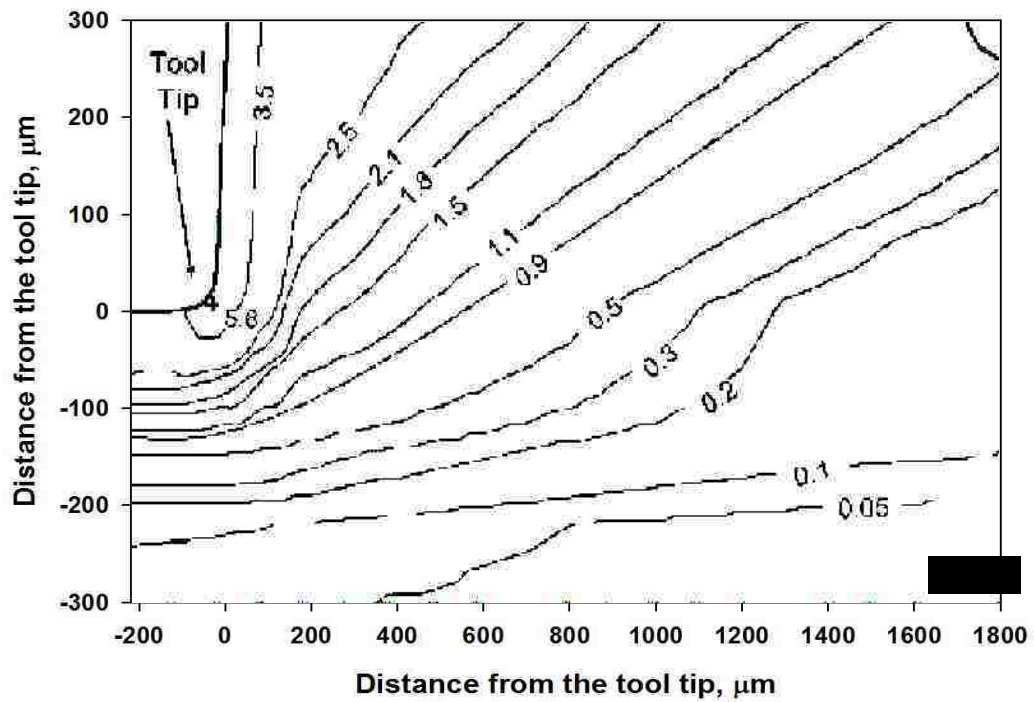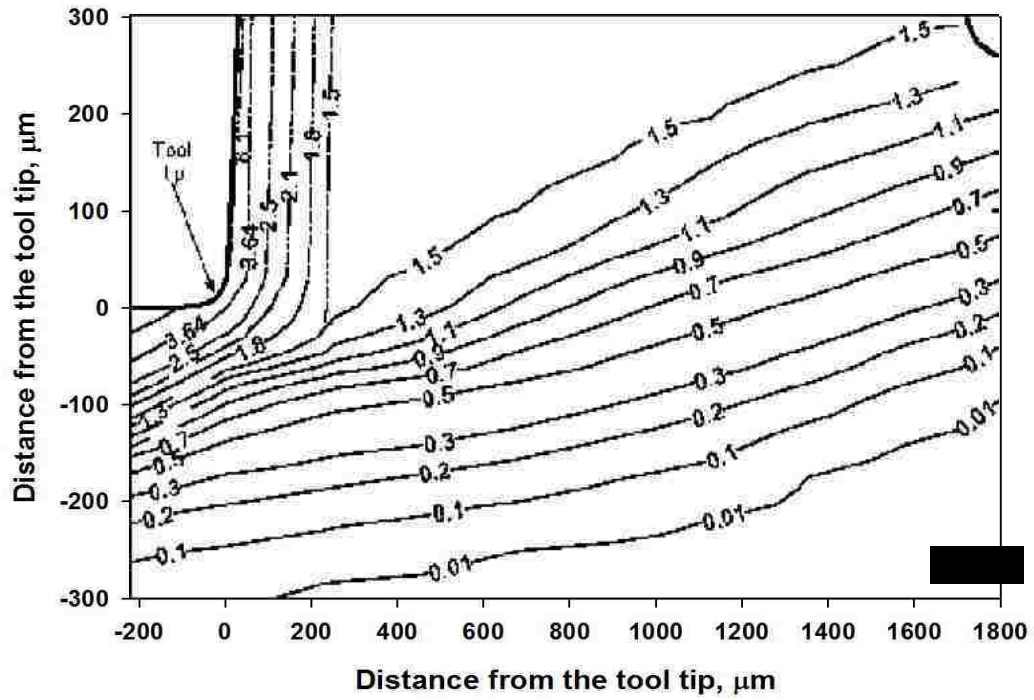
Fig. 2.31. Contours of equivalent strain in the material (ETP copper) ahead of the tool tip according to (a) experimental measurements, (b) numerical model using a hydrodynamic material model in Eulerian FE formulation [149].

69
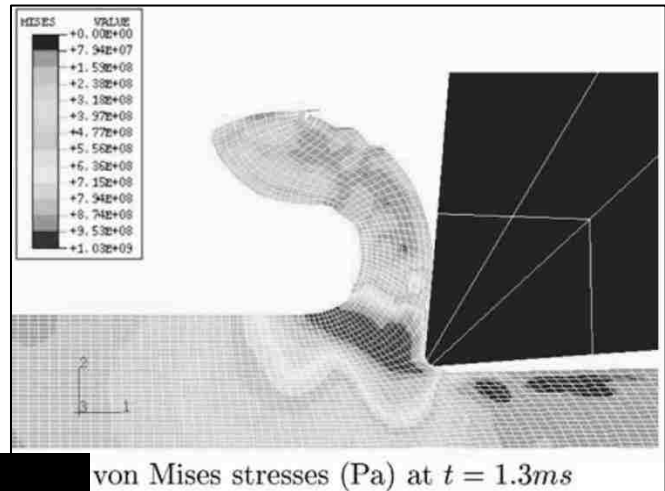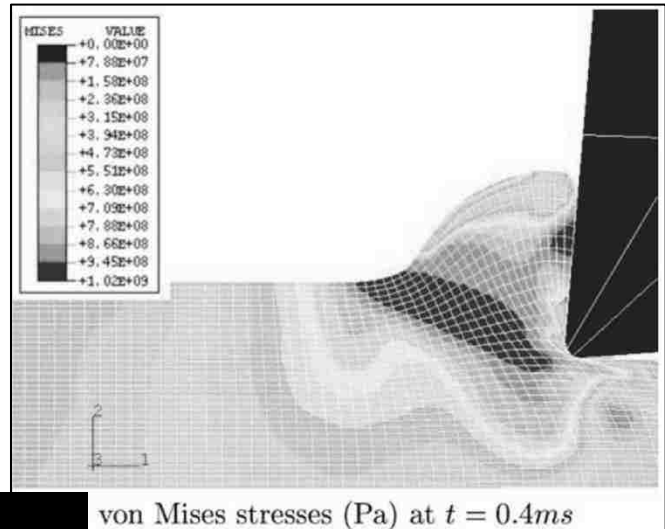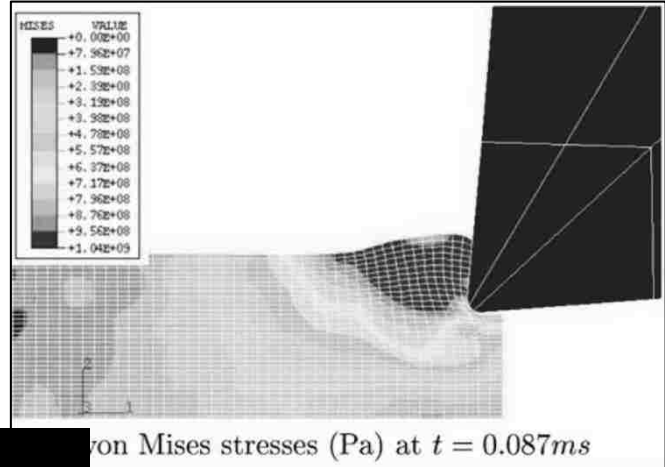
Fig. 2.32. Continuous chip formation and von Mises stress distribution at (a) 0.087 ms,
(b) 0.4 ms & (c) 1.3 ms using ALE [160].
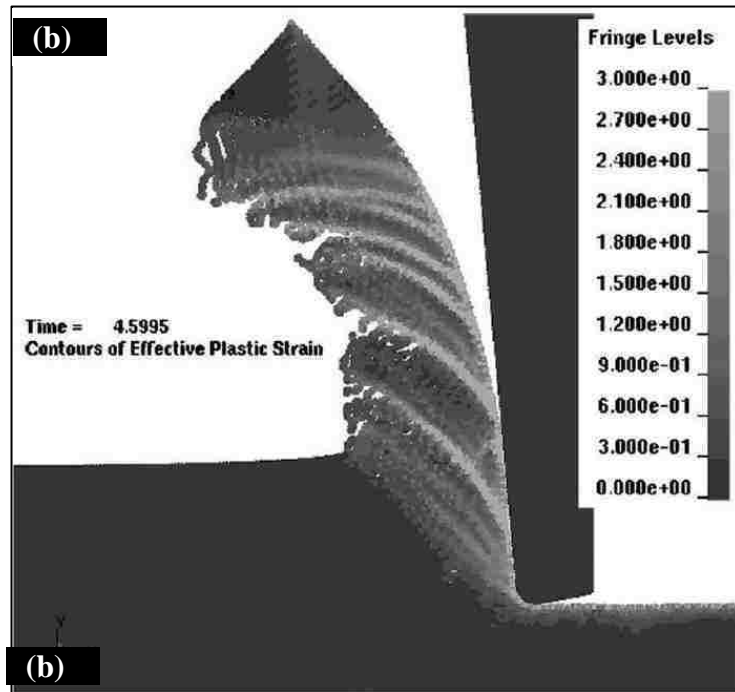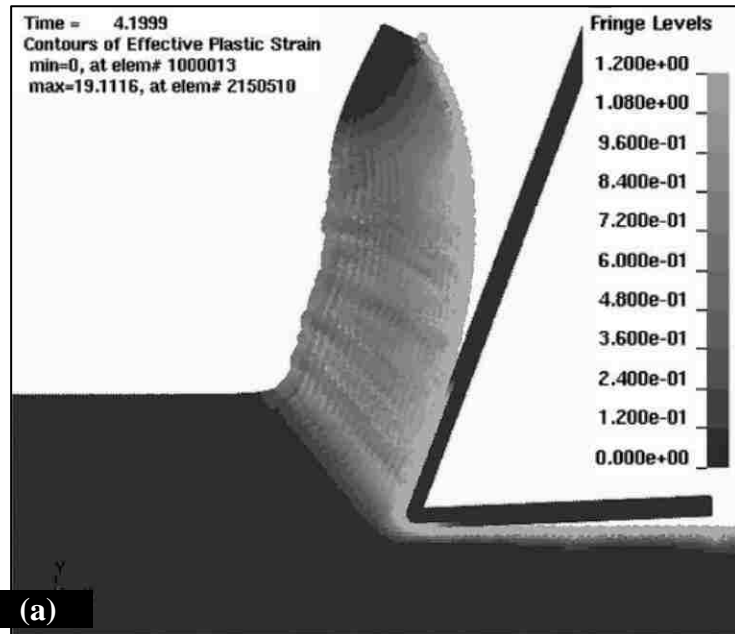
Fig. 2.33. Plastic strain distribution ahead of the tool tip of (a) Al6061–T6 and (b) AISI 4340 steel using SPH formulation [13].

CHAPTER 3: Experimental and Numerical Procedures

3.1. Experimental Approach

3.1.1. Workpiece geometry and composition

The material investigated in this study was the Ti-6Al-4V alloy which is one of the most widely used titanium alloys. The Ti-6Al-4V alloy is an α-β titanium alloy and composition of this alloy is given in Table 3.1. The alloy was obtained in the form of extruded rods with a diameter of 25.45 mm. Tubular samples with a wall thickness of 3.2 mm were machined for the orthogonal cutting tests from these extruded rods. The microhardness of the alloy was 380 ± 3 HV, measured using a microhardness tester with a 50 gram of load.

Table 3.1. Composition of Ti-6Al-4V alloy

Elements	Al	V	Fe	O_2	C	N_2	Ti
Weight %	5.5-6.76	3.5-4.5	< 0.25	< 0.2	< 0.08	< 0.05	The Balance

A small piece of sample was cut and prepared to observe the microstructure of Ti-6Al-4V alloy using the standard metallographic preparation techniques. The sample was ground using silicon carbide paper and water, starting with grade 180 followed by 240, 320, 400, 600, 800 and 1200 using light pressure applied to the center of the small sample. Next, the sample was cleaned by washing with water followed by rinsing in alcohol and drying. Then the sample was polished using diamond suspension, starting

from 3 μm and going down to 0.1 μm. Care was taken to wash the sample thoroughly with soapy water before moving on to the 1 μm stage so as to avoid contamination of the disc. Then the sample was cleaned with ethanol and etched with Kroll's solution (92% H_2O, 6% HNO_3 and 2% HF) for 18-25 sec. The microstructure of this alloy consisted of α and β phases (Fig. 3.1) where α phase is the h.c.p. structure and β phase is the b.c.c. structure. The β phase is elongated along the extruded direction. The average length and width of β phase are 4.86 ± 2.86 μm and 1.03 ± 0.46 μm.

3.1.2. Orthogonal cutting tests

All orthogonal cutting tests were executed on a Harrison M300 lathe which is a compact, simple-to-operate and reliable center lathe (Fig.3.2). It has a long, foot-operated and very powerful spindle-brake with electrical disengagement for interrupted cutting and is powered by a fan-cooled 2.2 kW (3 HP.) 3-phase, 1500 rpm motor. The spindle rotation speed can be chosen from twelve different speeds ranging from 40 to 2500 rpm. The range of power sliding feeds varies from 0.03 mm to 1 mm per revolution of the spindle in metric mode.

Different cutting conditions were used for the orthogonal cutting test. The cutting speeds were 180 RPM (14.4 m/min), 370 RPM (29.6 m/min), 540 RPM (43.2 m/min) and 800 RPM (63.5 m/min) and the feed rates were 0.1 mm/rev, 0.15 mm/rev, 0.2 mm/rev and 0.25 mm/rev. The use of four different values ensured enough data points for analyzing the effects of cutting speed and feed rate on the machinability of Ti-6Al-4V alloy. The rake angle and the clearance angles were 0° and 7° respectively. Polycrystalline diamond (PCD) insert (VCMW 332FP) shown in Fig. 3.3, was used as a

cutting tool for the cutting experiments. A polycrystalline diamond insert was chosen as it is has excellent high wear resistance, high fracture strength and high dimensional stability properties [16]. It was reported that the PCD tool performed better in terms of wear rate during machining of titanium alloy [108].

3.1.3. Force measurement

During orthogonal cutting, cutting and thrust forces are two important forces exerted by tool on the workpiece. The direction of the each force on a SEM of the machined sample is shown in Fig.3.4. A two-axis force sensor system developed by [73] was used for measuring cutting and thrust forces. A detachable unit (Fig. 3.5) contains a modified tool holder along with the tool-holder-mounting with the strain sensor with the wireless transmitter, was used which could easily be installed on the machine without requiring any change in the normal configuration of the lath or the work-piece. The data acquisition system was comprised of a strain sensor, a wireless transmitter system (V-Link 2.4 GHz Wireless Voltage Node), an analog base station (MicroStrain Micro TxRx wireless base station w/ analog outputs) and a computer loaded with data acquisition software 'Agile Link'. Fig. 3.6 represents the schematic diagram showing the different components of the force sensor and data acquisition system. The sampling rate of the data acquisition system was 680 Hz.

The strain sensor (V-Link 2.4 GHz Wireless Voltage Node) attached to the narrow groove in the modified tool holder (Fig. 3.5) picked up the strains produced in the tool holder as it bent under the loads exerted on it during turning operation. It transmitted the signals via electrical wires to the strain sensor which then wirelessly transmitted them

to the base station. The bases station transmitted the data to the PC via a USB cable and 'Agile Link' was used to convert the streamed data to a readable format.

The system was calibrated before measuring the forces. The system was first mounted on a vice in such a way that the force of gravity, acting vertically downwards, acted in the direction cutting force would act in during cutting tests. Then a known load was applied to the cutting direction and the corresponding output (milivolt) was measured via data acquisition system. Same procedure was used for measuring the output values at different loads. The relationship between the applied load in the cutting force direction and the corresponding output value was linear ($R^2 = 1$) and the relationship shown in Fig. 3.7a, can be described as:

$$F_c = -1.1618a + 2376.6 \qquad \text{(in units of Newton)} \tag{3.1}$$

where F_c is the cutting force, 'a' is the output value for cutting force direction.

In order to calibrate the system for measuring thrust forces, it was remounted on the vice in such a way that the force of gravity would now act in the direction of thrust force. The rest of the steps followed were same as described above for calibrating the system for cutting forces. The relationship between the applied load in the thrust force direction and the corresponding output value was linear ($R^2 = 1$) and the relationship shown in Fig. 3.7b, can be described as:

$$F_t = 1.1853b - 2409.3 \qquad \text{(in units of Newton)} \tag{3.2}$$

where F_t is the thrust force and 'b' is the output value for thrust force direction.

The cutting and thrust forces were measured using the force measurement system for different cutting conditions. The output data obtained from the data acquisition software was converted into different forces using the calibration equations (Eq. 3.1 and 3.2). Fig.3.8 shows a typical output force curve from the force measurement system. In this case the cutting conditions were. As the tool came into contact with the workpiece, force measurements showed a rapid rise in magnitude of forces followed by a steady state system response. As the quick stop foot controlled brakes are applied almost instantaneously, the forces rapidly reduce to zero.

3.1.4. Surface quality measurement

A WYKO NT 1100 Optical Profiling System was used to analyze the finish of the machined surfaces for the samples turned under the different cutting conditions where the surface roughness value is expressed in terms of R_a, R_q, R_z and R_t.

Optical interferometry is the principle of superposition of separate light waves of similar frequency, to combine in such a way that conveys the information about the original state of the waves. A single light beam emitted from a coherent light source, are split into two identical beams by an inclined mirror. After traversing through different paths these two beams eventually recombine to create a resulting pattern with a phase difference between the two waves. This phase difference creates the interference pattern between the two waves, thus imparting information regarding the cause of the phase difference, which in case of an optical interferometer is the specimen being studied.

In a modern day optical profilometer, such as WYKO NT 1100, similar principle is used where the resulting interference phenomena, as a result of recombination of

76

separated beam from a single source, is recorded in the form of an interferogram. The original beam is separated into two by the beam-splitter. The beam which moves towards the test piece passes through a reference surface where most of the light passes through the surface on to the test piece, while rest of the light (Reference beam) is reflected back to the detector. The light reflected from the test piece returns to the interferometer where it interferes with the reference beam. The recombined beams create bright (constructive interference) and dark bands (destructive interference) called fringes acting like topographic maps thus recreating the map of the surface of the object under observation. The CCD detector registers the interferogram and forwards the frame to the computer which processes the data using interferometric phase mapping programs.

In this research for measuring the surface roughness of the machined surfaces, the Vertical Scanning Interferometry (VSI) mode was used instead of the Phase Shifting Interferometry (PSI) mode due to the higher roughness of the machined surface. VSI is useful for rough surface and PSI is more appropriate and accurate for smooth surface and short measurement time. However, the use of PSI is limited for objects that have large step-like height changes and this method becomes ineffective as height discontinuities of adjacent pixels exceed one quarter of the used wavelength ($\lambda/4$).

3.1.5. Sample preparation and metallographic analysis

The machined samples were sectioned as shown in Fig. 3.9 for metallographic examination of their deformation microstructures ahead of the tool tip. The samples were mounted with the mounting materials (Lecoset^{TM} 7007 Cold-curing resin (Powder: Liquid = 2:1) for metallographic applications) to observe the desired metallographic

sections. Samples were prepared using the standard metallographic preparation techniques described in section 3.1.1.

The microstructure of the polished surface was observed using a scanning electron microscope (SEM, JEOL JSM-5800LV). The main areas examined included the primary and secondary deformation zones, the chip region, the machined surface and the work-piece bulk material region. Energy dispersive spectroscopy or EDS was done to analyze the transferred material on the tool surface.

3.1.6. Stain measurement

A cross-sectional SEM image of the deformation microstructure of the material ahead of the tool tip, taken by interrupting the orthogonal cutting process is presented in Fig. 3.10. Plastic strains induced in the workpiece during cutting were estimated from the orientation change of the deformed β phase grains of the alloy on the cross sectional plane of the material ahead of the tool tip. Fig. 3.11 depicts the schematic representation the deformation pattern of Ti-6Al-4V alloy obtained by plotting orientation changes of the β phase grains at the same scale as in the actual microstructure in Fig. 3.10. However, Fig. 3.12 shows the displacement of the β phase grains in the material ahead of the tool tip at the same scale as in the actual microstructure in Fig. 3.10. For measuring the deformation angle at different points a curve fitting software "TableCurve 2D" was used which is discussed in Appendix A. Effective plastic strains or equivalent strains were estimated at the points of intersection of an imaginary grid (50μm by 50μm) using Eqn. 2.15 that is discussed in section 2.1.5.2.

$$\bar{\varepsilon} = \frac{\sqrt{(3)}}{3} \tan \theta \qquad\qquad (2.15)$$

The strains were then plotted on an outline of the micro graph and points having same magnitude of strains were connected together to yield isostrain lines. The results of the strains distribution ahead of the tool tip are described in greater details in section 4.6.

3.1.7. Microhardness measurement-Flow stress estimation

Vickers Hardness (HV) was measured using a Buehler Micromet II microhardness tester. The load used for all the indentations was 50 grams. Indentations were place at the points of intersection of an imaginary grid of 50μm x 50μm. The points on an outline of the micrograph for the area ahead of the tool tip location, which exhibited same magnitude of hardness have been connected together to obtain iso-hardness contours. Flow stresses in the workpiece at the locations of the indentations were estimated using Eqn. 2.18.

$$\sigma = \frac{H}{3} \qquad\qquad (2.18)$$

The results of the flow stress measurement have been discussed in details in section 4.7.

3.1.8. Temperature measurement

During machining of Ti-6Al-4V alloy the temperature at the tool tip was measured different feed rates and cutting speeds. To measure the temperature during orthogonal cutting of Ti-6Al-4V alloy at the tool tip, a modified carbide tool (Fig. 3.13),

a K-type (Cbromel-Alumel) thermocouple (diameter 0.52 mm), a data acquisition system and a computer loaded with data acquisition software 'pDaqView' were used. The thermocouple was mounted at the rake face of the tool through the small hole (diameter 0.7 mm), and near the cutting edge (distance between edge and the center of the hole = 0.8 mm). Schematic diagram of the temperature measurement system is shown in Fig. 3.14. The sampling rate of the data acquisition system was 120 Hz.

The thermocouple installed in the modified tool measured the temperature difference and converted it into electrical signals and transmitted the signals to the strain sensor which then wirelessly transmitted them to the data acquisition and then the data acquisition transmitted the data to the PC via a USB cable and 'pDaqView' was used to convert the streamed data to a readable format.

The system was calibrated before measuring the temperature. A small electrical furnace was used for calibration. The furnace was heated to a known temperature and the corresponding output value (milivolt) was measured via data acquisition system. Same procedure was used for measuring the output values at different temperatures. The relationship between the temperature and the corresponding output value was linear ($R^2 = 0.996$) and the relationship can be described as:

$$T = 33003x + 20.98 \quad \text{(in units of degree Celsius)} \tag{3.3}$$

where, 'x' is the value obtained from the data acquisition system for temperature measurement and T is the corresponding temperature.

The output data obtained from the data acquisition software was converted into temperature using the calibration equations. Fig. 3.15 depicts a typical output temperature curve from the temperature measurement system. As the tool came into contact with the workpiece, temperature measurements showed a rapid rise in magnitude of temperature until it reached to a steady state region. As the quick stop foot controlled brakes were applied the temperature dropped rapidly and reached to room temperature (23 ˚C). Average tool tip temperature was calculated from the steady state zone in Fig. 3.15.

3.2. Finite Element Simulations

All the finite element simulations were performed using the finite-element program LS-DYNA version 971, release R.4.2.1. Two different formulations were used to simulate the orthogonal cutting of Ti-6Al-4V alloy, namely, 2D Lagrangian element formulation and smoothed particle hydrodynamic (SPH) formulation.

3.2.1. 2D Lagrangian Element Formulation

The termination time specified for this simulation was 1 millisecond and the processing time for the simulation was approximately 75 hours using a personal computer with Intel Xeon 3.0 GHz processors with 4 CPU and 16 gigabyte of memory. Explicit time integration was used for this formulation. The scale factor for computed time step was 0.90. Coupled structural thermal analysis was performed for all the simulations. The initial thermal time step size was 100 ns. A Crank-Nicholson scheme was used in time integration. The solution results were then viewed and analyzed in the post-processing

software package LS-PREPOST (Version 2.4). The summary of the FE input file is contained in Appendix B.

3.2.1.1. Model Geometry and Discretization

To model the orthogonal cutting process two parts, namely, a workpiece and a tool were considered (Fig. 3.16). The FE mesh of the upper part of the workpiece were finer (3µm × 3µm), compared to the mesh of the lower portion (6µm × 6µm) of the workpiece. This was performed to predict the stress, strain and temperature distributions in the workpiece ahead of the tool tip more accurately. Transition elements were used to avoid the stress concentration in between the finer mesh and the course mesh. The aspect ratio of the mesh size of the workpiece was 1.0. The workpiece consists of 74560 plane strain elements utilizing a 3×3 integration point scheme, and the tool was modeled using a plane strain elements formulation also having 3×3 integration. A finer discretization (20µm × 2.5µm) was utilized near the tool tip. However, the aspect ratio of the mesh size of tool was 8.0. The radius of the tool tip used for modeling was 15 µm, which was consistent with the experimental setup (Fig. 3.17).

3.2.2. Smoothed-Particle Hydrodynamics (SPH) Formulation

Each simulation had a termination time of 1 millisecond and the total simulation time was approximately 88 hours using a personal computer with Intel Xeon 3.0 GHz processors with 4 CPU and 16 gigabyte of memory. The scale factor for computed time step was 0.15. Coupled structural thermal analysis was performed for all the simulations. The initial thermal time step size was 100 ns and the Crank-Nicholson scheme was used in time integration. The solution results were then viewed and analyzed in the post-

processing software package LS-PREPOST (Version 2.4). The summary of the FE input file is contained in Appendix C.

3.2.2.1. Model geometry and Discretization

In the SPH model (Fig. 3.18), two parts, namely workpiece and cutting tool were used to model the cutting process. The workpiece in the SPH model consisted of 31500 SPH particles. The distance between two particles was 8 μm in all directions. The initial number of neighbors per particle was 150. The aspect ratio of the distance between the particles was 1.0.

The cutting tool was discretized using solid Lagrangian formulation elements. The geometry of the tool was same as the tool used in 2D Lagrangian element formulation method, while the thickness of the solid tool element was 10 μm.

3.2.2. Workpiece and Tool Material Modeling

The Johnson-Cook (JC) material model (*MAT_JOHNSON_COOK, material type 15 within LS-DYNA) was used to represent the workpiece material behaviour. Details of this material model were discussed in section 2.3.5.1, where the general form of the Johnson–Cook equation is as follows:

$$\sigma = (\sigma_y + B\bar{\varepsilon}^{p^n})(1 + c\ln\dot{\varepsilon}^*)(1 - T^{*^m}) \hspace{4cm} (2.29)$$

The parameters used to define the deformation behaviour of Ti-6Al-4V alloy according to the Johnson–Cook equation were obtained from the experimental results and reference [181], and have been discussed in details in section 5.2. The density, shear

modulus, elastic modulus, specific heat and Poisson's ratio of the workpiece were specified as 4.43 g/cm^3, 55.0 GPa, 110 GPa, 0.568 J/g °C and 0.33 respectively.

For the formation of serrated chips, the Johnson-Cook damage criteria were used. The model defines the strain at fracture as:

$$\varepsilon_f = [D_1 + D_2 \exp(D_3\sigma^*)][1 + D_4\ln(\dot{\varepsilon}^*)][1 + D_5 T^*] \qquad (2.32)$$

where the five constants D_1, D_2, D_3, D_4 and D_5 are Johnson-Cook failure parameter.

Fracture occurs in the Johnson-Cook model when the damage parameter D exceeds 1.0. The evolution of D is given by the accumulated incremental effective plastic strains divided by the current strain at fracture

$$D = \sum \frac{\Delta\bar{\varepsilon}^P}{\varepsilon_f} \qquad (2.33)$$

The Johnson-Cook damage law parameters of Ti-6Al-4V alloy are given in Table. 3.2.

Table 3.2. The Johnson-Cook damage law parameters of Ti-6Al-4V alloy [181]

Initial failure strain, D_1	Exponential factor, D_2	Triaxiality factor, D_3	Strain rate factor, D_4	Temperature factor, D_5
-0.09	0.5	0.48	0.014	2.5

The Grüneisen equation of state (*EOS_GRUNEISEN, in LS-DYNA) was utilized to describe the pressure-volume relationship of the workpiece. It defines the pressure for compressed materials by relating the material shock velocity and particle velocity through a cubic equation:

$$P = \frac{\rho_0 C^2 \mu \left[1 + \left(1 - \frac{\gamma_0}{2}\mu\right) - \frac{a}{2}\mu^2\right]}{\left[1 - (S_1 - 1)\mu - S_2 \frac{\mu^2}{\mu+1} - S_3 \frac{\mu^3}{(\mu+1)^2}\right]^2} + (\gamma_0 + a\mu)E \qquad (3.4)$$

and for expanded materials as:

$$P = \rho_0 C^2 \mu + (\gamma_0 + a\mu)E \qquad (3.5)$$

where, μ is the volumetric parameter that can be expressed by:

$$\mu = \frac{1}{V_r} - 1 = \frac{V_0 - V}{V} = -\frac{dV}{V} = \frac{\rho}{\rho_0} - 1 \qquad (3.6)$$

Here, C = Bulk sound speed, γ_0 = Initial value of Gruneisen's gamma, a = coefficient of the volume dependence of gamma, S_1 = Linear coefficients, S_2 = Quadratic coefficients, S_3 = Cubic coefficients, ρ_0 is the density at nominal/reference state, usually non-stress or non-deformed state, E is the initial internal energy and ρ is the current density.

Table 3.3. The Grüneisen equation of state parameters [182]

C_0 (cm/μs)	S_1	S_2	S_3	γ_0	b	E	V
0.513	1.028	0	0	1.23	0.17	0	1

As the deformation of the tool is negligible compared to the workpiece, the tool was modeled as a rigid (*MAT_RIGID, material type 20 within LS-DYNA). The properties of the cutting tool were specified as follows: the density ρ = 7.1 g/cm^3, Young's modulus E = 210 GPa, and Poisson's ratio ν = 0.33.

3.2.3. Workpiece-Tool Contact

The contact between the tool and the workpiece was modeled using a penalty type contact algorithm, where the penetration of slave nodes into the master segment is checked and prohibited. At contact, the coefficient of friction is determined by:

$$\mu = \mu_D + (\mu_S - \mu_D)\exp(-DC|v_{rel}|) \tag{3.7}$$

Here, μ_D and μ_S are the dynamic and static coefficient of friction respectively, DC is the exponential decay coefficient and v_{rel} is the relative velocity of the surfaces in contact. The assigned value of coefficient of friction for contact between the tool and the workpiece was also determined from the experimental work which is discussed in section 5.2.

3.2.4. Boundary Conditions

To represent the experimental setup, the tool was assigned to move towards the workpiece (X-direction) at a velocity of 63.5 m/min or 1.058 m/s. No other translations or rotations in any other directions were permitted. The bottom nodes of the workpiece were restricted in all degrees of freedom. To impose the symmetrical conditions in x-y plane, the movement of the workpiece in z-direction and the rotation in x and y directions were restricted.

FIGURES- CHAPTER 3
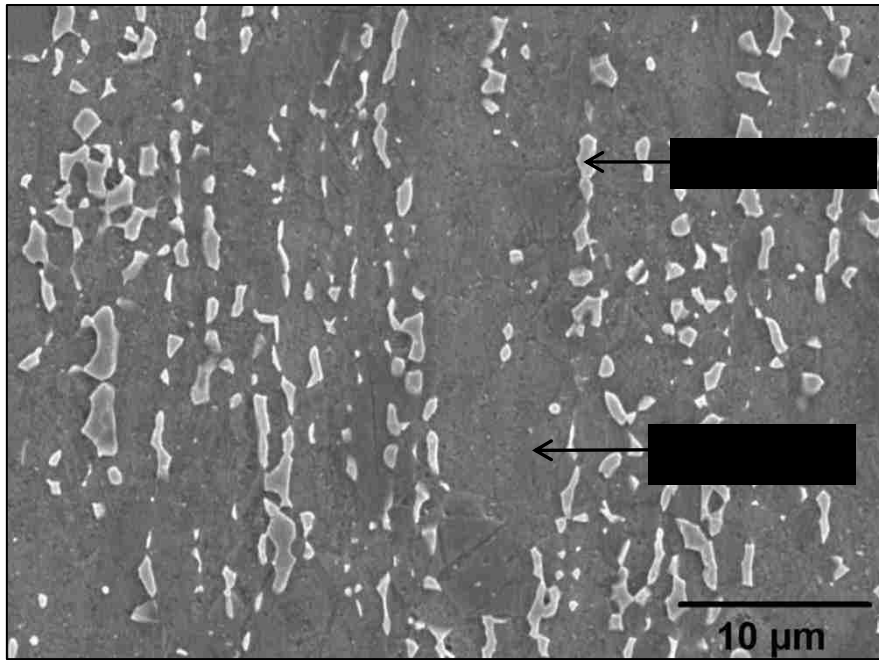
Fig. 3.1. SEM image of the microstructure of Ti-6Al-4V alloy.
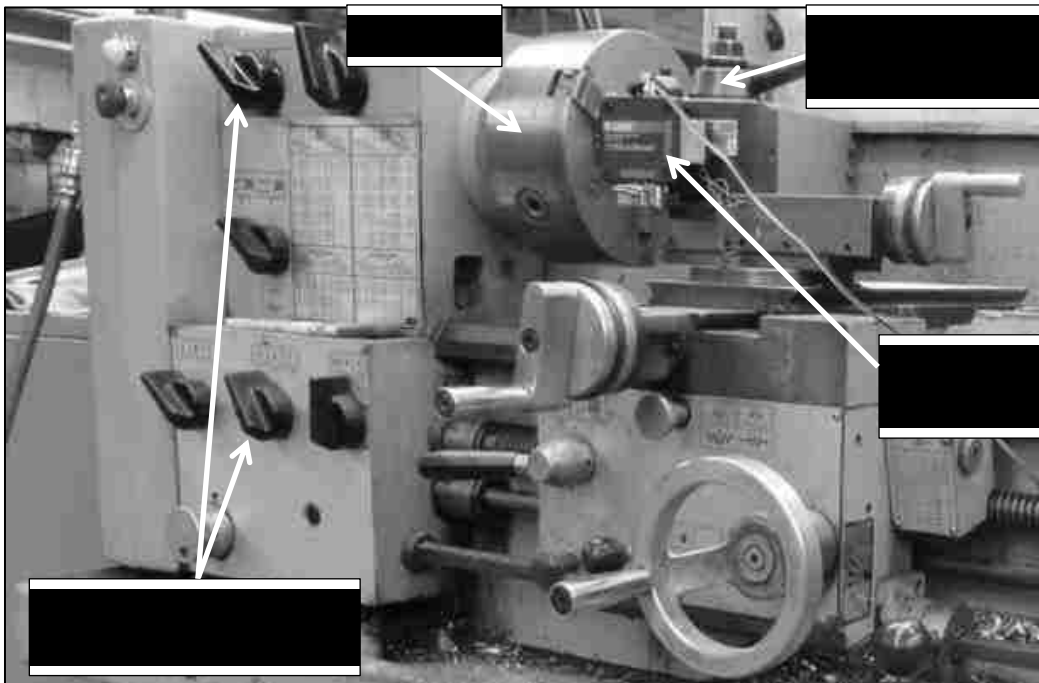
Fig. 3.2. Harrison M300 lathe used for the orthogonal cutting experiments.
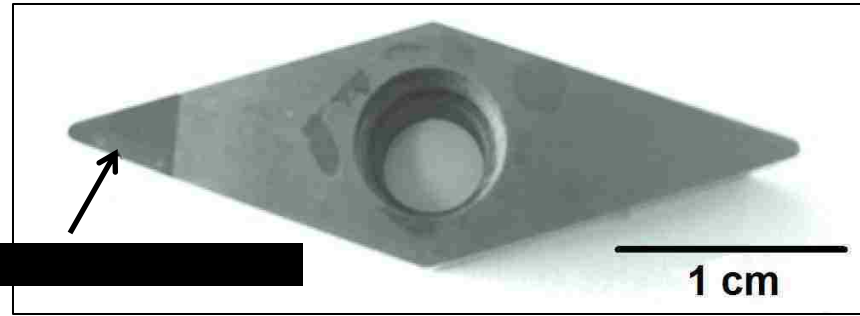
Fig.3.3. Polycrystalline diamond (PCD) insert (VCMW 332FP) used for orthogonal turning of Ti-6Al-4V alloy.

.
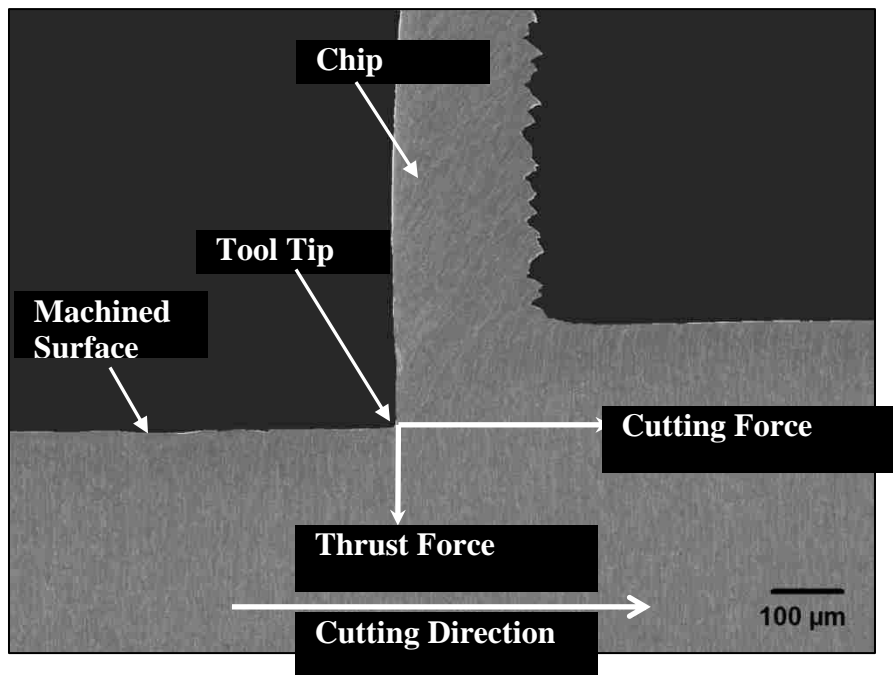
Fig. 3.4. SEM image showing the direction of cutting and thrust force on a section of an orthogonally cut sample. Cutting conditions: cutting speed 43.2 m/min and feed 0.15 mm per revolution.
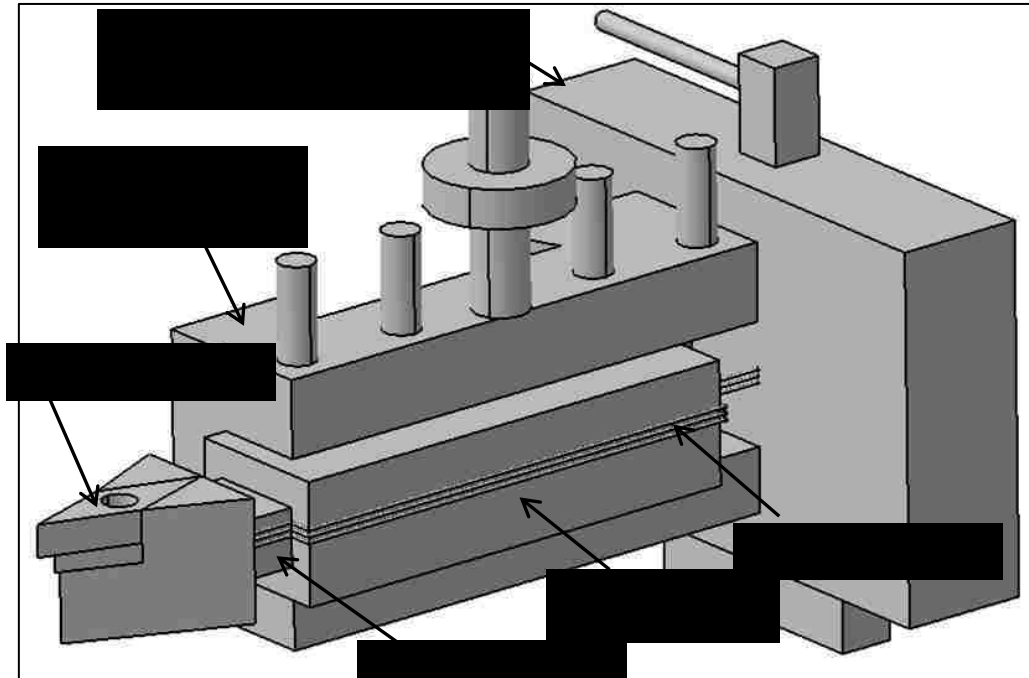
Fig. 3.5. Part of the portable force measurement system which was mounted on the lathe during machining experiments.
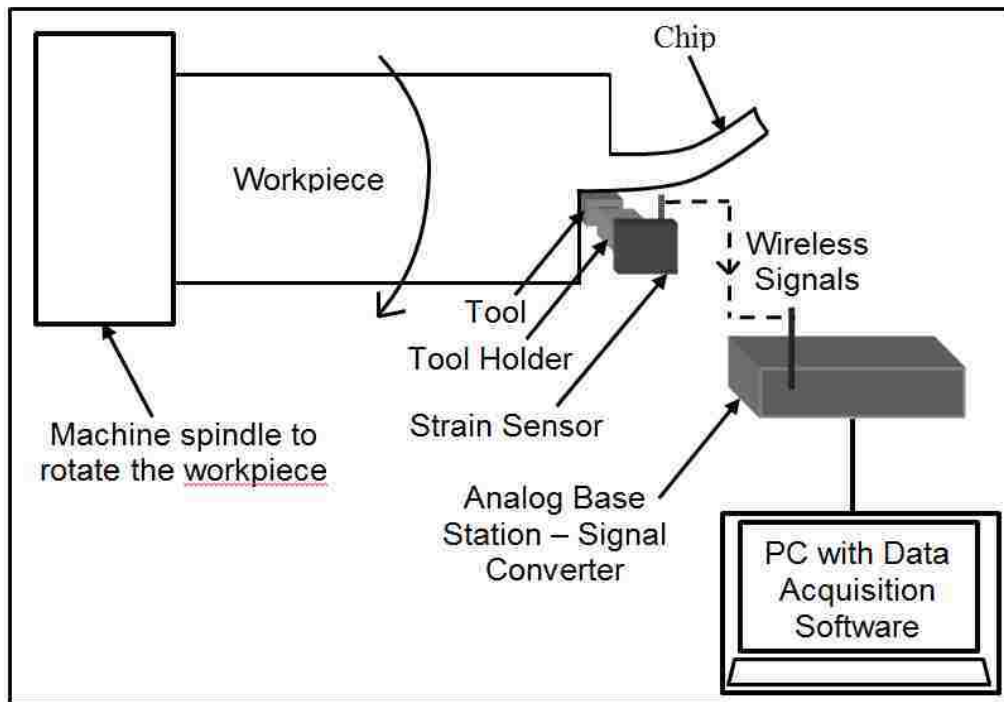
Fig. 3.6. Schematic diagram showing the different components of the force sensor and data acquisition system.
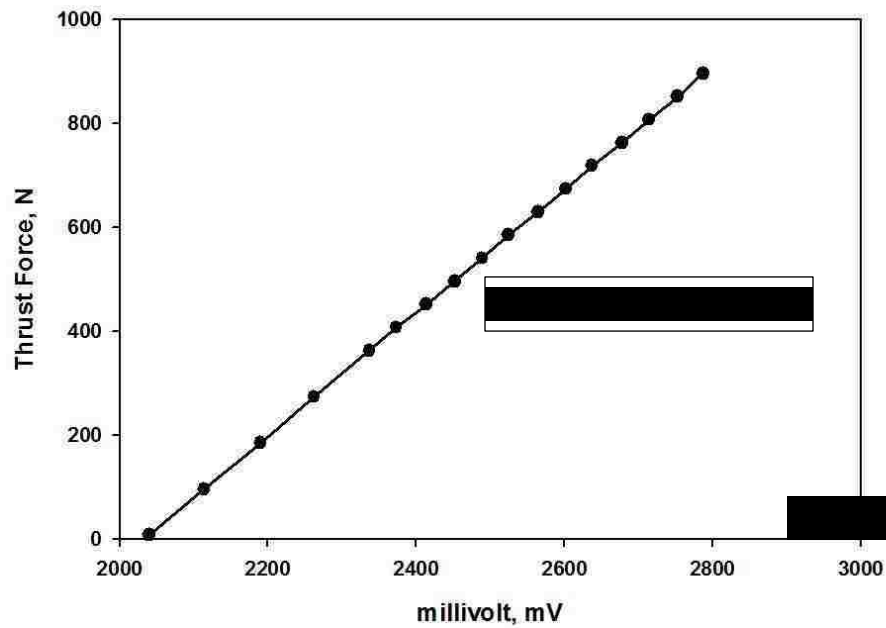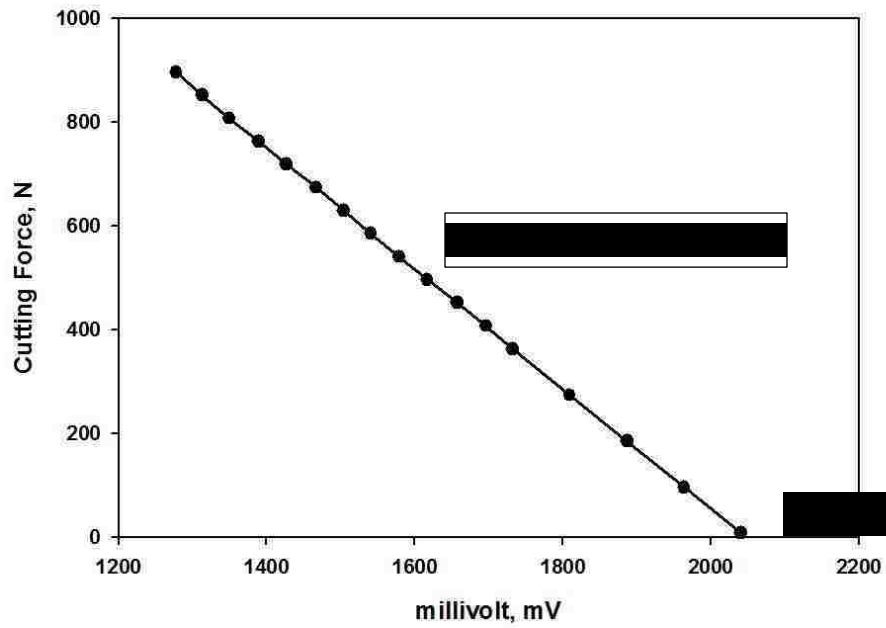
Fig. 3.7. Curves for relation between readings on Agile Link output (millivolt) and force (N) applied on force measuring system during loading and unloading for (a) cutting forces and (b) thrust forces. The corresponding equations for loading and unloading are also shown on the plots.
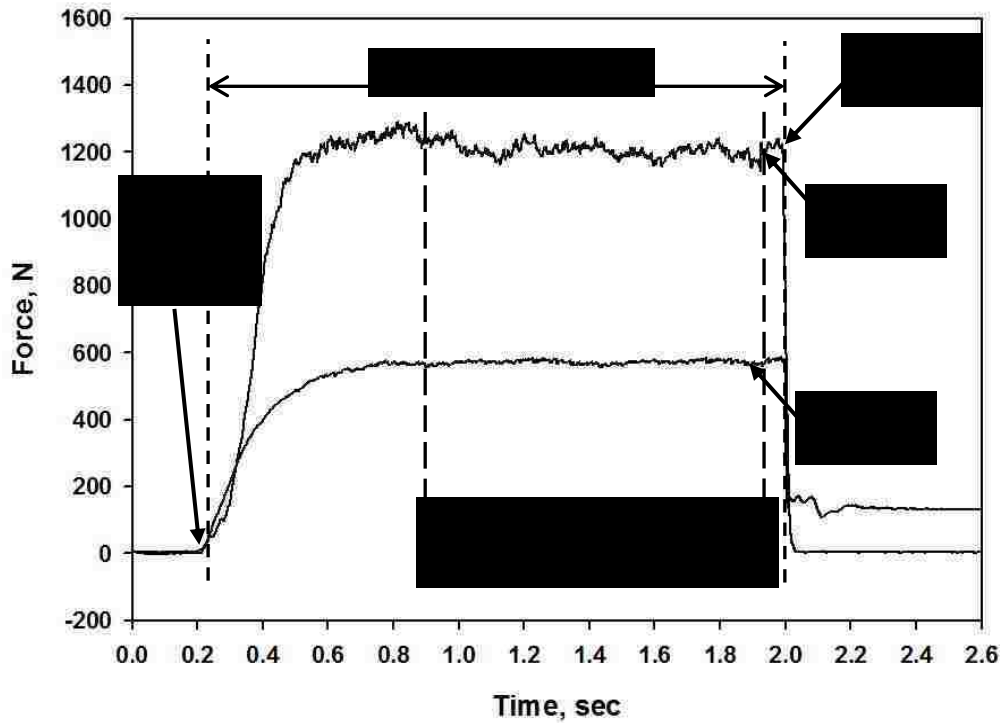
Fig. 3.8. Typical force plot showing cutting and thrust forces obtained after analysis of output data from the force-measuring system and different stages in a typical force vs. time plot obtained for orthogonal cutting experiments (Cutting speed 43.5 m/min and feed rate 0.25 mm/rev).
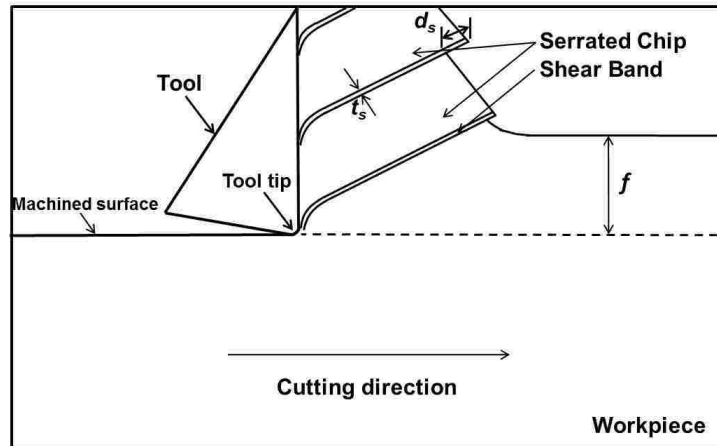
Fig. 3.9. Schematic of metallographic section taken from the workpiece for microstructural analyses, where f is feed rate, t_s thickness of the shear band and d_s is shear displacement within the shear band.
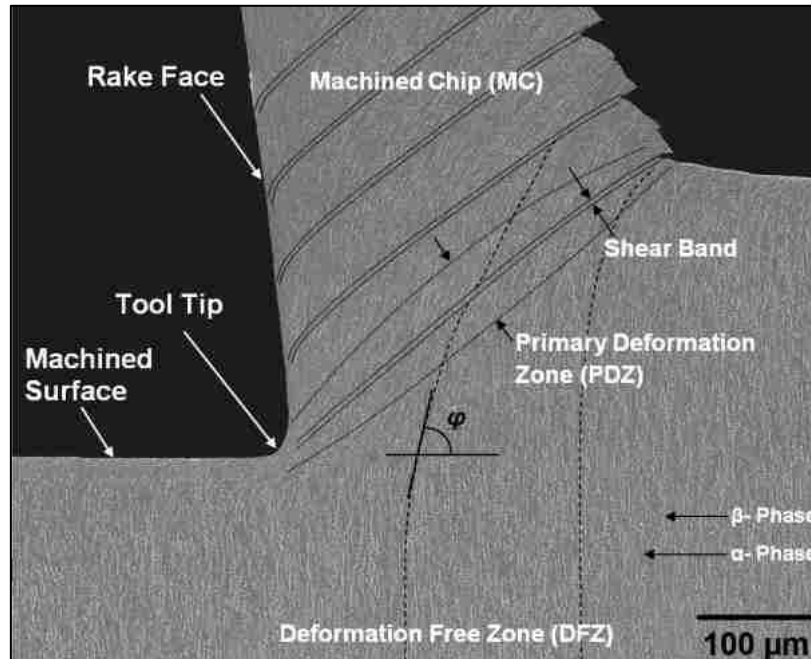
Fig. 3.10. Cross-sectional SEM image of the material ahead of the tool tip of Ti-6Al-4V alloy. Cutting speed = 63.5 m/min, feed rate = 0.25 mm/rev.
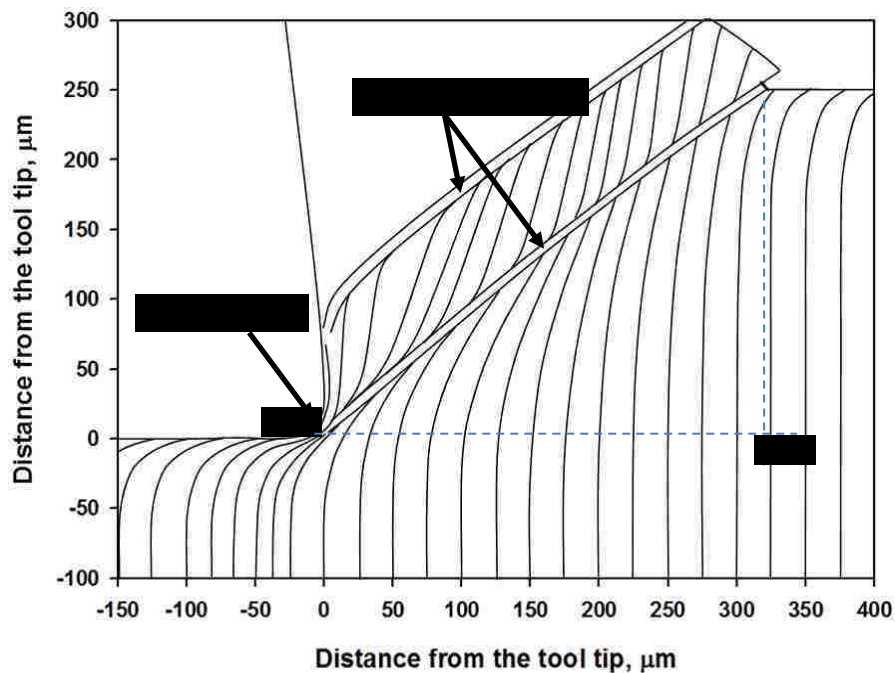
Fig. 3.11. Schematic representation the deformation pattern of Ti-6Al-4V alloy obtained by plotting orientation changes of the β phase grains at the same scale as in the actual microstructure in Fig. 3.10. OC is the cutting line.

92
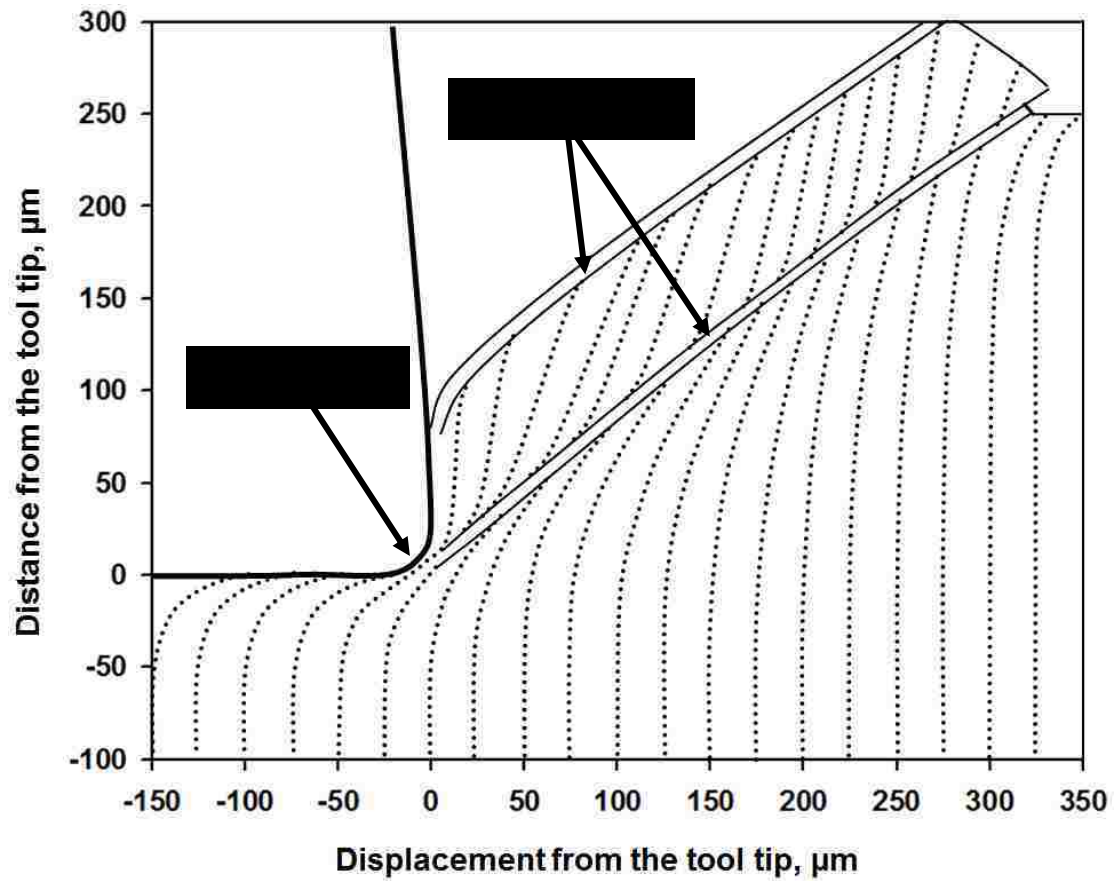
Fig. 3.12. Diagram showing the displacement of the β phase grains in the material ahead of the tool tip at the same scale as in the actual microstructure in Fig. 3.10.

Diameter =
0.7 mm

0.8 mm
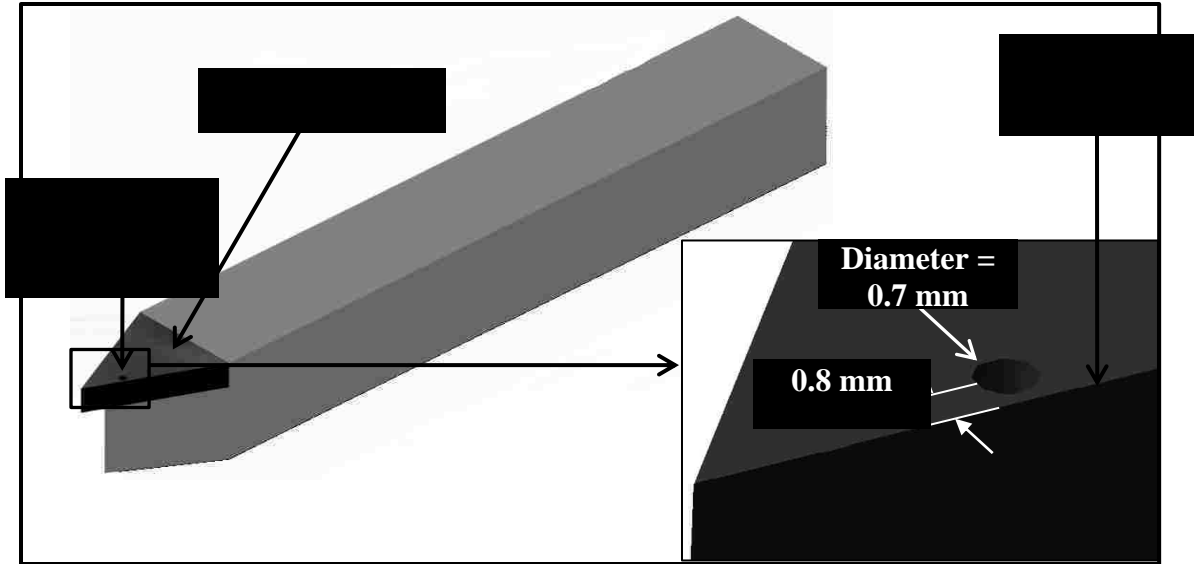
Fig. 3.13. Modified carbide tool for temperature measurement. A small hole was drilled using EDM on the rake face of the tool to install the thermocouple. A close view of the hole was shown in the insert.
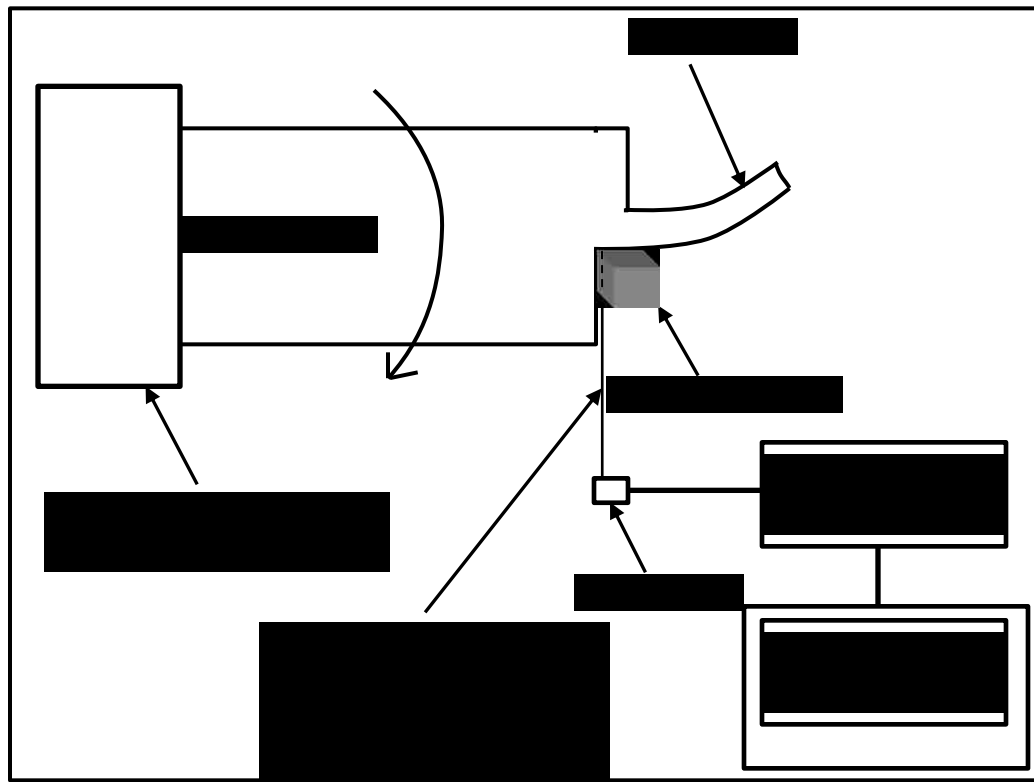
Fig. 3.14. Schematic diagram of the temperature measurement system.
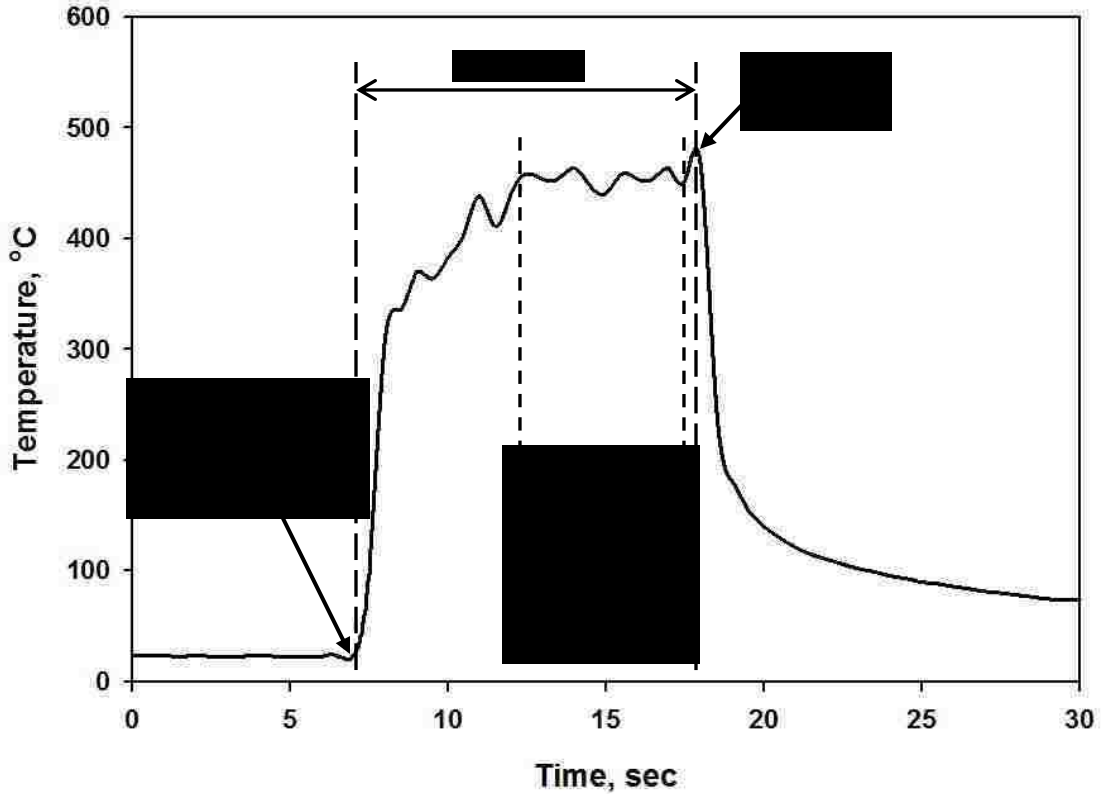
Fig. 3.15. Typical temperature plot showing temperature obtained after analysis of output data from the temperature measurement system and different stages in a typical temperature vs time plot obtained for orthogonal cutting experiments at 43.2 m/min of cutting speed and 0.25 mm/rev of feed rate.

Fig. 3.16. Schematic diagram showing the geometry of the finite element model of the tool and the workpiece (2D Lagrangian element formulation method).
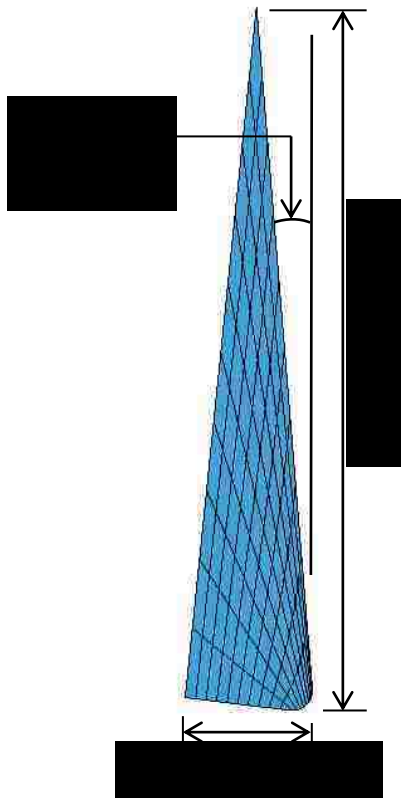
Fig. 3.17. Schemetic diagram showing the tool geometry.
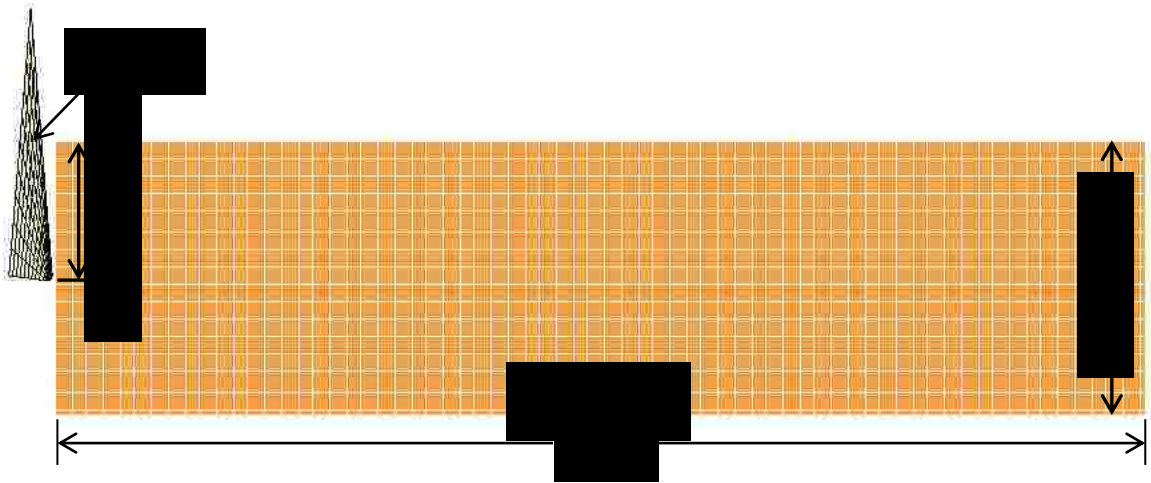
Fig. 3.18. Schematic diagram showing the geometry of the finite element model of the tool and the workpiece (SPH formulation).

CHAPTER 4: Experimental Results

4.1. Introduction

This chapter presents the experimental results conducted in order to determine the machining performance of Ti-6Al-4V alloy subjected to orthogonal cutting under different cutting conditions. The effect of feed rate and cutting speed on the machining of the alloy was examined by conducting turning experiments at different feed rates and different cutting speeds. The cutting speed was varied from 14.4 m/min to 63.5 m/min maintaining the maximum feed rate constant at 0.25 mm/rev in order to understand the effect of cutting speed. However, for understanding the effect of feed rate, feed rate was varied from 0.10 mm/rev to 0.25 mm/rev keeping a constant moderate cutting speed of 43.2 m/min. Four different values were used to ensure the statistical viability of the effects of cutting speed and feed rate on the machinability of Ti-6Al-4V alloy.

SEM and surface profilometer, WYKO was used to observe the machined surface quality. Microstructural observations using SEM was performed to determine the deformation state in the material ahead of the tool tip and below the machined surface. Variation of hardness value in the material ahead of the tool tip was measured and analyzed. Also, deformation of material in front of the tool tip was studied by estimating flow stress and plastic strain distribution in the region. These results were used subsequently to calculate the work of deformation, temperature distribution in the material ahead of the tool tip and used in the material models in FEA in chapter 5.

The results obtained from the experimental work are presented in the following sections.

4.2. Analysis of forces generated during dry orthogonal cutting

4.2.1. Cutting force measurements

Figures 4.1 (a and b) illustrate cutting forces measured for Ti-6Al-4V alloy under different conditions. Cutting forces were measured for different feed rates including 0.10 mm/rev, 0.15 mm/rev, 0.20 mm/rev and 0.25 mm/rev where the cutting speed was constant (43.2 m/min). Cutting forces were also measured for different cutting speeds such as 14.4 m/min, 29.6 m/min, 43.2 m/min and 63.5 m/min where the feed rate was constant (0.25 mm/rev). An examination of the responses revealed that there was no significant change in measured force values in the cutting zone for fixed cutting conditions.

Average cutting force for each cutting condition studied was estimated from the force data of the steady state cutting zone, immediately before the brake was applied. Fig. 4.2a presents the variation of the average cutting forces with different feeds at 43.2 m/min of cutting speed. It was found that the cutting force was increased from 504 N to 1150 N with feed rate from 0.10 mm/rev to 0.25 mm/rev. The variation of average cutting force from 898 N to 1240 N with different cutting speeds is depicted in Fig. 4.2b. The general trend outlined that the cutting force decreased in magnitude with an increase in cutting speed.

4.2.2. Thrust force measurements

Thrust forces were measured for different feed rates (Fig. 4.3a) such as 0.10 mm/rev, 0.10 mm/rev, 0.15 mm/rev, 0.20 mm/rev and 0.25 mm/rev where the cutting speed was constant (43.2 m/min). Thrust forces were also measured for different cutting speeds namely 14.4 m/min, 29.6 m/min, 43.2 m/min and 63.5 m/min where the feed rate was constant (0.25 mm/rev). Average thrust force for each cutting condition studied was estimated from the force data of the stable cutting zone. Fig.4.4a presents the variation of the average thrust forces with different feeds at 43.2 m/min cutting speed. The thrust force was increased from 254 N to 538.5 N with feed rate from 0.10 mm/rev to 0.25 mm/rev. A direct relationship was observed between thrust force and feed rate. However, the average thrust force varied from 430 N to 543 N with different cutting speeds depicted in Fig. 4.4b.

4.2.3. Normalized cutting and thrust forces measurements

Normalized cutting and thrust force measurement is effective to analysis the force results. Normalized cutting force is equal to the cutting force per unit depth of cut or thickness and normalized thrust force is equal to the thrust force per unit depth of cut or thickness or $F_{normalized} = {}^{F_{Cutting\ or\ Thrust}}/_{W}$, where w is the depth of cut (= 3.2 mm).

The variation of normalized cutting and thrust forces are shown in Fig. 4.5. The trends outlined that the cutting and thrust forces increased with an increase in feed rate and decreased with an increase in cutting speed.

4.3. Chip Morphology Produced During Dry Orthogonal Cutting of Ti-6Al-4V Alloy

Serrated chips were formed during the machining of Ti-6Al-4V alloy at the experimental cutting conditions. The cross-sectional SEM images of deformational microstructure in the material ahead of the tool tip for different cutting conditions such as cutting speed 43.2 m/min and feed rate 0.10 mm/rev, cutting speed 43.2 m/min and feed rate 0.15 mm/rev, cutting speed 43.2 m/min and feed rate 0.20 mm/rev, cutting speed 43.2 m/min and feed rate 0.25 mm/rev, cutting speed 14.4 m/min and feed rate 0.25 mm/rev, and cutting speed 29.6 m/min and feed rate 0.25 mm/rev are shown in Fig. 4.6-4.11 respectively. It was observed that the chip thickness, distance between two shear bands, length of primary deformation zone and depth of deformed zone from the machined surface depended on the cutting conditions. It was confirmed for the SEM image of the shear band (Fig. 4.12) that the serrated chips were formed during the machining of Ti-6Al-4V alloy under these cutting conditions due to the adiabatic shear band formation.

4.3.1. Chip Thickness Variation

A cross sectional view of the machined chips (Fig. 4.13) reveals that the chip thickness varied with the feed rate. Fig. 4.14 also depicts that the chip thickness changes with the cutting speed. Average chip thickness measured from the different location of the chip, increased with the feed rate (Fig.4.15a) and also with the cutting speed (Fig. 4.15b). The average chip thickness increased from 96 μm to 199.6 μm for the increment of feed rate from 0.10 mm/rev to 0.25 mm/rev. However, the ratio between the maximum

thickness (t_{max}) and minimum thickness (t_{min}) of the chips varied from 1.13 to 1.9 with the increment of feed rate from 0.10 mm/rev to 0.25 mm/rev (Fig. 4.16).

4.3.2. Shear Band Frequency Variation

The shear banding frequency or the average distance between the center-line of two consecutive shear bands was observed to vary with the feed rate (Fig. 4.13) and cutting speed (Fig. 4.14). The average shear band frequency increased with an increase in feed rate and cutting speed (Fig. 4.17). Shear band frequency increased from 23 μm to 136 μm for the increment of feed rate from 0.10 mm/rev to 0.25 mm/rev. It was observed that the shear band frequency was lowest (23 μm) for the cutting conditions of 0.10 m/rev feed rate and 43.2 m/min cutting speed. However, the maximum shear band frequency (143 μm) was noted for the cutting conditions of 0.25 mm/rev feed rate and 63.5 m/min cutting speed.

Figures 4.18 (a and b) show the variation of cutting force with the shear band frequency for different cutting conditions. However, it was observed that the cutting force was increased with the shear band frequency for different feed rates and decreased with the shear band frequency for different cutting speed.

4.3.3. Shear Displacement Variation

Shear displacement can be defined as the displacement between two consecutive chip segments along the shear band. Shear displacement varied with the cutting conditions (Fig. 4.19). The average shear displacement increased with an increase in feed rate and cutting speed. The average shear displacement increased from 15 μm to 108 μm

for the increment of feed rate from 0.10 mm/rev to 0.25 mm/rev. However, the maximum average shear displacement (110 µm) was noted for the cutting conditions of 0.25 mm/rev feed rate and 63.5 m/min cutting speed.

4.3.4. Shear Band Width Variation

Fig. 4.20 and Fig. 4.21 depict the shear bands formed under different cutting conditions. The average width of the shear band increased with the feed rate and cutting speed (Fig. 4.22). The average width of the shear band varied between 2.4 µm and 8.5 µm for the feed rate from 0.10 mm/rev to 0.25 mm/rev. The maximum width of the shear band was 8.9 µm obtained during machining at 63.5 m/min and 0.25 mm/rev feed rate. However, the smallest width of the shear band (2.3 µm) was observed for the cutting condition of 43.2 m/min cutting speed and 0.10 mm/rev feed rate.

4.3.5. Shear Strain within the Shear Band

The shear strain within the shear band varied with the cutting conditions (Fig. 4.23). It was observed that the shear strain within the shear band varied from 6.25 to 14.7 for different cutting conditions and the maximum shear strain (14.7) was obtained during machining at 43.2 m/min cutting speed and 0.15 mm/rev feed rate. In case of different feed rate, the lowest shear strain value was 6.25 for cutting condition of 43.2 m/min cutting speed and 0.10 mm/rev feed rate. However, for different cutting speed, the lowest shear strain value was 8.5 for cutting condition of 14.4 m/min cutting speed and 0.25 mm/rev feed rate.

4.4. Subsurface Microstructure below the Machined Surface:

During machining the subsurface grains are deformed along the cutting direction. The deformation of the grains and the depth of deformation zone form the machined surface depend on the machining parameters. Fig. 4.24 and Fig. 4.25 depict the subsurface microstructure and the variation of depth of deformed zone for different cutting conditions.

A close observation was done on the subsurface microstructure to find the white layer zone. Fig. 4.26 confirmed that no white layer was found below the machined surface.

4.4.1. Strain Gradient

The maximum strain generated below the machined surface and strain gradient that were measured using the 'TableCurve 2D' software, depended on the cutting conditions. Figures 4.27 (a and b) show the variation of strain gradient or the maximum strain generated below the machined surface with feed rate and cutting speed. For 43.2 m/min of cutting speed the maximum strain below the machined surface at feed rate of 0.10 mm/rev, 0.15 mm/rev, 0.20 mm/rev and 0.25 mm/rev were 1.1, 1.2, 1.3 and 1.5 respectively. The highest value of strain generated at the machined surface was 1.66 observed for the cutting conditions of 63.5 m/min cutting speed and 0.25 mm/rev feed rate.

A relationship was developed between the distance below the machined surface (l) and the average equivalent strain ($\bar{\varepsilon}$) for different cutting conditions. This relationship ($R^2 = 0.98$) is defined as:

$$\bar{\varepsilon} = 1.55 \exp(-0.1021\,l) \tag{4.1}$$

Using Eq. 4.1, the average strain below the machined surface at any location can be measured.

4.4.2. Depth of Deformed Zone

The average depth of deformed zone calculated from Fig. 4.27, increased with an increase in feed rate and cutting speed (Fig. 4.28). It was observed that the depth of deform zone varied form 30 µm to 51 µm for the feed rate from 0.10 mm/rev to 0.25 mm/rev. The maximum depth of deformed zone (55.1 µm) was observed for the cutting condition of 63.5 m/min cutting speed and 0.25 mm/rev feed rate.

4.5. Analysis of Surface Finish of Machined Surface

Surface finish is one of the most important factors in determining the machinability of an alloy and suitability of a component for a given application. Surface finish varies with the machining parameters. Surface roughness of the machined surface was studied in order to investigate the effect of cutting conditions such as cutting speed and feed per revolution on surface quality of the material.

Surface profilometer, WYKO images and corresponding SEM images of the machined surface for different feed rates are shown in Fig. 4.29(a-d). It was found that

the surface roughness (R_a) of the machined surface increased with the feed rate. Figures 4.30(a-d) illustrate the WYKO images and corresponding SEM images of the machined surface for different cutting speeds. For 43.2 m/min of cutting speed the average surface roughness of the machined surface at feed rate of 0.10 mm/rev, 0.15 mm/rev, 0.20 mm/rev and 0.25 mm/rev were 210 μm, 291 μm, 361 μm and 440 μm respectively. However, for 0.25 mm/rev of feed rate the average surface roughness of the machined surface at cutting speed of 14.4 m/min, 29.6 m/min, 43.2 m/min and 63.5 m/min were 219 μm, 320 μm, 440 μm and 498 μm respectively. The variation of the average surface roughness with feed rate and cutting speed are shown in Fig. 4.31a and Fig. 4.31b respectively. It was observed that the surface quality decreased with an increase in feed rate and cutting speed.

From the Figures 4.28 (a and b) and Figures 4.31 (a and b), it was observed that the both surface roughness and depth of deformed zone varied with the feed rate and cutting speed. As the feed rate or cutting speed was increased, the depth of deformed zone was increased and the surface roughness was also increased (Fig. 4.32). Surface roughness increased almost linearly with the depth of deformed zone.

Fig. 4.33 depicts the relationship between the surface roughness and the maximum strain below the machined surface. It was noted that the surface roughness increased with the strain below the machined surface. However, the relationship between surface roughness and the shear band frequency (Fig. 4.34) suggested that the surface roughness also increased with the shear band frequency.

4.6. Strain Distribution in the Material Ahead of the Tool Tip

A close and careful examination of the cross-sectional area of the machined section revealed that the β phase grains trace out well defined patterns which are very similar to flow lines present in the machined cross-section of softer materials such as copper [31] and Aluminum 1100 [28].

The strain distributions in the material ahead of the tool tip for different cutting conditions such as cutting speed 63.5 m/min and feed rate 0.25 mm/rev, cutting speed 43.2 m/min and feed rate 0.10 mm/rev, cutting speed 43.2 m/min and feed rate 0.15 mm/rev, cutting speed 43.2 m/min and feed rate 0.20 mm/rev, cutting speed 43.2 m/min and feed rate 0.25 mm/rev, cutting speed 14.4 m/min and feed rate 0.25 mm/rev, and cutting speed 29.6 m/min and feed rate 0.25 mm/rev are shown in Fig. 4.35-4.41 respectively.

It was observed that the strains decreased along the cutting line from the tool tip in the X-direction. The maximum strain is generated in the material at the tool tip for all the cutting conditions. For 43.2 m/min of cutting speed the maximum strain, at feed rate of 0.10 mm/rev, 0.15 mm/rev, 0.20 mm/rev and 0.25 mm/rev were 1.1, 1.2, 1.32 and 1.52 respectively. However, for 0.25 mm/rev of feed rate the maximum strain, at cutting speed of 14.4 m/min, 29.6 m/min, 43.2 m/min and 63.5 m/min were 1.4, 1.45, 1.52 and 1.66 respectively.

4.7. Flow Stress Distribution in the Material Ahead of the Tool Tip

Vickers hardness measurements were used to find the variation in hardness in the material ahead of the tool tip of an orthogonally cut sample machined under different cutting conditions. Fig. 4.42 depicts the results of the microhardness measurements in the material ahead of the tool tip which were measured at regular intervals of 50 µm both parallel and normal to the cutting direction. Two additional measurements were made at 30 µm above and below each indentation point, and the mean value of these measurements was used to represent the local microhardness. The maximum hardness was obtained in the material at the tool tip.

The local flow stress values were estimated from the Vickers hardness measurements using the Eq.2.18. The stress distribution in the material ahead of the tool tip for the cutting condition of 63.5 m/min cutting speed and 0.25 mm/rev feed rate is shown in Fig. 4.43. The points on the micro-graph outline having the same value for stresses have also been connected together to obtain iso-stress contours.

The flow distributions obtained from the hardness measurement, in the material ahead of the tool tip for different cutting conditions such as cutting speed cutting speed 43.2 m/min and feed rate 0.10 mm/rev, cutting speed 43.2 m/min and feed rate 0.15 mm/rev, cutting speed 43.2 m/min and feed rate 0.20 mm/rev, cutting speed 43.2 m/min and feed rate 0.25 mm/rev, cutting speed 14.4 m/min and feed rate 0.25 mm/rev, and cutting speed 29.6 m/min and feed rate 0.25 mm/rev are shown in Fig. 4.44-4.49 respectively. For all the cutting conditions the maximum stress was observed at the tool tip and also the flow stress decreased along the cutting line from the tool tip in the X-

107

direction. For 43.2 m/min of cutting speed the maximum flow stress, at feed rate of 0.10 mm/rev, 0.15 mm/rev, 0.20 mm/rev and 0.25 mm/rev were 1439.1 MPa, 1446 MPa, 1443 MPa and 1452.7 MPa respectively. However, for 0.25 mm/rev of feed rate the maximum flow stress, at cutting speed of 14.4 m/min, 29.6 m/min, 43.2 m/min and 63.5 m/min were 1442 MPa, 144 MPa, 1452.7 MPa and 1457 MPa respectively.

4.8. Cumulative Stress-Strain Curve

A relationship between the plastic stresses and strains was established by plotting corresponding stress and strain values at each point in the material ahead of the tool tip. Fig. 4.50 reveals the flow curve that represents the relationship between the flow stresses, and equivalent strains developed during orthogonal cutting of Ti-6Al-4V alloy at cutting speed of 63.5 m/min and feed per revolution of 0.25 mm. A regression analysis showed that $\bar{\sigma}$ and $\bar{\varepsilon}$ relationship in Fig. 4.50 can be described using a phenomenological equation proposed by Voce [36]:

$$\bar{\sigma} = \bar{\sigma}_s - (\bar{\sigma}_s - \bar{\sigma}_o)\exp(-\frac{\bar{\varepsilon}}{\bar{\varepsilon}_c})$$

(4.2)

Cumulative stress strain curves for different cutting condition were also determined from the stress strain values in the material ahead of the tool tip. The magnitude of the cumulative stress-strain curve varied with the cutting conditions. The variation of the cumulative stress-strain curve with different feed rates and different cutting speeds are shown in Fig. 4.51 and Fig. 4.52 respectively. It was observed that the trend of the curves at different cutting conditions was almost identical. However, the

magnitude of the saturation stress varied in a short range from 1439.1 MPa to 1457 MPa for the increment of cutting speed due to the strain rate sensitivity of this alloy. In this case the strain rates were 800 s^{-1}, 1630 s^{-1}, 2400 s^{-1} and 3525 s^{-1} for cutting speeds of 14.4 m/min, 29.6 m/min, 43.4 m/min and 63.5 m/min respectively.

The Eq. 4.2 can be expressed in terms of a work hardening rate, $(\frac{d\bar{\sigma}}{d\bar{\varepsilon}})$ at a flow stress $\bar{\sigma}$ as:

$$\frac{d\bar{\sigma}}{d\bar{\varepsilon}} = \frac{\bar{\sigma}_s}{\bar{\varepsilon}_c}(1 - \frac{\bar{\sigma}}{\bar{\sigma}_s}) \tag{4.3}$$

where, $\bar{\sigma}_s$ is the saturation stress at which work hardening rate becomes zero, $\bar{\sigma}_o(= 1{,}242 \text{ MPa})$ is the yield strength of the material, and $\bar{\varepsilon}_c(= 0.13)$ is a constant.

A plot of the work hardening rate, $(\frac{d\bar{\sigma}}{d\bar{\varepsilon}})$ versus the flow stress curves for different cutting conditions are given in Figures 4.53 (a and b), It was observed that the work hardening rate of the material decreased with the flow stress and became zero at the saturation stress. However, the magnitude of the saturation stress varied in order with the cutting speed.

4.9. Energy Expended during Plastic Deformation

The energy consumption rate, i.e., the total energy consumed per unit time (P) during machining can be considered equal to the product of speed, V, and cutting force, F_c (i.e. $P = VF_c$). It was observed that the energy consumption rate increased with the cutting speed and feed rate (Fig. 4.54). The maximum value of the energy consumption

rate was 950.1 W observed during the machining at 63.5 m/min cutting speed and 0.25 mm/rev feed rate. However, the minimum value of the energy consumption rate (363 W) was observed during the machining at 43.2 m/min cutting speed and 0.10 mm/rev feed rate.

The energy consumption per unit volume of material removal or specific cutting energy, U, was calculated as:

$$U = {F_c}/{tf} \qquad (4.4)$$

where t is the depth of cut (= 3.2 mm) and f is the feed rate.

Specific energy is the total energy expended during the cutting process. It was observed that the specific cutting energy decreased with the cutting speed and feed rate (Fig. 4.55). The minimum value of the specific cutting energy (1122.4 MJ/m^3) was observed during the machining at 63.5 m/min cutting speed and 0.25 mm/rev feed rate.

The energy expended during the deformation of the material ahead of the tool tip can also be calculated from the area under the stress/strain curve. For each increment of strain, the work of plastic deformation, W, (per unit volume) is calculated using the Eq. 2.20.

$$W = \int_{\bar{\varepsilon}_n}^{\bar{\varepsilon}_{n+1}} (\overline{\sigma_s} - (\overline{\sigma_s} - \overline{\sigma}_o)\exp(-\frac{\bar{\varepsilon}}{\bar{\varepsilon}_c}))d\bar{\varepsilon} \qquad (2.20)$$

The stress relationship obtained from cumulative stress-strain plot shown in Fig.4.51 was found to follow Voce's equation and this relationship was used for estimation of work of plastic deformation using Eq. 2.20.

The iso-strain lines for the deformed material ahead of the tool tip are plotted in Fig. 4.56, and the (average) plastic work extended per unit volume (W) of the material between the iso-strain lines was given (numbers in brackets). For the cutting condition of 43.2 m/min cutting speed and 0.10 mm/rev feed rate, the cumulative plastic work expended per unit volume of material in the region between lowest strain and highest strain, which was approximately bound by the isostrain lines of 0.01 and 1.10, was computed as 1537.2 MJm^{-3} (Fig. 4.56).

However, For the cutting condition of 63.5 m/min cutting speed and 0.25 mm/rev feed rate, the cumulative plastic work expended per unit volume of material in the region between lowest strain (0.1) and highest strain (1.66) was computed as 2253.9 MJm^{-3} (Fig. 4.57).

4.10. Temperature Rise Due to Plastic Deformation

The temperature increase (ΔT) due to conversion of deformation energy to heat within a unit volume of material can be expressed by Eq. 2.21.

$$\Delta T = \frac{\beta}{\rho C} \int_{\bar{\varepsilon}_n}^{\bar{\varepsilon}_{n+1}} (\overline{\sigma_s} - (\overline{\sigma_s} - \overline{\sigma_o}) \exp(-\frac{\bar{\varepsilon}}{\bar{\varepsilon}_c})) d\bar{\varepsilon} \qquad (2.21)$$

where, β is the fraction of plastic work converted into heat and it is taken as 0.95 [18], $\rho = 4.43$ gm/cm^3, and specific heat, C = 0.526 J/g. ˚C.

Fig. 4.58 reveals the temperature distribution diagram in the material ahead of the tool tip for the cutting condition of 63.5 m/min cutting speed and 0.25 mm/rev feed rate. Maximum temperature was 1217 K (944 ˚C) generated in the material ahead of the tool tip and in the secondary deformation zone (SDZ). The temperature decreased along the cutting line from the tool tip in the X-direction.

Similarly, the temperature distributions diagram obtained from the cumulative stress-strain curve, for different cutting conditions such as cutting speed cutting speed 43.2 m/min and feed rate 0.10 mm/rev, cutting speed 43.2 m/min and feed rate 0.15 mm/rev, cutting speed 43.2 m/min and feed rate 0.20 mm/rev, cutting speed 43.2 m/min and feed rate 0.25 mm/rev, cutting speed 14.4 m/min and feed rate 0.25 mm/rev, and cutting speed 29.6 m/min and feed rate 0.25 mm/rev are shown in Fig. 4.59-4.64 respectively. It was observed at the tool tip temperature varied with the cutting conditions and the temperature decreased along the cutting line from the tool tip in the X-direction. For 43.2 m/min of cutting speed the tool tip temperature, at feed rate of 0.10 mm/rev, 0.15 mm/rev, 0.20 mm/rev and 0.25 mm/rev were 900 K (627 ˚C), 959 K (686 ˚C), 1055 K (782 ˚C) and 1125 K (852 ˚C) respectively. However, for 0.25 mm/rev of feed rate the tool tip temperature, at cutting speed of 14.4 m/min, 29.6 m/min, 43.2 m/min and 63.5 m/min were 997 K (724 ˚C), 1040 K (767 ˚C), 1125 K (852 ˚C) and 1217 K (944 ˚C) respectively. It was observed that the temperature at the tool tip was increased with the feed rate (Fig. 4.65a) and also with the cutting speed (Fig. 4.65b).

Temperatures at the tool tip for different cutting condition were measured using the temperature measurement system and it was observed that the tool tip temperature increased with increasing the feed rate (Fig. 4.66a) and cutting speed (Fig. 4.66b). A comparison between the calculated temperature using Eq. 2.21 and the temperature measured by temperature measurement system was also observed for different cutting conditions. It was observed that the temperature values measured by temperature measurement system were lower than the calculated values due to the heat loss and location of the thermocouple. The thermocouple was mounted at the rake face and 0.8 mm away from the cutting edge.

4.11. Temperature and Hardness of the shear band

The temperature within the shear zone, T_{sz} was measured by Eq. 2.25.

$$T_{sz} = \frac{\tau \gamma}{\rho C} \left[\frac{1}{1 + 1.328 \sqrt{\frac{K\gamma}{V_c d}}} \right] + T_{amb} \qquad (2.25)$$

where, V_c is the cutting speed (63.5 m/min or 1.05 m/s) and d is depth of cut which is equal to the feed rate (0.25 mm/rev), T_{amb} is the ambient temperature (23 °C), K is the thermal diffusivity of Ti-6Al-4V alloy (2.87×10^{-6} m^2/s).

The shear stress on the shear plane τ was calculated from the Eq. 2.6.

$$\tau_s = \frac{F_c \cos \varphi - F_t \sin \varphi}{\left[\frac{w.f}{\sin \varphi} \right]} \qquad (2.6)$$

where, the cutting and thrust forces for 63.5 m/min cutting speed and 0.25 mm/rev feed rate, were 898 N and 430 N respectively. The width or thickness of the workpiece (w) was 3.2 mm and the shear angle, φ was 39 ˚. Therefore, the calculated shear stress was 336.11 MPa. Under this cutting condition the shear strain, $\gamma_{sb} (= \frac{d_s}{t_s})$, within the shear band was 12.54 where d_s was calculated from the Fig. 4.15d as 110.32 $\pm$ 23.71 µm and t_s was calculated from Fig. 4.22, was 8.79 $\pm$ 1.45 µm.

Therefore, the temperature within the shear band was 1235.5 ˚C or 1508.5 K which was greater than the (α + β)/β transus temperature 1268±15 K (995±15 ˚C).

Shear band temperature within the shear band for different cutting conditions are shown in Fig. 4.67. It was observed that the temperature within the shear band was higher than the transformation temperature for the cutting conditions of 43.2 m/min cutting speed and 0.15 mm/rev feed rate, 43.2 m/min cutting speed and 0.20 mm/rev feed rate, 43.2 m/min cutting speed and 0.25 mm/rev feed rate, 29.6 m/min cutting speed and 0.25 mm/rev feed rate, and 63.5 m/min cutting speed and 0.25 mm/rev feed rate. However, the shear band temperature was lower than the transformation temperature for the cutting conditions of 43.2 m/min cutting speed and 0.10 mm/rev feed rate, and 14.4 m/min cutting speed and 0.25 mm/rev feed rate.

Microhardness of the shear band measured using the Vickers hardness measurement with 10 gm load, was 395.4 $\pm$ 4.1 HV. Fig. 4.68 shows the SEM image of indentations of microhardness measurements. The spacing distance of indentation was approximately 20 µm. It was observed in Fig. 4.69 that the microhardness value of the shear band was lower than the surrounding deformed grains (409.1 $\pm$ 5.5 HV).

However, cracks were observed at the shear band (Fig. 4.12) and the microhardness ahead of the crack tip was high (402.1 $\pm$ 7.9 HV). The microhardness varied with the distance from the crack tip (Fig. 4.70).

4.12. Tool Surface

Tool surface and edge were observed before (Fig. 4.71a) and after (4.71b) the machining of Ti-6Al-4V alloy. Transferred material was observed after the machining operation on the cutting edge of the cutting tool. EDS results (Fig. 4.72a) and the EDS mapping results (Fig. 4.72b) confirmed that the transferred material contained titanium, aluminum, vanadium etc. that came from the workpiece (Ti-6Al-4V alloy) during machining. It was also observed that the amount of transferred material depended on the cutting conditions (Fig. 4.73). At lower cutting speed the amount of transferred material was less (13.8 % area) compared to the amount of transferred material at higher cutting speed (23.6 % area).
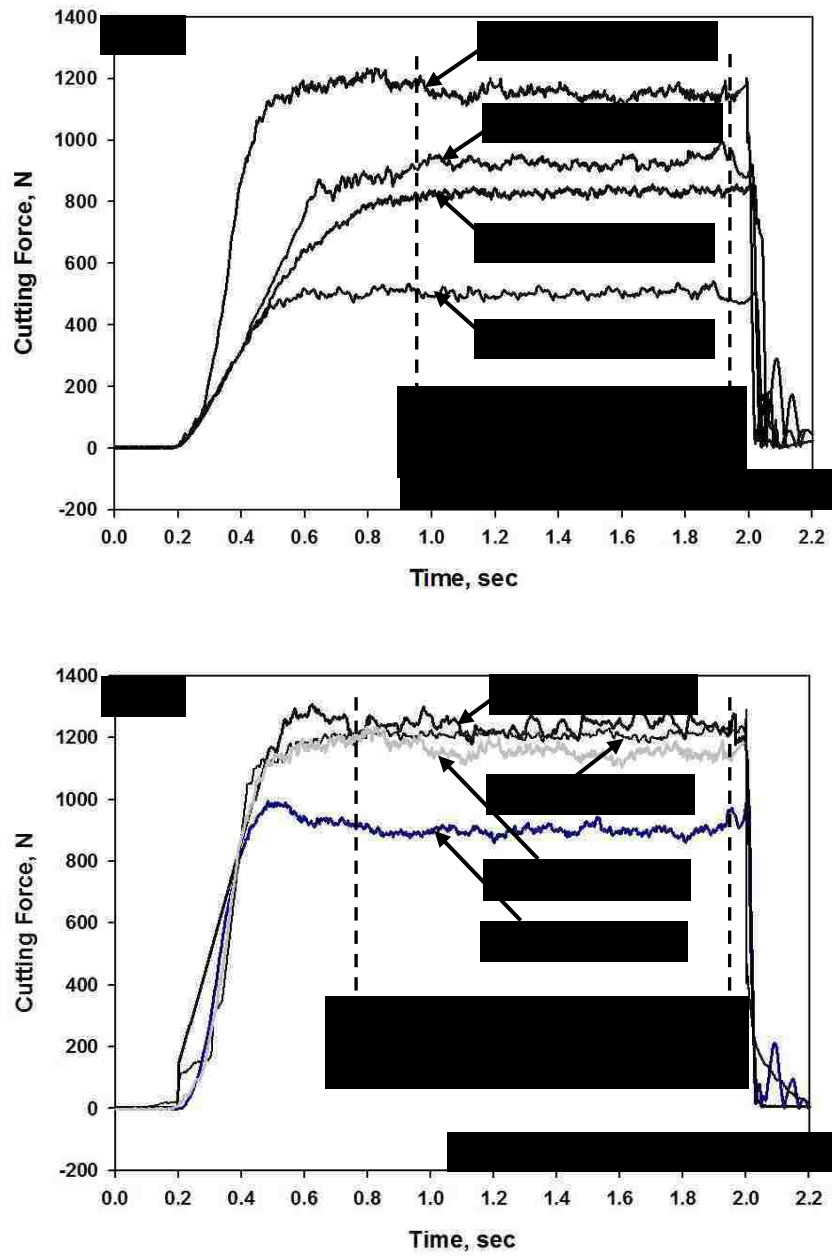
Fig. 4.1. Plots showing variation of cutting forces with time for Ti-6Al-4V alloy when machined under (a) different magnitudes of feed per revolution and a constant cutting speed or 43.2 m/min, (b) different magnitudes of cutting speed and a constant feed rate or 0.25 mm/rev.
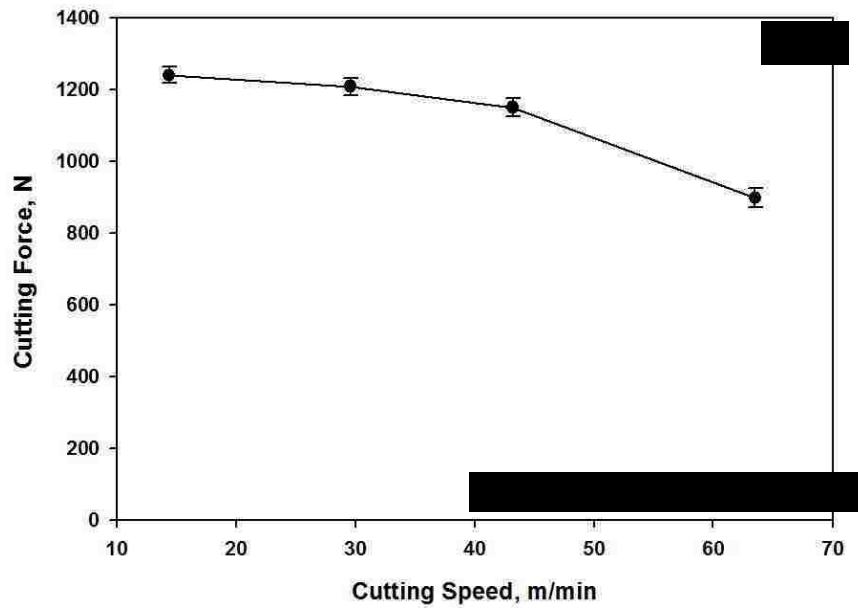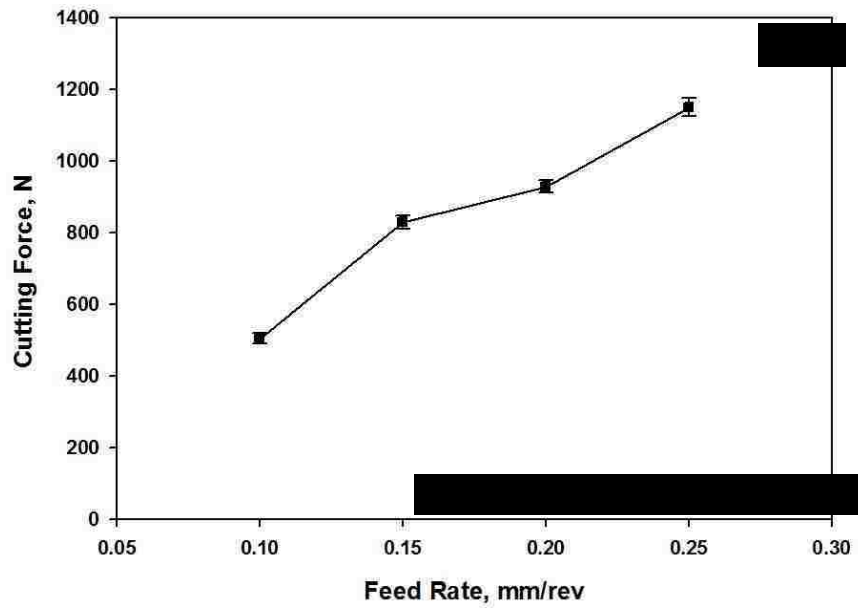
Fig. 4.2. Plot showing the variation of average cutting forces with increase in (a) feed for

43.2 m/min cutting speeds and (b) cutting speed for 0.25 mm feed per revolution.
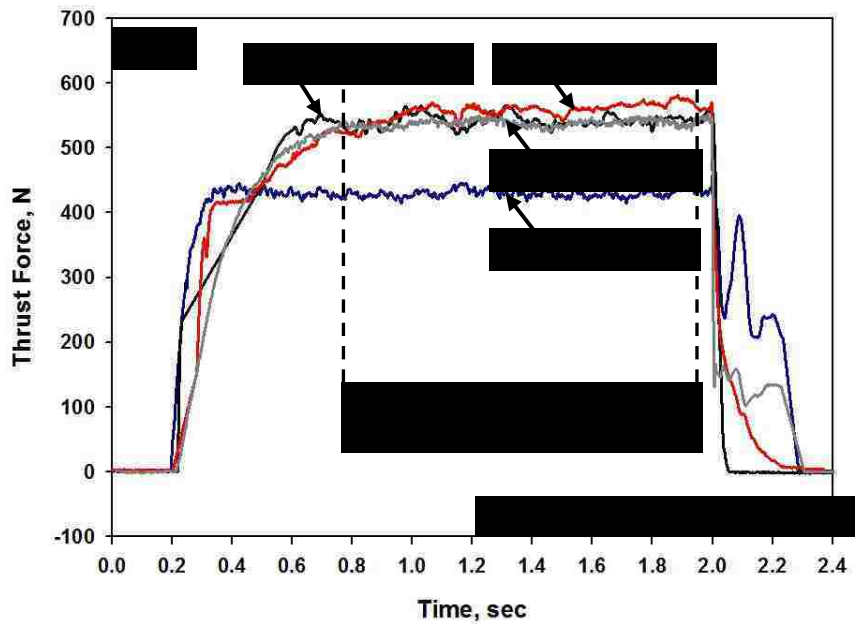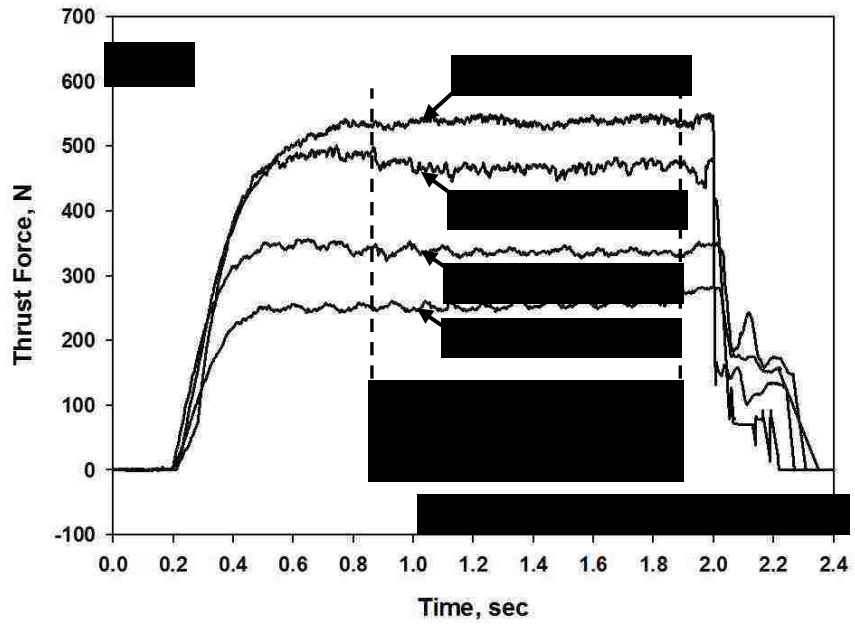
Fig.4.3. Plots showing variation of thrust forces with time for Ti-6Al-4V alloy when machined under (a) different magnitudes of feed per revolution and a constant cutting speed of 43.2 m/min, (b) different magnitudes of cutting speed and a constant feed rate or 0.25 mm/rev.
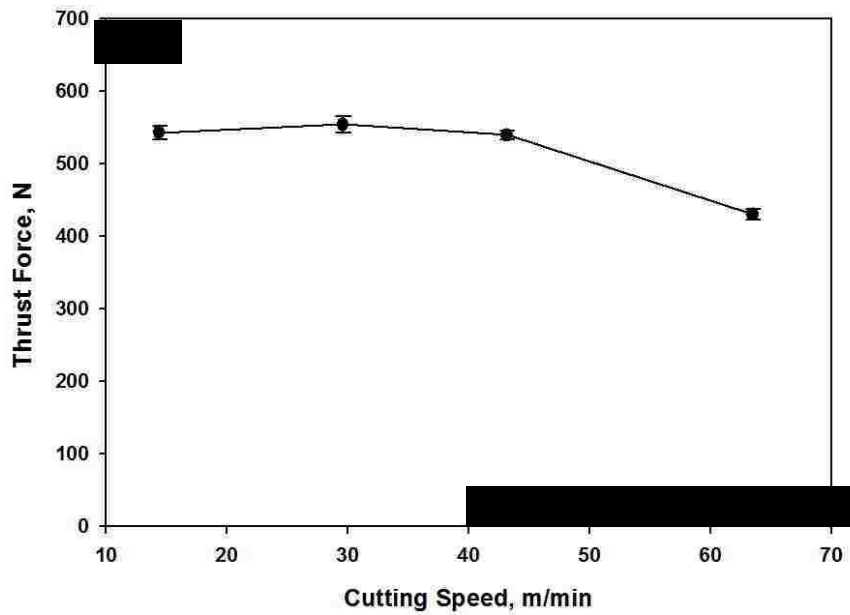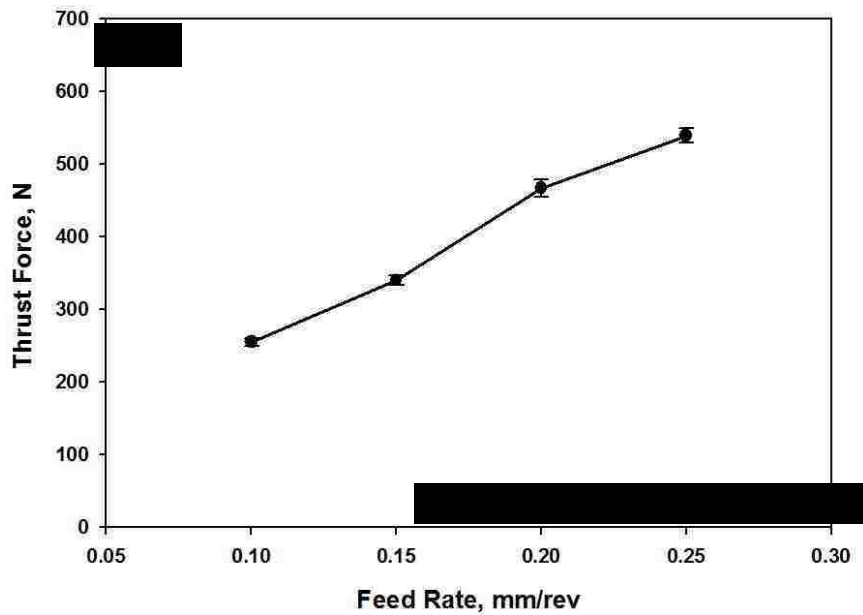
Fig. 4.4. Plot showing the variation of average thrust forces with (a) increase in feed for 43.2 m/min cutting speeds and (b) increase in cutting speed for 0.25 mm feed per revolution.
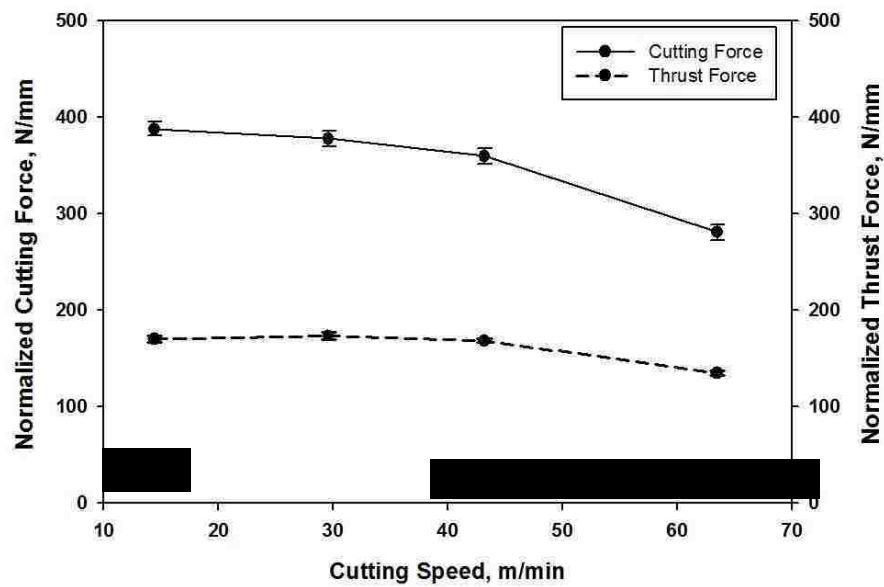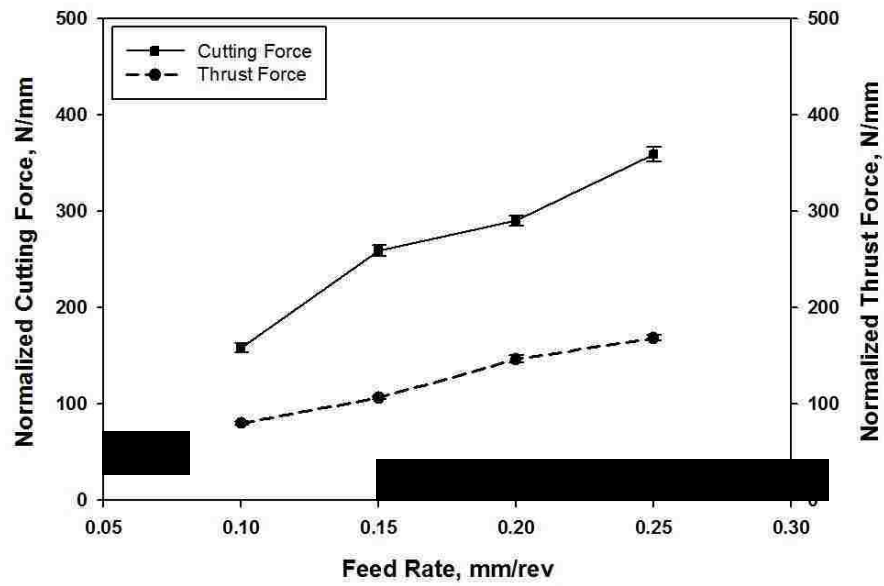
Fig. 4.5. Variation of cutting and thrust forces for per unit depth of cut, with (a) the feed rate and (b) the cutting speed.
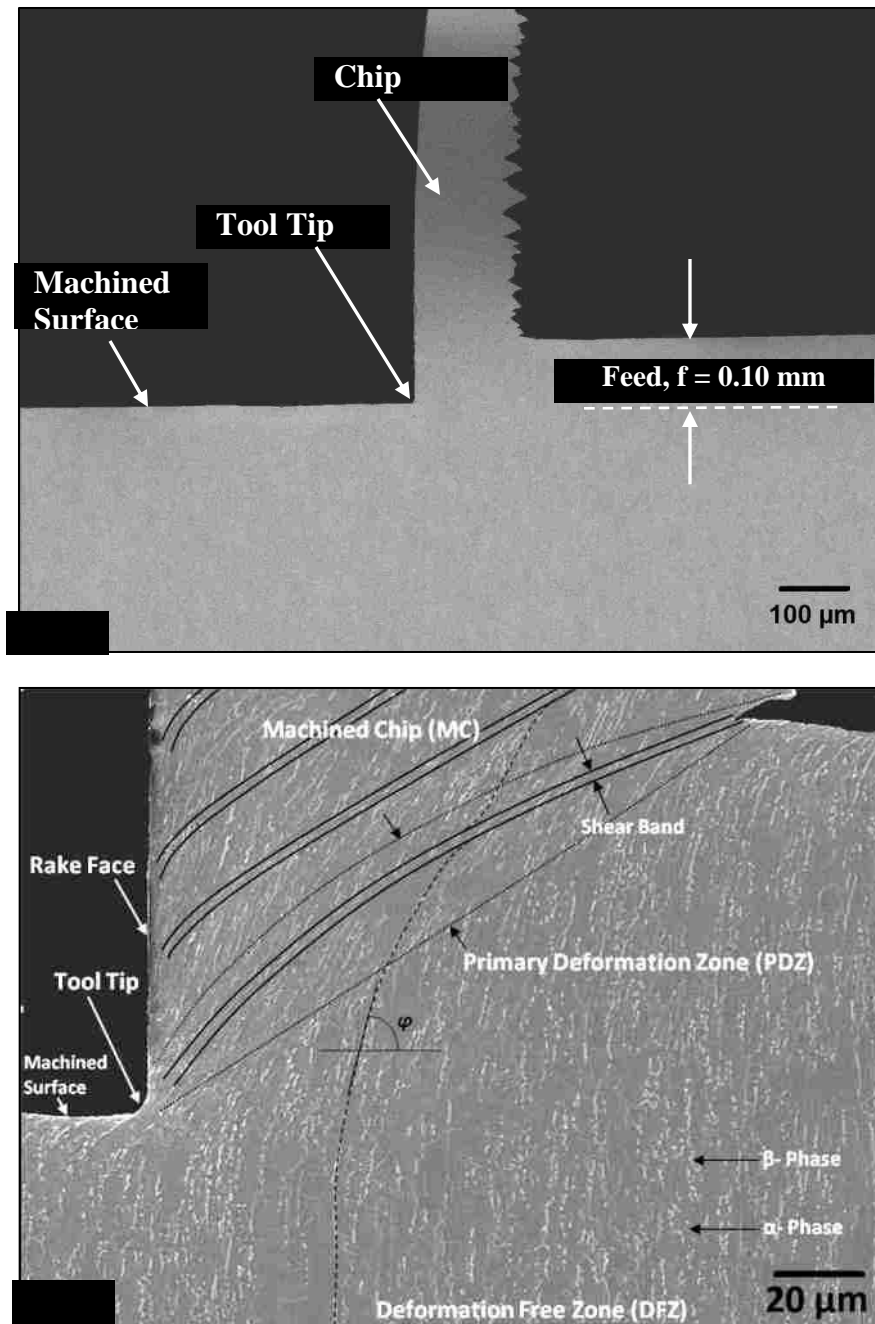
Fig. 4.6. (a) Cross-sectional SEM image of the material ahead of the tool tip of Ti-6Al-4V alloy. Cutting speed = 43.2 m/min and feed rate = 0.10 mm/rev, (b) Close view of the primary deformation zone.
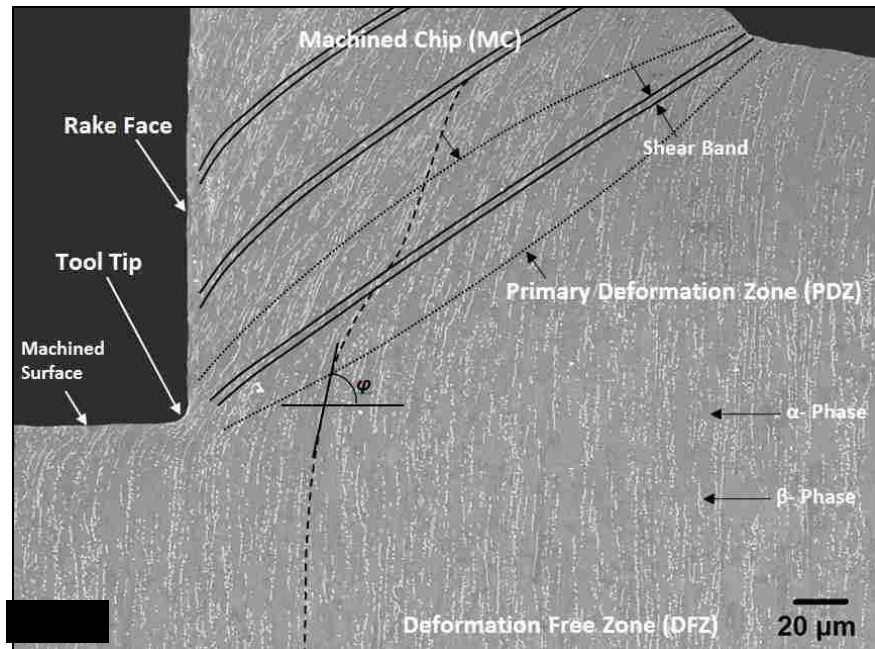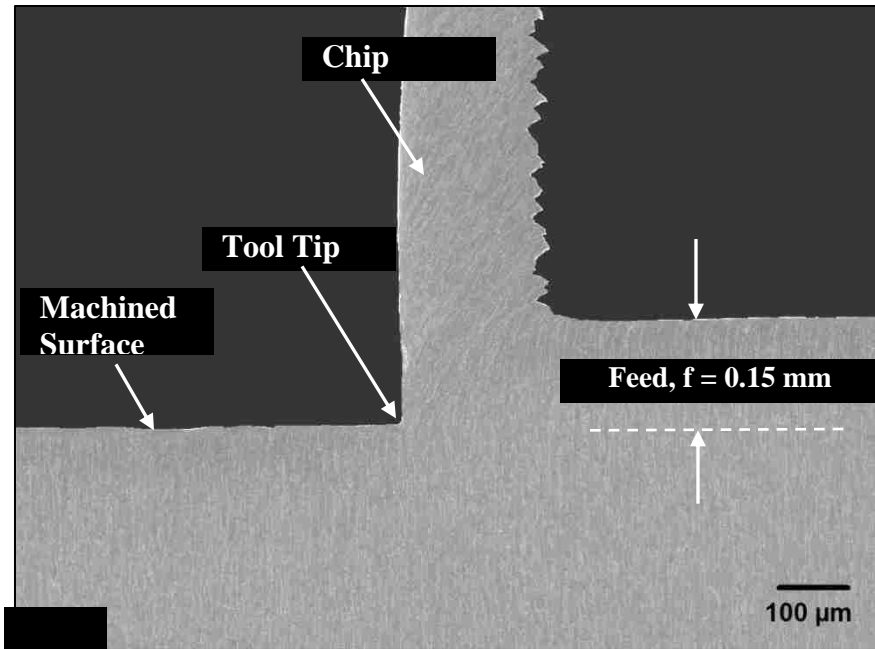
Fig. 4.7. (a) Cross-sectional SEM image of the material ahead of the tool tip of Ti-6Al-4V alloy. Cutting speed = 43.2 m/min and feed rate = 0.15 mm/rev, (b) Close view of the primary deformation zone.
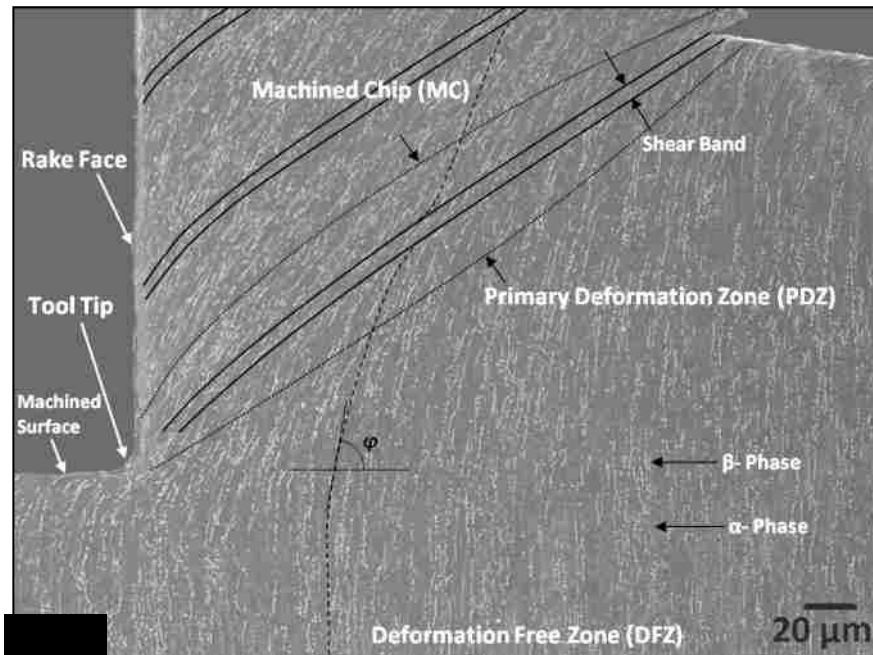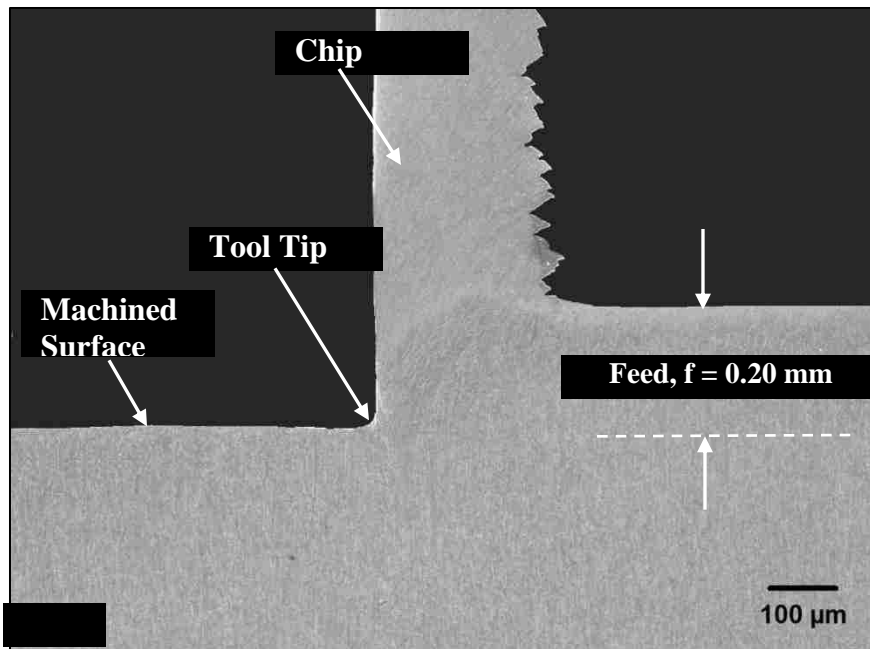
Fig. 4.8. (a) Cross-sectional SEM image of the material ahead of the tool tip of Ti-6Al-4V alloy. Cutting speed = 43.2 m/min and feed rate = 0.20 mm/rev, (b) Close view of the primary deformation zone.
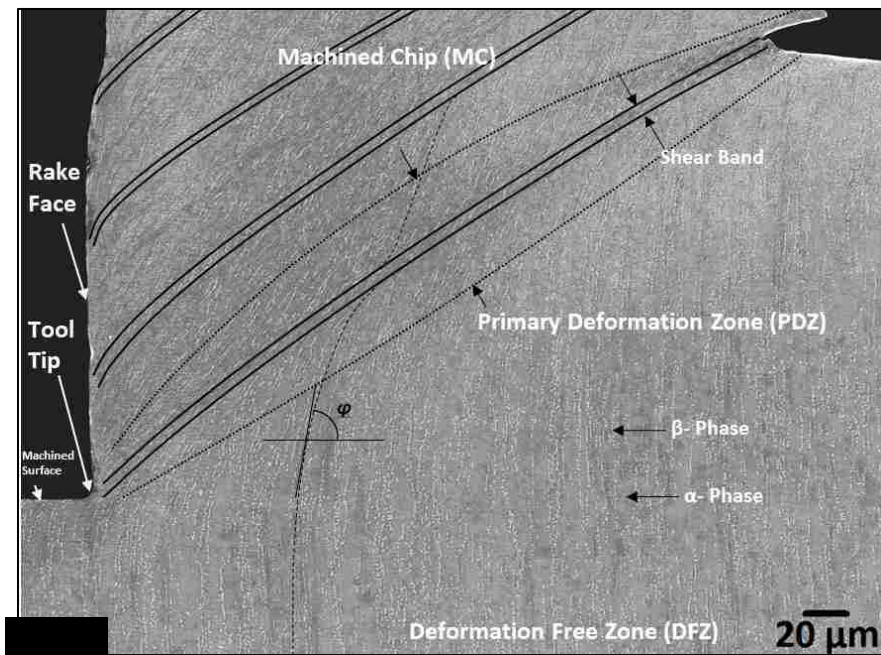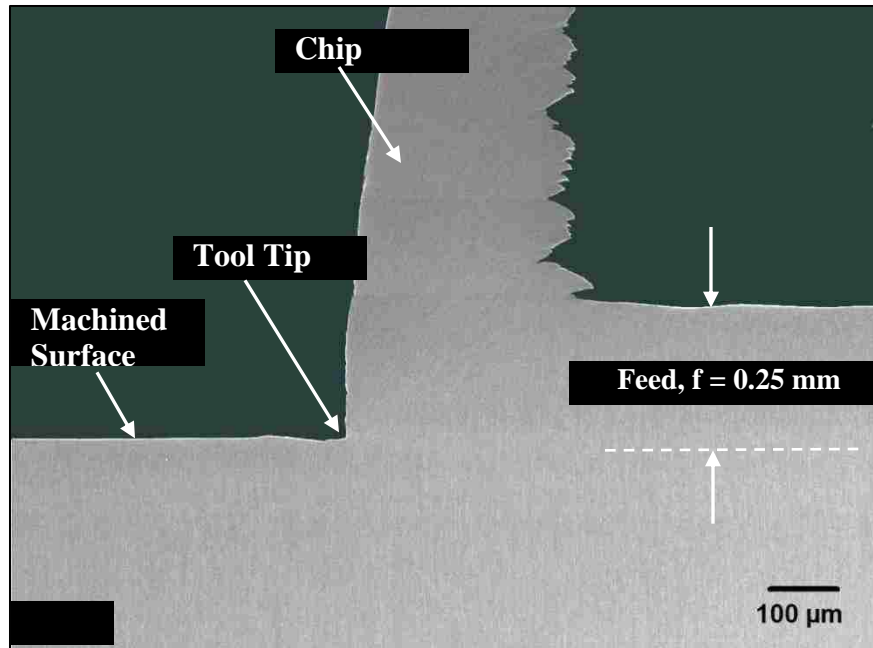
Fig. 4.9. (a) Cross-sectional SEM image of the material ahead of the tool tip of Ti-6Al-4V alloy. Cutting speed = 43.2 m/min and feed rate = 0.25 mm/rev, (b) Close view of the primary deformation zone.
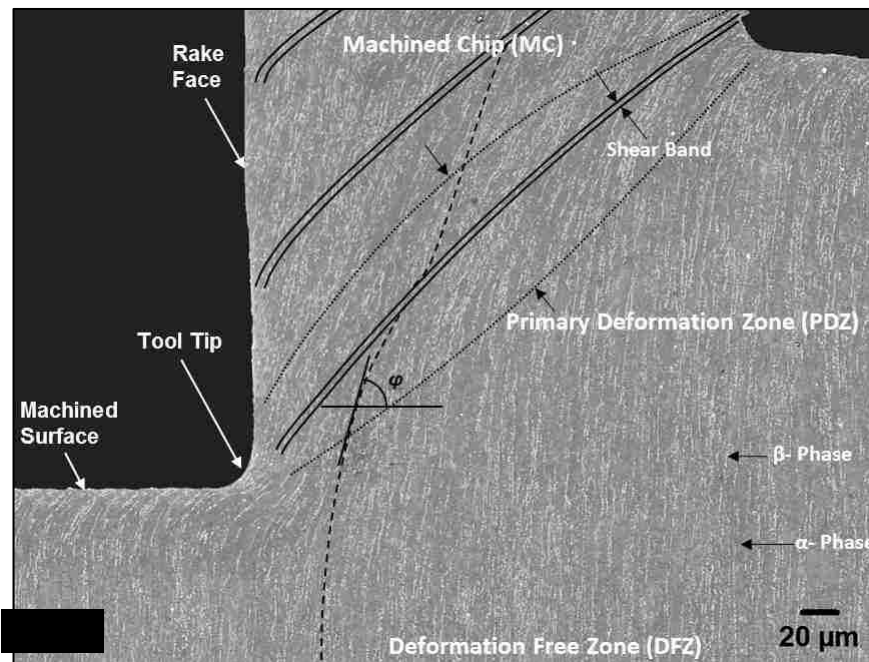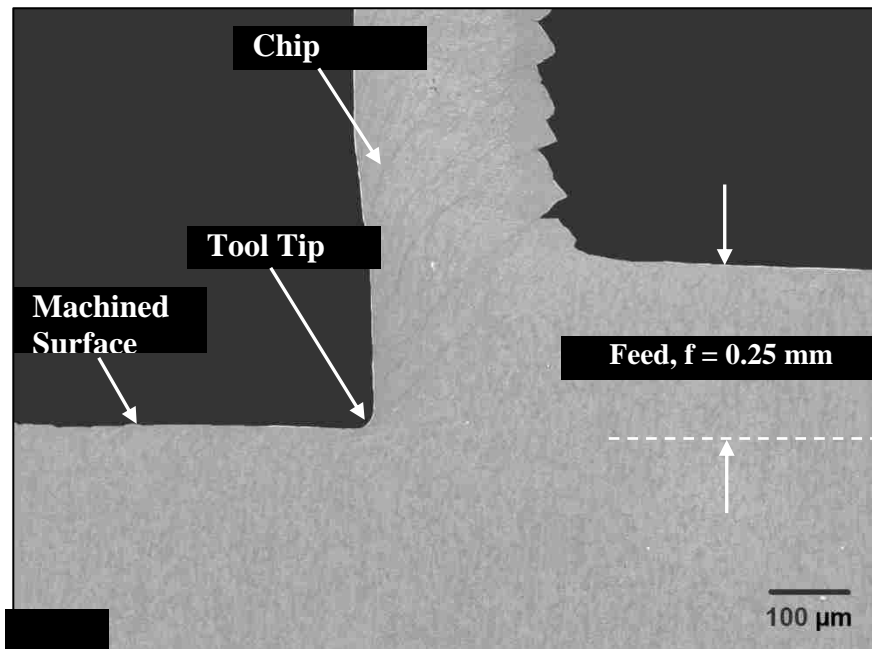
Fig. 4.10. (a) Cross-sectional SEM image of the material ahead of the tool tip of Ti-6Al-4V alloy. Cutting speed = 14.4 m/min and feed rate = 0.25 mm/rev, (b) Close view of the primary deformation zone.
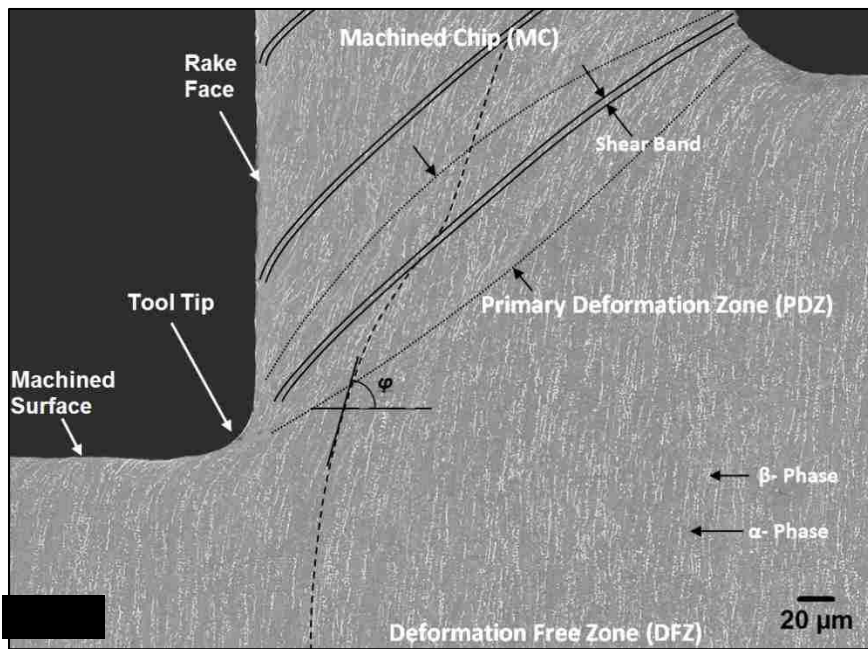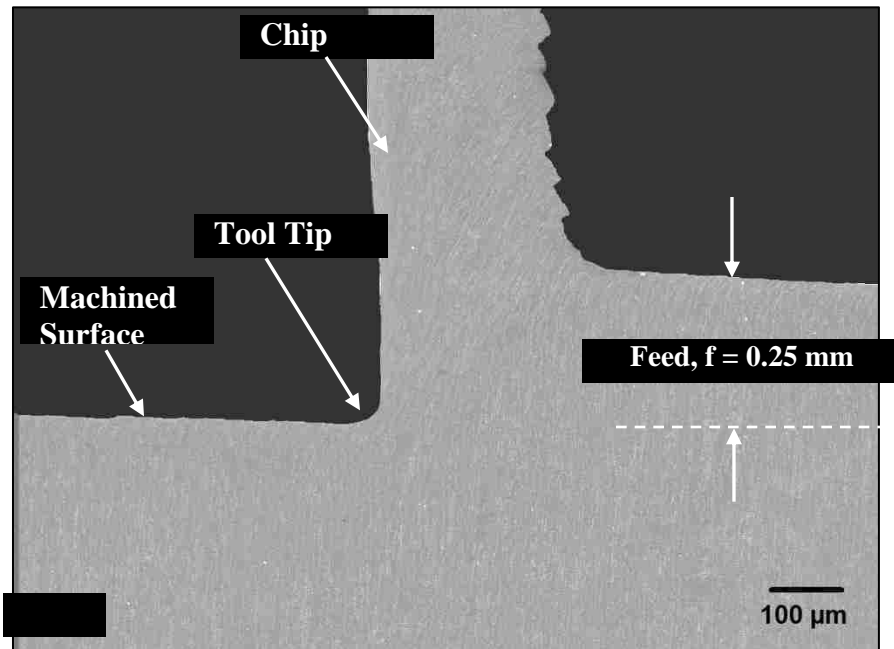
Fig. 4.11. (a) Cross-sectional SEM image of the material ahead of the tool tip of Ti-6Al-4V alloy. Cutting speed = 29.6 m/min and feed rate = 0.25 mm/rev, (b) Close view of the primary deformation zone.
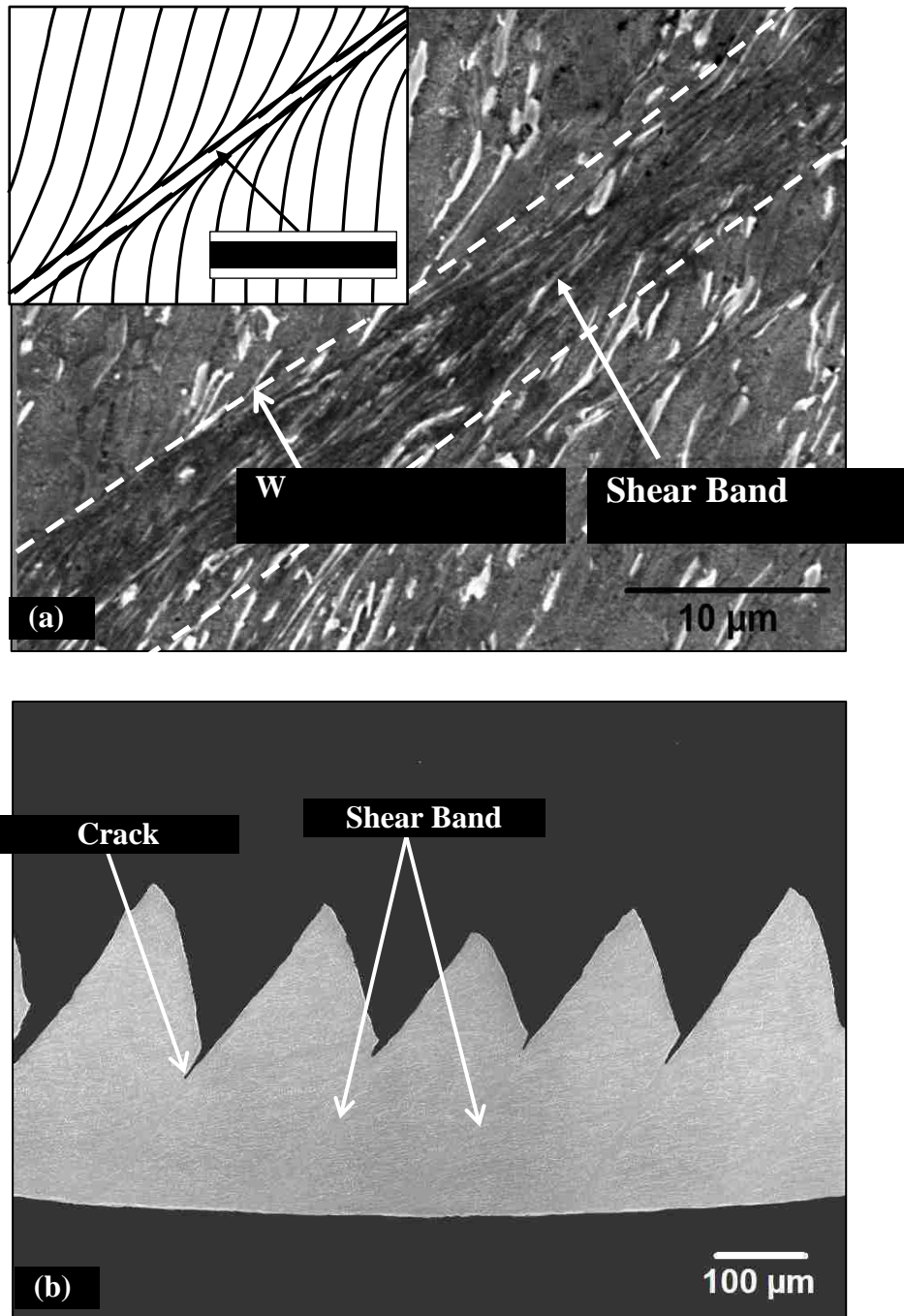
Fig. 4.12. (a) SEM image of the shear band. Schematic diagram of the shear band is shown in the insert. Here w is the width of the shear band, (b) Diagram showing the crack at the end of the shear band. Machining conditions: 63.5 m/min cutting speed and 0.25 mm/rev feed rate.
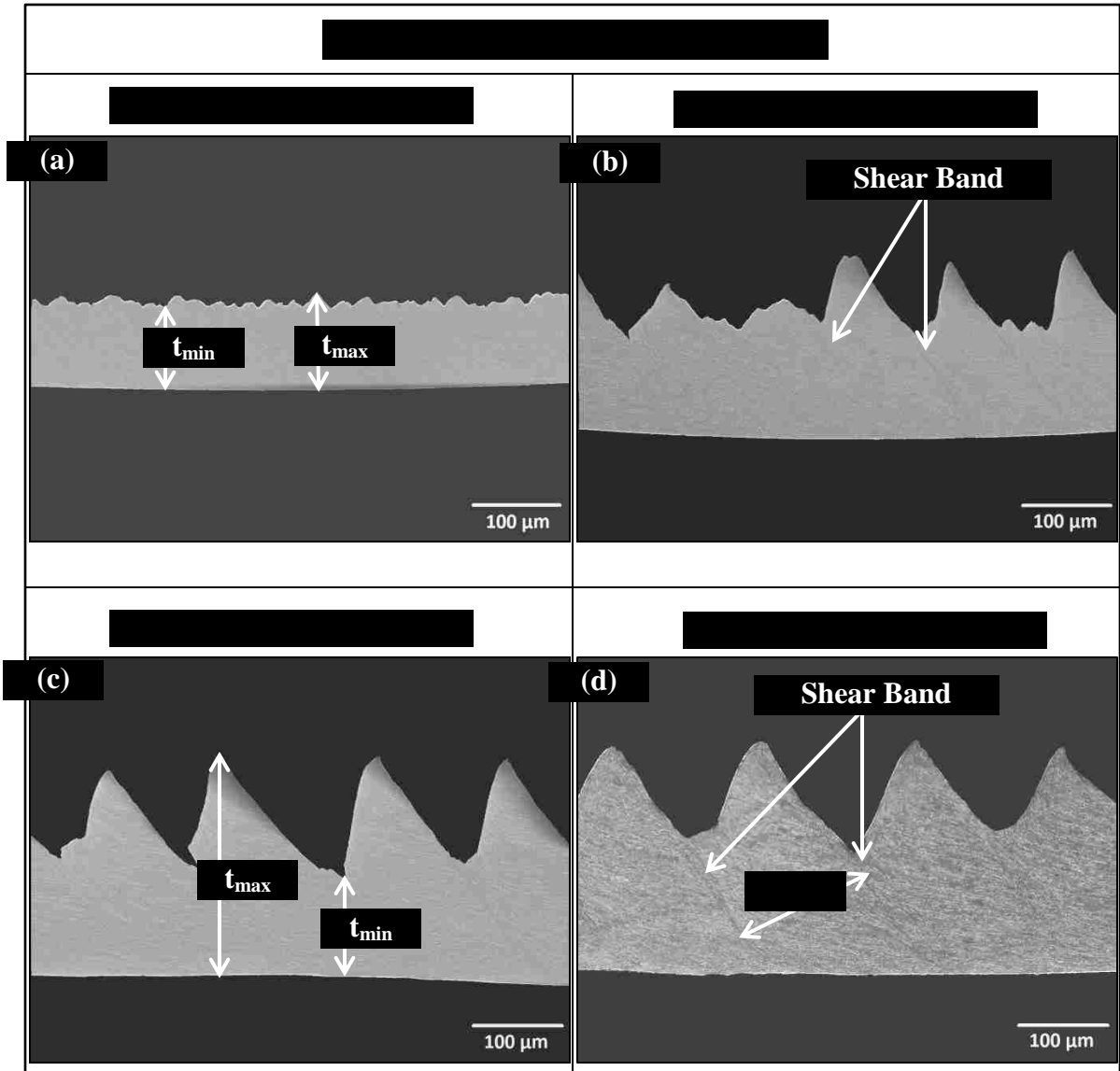
Fig. 4.13. Cross-sectional view of machined chips at different feed rates: (a) 0.10 mm/rev feed; (b) 0.15 mm/rev feed; (c) 0.20 mm/rev feed and (d) 0.25 mm/rev feed. t_{max} and t_{min} are the maximum and minimum chip thickness of the chip respectively. L_s is the distance between the center-line of two consecutive shear bands.
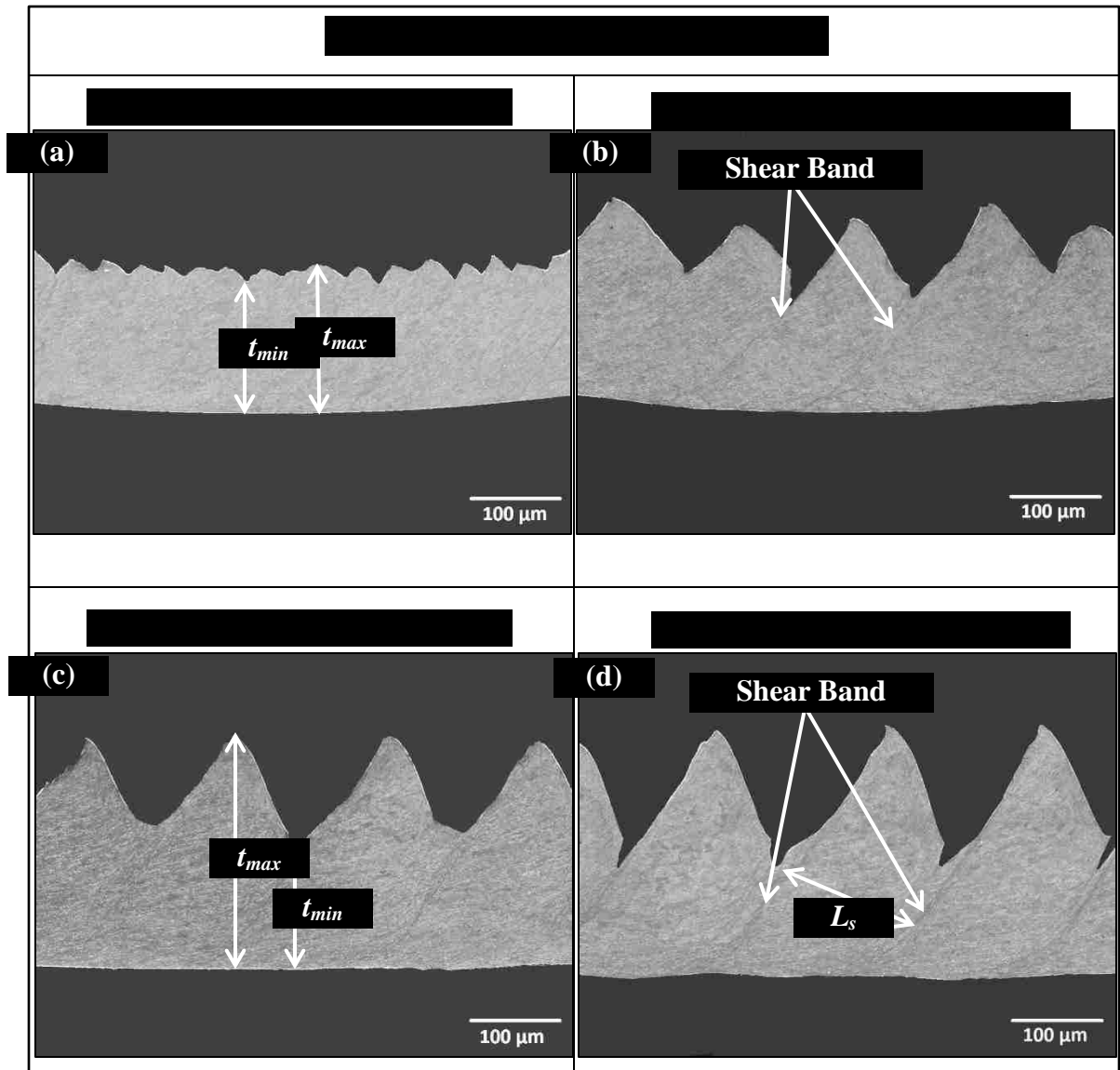
Fig. 4.14. Cross-sectional view of machined chips at different cutting speeds: (a) 14.4 m/min; (b) 29.6 m/min; (c) 43.2 m/min and (d) 63.5 m/min. t_{max} and t_{min} are the maximum and minimum chip thickness of the chip respectively. L_s is the distance between the center-line of two consecutive shear bands and d_s is the shear displacement.
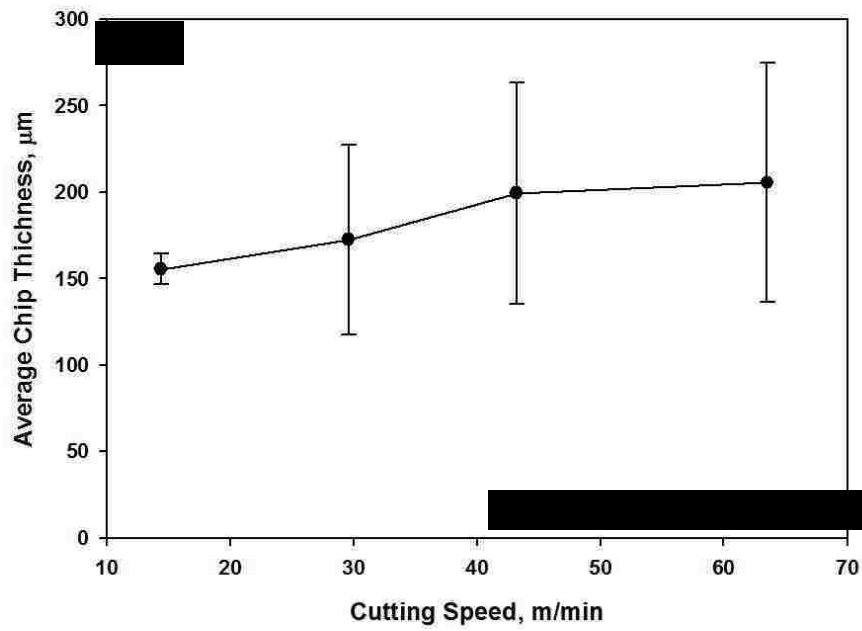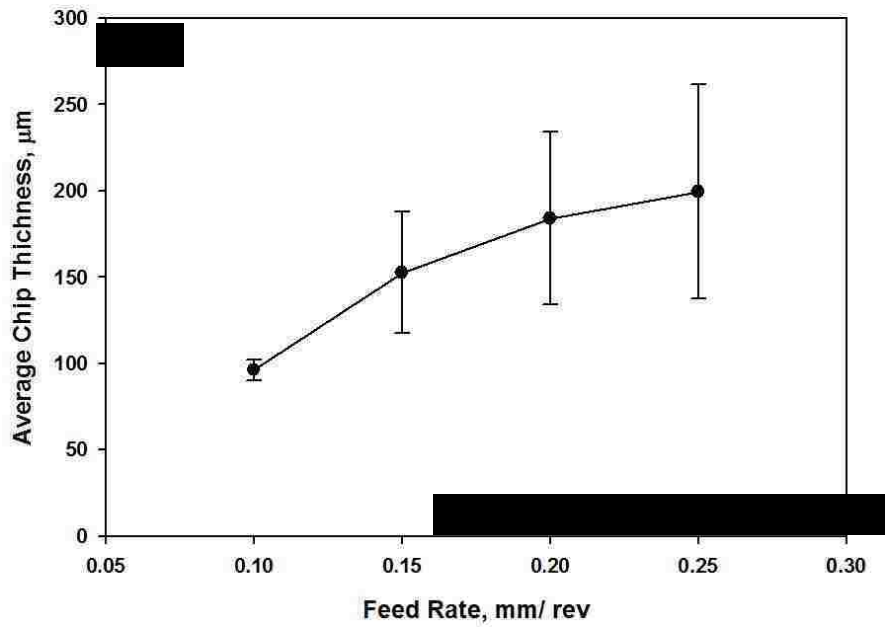
Fig. 4.15. Variation of average chip thickness with (a) the feed rate and (b) the cutting speed.
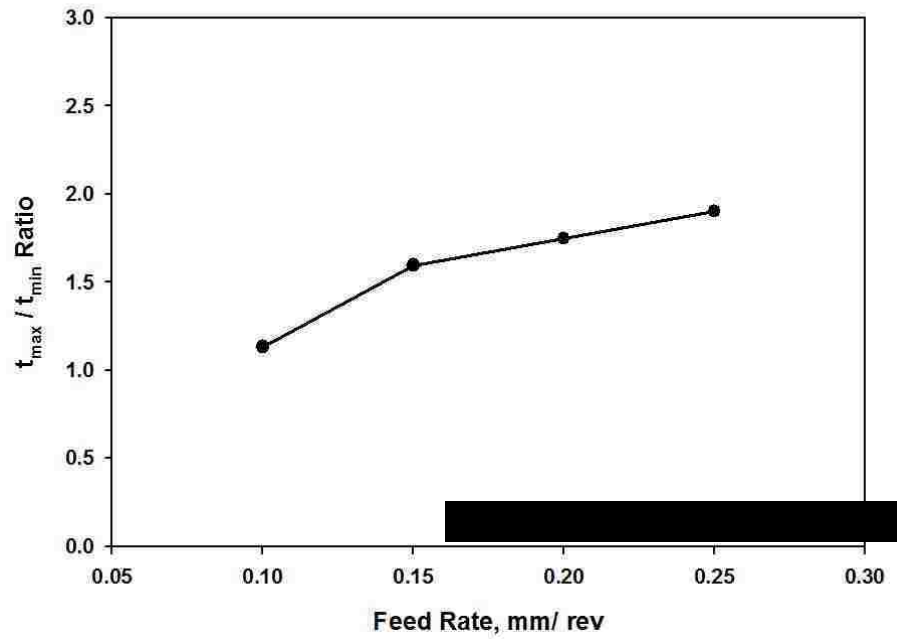
Fig. 4.16. Variation of the ratio between the maximum thickness (t_{max}) and minimum thickness (t_{min}) of the chips with feed rate.
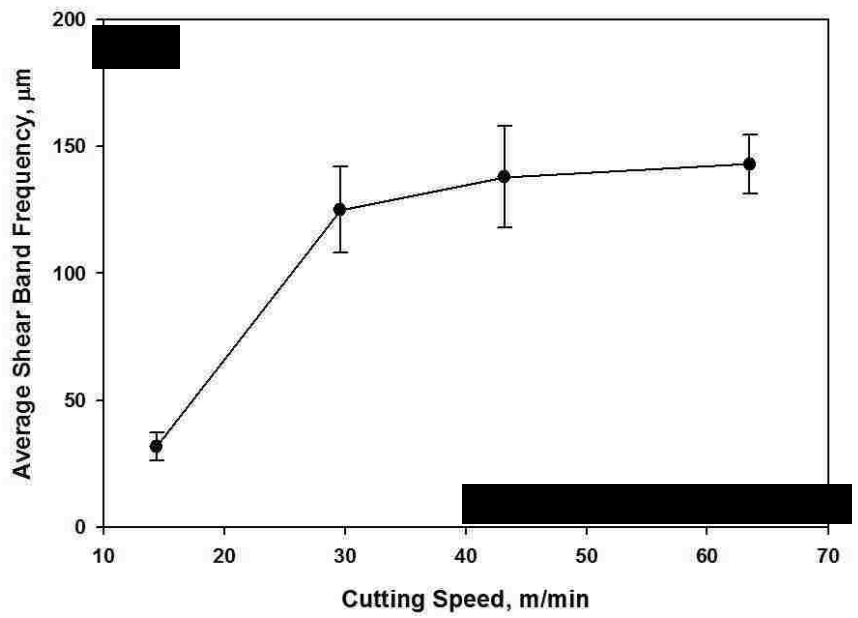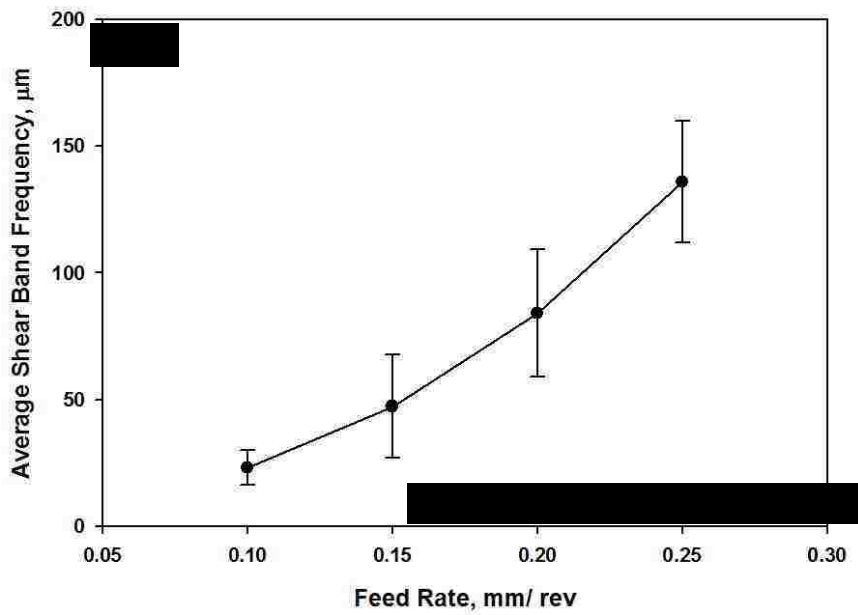
Fig. 4.17. Increment of the shear band frequency (the average distance between the centerline of two consecutive shear bands) with (a) the feed rate and (b) cutting speed.
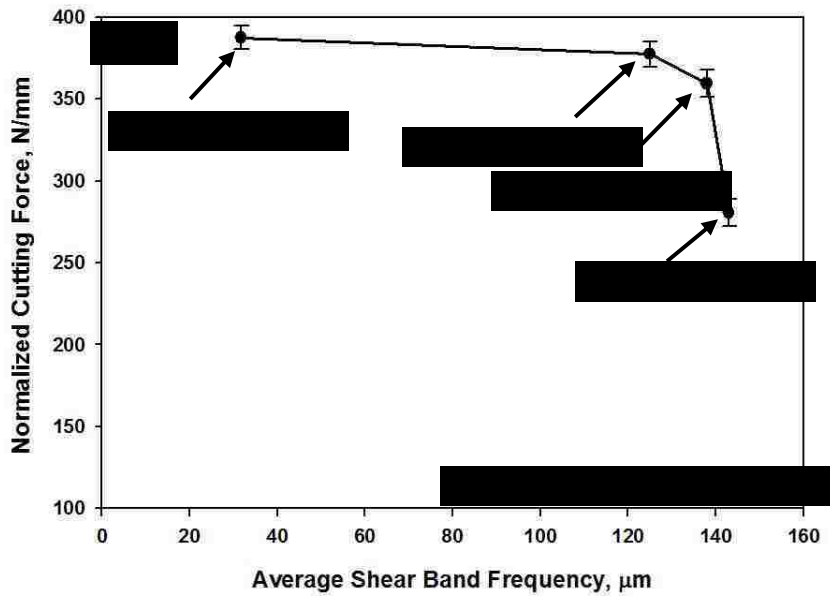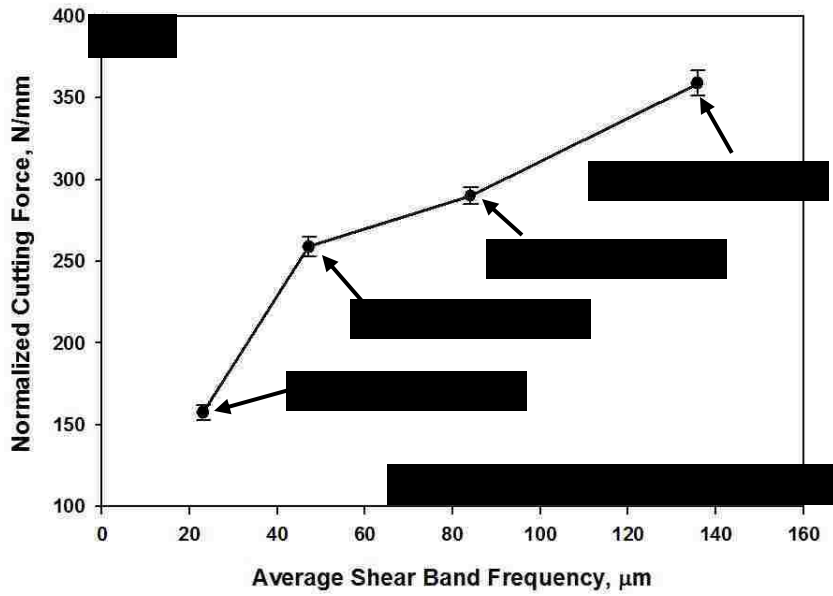
Fig. 4.18. Diagram showing the variation of normalized cutting force with the shear band frequency for different (a) feed rate and (b) cutting speed.
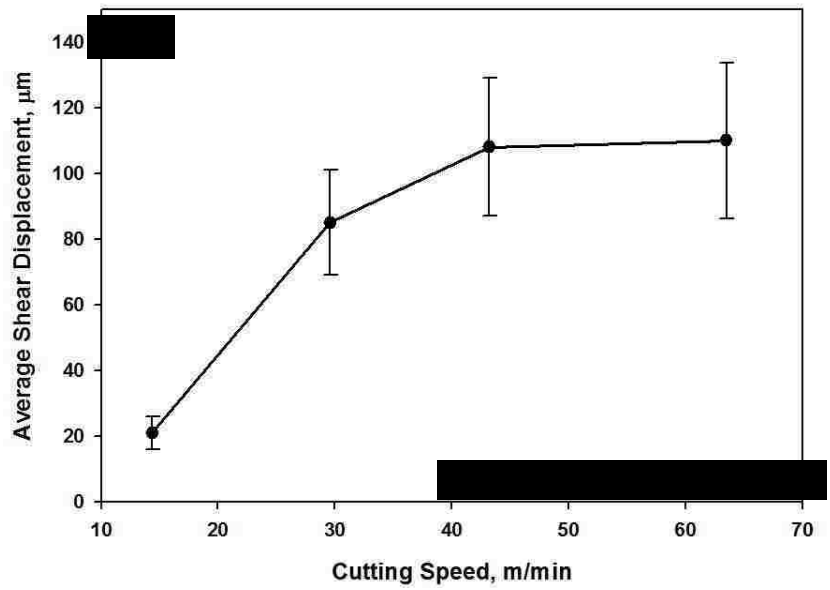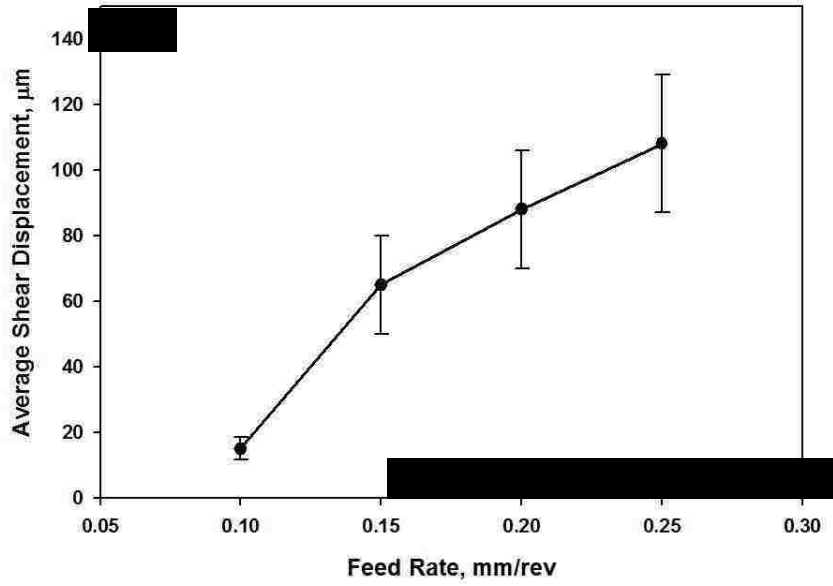
Fig. 4.19. Diagram showing the variation of shear displacement with the (a) feed rate and (b) cutting speed.
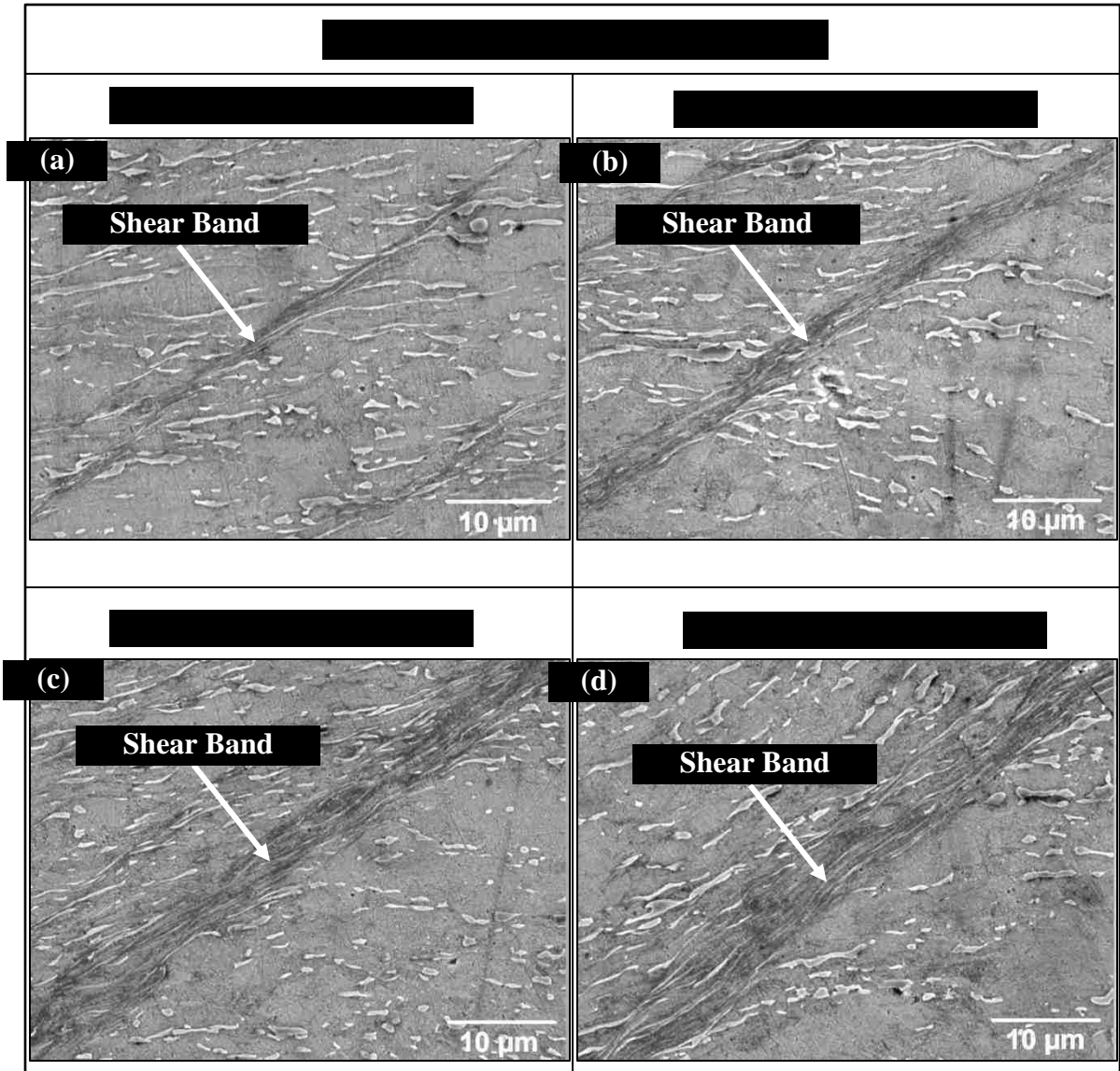
Fig. 4.20. SEM image of the shear band formed at different feed rates: (a) 0.10 mm/rev feed; (b) 0.15 mm/rev feed; (c) 0.20 mm/rev feed and (d) 0.25 mm/rev feed.
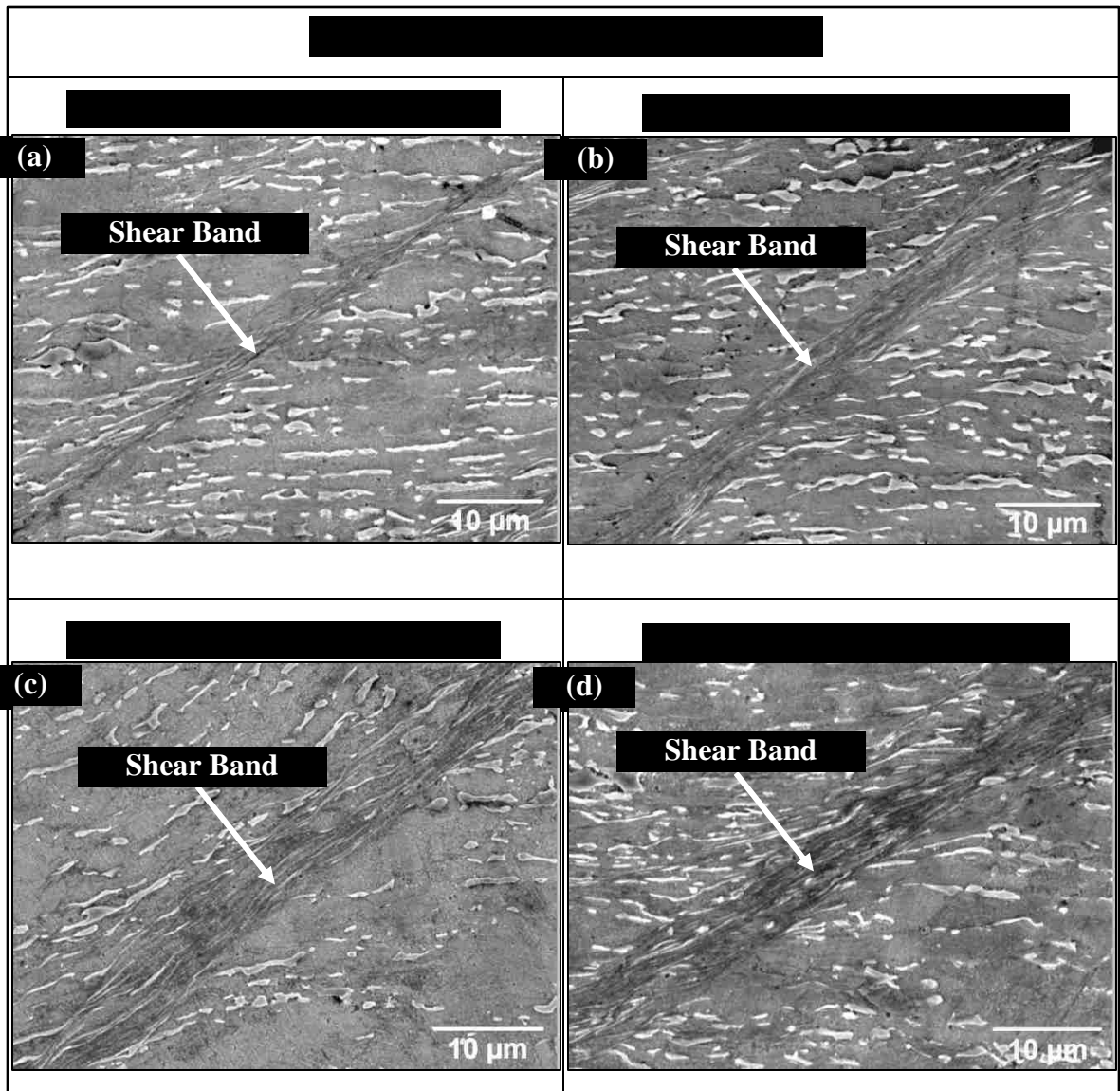
Fig. 4.21. SEM image of the shear band formed at different cutting speeds: (a) 14.4 m/min; (b) 29.6 m/min; (c) 43.2 m/min and (d) 63.5 m/min.
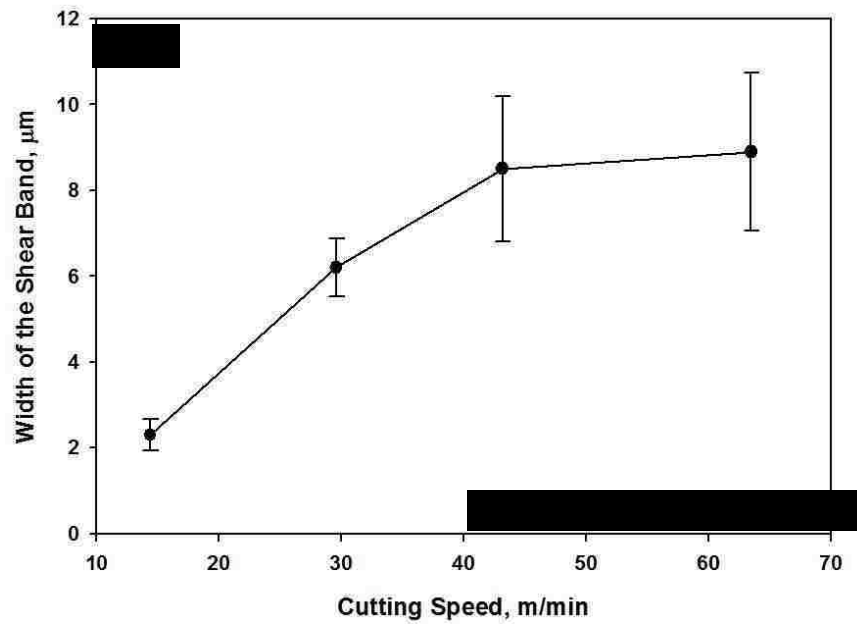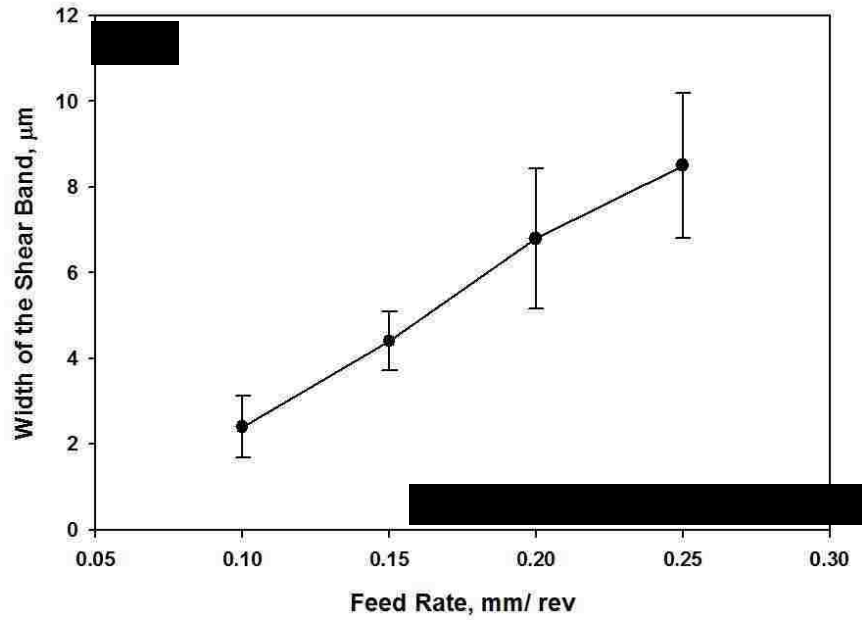
Fig. 4.22. Variation of the average width of the shear band with (a) the feed rate and (b) the cutting speed.

137
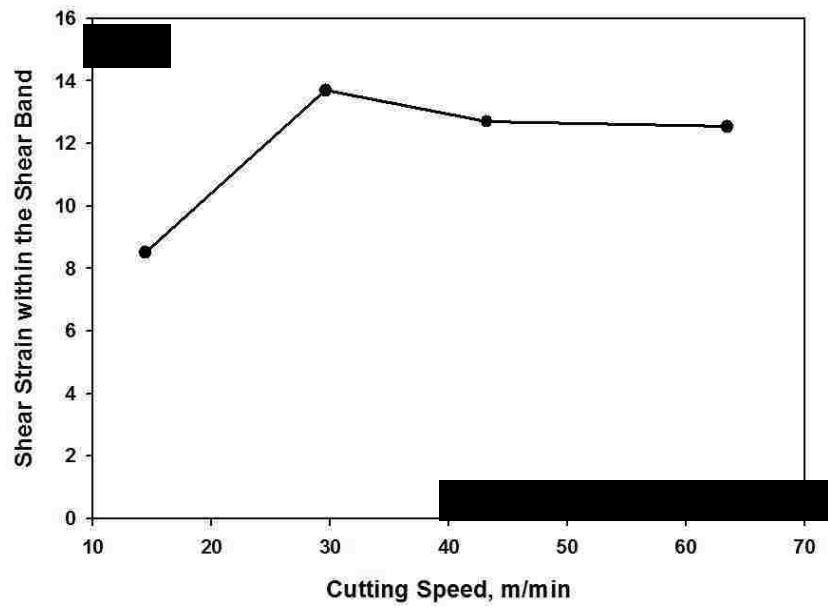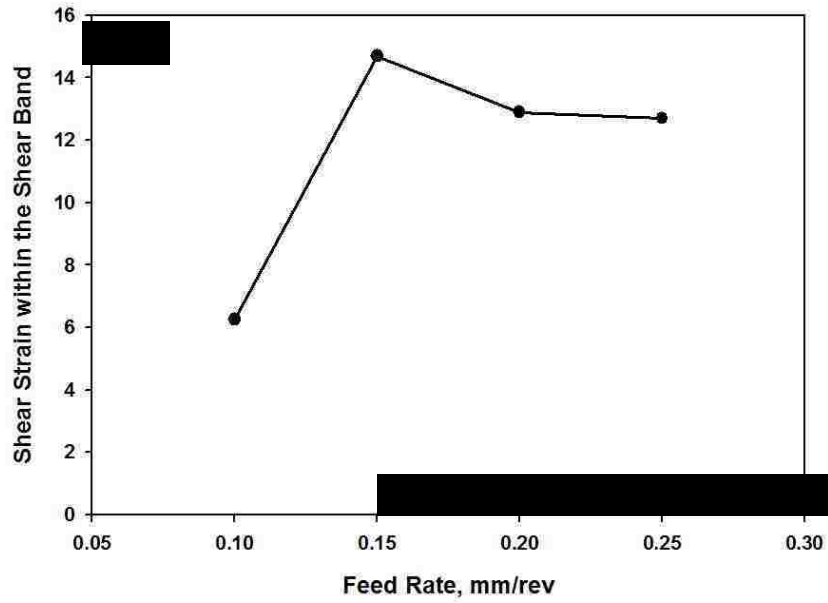
Fig. 4.23. Variation of the shear strain within the shear band with (a) the feed rate and (b) the cutting speed.

138
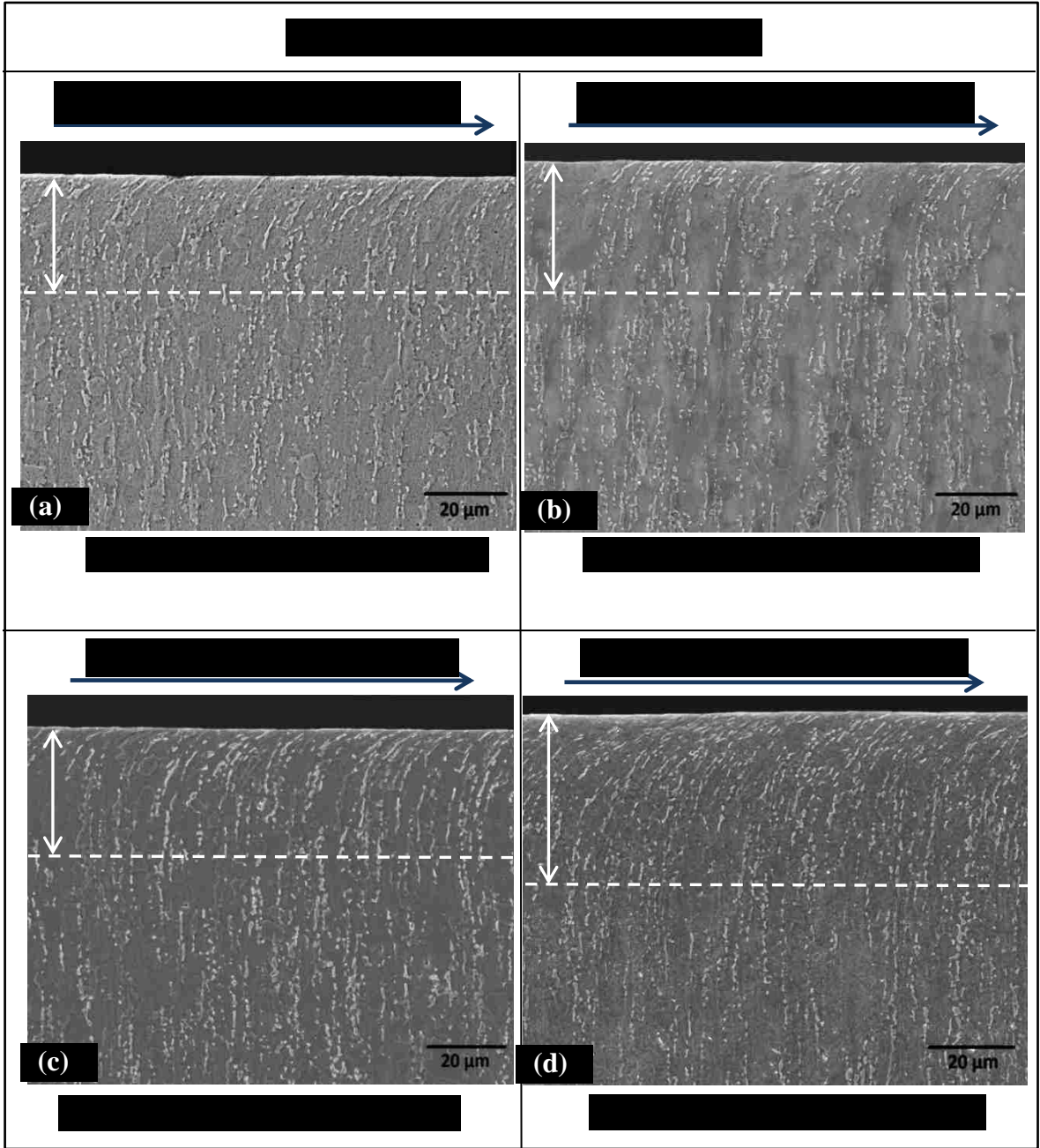
Fig. 4.24. Subsurface microstructure below the machined surface of Ti-6Al-4V alloy subjected to orthogonal cutting at different feed rates: (a) 0.10 mm/rev, (b) 0.15 mm/rev, (c) 0.20 mm/rev and (d) 0.25 mm/rev and constant cutting speed of 43.2 m/min;
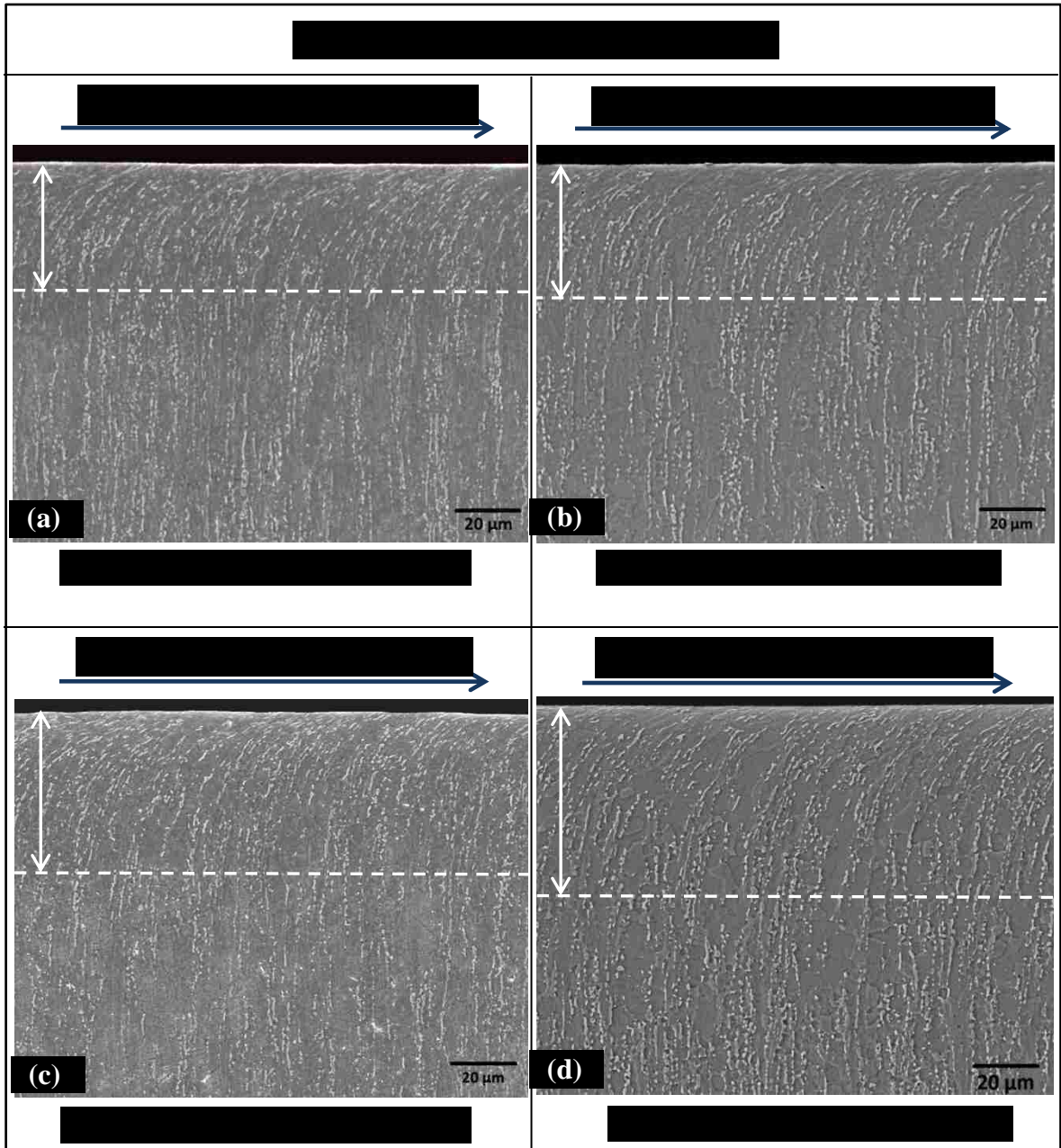
Fig. 4.25. Subsurface microstructure below the machined surface of Ti-6Al-4V alloy subjected to orthogonal cutting at different cutting speeds: (a) 14.4 m/min, (b) 29.6 m/min, (c) 43.2 m/min and (d) 63.5 m/min and constant feed rate of 0.25 mm/rev.
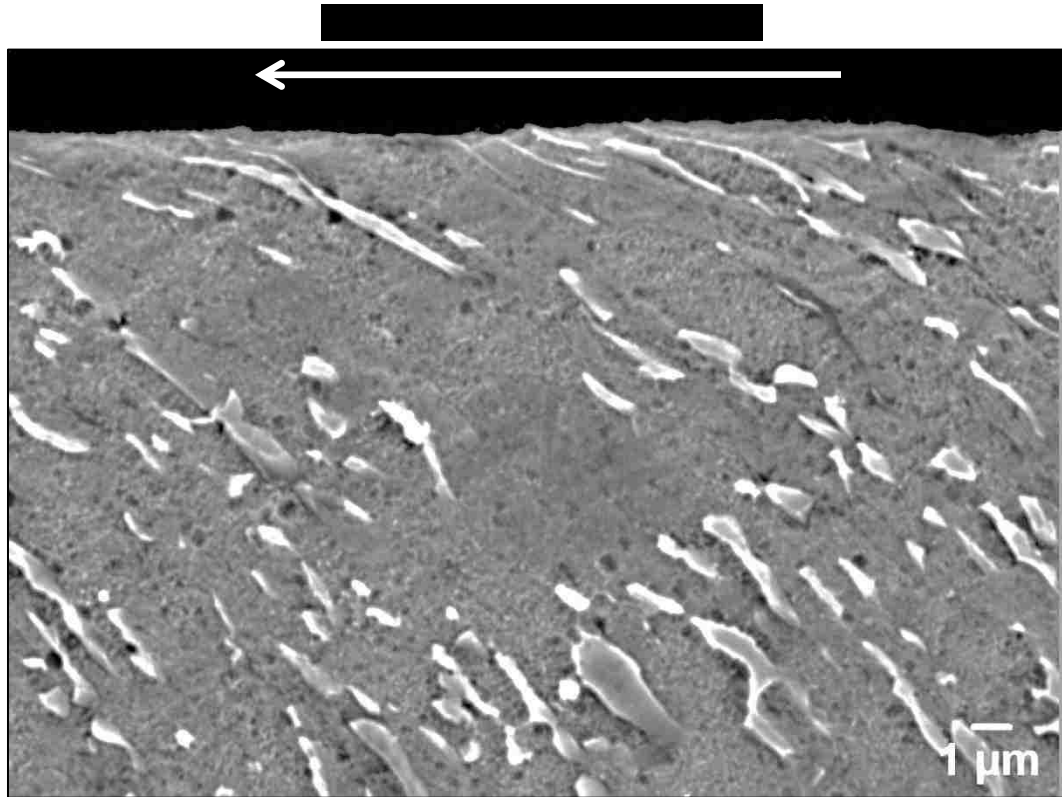
Fig. 4.26. High magnification (4000x) SEM image of the microstructure below the machined surface of Ti-6Al-4V alloy subjected to orthogonal cutting at 63.5 m/min cutting speed and 0.25 mm/rev feed rate. No white layer was observed below the machined surface.
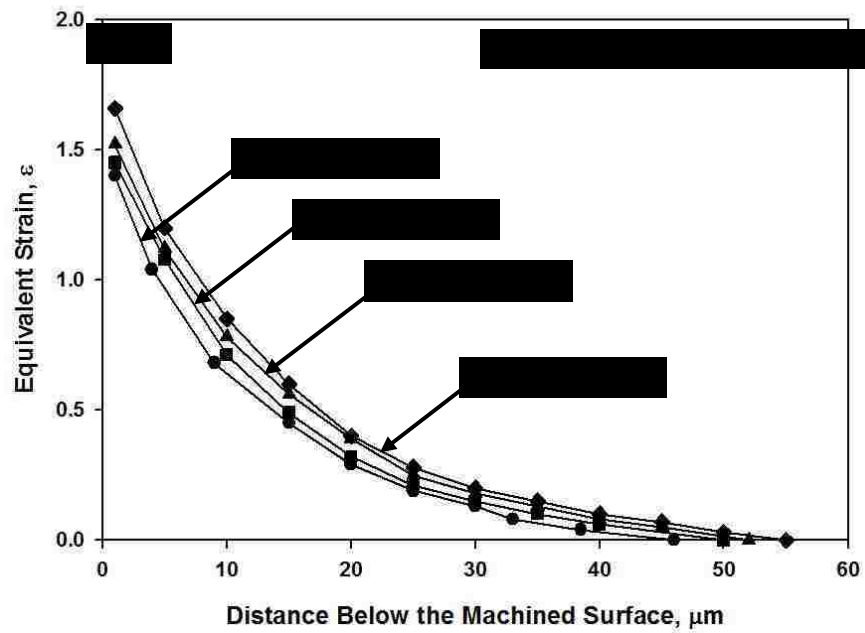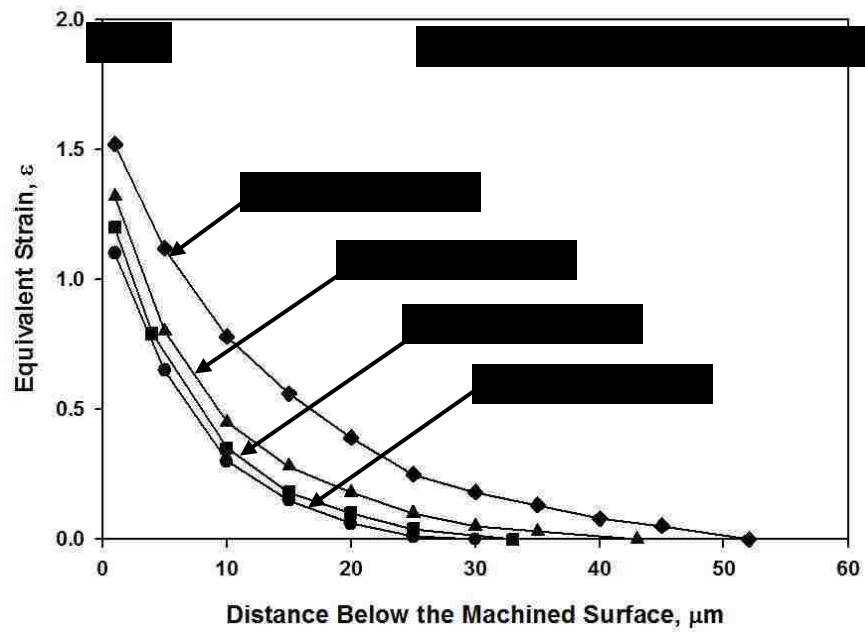
Fig. 4.27. Diagram showing the variation of strain gradient below the machined surface of Ti-6Al-4V alloy subjected to orthogonal cutting at different (a) feed rates and (b) cutting speeds.
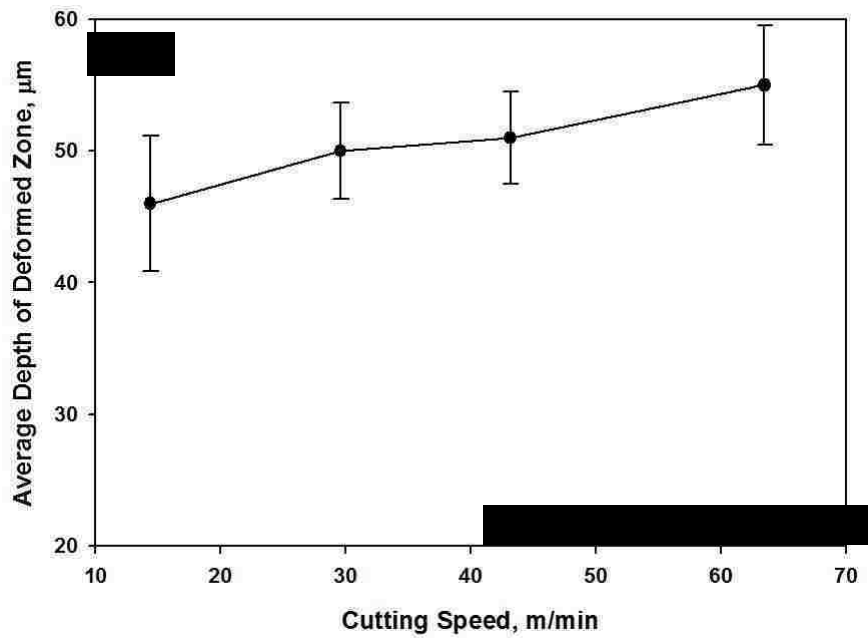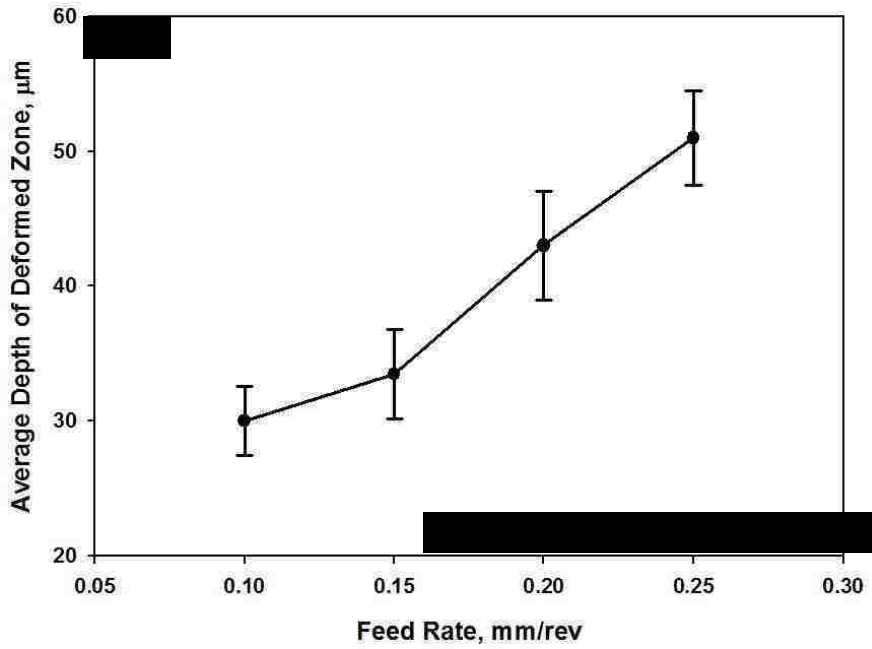
Fig 4.28. Diagram showing the variation of depth of deformed zone with the (a) feed rate and (b) cutting speed.
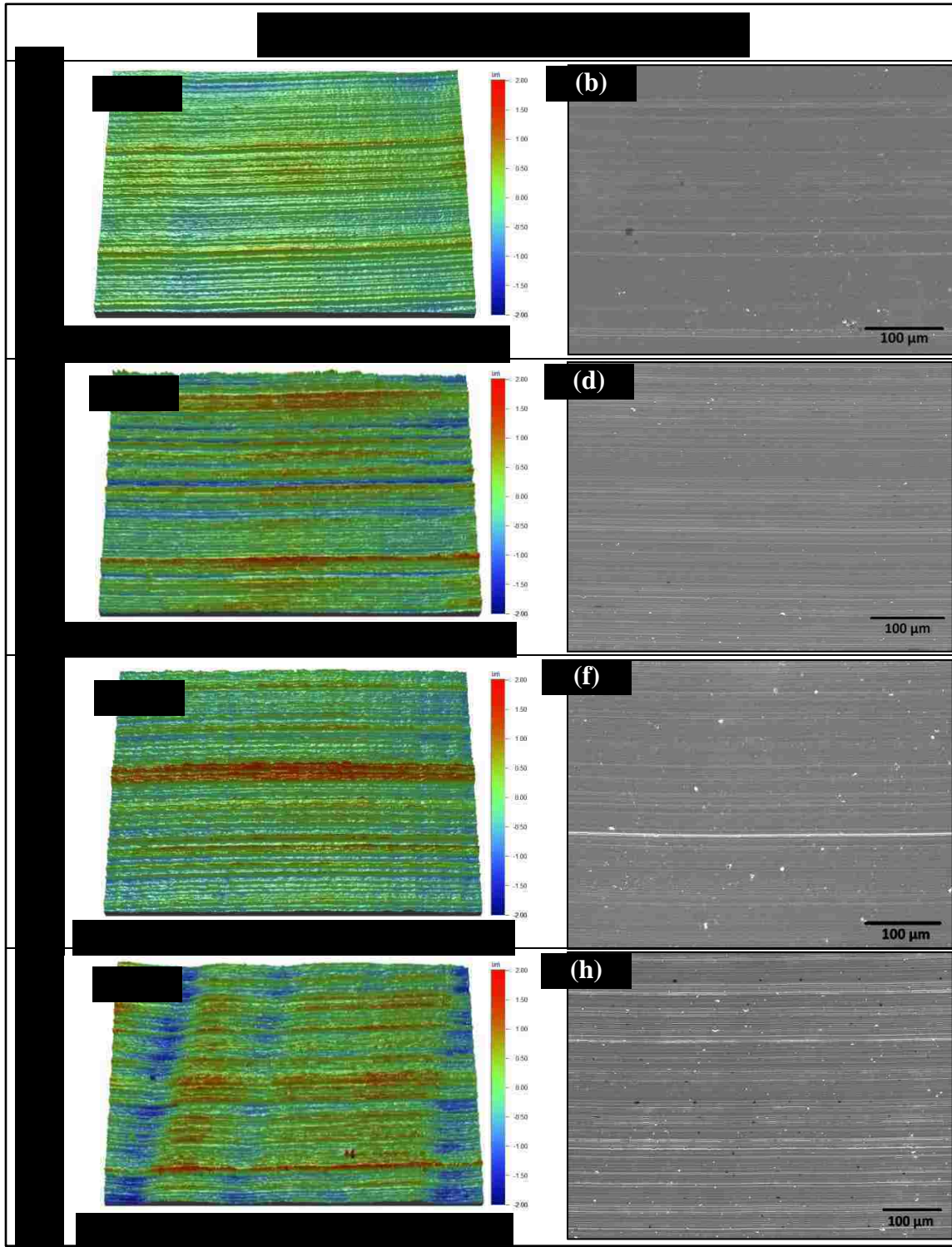
Fig. 4.29. WYKO images (595.1 μm × 452.8 μm) and corresponding SEM images of machined surface at different feed rates: (a,b) 0.10 mm/rev feed; (c,d) 0.15 mm/rev feed; (e,f) 0.20 mm/rev feed and (g,h) 0.25 mm/rev feed.

144
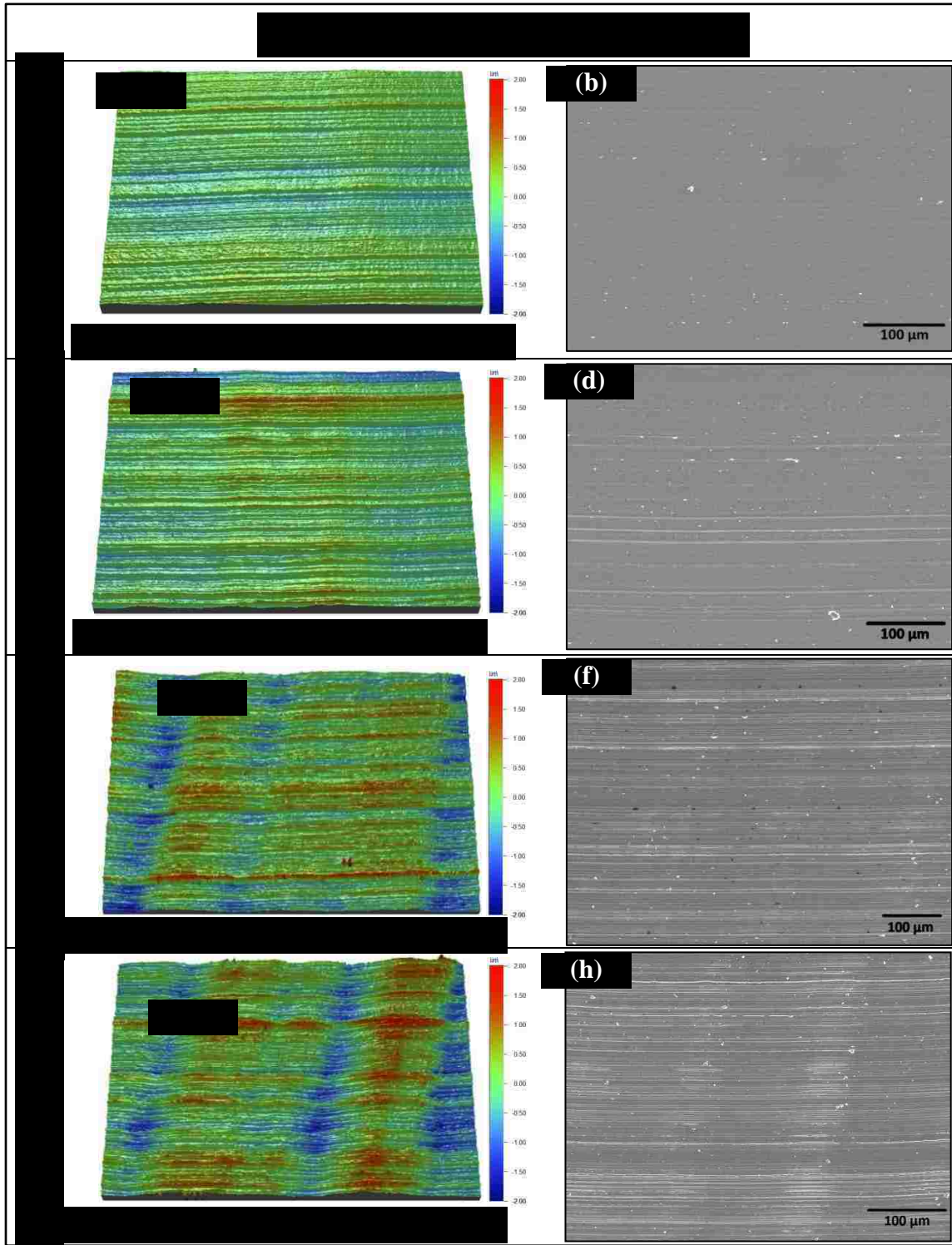
Fig. 4.30. WYKO images (595.1 μm × 452.8 μm) and corresponding SEM images of machined surface at different cutting speeds. (a,b) 14.4 m/min; (c,d) 29.6 m/min; (e,f) 43.2 m/min and (g,h) 63.5 m/min cutting speed.
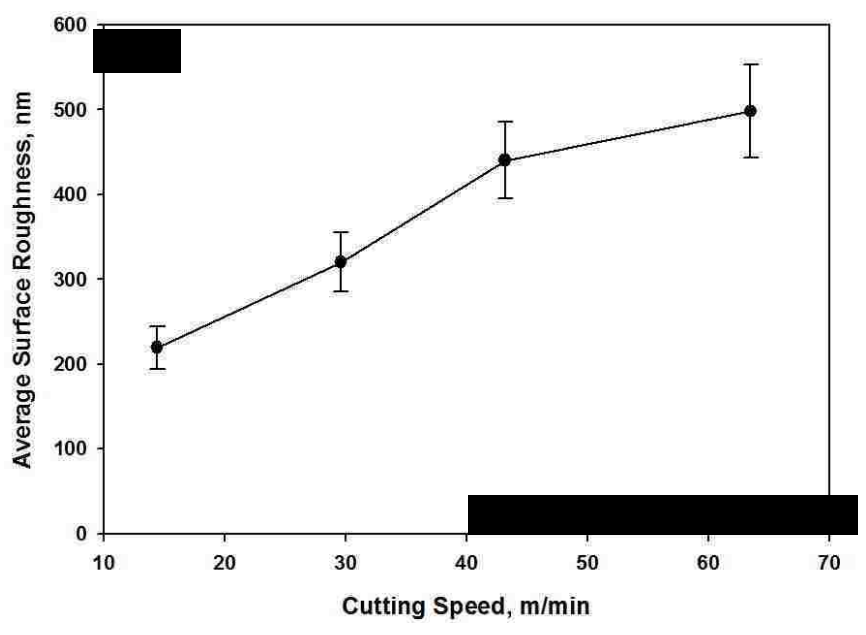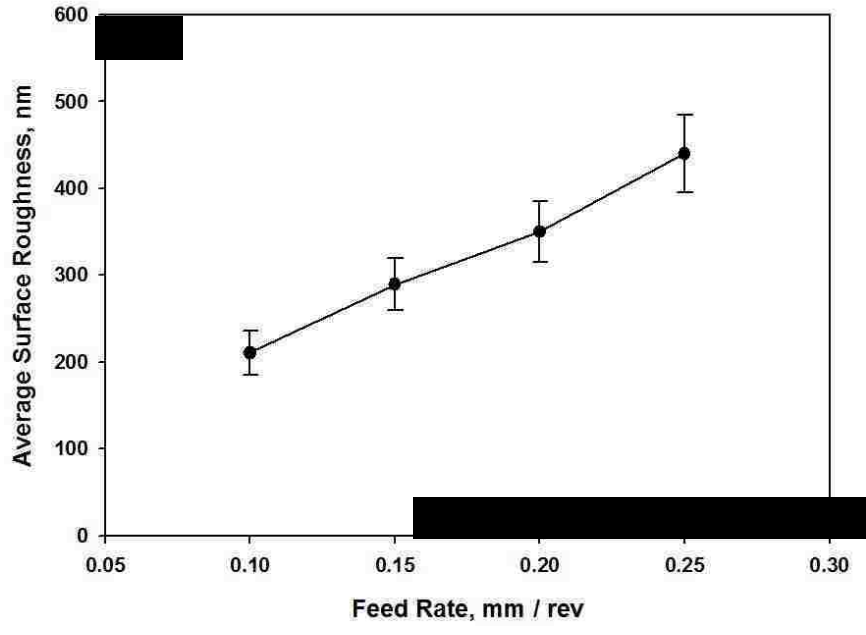
Fig. 4.31. Variation of average surface roughness with (a) feed rate and (b) cutting speed.
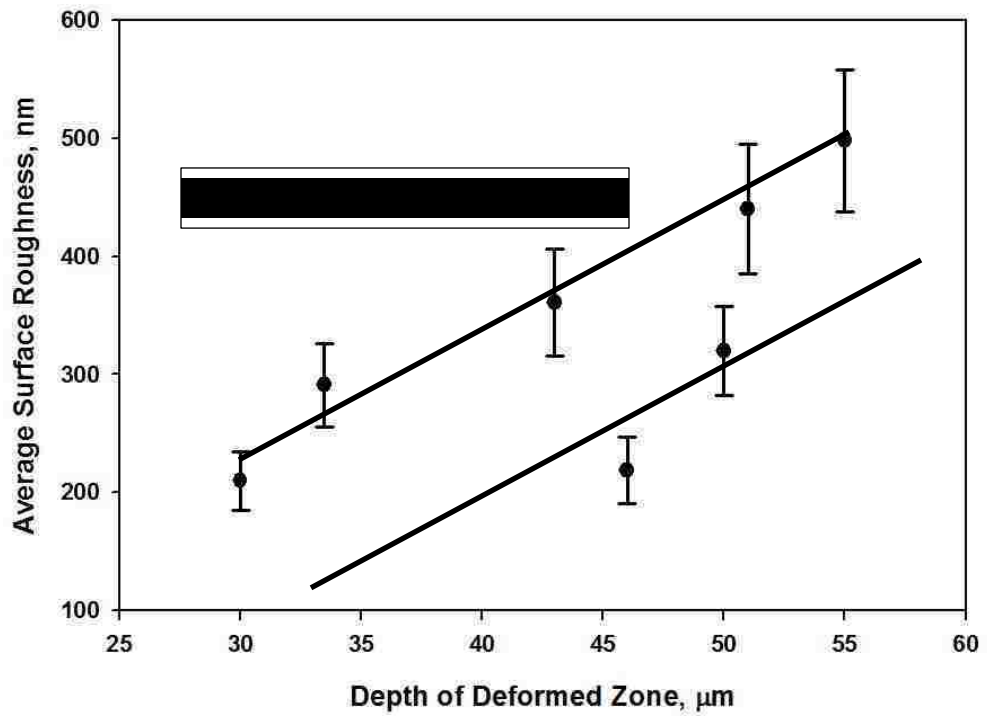
Fig. 4.32. Diagram showing the relationship between the surface roughness and the depth of deformed zone below the machined surface. Here R_a is the surface roughness, D is the depth of deformed zone and R_o is the initial surface roughness.
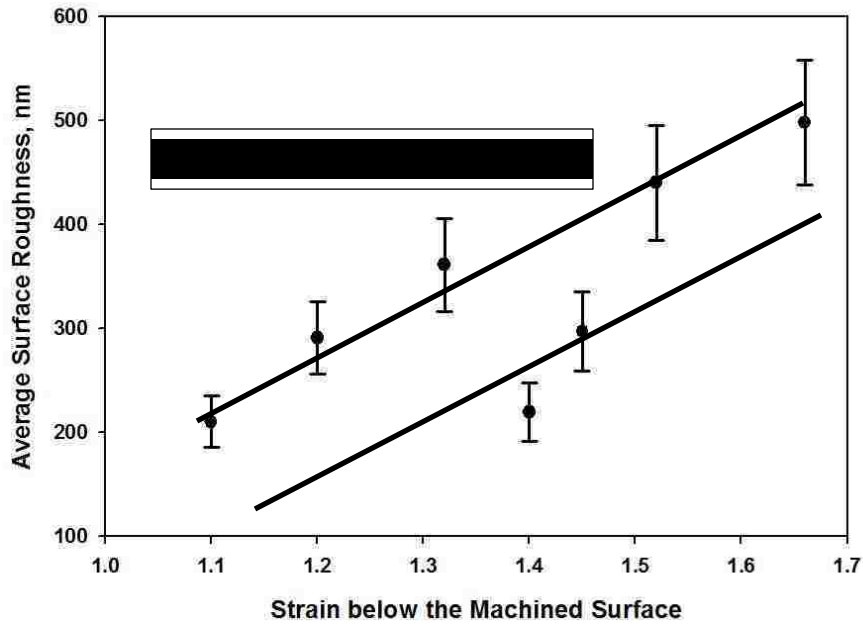
Fig. 4.33. Diagram showing the relationship between the surface roughness and the maximum strain below the machined surface. Here R_a is the surface roughness, $\bar{\varepsilon}$ is the strain below the machined surface and R_o is the initial surface roughness.
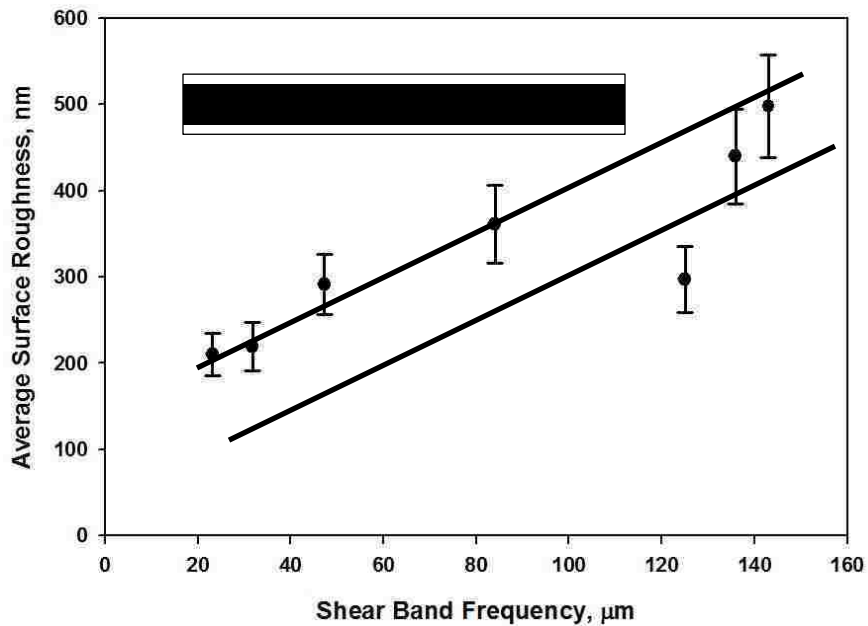
Fig. 4.34. Diagram showing the relationship between the surface roughness and the shear band frequency. Here R_a is the surface roughness, L_c is the shear band frequency and R_o is the initial surface roughness.
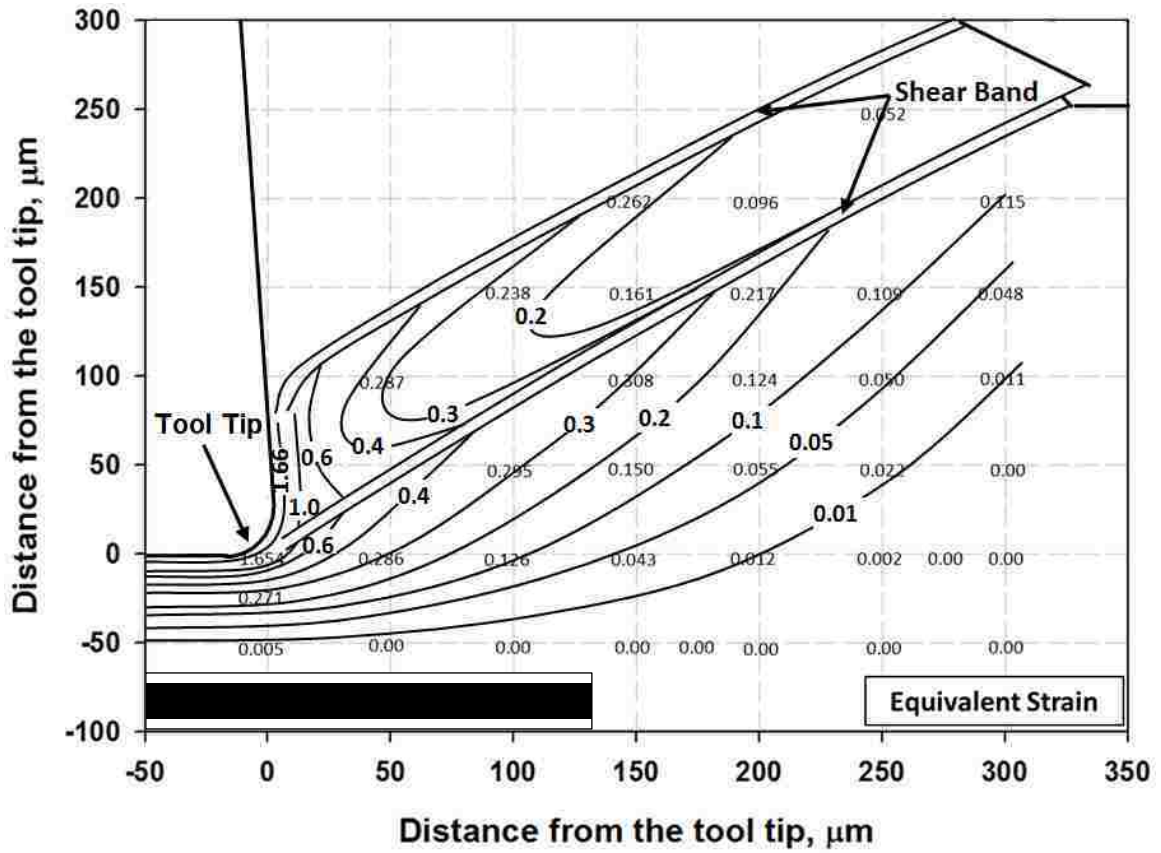
Fig. 4.35. Plastic strain distribution diagram where the equivalent strains were estimated using the value of shear angle at each location. Machining conditions: cutting speed of 63.5 m/min and feed per revolution of 0.25 mm.
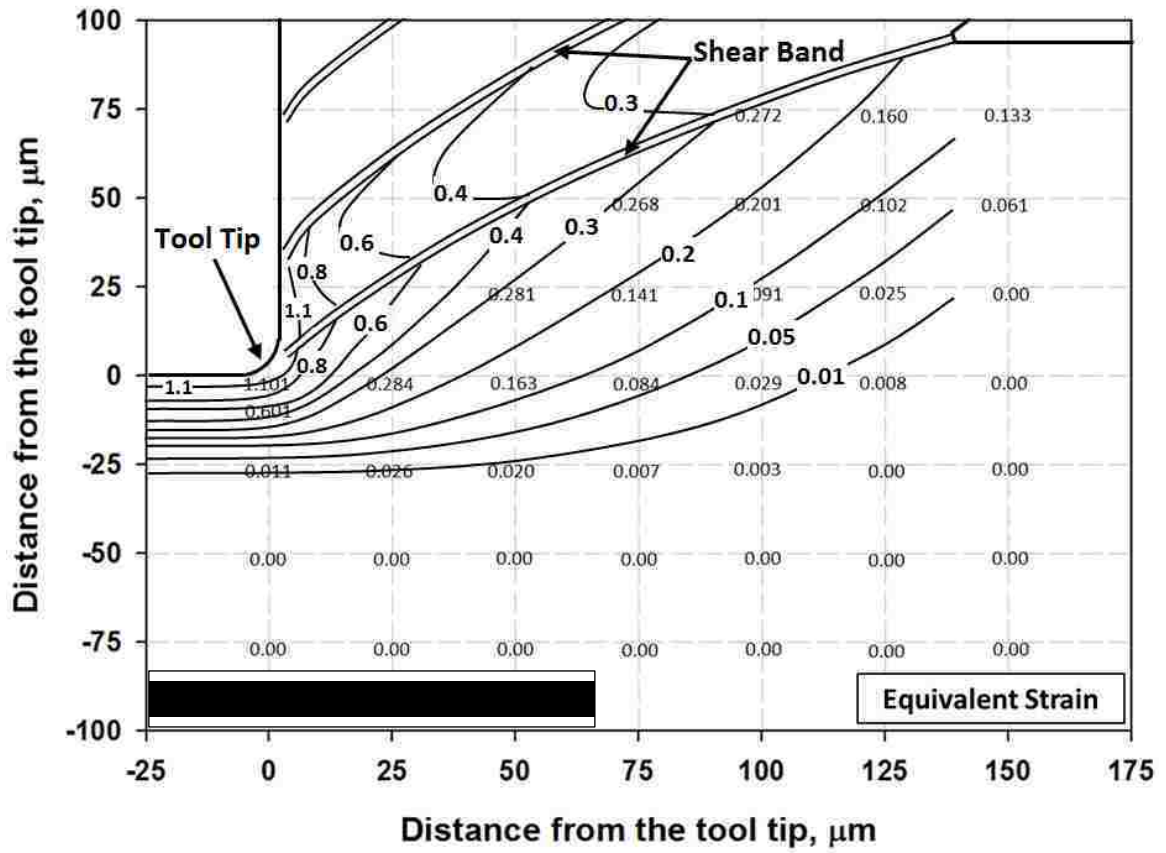
Fig. 4.36. Plastic strain distribution diagram for the machining conditions of 43.2 m/min cutting speed 0.10 mm/rev feed rate.
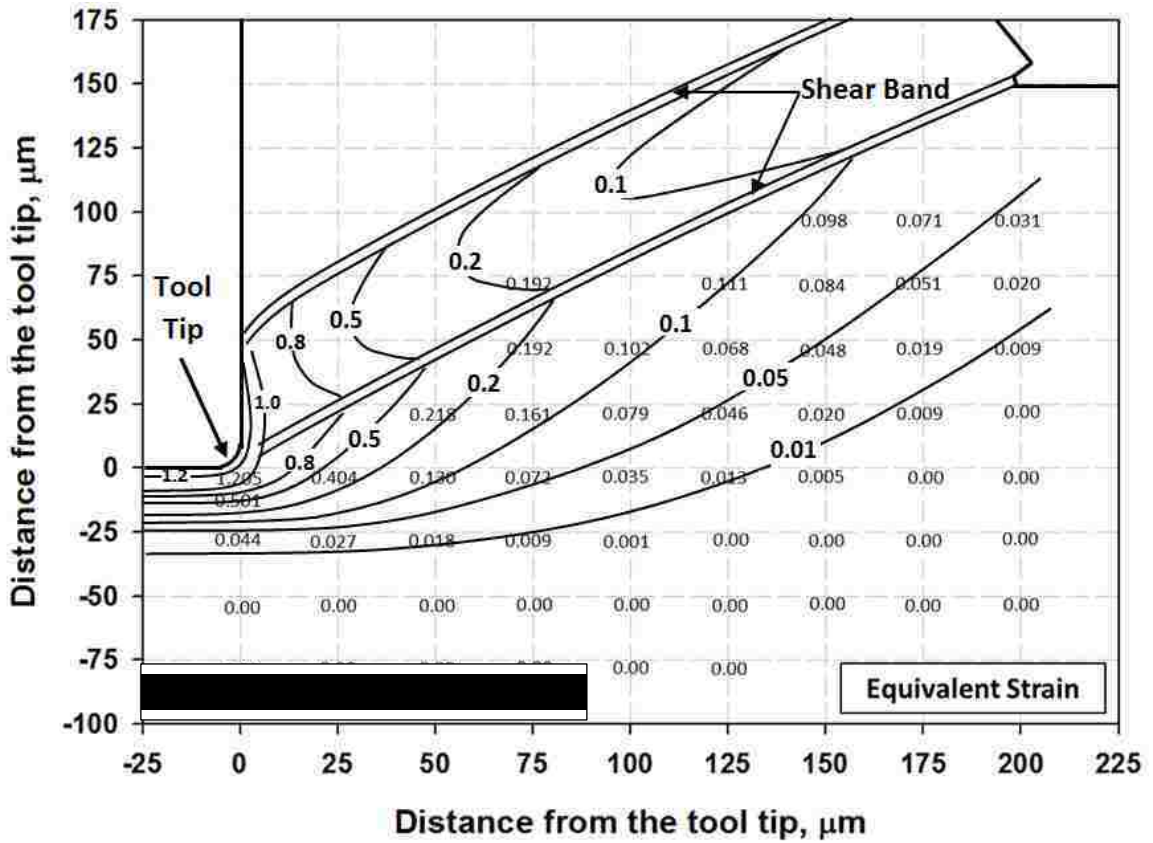
Fig. 4.37. Plastic strain distribution diagram for the machining conditions of 43.2 m/min cutting speed 0.15 mm/rev feed rate.
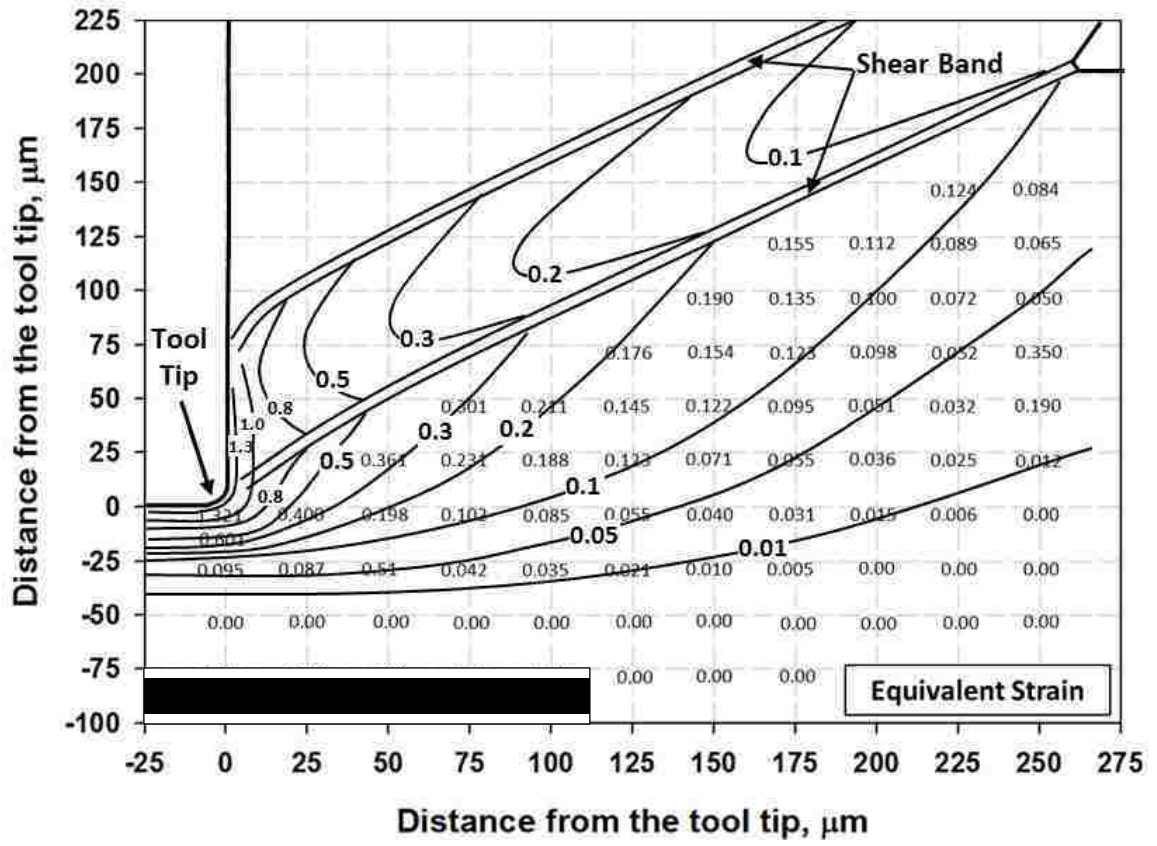
Fig. 4.38. Plastic strain distribution diagram for the machining conditions of 43.2 m/min cutting speed 0.20 mm/rev feed rate.
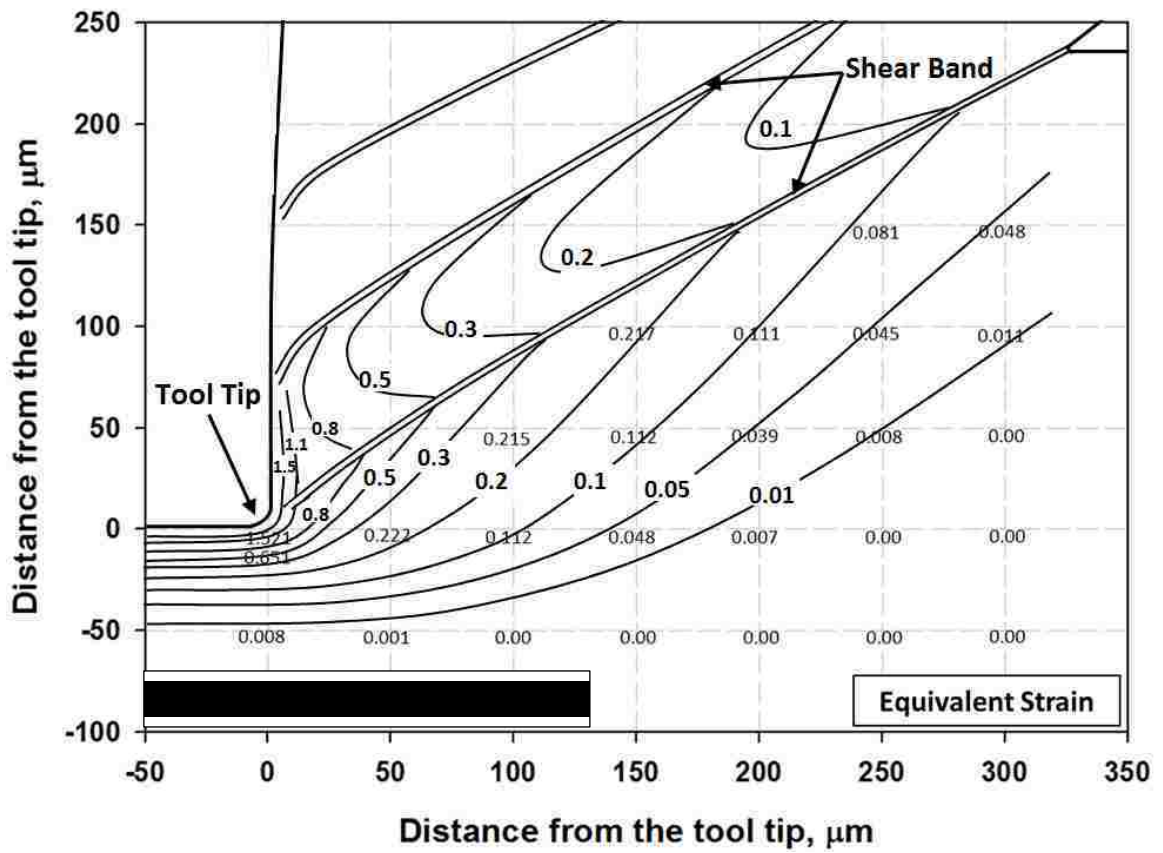
Fig. 4.39. Plastic strain distribution diagram for the machining conditions of 43.2 m/min cutting speed 0.25 mm/rev feed rate.
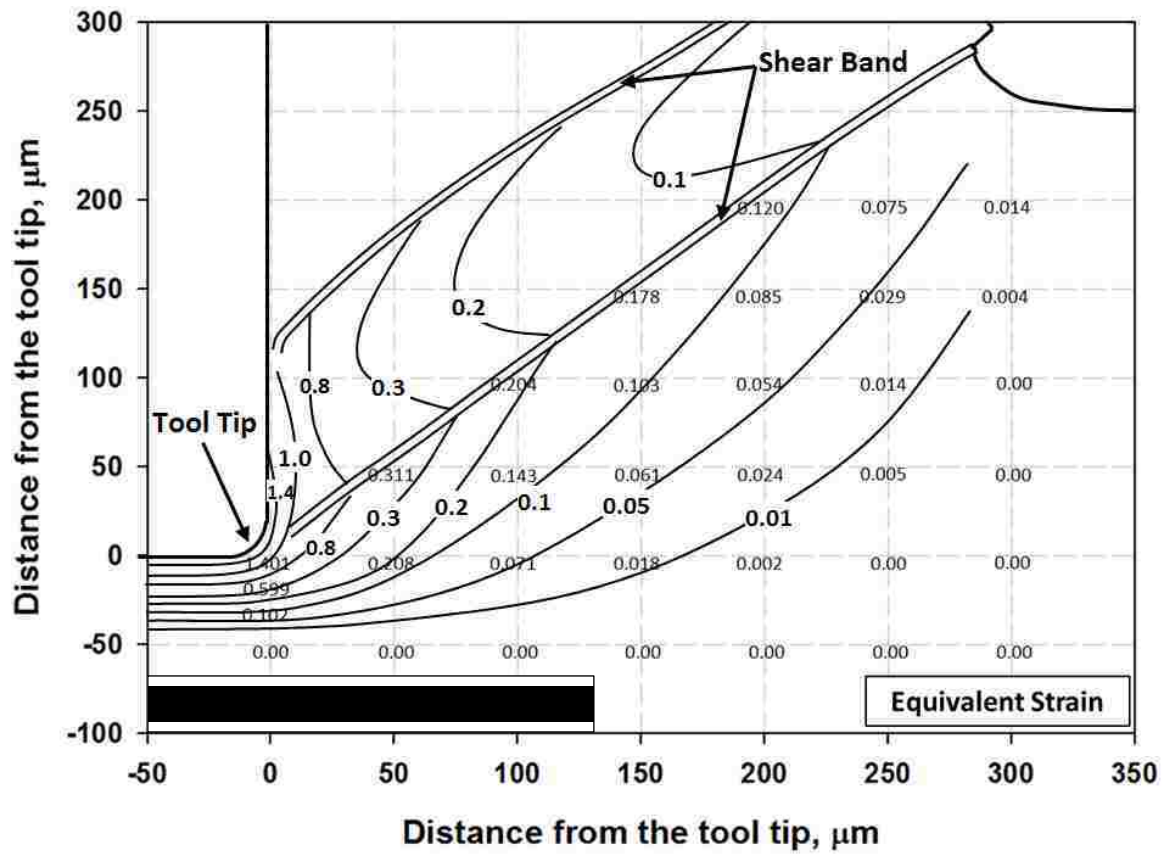
Fig. 4.40. Plastic strain distribution diagram for the machining conditions of 14.4 m/min cutting speed 0.25 mm/rev feed rate.
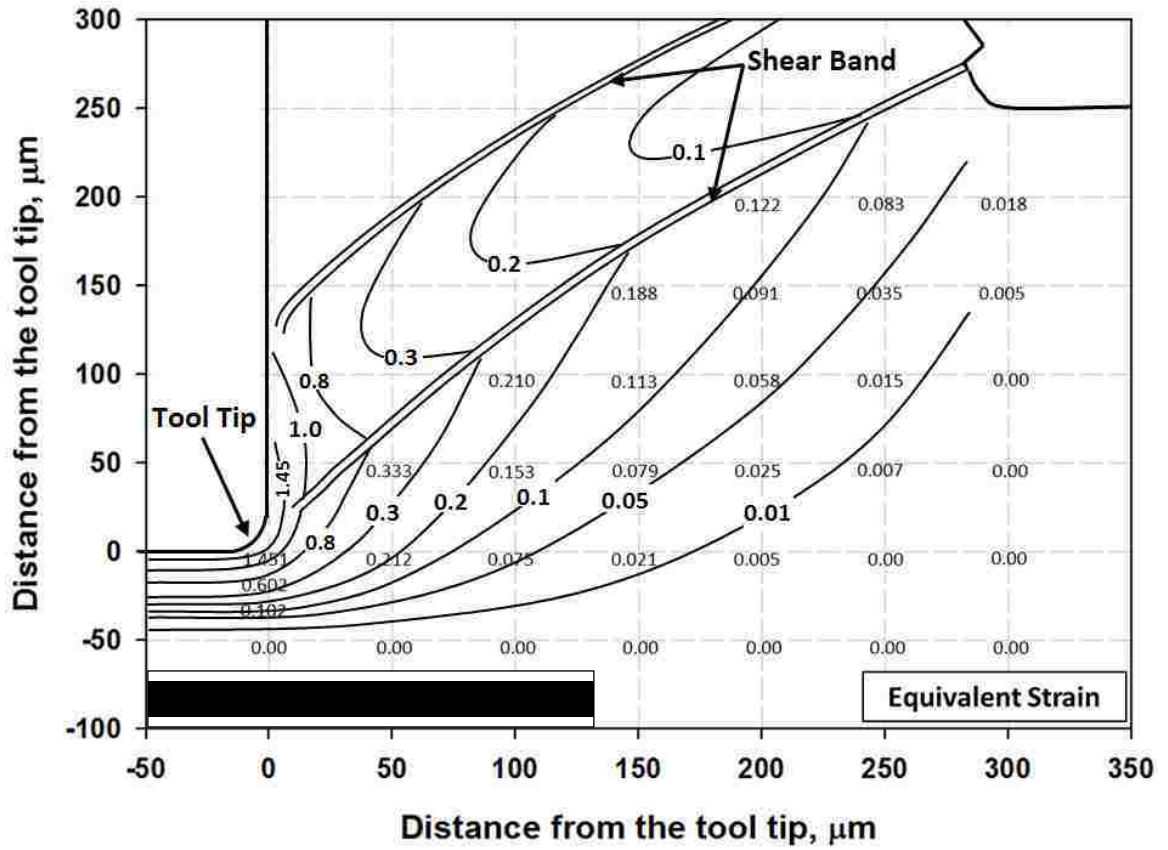
Fig. 4.41. Plastic strain distribution diagram for the machining conditions of 29.6 m/min cutting speed 0.25 mm/rev feed rate.
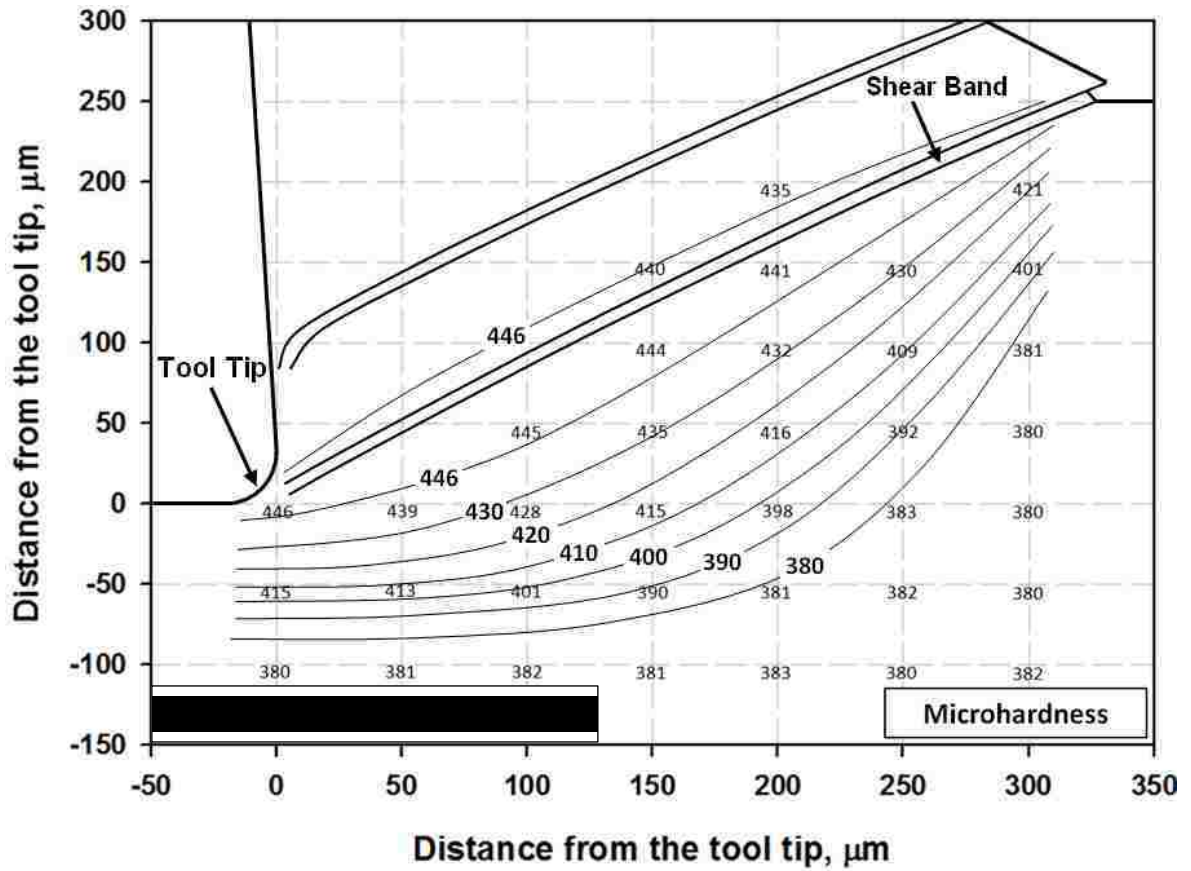
Fig. 4.42. Diagram showing the variation in hardness values in the material ahead of the tool tip for sample machined under cutting speed of 63.5 m/min and feed per revolution of 0.25mm. Average hardness value of three indentations, taken on the alloy, at the points of intersection of an imaginary grid of 50 μm X 50 μm, has been used for the diagram. 50 grams load was used for each measurement.
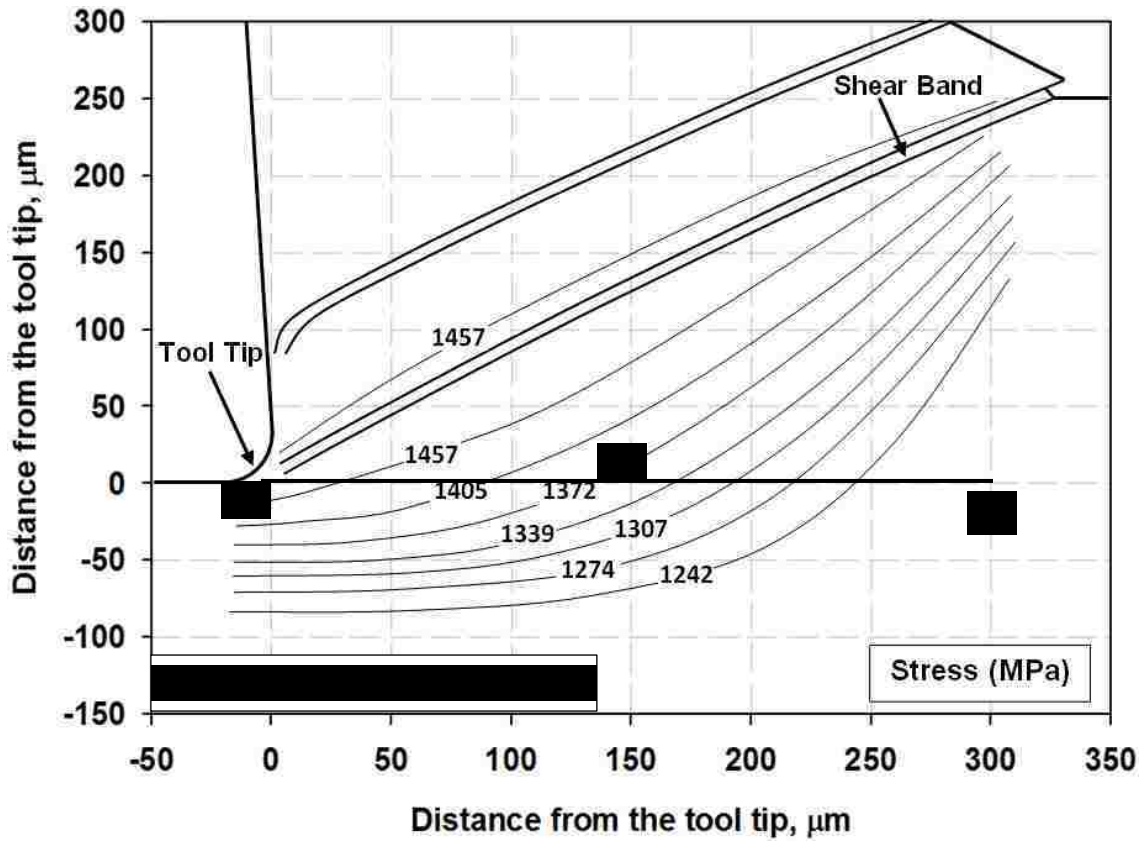
Fig. 4.43. Diagram showing the variation in flow stress (in units of MPa) values in the material ahead of the tool tip for sample machined under cutting speed of 63.5 m/min and feed per revolution of 0.25mm. Here OAC is the cutting line.
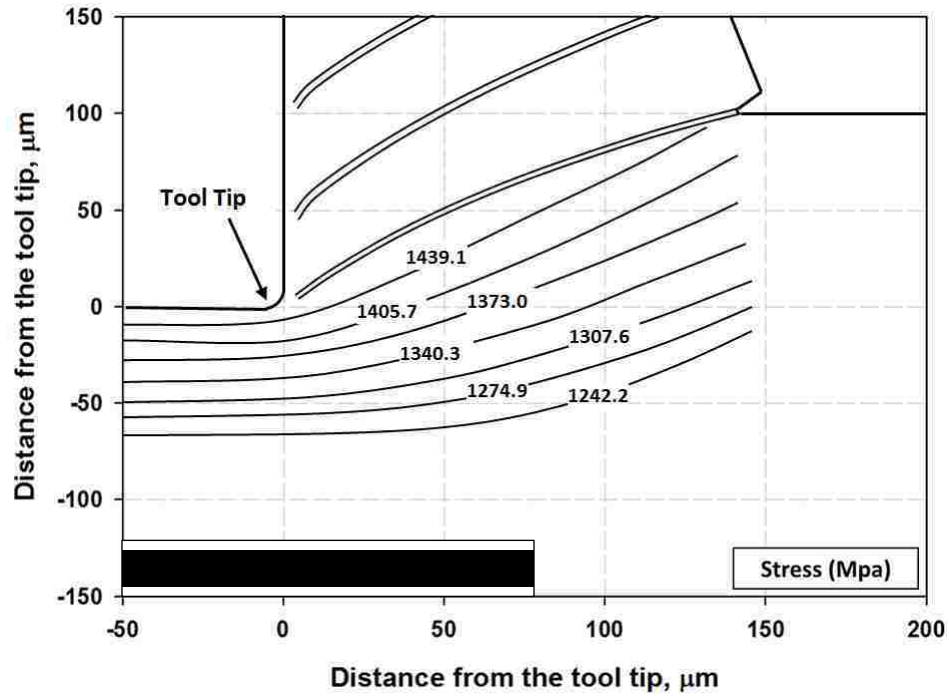
Fig. 4.44. Flow stress (in units of MPa) distribution diagram for the machining conditions

of 43.2 m/min cutting speed 0.10 mm/rev feed rate.
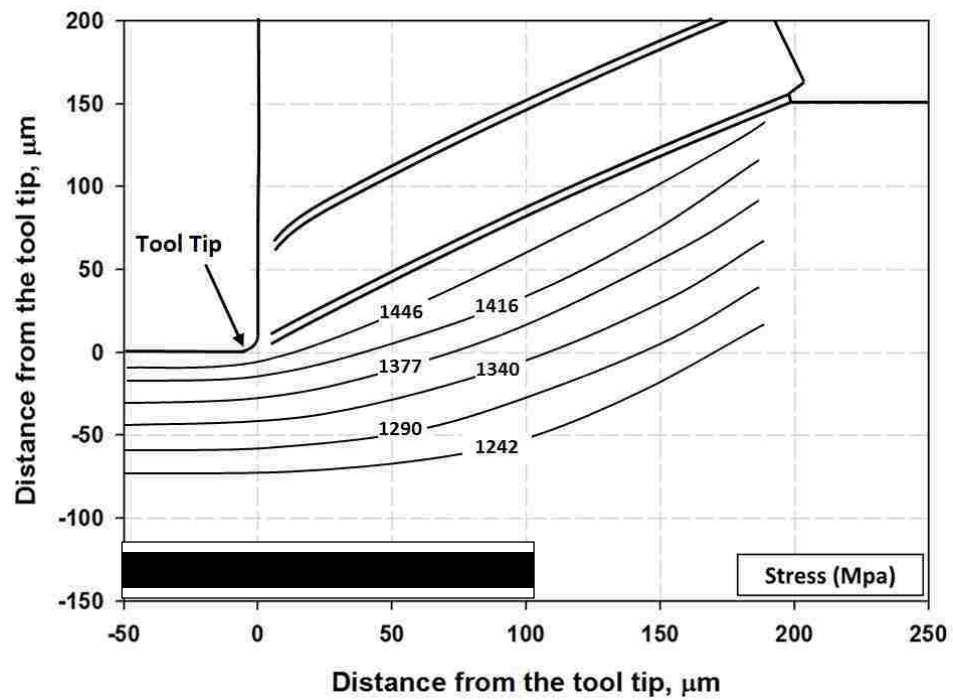
Fig. 4.45. Flow stress (in units of MPa) distribution diagram for the machining conditions

of 43.2 m/min cutting speed 0.15 mm/rev feed rate.
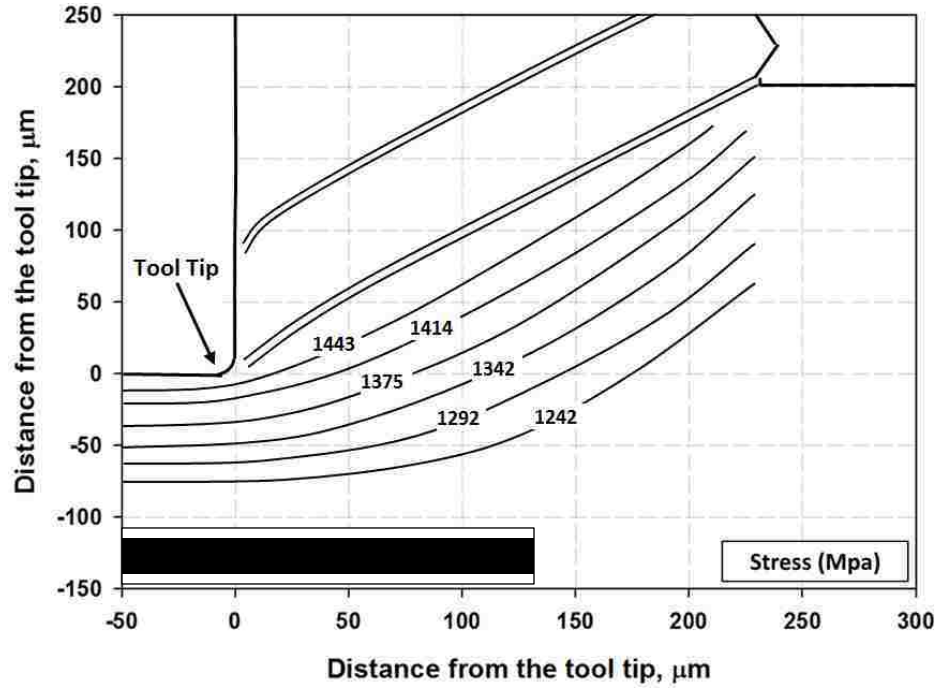
Fig. 4.46. Flow stress (in units of MPa) distribution diagram for the machining conditions of 43.2 m/min cutting speed 0.20 mm/rev feed rate.
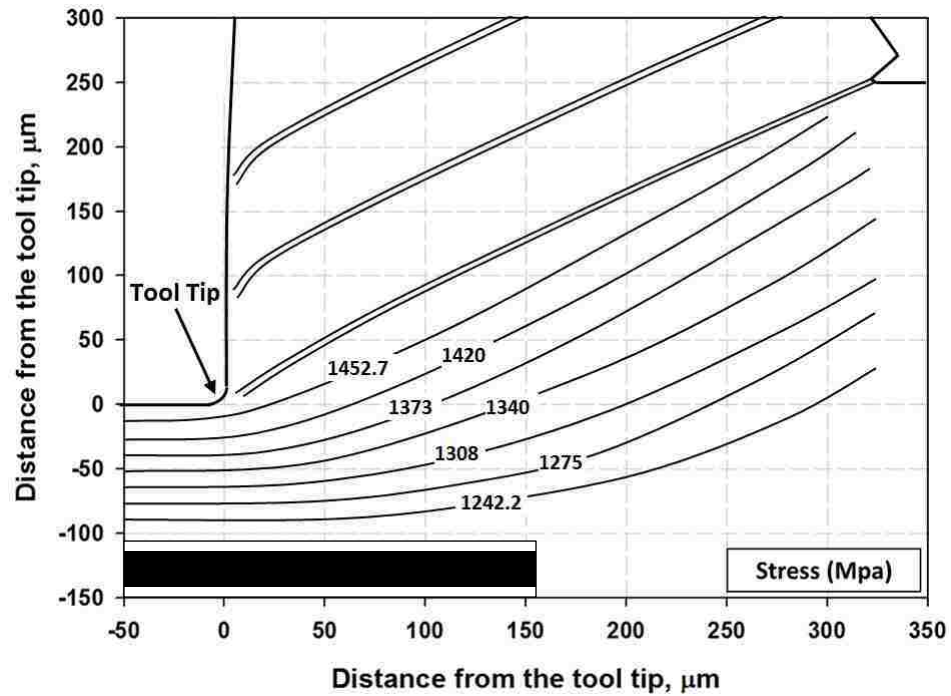
Fig. 4.47. Flow stress (in units of MPa) distribution diagram for the machining conditions of 43.2 m/min cutting speed 0.25 mm/rev feed rate.
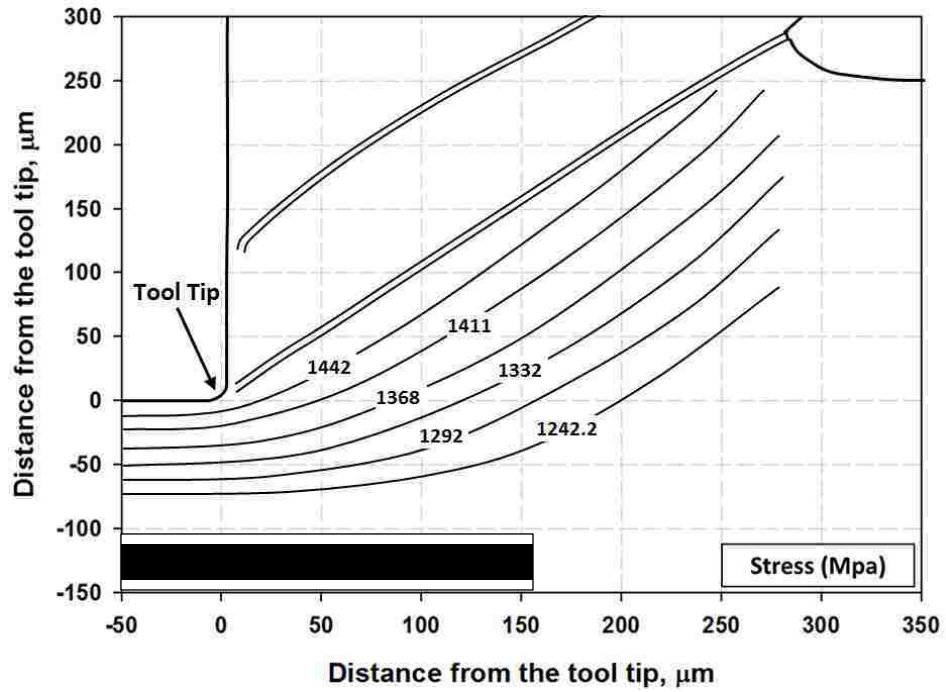
Fig. 4.48. Flow stress (in units of MPa) distribution diagram for the machining conditions

of 14.4 m/min cutting speed 0.25 mm/rev feed rate.
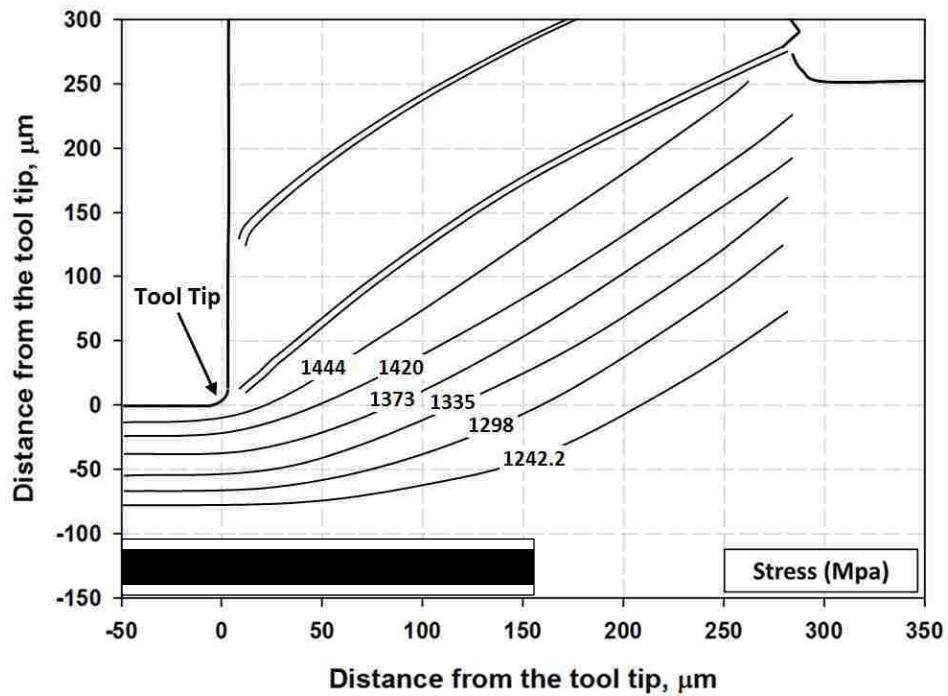
Fig. 4.49. Flow stress (in units of MPa) distribution diagram for the machining conditions

of 29.6 m/min cutting speed 0.25 mm/rev feed rate.
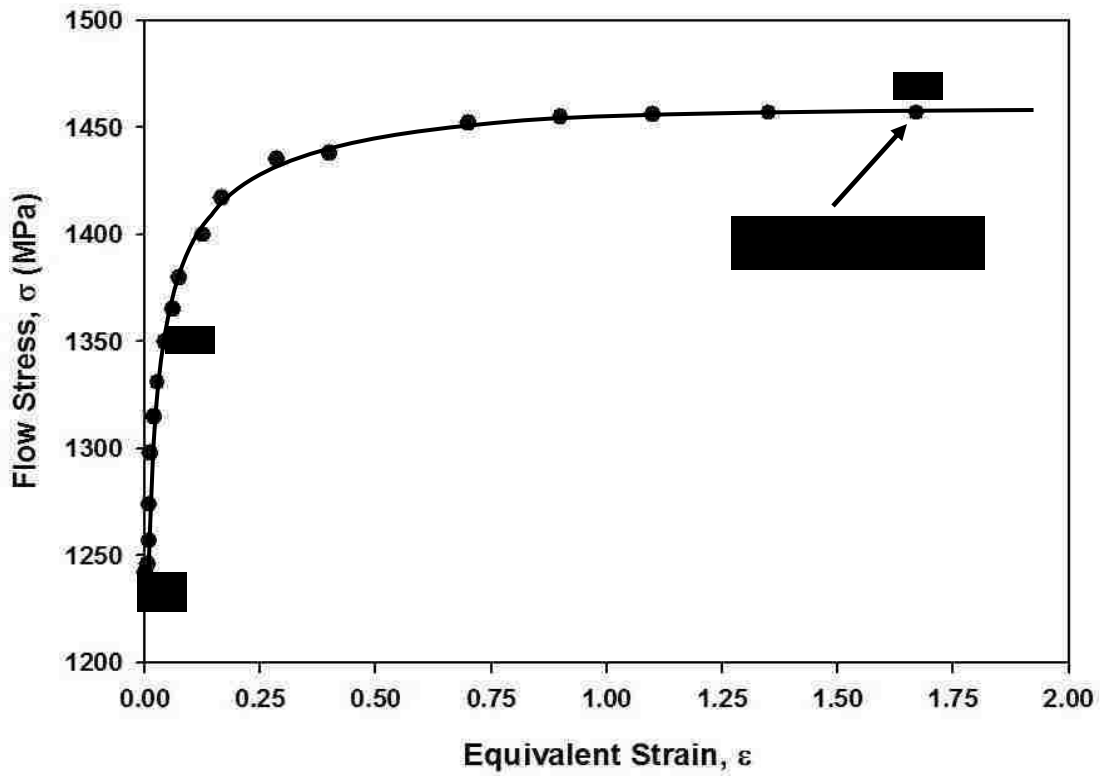
Fig. 4.50. The cumulative stress–strain curves of Ti-6Al-4V alloy subjected to orthogonal cutting. Machining conditions were cutting speed of 63.5 m/min and feed per revolution of 0.25 mm. O, A and C are the different points on the cutting line shown in Fig. 4.43.
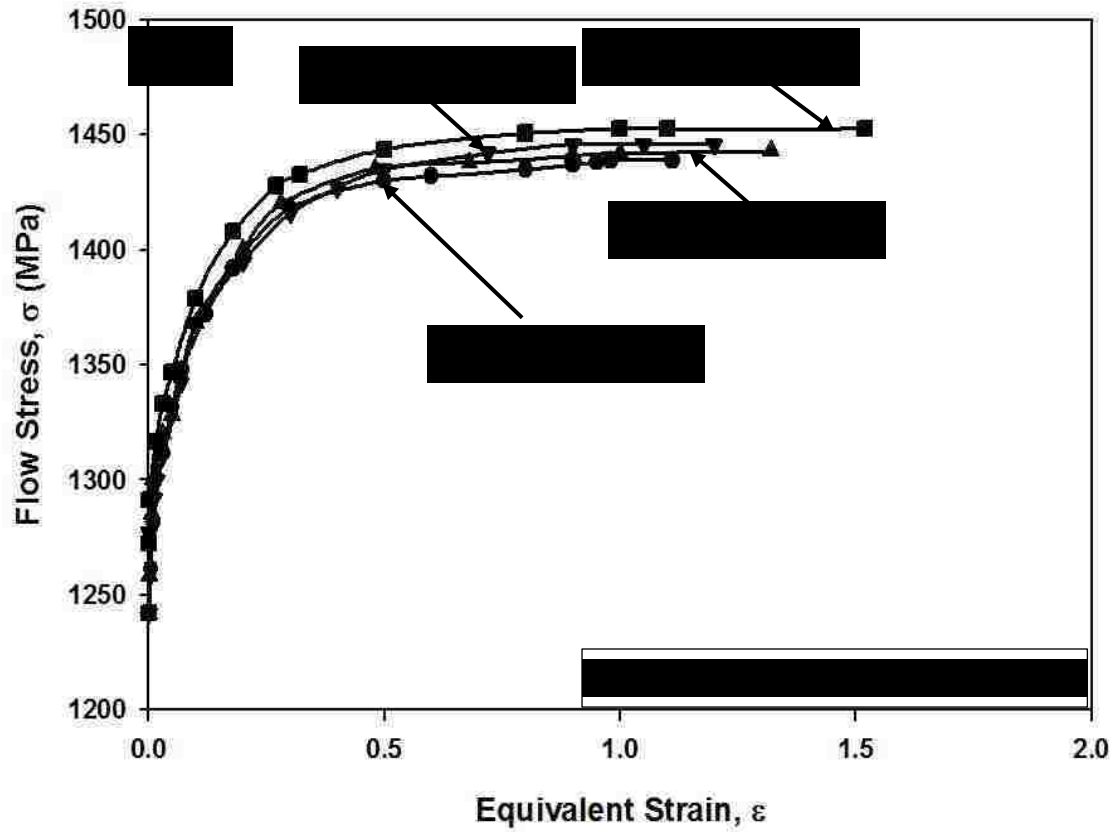
Fig. 4.51. The cumulative stress–strain curves of Ti-6Al-4V alloy subjected to orthogonal cutting at different feed rates such as: 0.10 mm/rev, 0.15 mm/rev, 0.20 mm/rev and 0.25 mm/rev, and constant cutting speed 43.2 m/min.
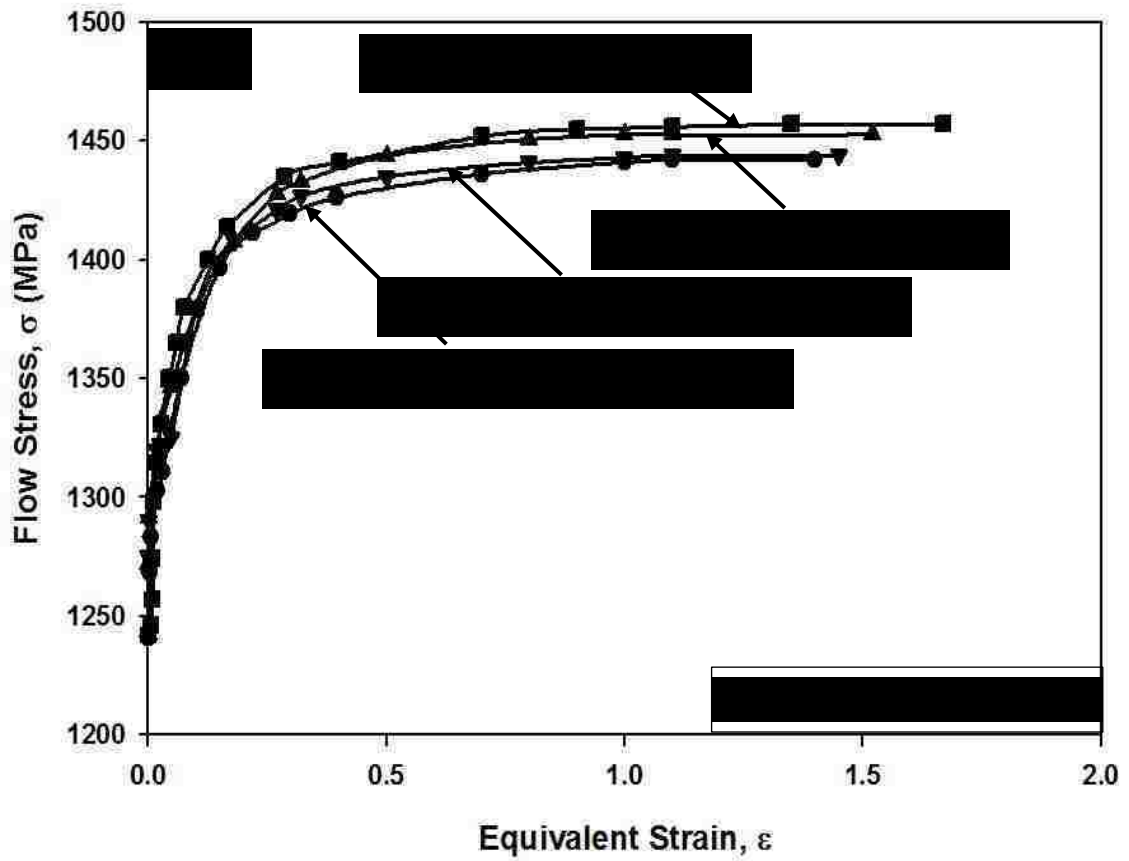
Fig. 4.52. The cumulative stress–strain curves of Ti-6Al-4V alloy subjected to orthogonal cutting at different cutting speeds such as: 14.4 m/min, 29.6 m/min, 43.2 m/min and 63.5 m/min, and constant feed rate 0.25 mm/rev.
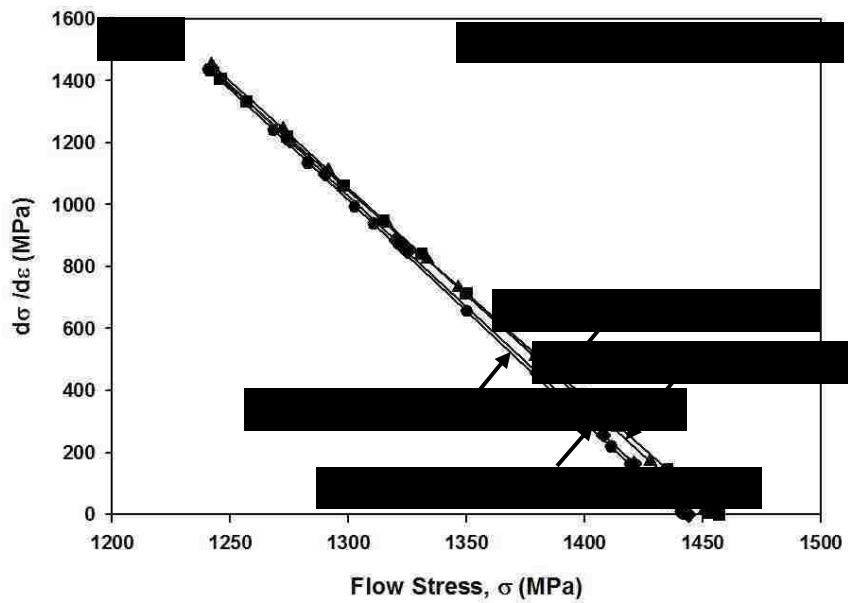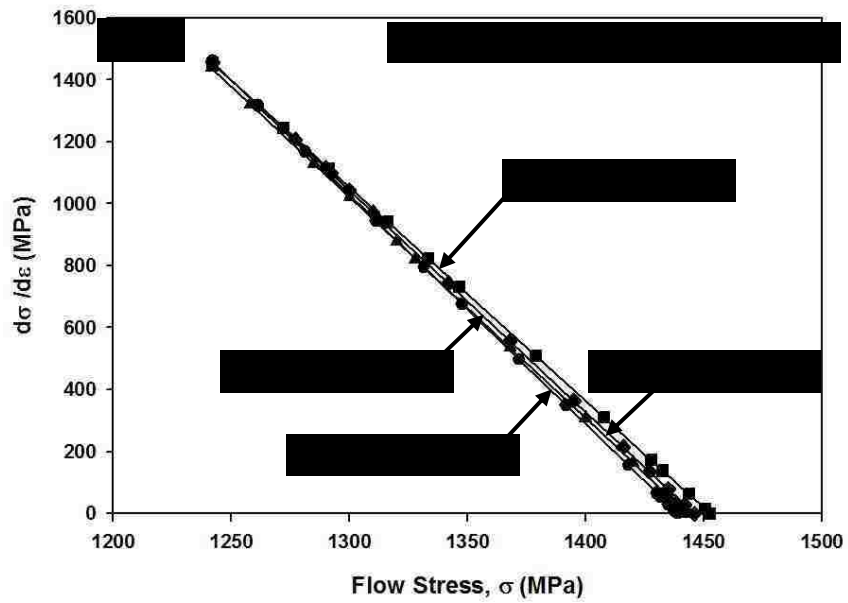
Fig. 4.53. The variation of work hardening rates with the flow stress for Ti-6Al-4V alloy subjected to orthogonal cutting at: (a) different feed rates and (b) different cutting speeds.
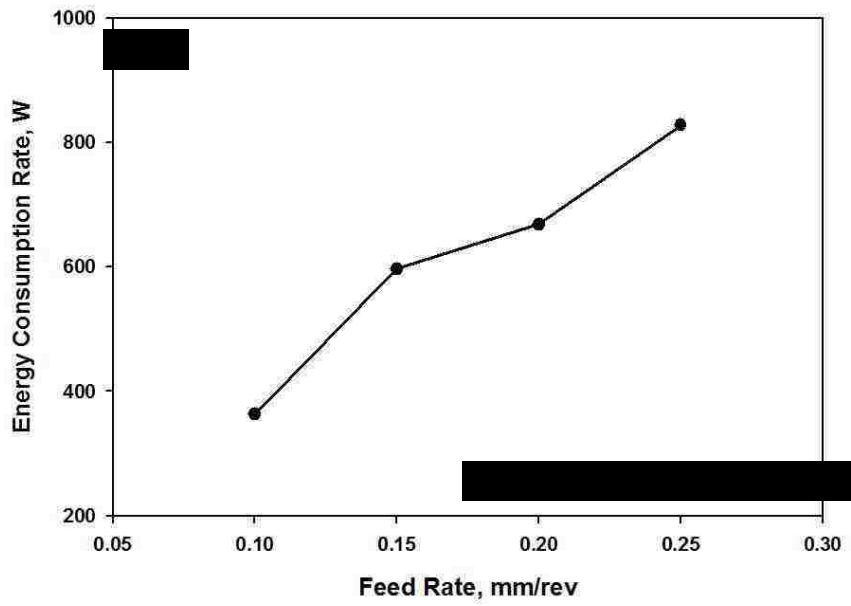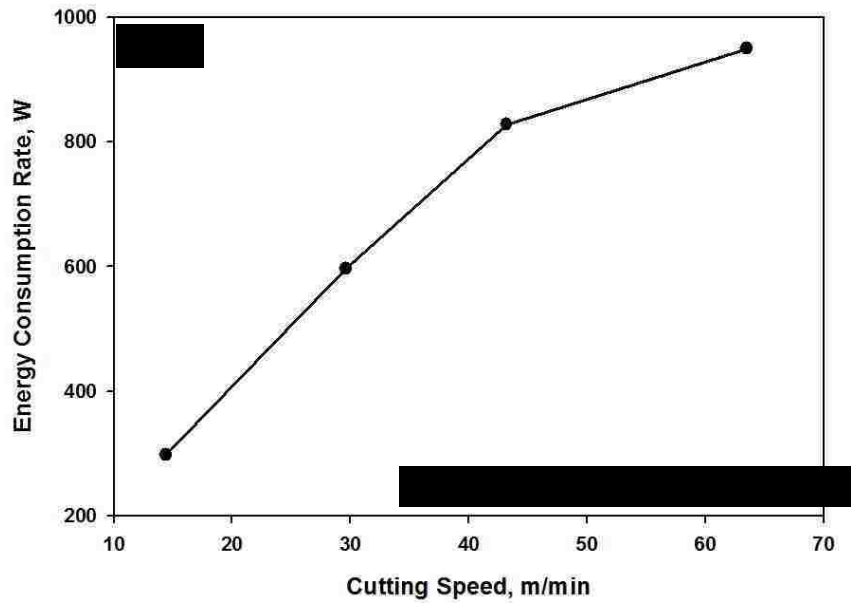
Fig. 4.54. Diagram showing the energy consumption rate duting machining of Ti-6Al-4V

alloy subjected to orthogonal cutting at different (a) feed rates and (b) cutting speeds.
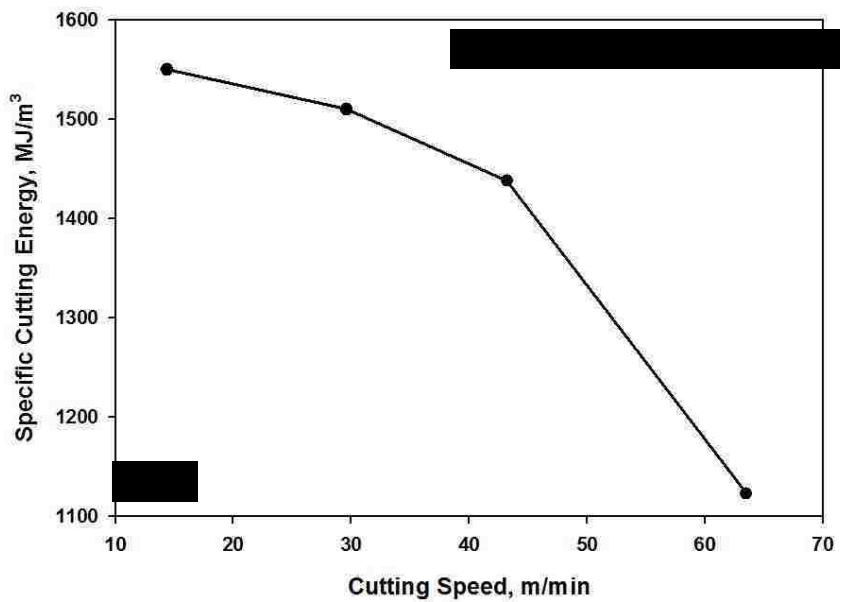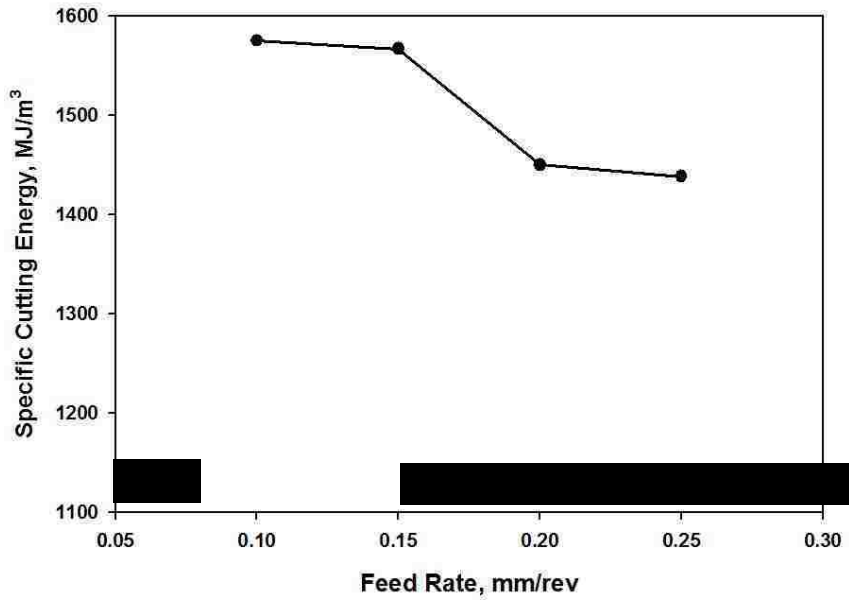
Fig. 4.55. Diagram showing the specific cutting energy duting machining of Ti-6Al-4V alloy subjected to orthogonal cutting at different (a) feed rates and (b) cutting speeds.
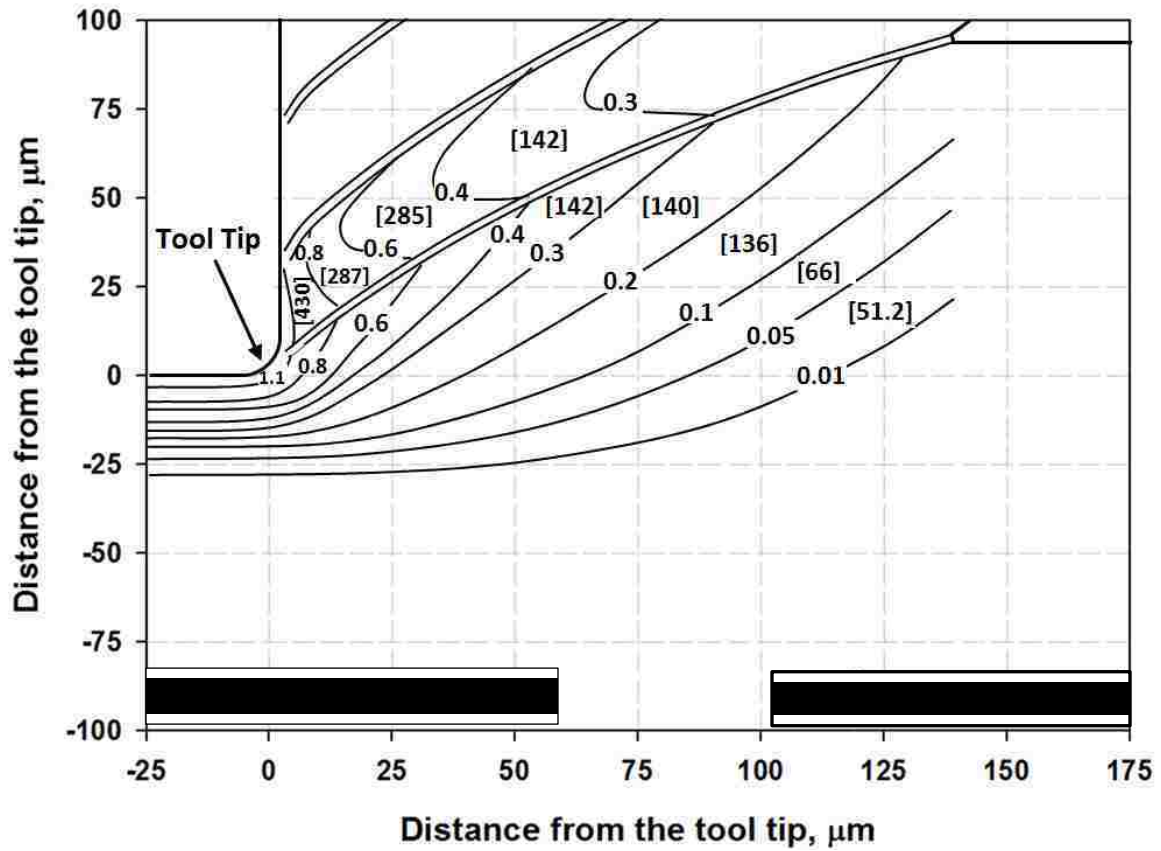
Fig. 4.56. The work of plastic deformation per unit volume of material (MJ m^{-3}) between each increment of equivalent strain. The average plastic work values for each strip of material bound between two iso-strain lines are indicated inside square brackets. Machining conditions were 43.2 m/min cutting speed and 0.10 mm feed per revolution.
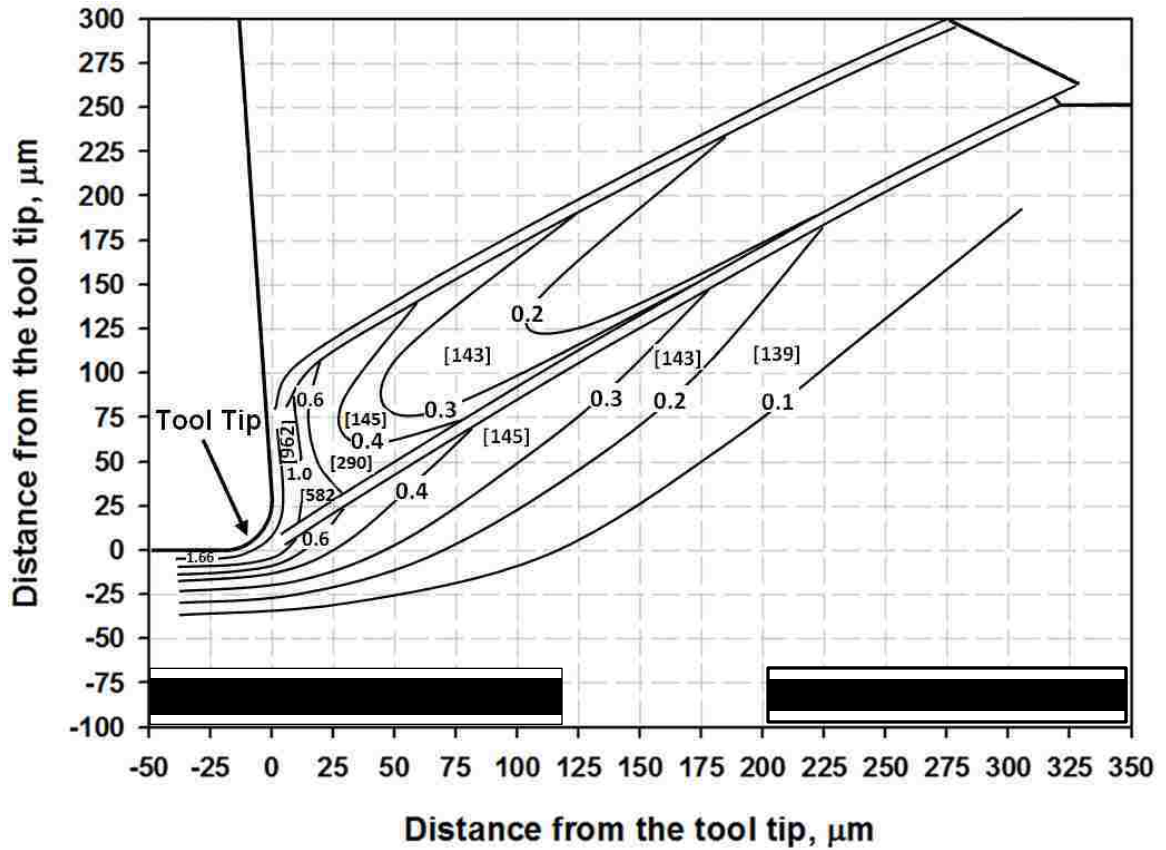
Fig. 4.57. The work of plastic deformation per unit volume of material (MJ m^{-3}) between each increment of equivalent strain. The average plastic work values for each strip of material bound between two iso-strain lines are indicated inside square brackets. Machining conditions were 63.5 m/min cutting speed and 0.25 mm feed per revolution.
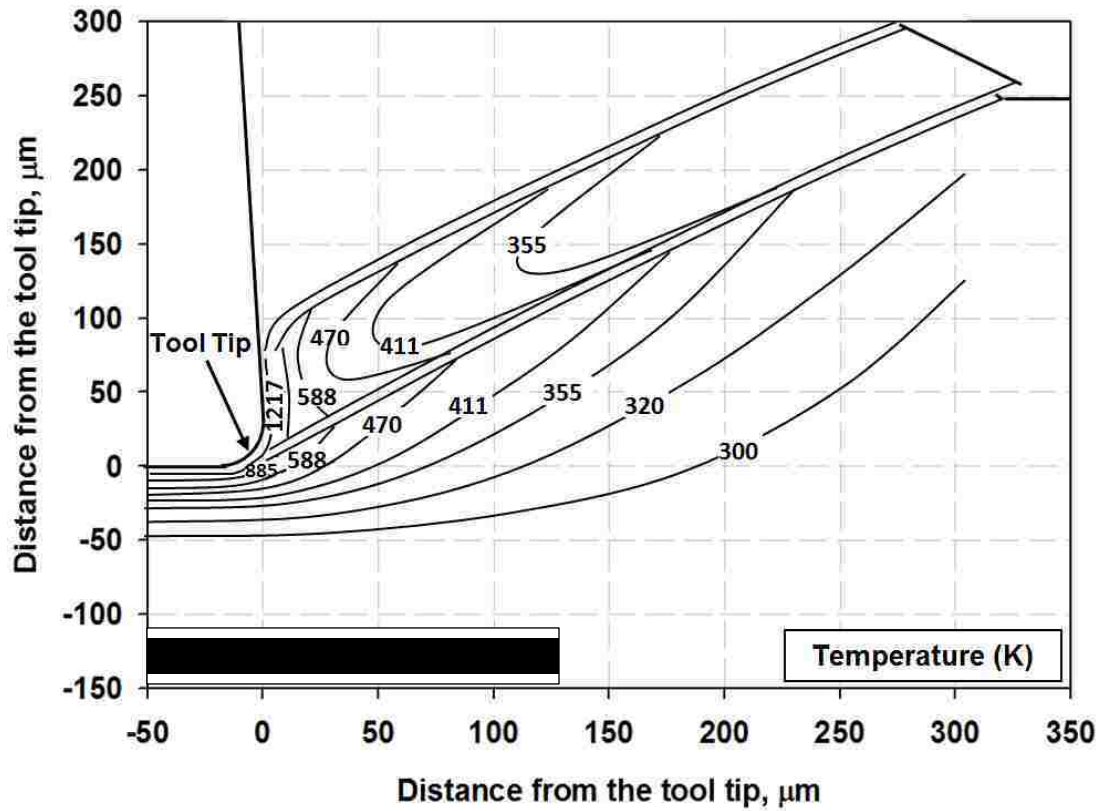
Fig. 4.58. Temperature map (in units of Kelvin) showing local increases in temperature as a result of transformation of the work done during plastic deformation into heat. Machining conditions were cutting speed of 63.5 m/min and feed per revolution of 0.25 mm.
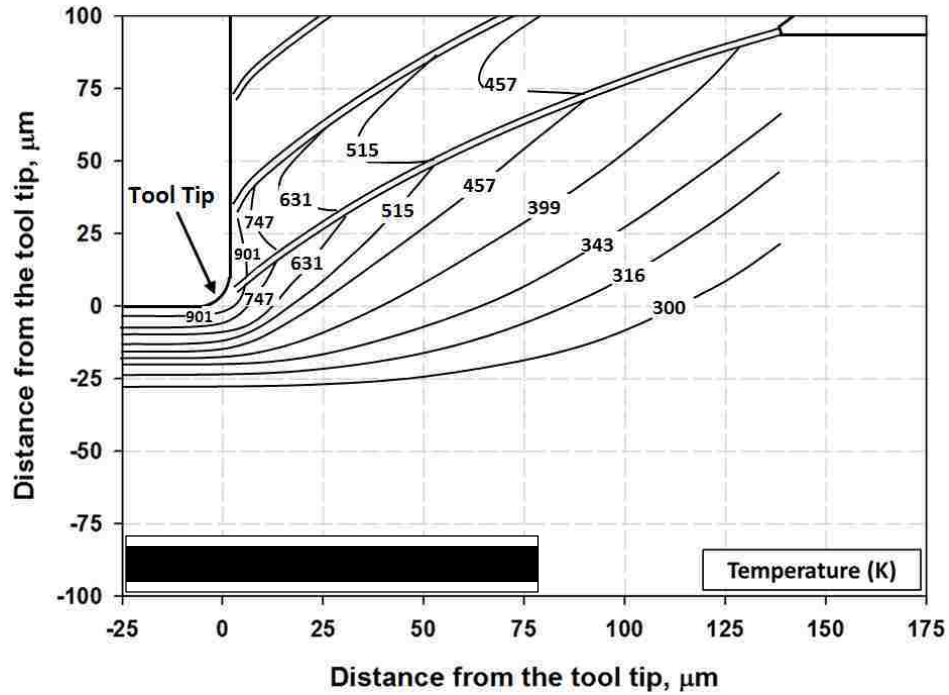
Fig. 4.59. Temperature (in units of Kelvin) distribution diagram for the machining conditions of 43.2 m/min cutting speed 0.10 mm/rev feed rate.
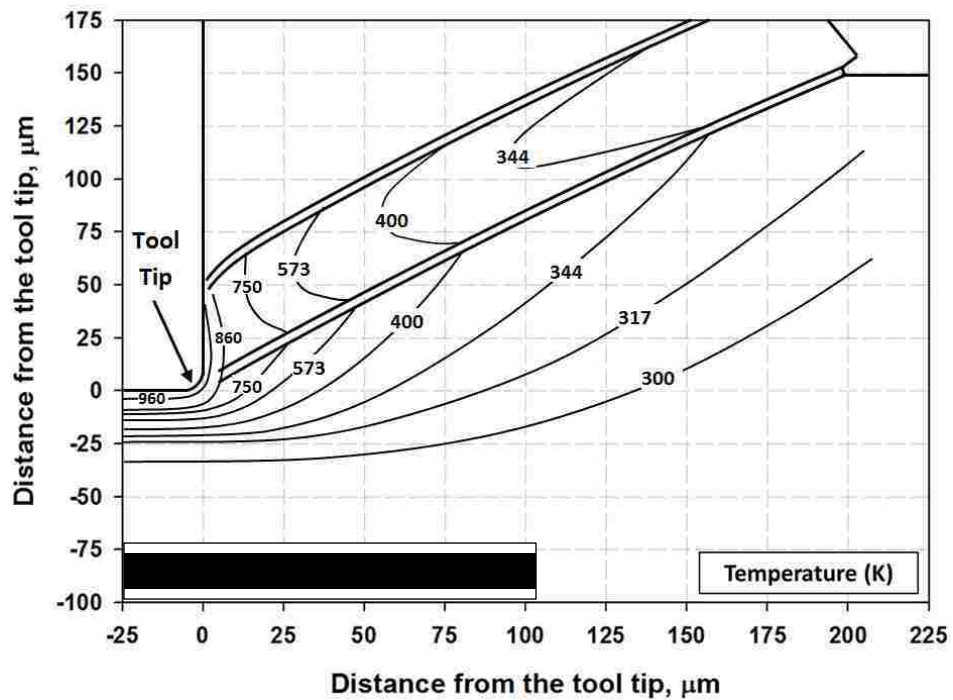
Fig. 4.60. Temperature (in units of MPa) distribution diagram for the machining conditions of 43.2 m/min cutting speed 0.15 mm/rev feed rate.
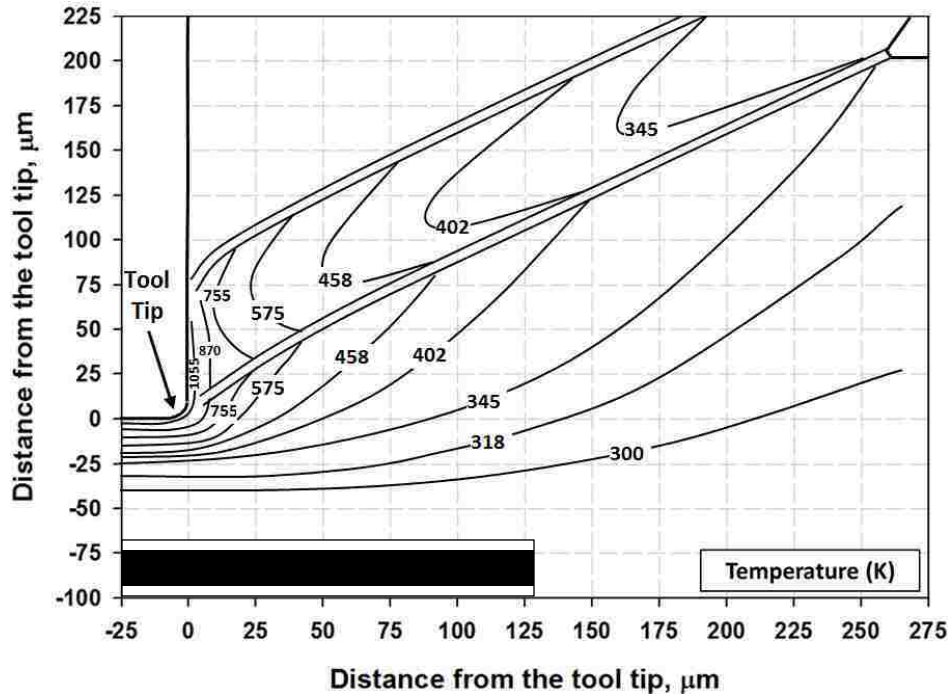
Fig. 4.61. Temperature (in units of MPa) distribution diagram for the machining conditions of 43.2 m/min cutting speed 0.20 mm/rev feed rate.
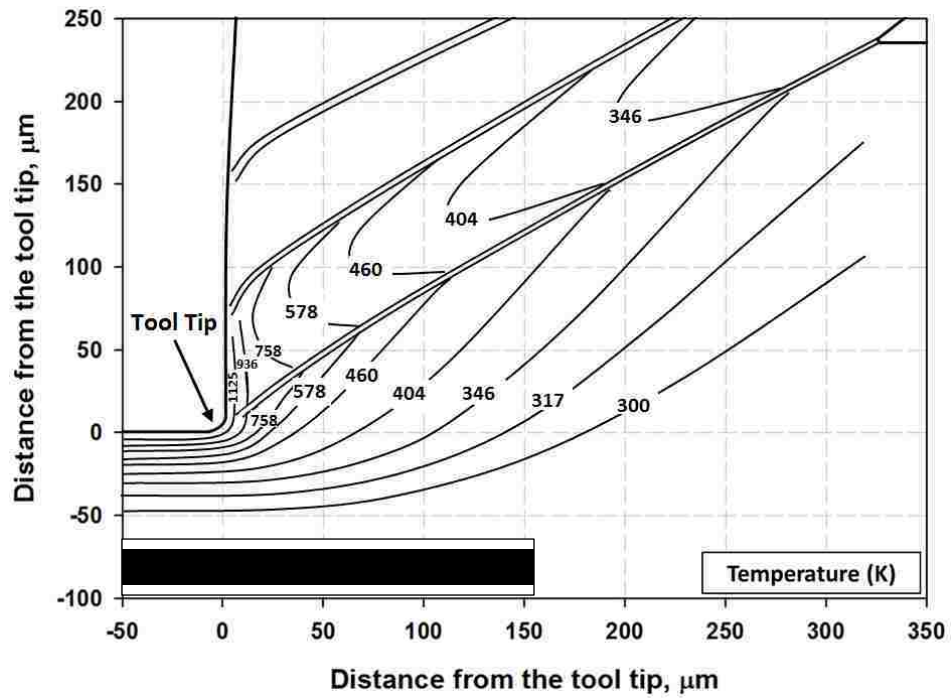
Fig. 4.62. Temperature (in units of MPa) distribution diagram for the machining conditions of 43.2 m/min cutting speed 0.25 mm/rev feed rate.
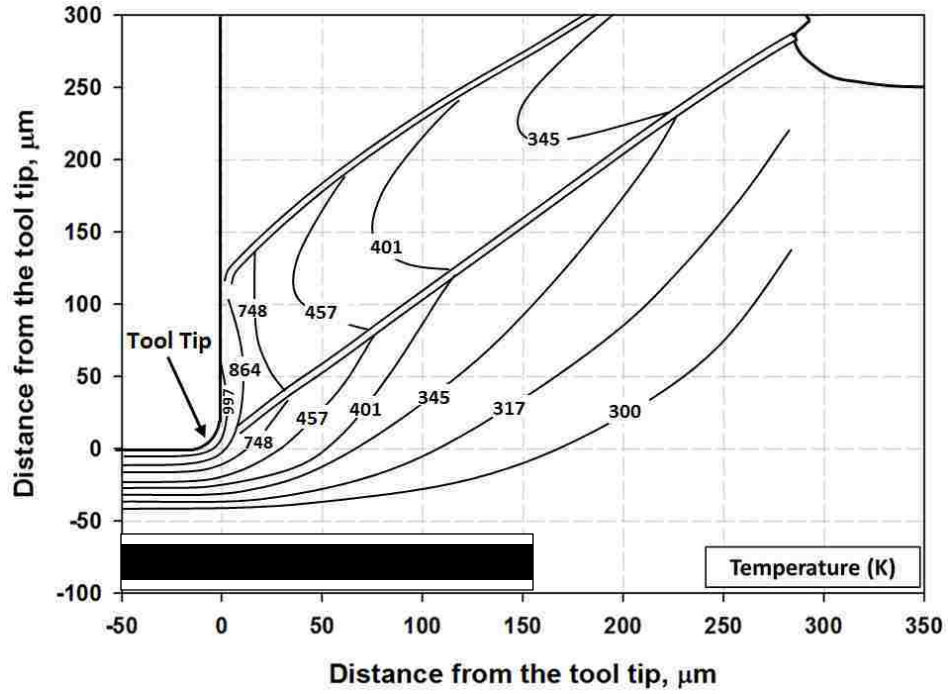
Fig. 4.63. Temperature (in units of MPa) distribution diagram for the machining conditions of 14.4 m/min cutting speed 0.20 mm/rev feed rate.
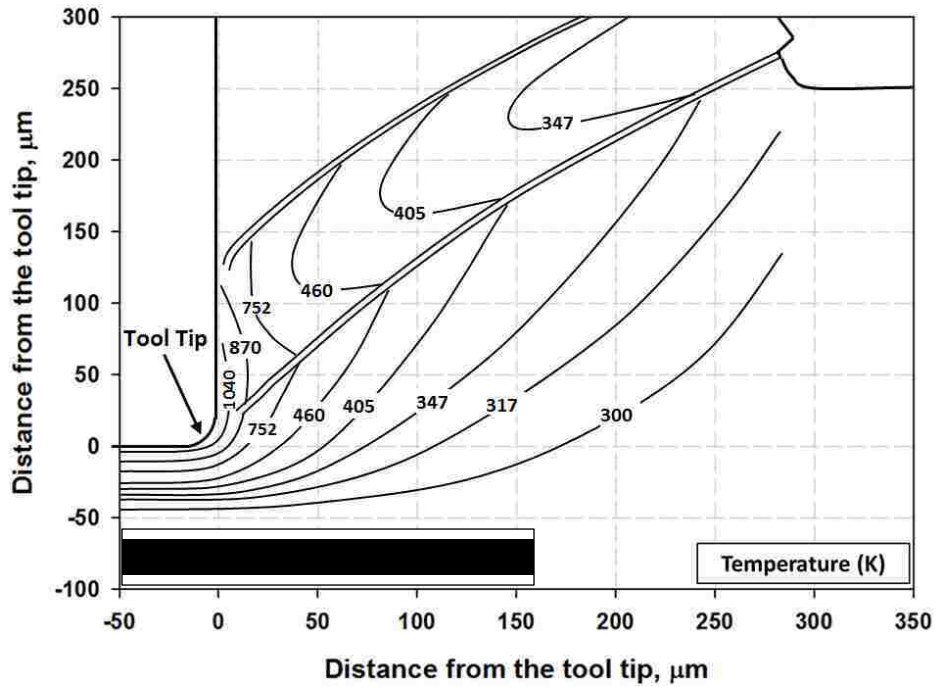
Fig. 4.64. Temperature (in units of MPa) distribution diagram for the machining conditions of 29.6 m/min cutting speed 0.25 mm/rev feed rate.
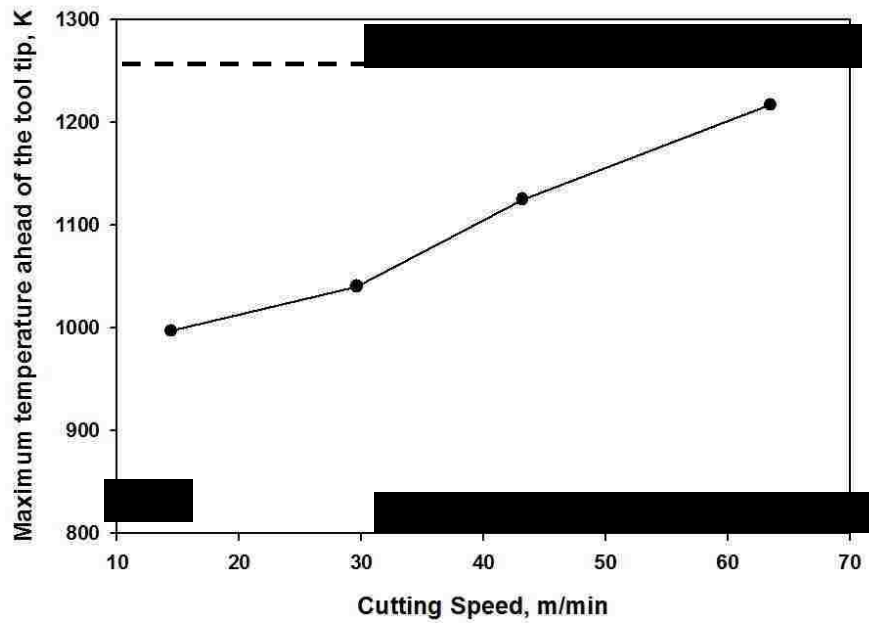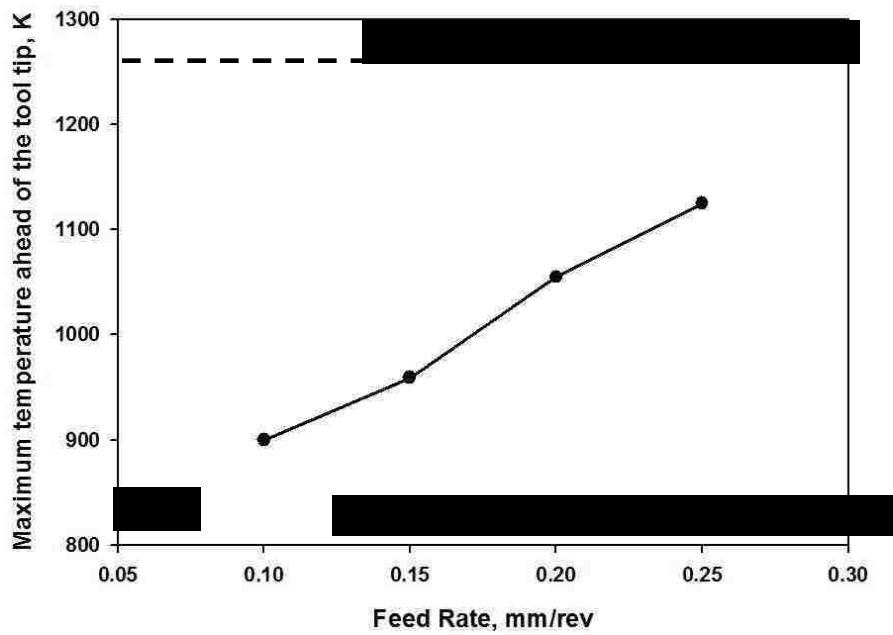
Fig. 4.65. Variation of the maximum temperature ahead of the tool tip with (a) the feed rate and (b) cutting speed.
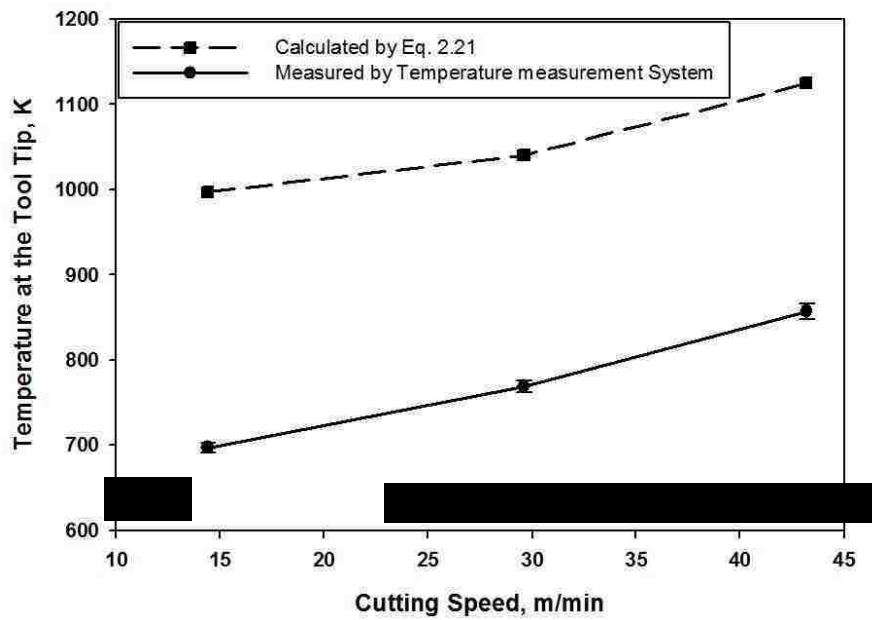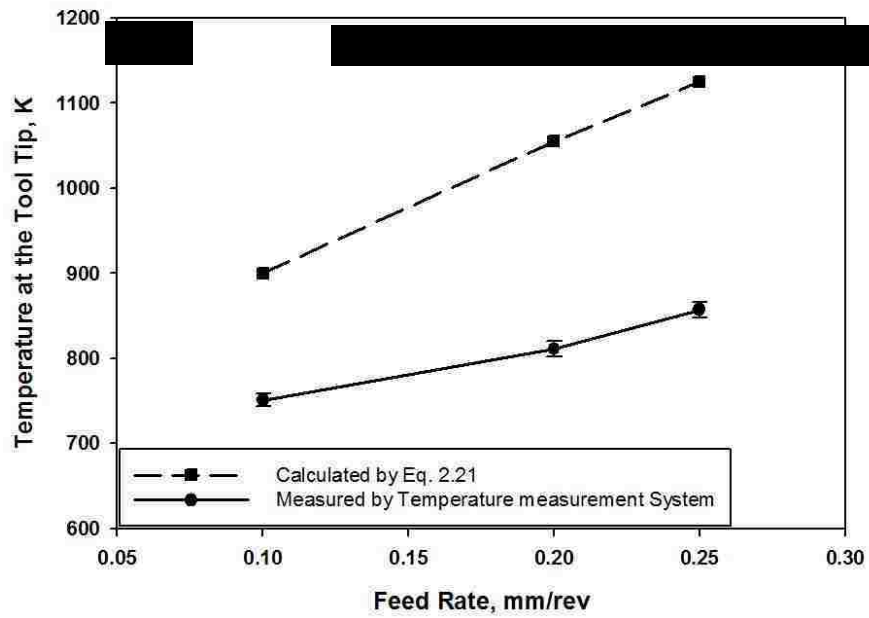
Fig. 4.66. Plots showing the variation of tool tip temperature with increasing the (a) feed rate and (b) cutting speed.
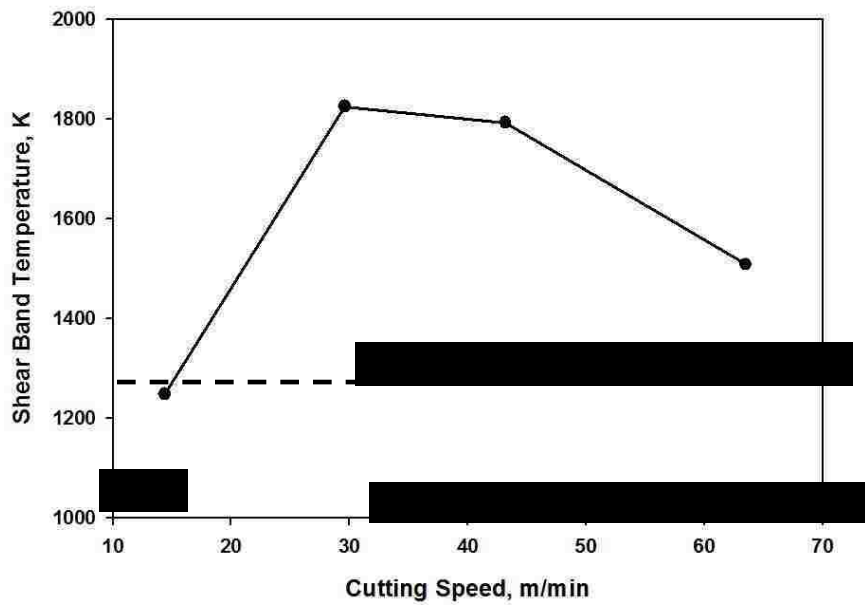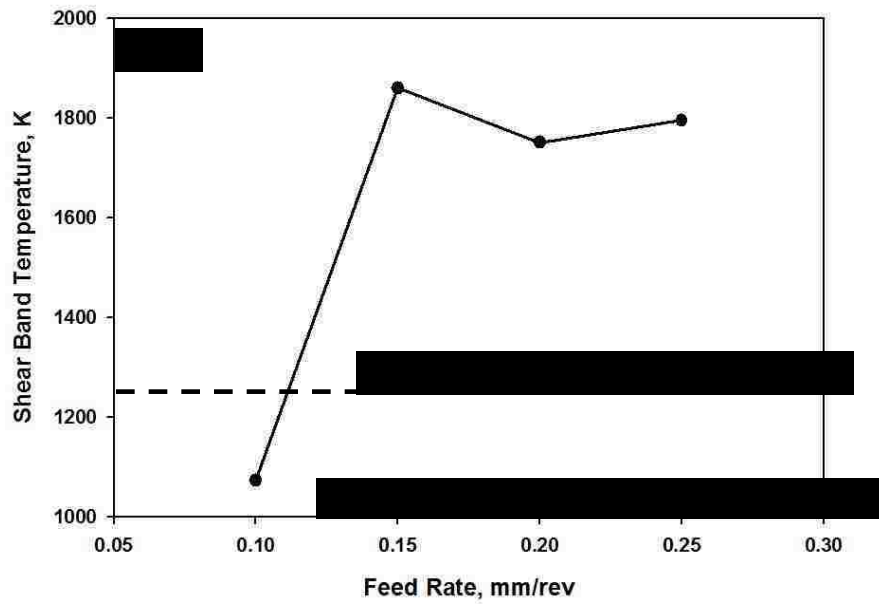
Fig. 4.67. Variation of the temperature within the shear band with the (a) feed rate and (b) cutting speed.
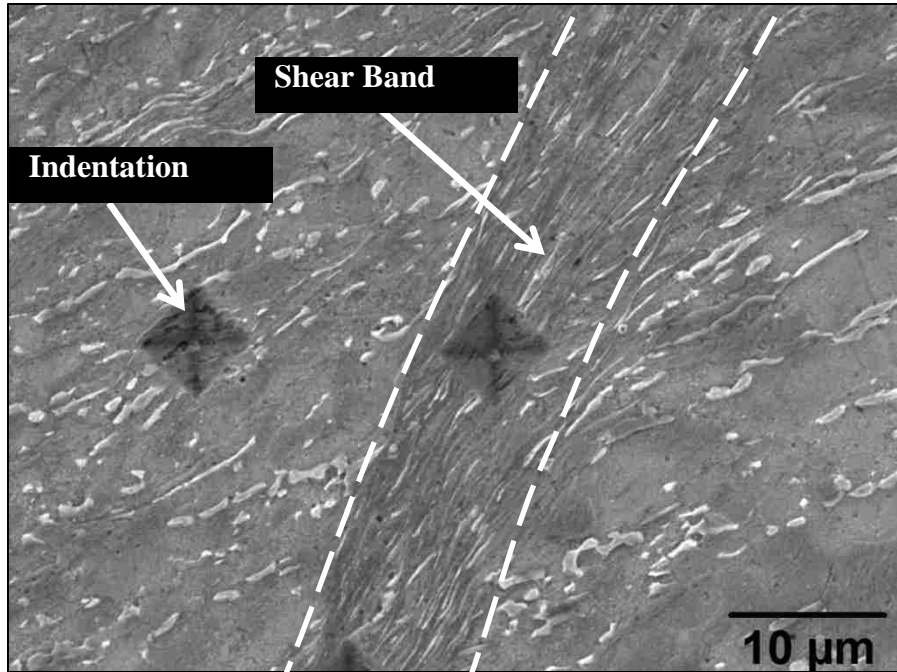
Fig. 4.68. SEM image of the indentations of microhardness measurements within the shear band and outside of the shear band.
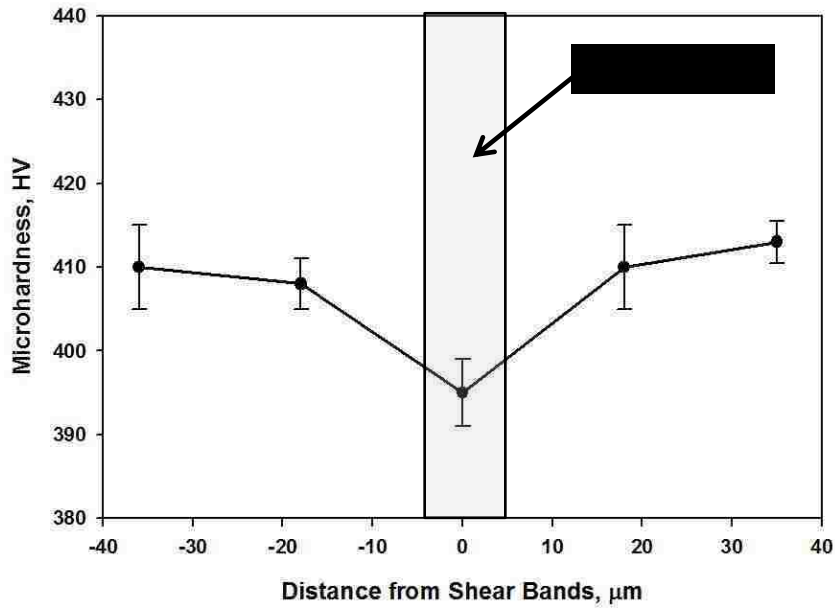
Fig. 4.69. Microhardness distribution across the shear band formed under the cutting condition of 63.5 m/min cutting speed and 0.25 mm/rev feed rate.
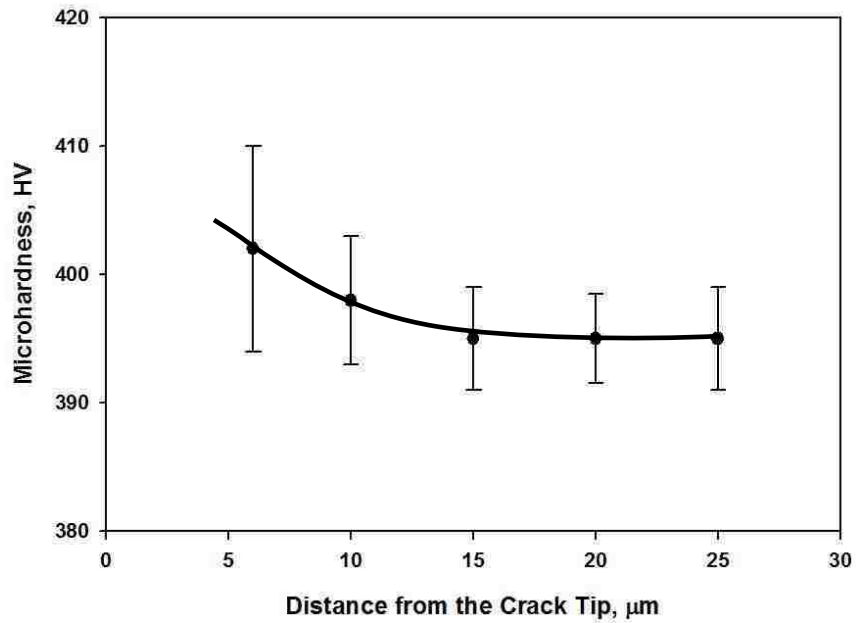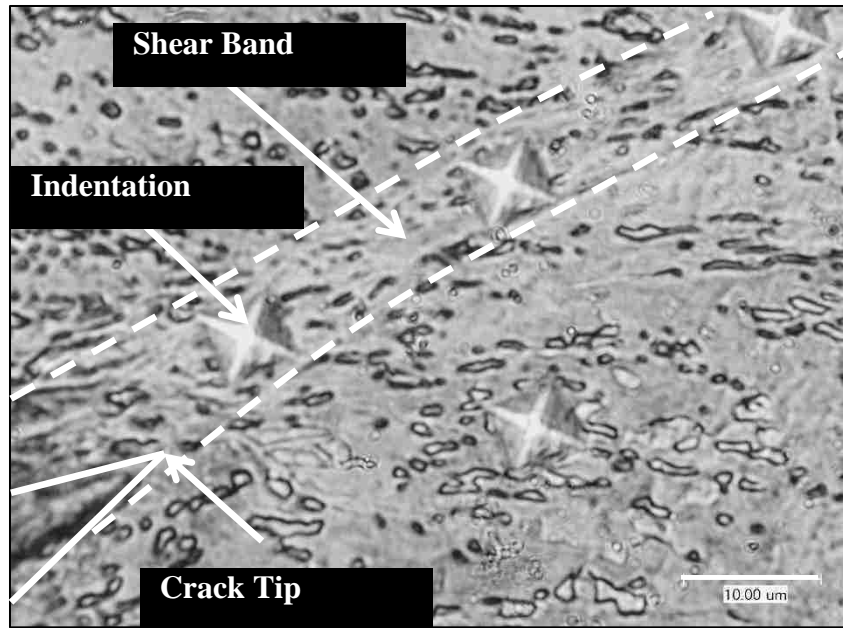
Fig. 4.70. (a) Optical image of the indentations of microhardness measurements within the shear band and near the crack tip. (b) Variation of microhardness within the shear band with the distance form the crack tip.
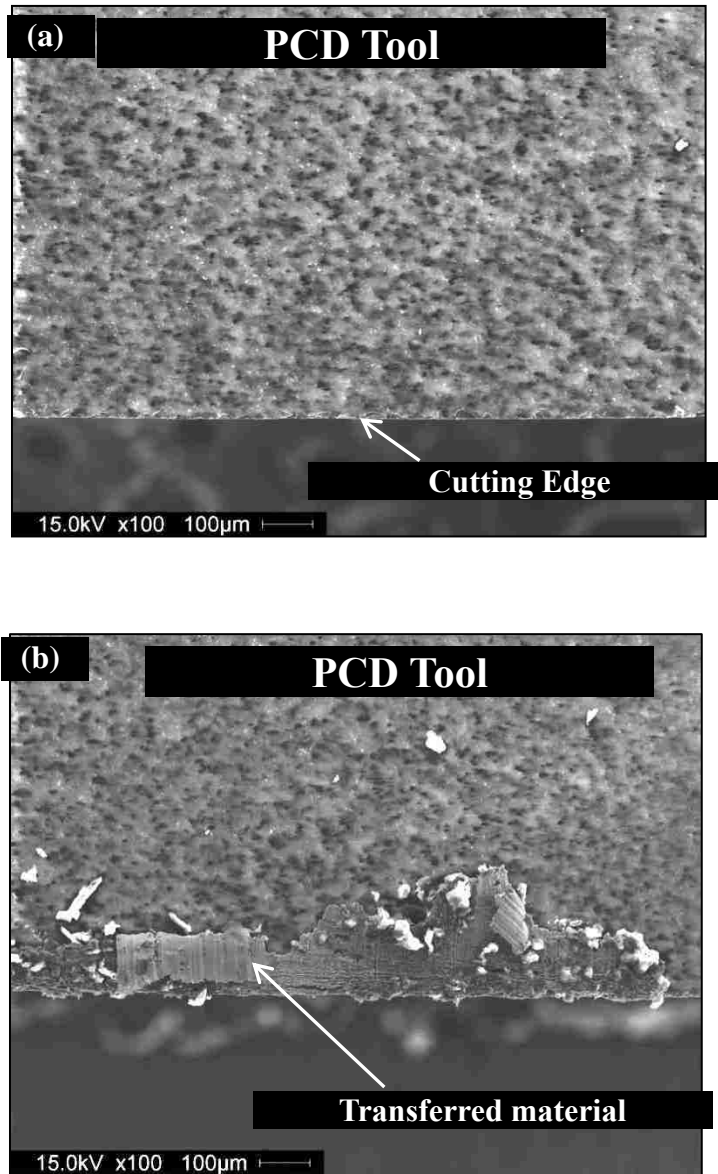
Fig. 4.71. SEM images of the polycrystalline diamond (PCD) tool (a) before the machining test, (b) after the machining of Ti-6Al-4V alloy. Transferred material was observed at the edge of the tool after the cutting.
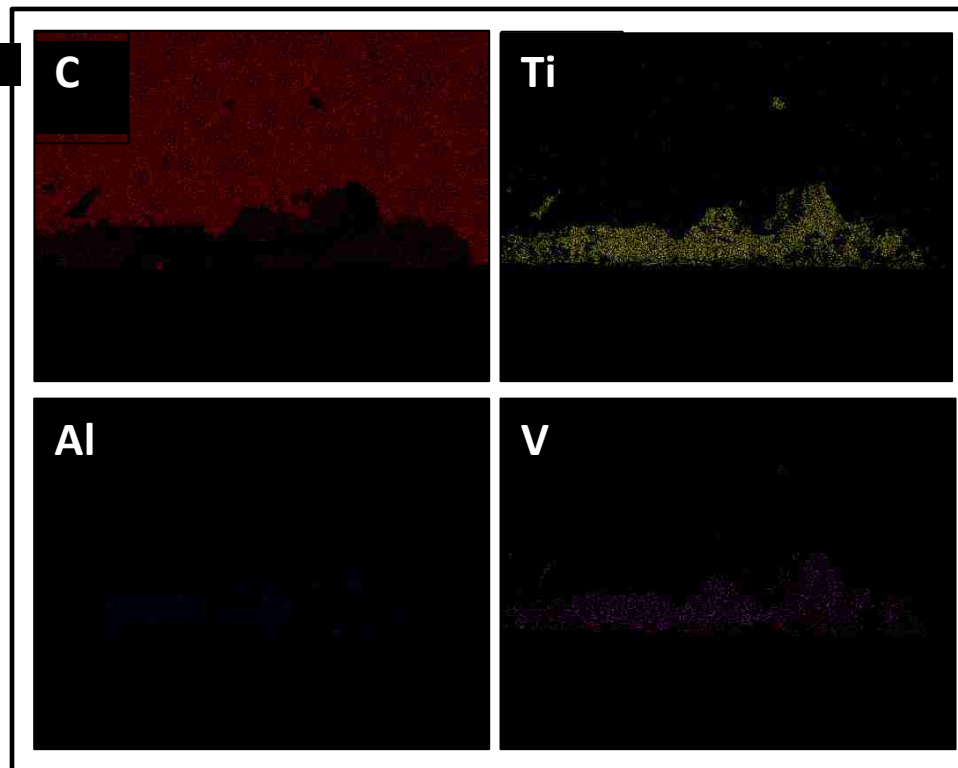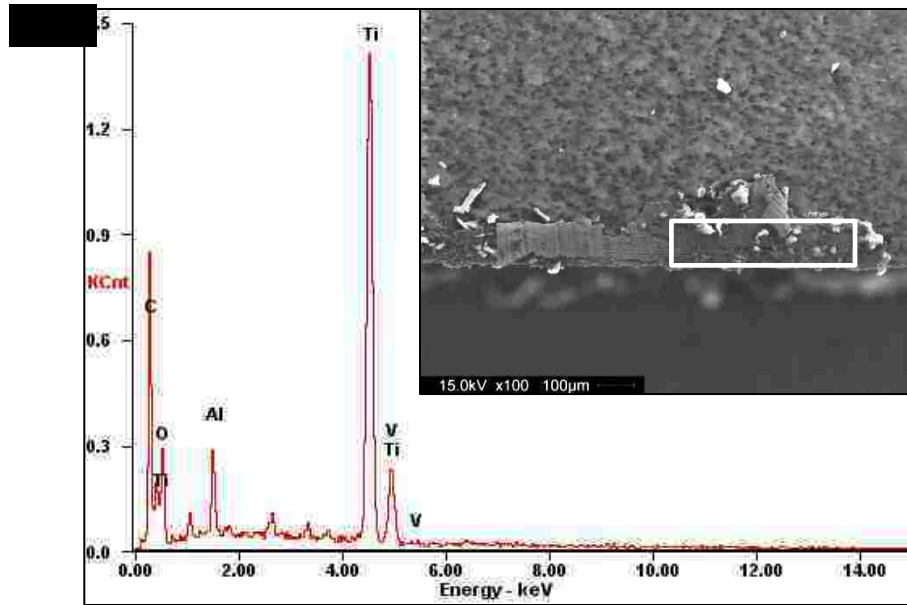
Fig. 4.72. (a) EDS results of the transferred material on the tool edge. (b) EDS mapping of the tool surface confirms that the transferred material mainly contains titanium, aluminum, and vanadium that comes from the workpiece material (Ti-6Al-4V alloy).
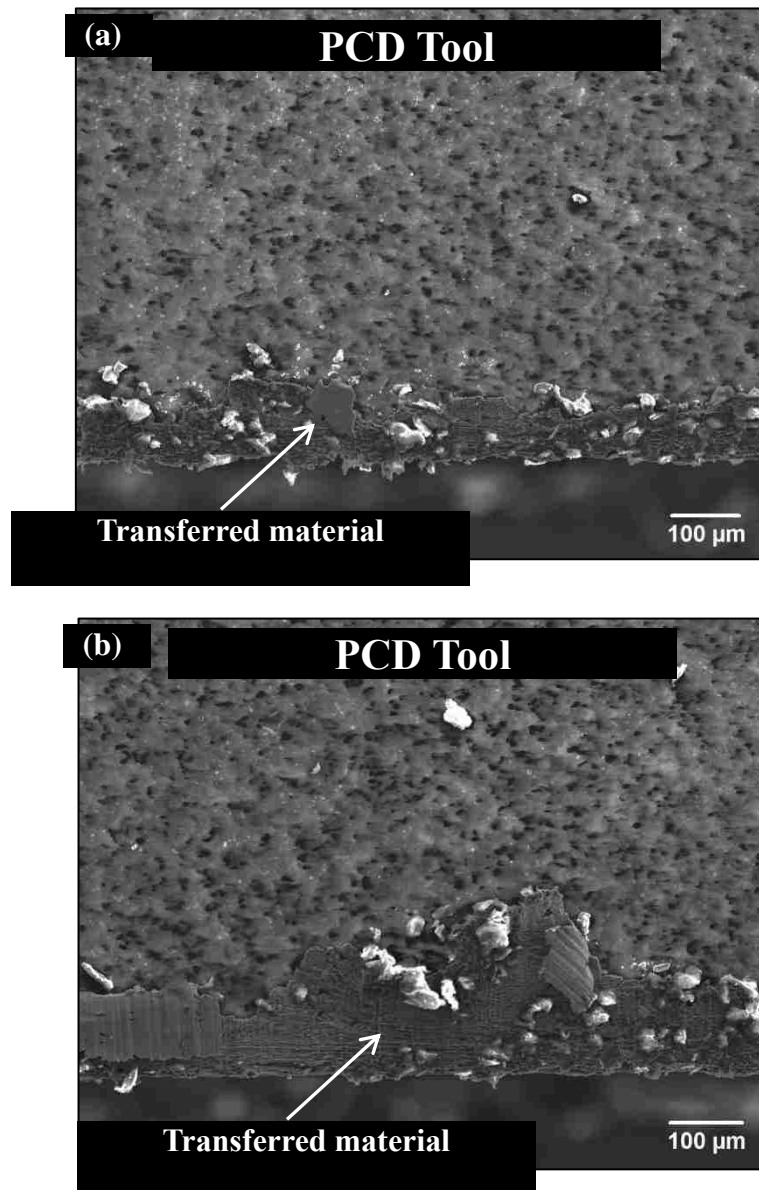
Fig. 4.73. SEM images of the polycrystalline diamond (PCD) tool after the machining of Ti-6Al-4V alloy at (a) 43.2 m/min of cutting speed and 0.25 mm/rev of feed and (b) 63.5 m/min of cutting speed and 0.25 mm/rev of feed rate. More transferred material was observed at the edge of the tool for higher cutting speed.

CHAPTER 5: Numerical Results

5.1. Introduction

In this chapter the numerical results obtained using the two different methods, namely, 2D Lagrangian element formulation method and smoothed particle hydrodynamic (SPH) formulation, are discussed. In this research the numerical models were developed using the experimental data. The results obtained from the numerical models have been presented in the following sections:

5.2. Johnson-Cook Material Model

The Johnson–Cook equation (Eq. 2.29) constants for Ti-6Al-4V alloy were determined from the experimentally observed stress–strain behaviour (Fig. 4.23).

$$\sigma = (\sigma_y + B\bar{\varepsilon}^{p^n})(1 + c\,ln\,\dot{\varepsilon}^*)(1 - T^{*^m}) \tag{2.29}$$

Experimentally determined the stress-strain curve was fitted with Eq. 5.3 using a curve fitting software called 'TableCurve 2D(v5.01)' shown in Fig. 5.1.

$$\sigma = 1240 + 220\bar{\varepsilon}^{p\,0.26} \tag{5.3}$$

Accordingly, σ_0, B, and n were found to 1240 MPa, 220 MPa, and 0.26, respectively for machining conditions of 63.5 m/min or 1.05 m/sec of cutting speed and 0.25 mm/rev of feed rate.

The strain rate sensitivity, c, was calculated using the Eq. 2.31, from the stress-strain curve for different cutting speeds (Fig. 4.25b).

$$c = \frac{\dot{\varepsilon}}{\sigma}\left(\frac{\delta\sigma}{\delta\dot{\varepsilon}}\right)_{\varepsilon,T} = \frac{log(\sigma_2/\sigma_1)}{log(\dot{\varepsilon}_2/\dot{\varepsilon}_1)}$$

(2.31)

The strain rates for 63.5 m/min and 29.6 m/min cutting speeds are 3525 s^{-1} and 1630 s^{-1} respectively, and the corresponding saturated stresses are 1457 MPa and 1444 MPa. The calculated value of the strain rate sensitivity, c, is 0.012.

In the JC material model, another failure criteria such as maximum effective strain at failure (= 1.66) and shear strain at failure (= 2.2) obtained from the experimental strain distribution diagram (Fig. 4.20), were also imposed.

The assigned value of coefficient of friction (COF) in contact between tool and workpiece in the numerical model was also calculated from the experimental results. COF value was calculated using the Eq. 2.5. The cutting and thrust force were 898 N and 430 N respectively, for the machining conditions of 63.5 m/min or 1.05 m/sec of cutting speed, 0.25 mm/rev feed rate and +5° of rake angle. The calculated value of the coefficient of friction, μ, is 0.6. The values of the static and dynamic coefficients of friction for contact between tool and workpiece were specified as 0.6 since it was assumed that the COF was constant during cutting.

5.2.1. 2D Lagrangian element formulation

Serrated chips were obtained using 2D Lagrangian Element Formulation implementing the Johnson-Cook material model with damage criteria.

5.2.1.1. Energy balance

The balance between external work and total energy in a numerical simulation is very important to the validity of the results. Fig. 5.2 shows the typical energy balance of the serrated chip formation simulation using 2D Lagrangian element formulation, including the external work, total energy, kinetic energy, internal energy, hourglass energy and sliding energy. The total energy of the system was almost equivalent to the external work. The total energy was composed of internal energy stored in the deformed workpiece and kinetic energy of the moving tool and workpiece. The sliding and hourglass energies were negligible, confirming that neither hourglass deformation nor penetration occurred. The energy ratio was 1.0 throughout the simulation, which established the results were valid with respect to the energy balance

5.2.1.2 Deformation of the workpiece

During the simulation, force applied by the rigid tool imposed a displacement on the workpiece and caused mesh deformation (Fig. 5.3a). A very fine Lagrangian mesh (3 µm X 3 µm) compared to the mesh used by [149], was used to avoid the mesh distortion and usually a finer mesh distribution is favorable in numerical modeling to ensure more precise calculations. Fig. 5.3b depicts that excessive deformation is occurred in the workpiece at the tool tip. Large amount of deformation also occurred at the PDZ.

183

As the strain value in the material reaches to the failure strain calculated from the Johnson-Cook failure equation (Eq. 2.32), the corresponding elements of the workpiece are deleted and finally serrated chips are formed. The average width of the chip which is equal to the average chip frequency, is about 118.6 ± 11.8 µm. However, in experimental case serrated chips were formed due to the formation of adiabatic shear band.

5.2.1.3. Strain Distribution

The strain distribution in the workpiece model is shown in Fig. 5.4a. Fig. 5.4b depicts the contours of strain distribution in the workpiece model. It was observed that the maximum strain was generated in the workpiece ahead of the tool tip. The model predicted the maximum strain as 1.65 at the tool tip (Fig. 5.4b) and the strain decreased along the cutting line from the tool tip in the X-direction. Numerically predicted depth of deformed zone and length of the primary deformation zone (from tool tip to chip root) were 35 µm and 400 µm respectively.

5.2.1.4. Stress Distribution

The stress distribution in the workpiece model is shown in Fig. 5.5a. Fig. 5.5b depicts the contours of stress distribution in the workpiece model. It was observed that the maximum predicted stress was generated in the PDZ of the workpiece. The model predicted the maximum stress as 1464 MPa at the primary deformation zone (Fig. 5.5b).

5.2.1.5. Temperature Distribution

Fig. 5.6a represents the temperature profile and Fig. 5.6b depicts the temperature distribution contours in the workpiece ahead of the tool tip. It was observed that the

maximum temperature was generated in the material at the tool tip and also in the secondary deformation zone (SDZ). The maximum predicted temperature was 1222 K occurred during machining of Ti-6Al-4V alloy at 63.5 m/min cutting speed and 0.25 mm/rev feed rate.

5.2.1.6. Cutting Force Prediction

The force that is required to move the tool to the workpiece in the X-direction is equal to the cutting force for that machining condition. Fig. 5.7 depicts the variation of cutting force per unit thickness with time. Due to the formation of segmented chips, the force varied in a long range. The predicted average cutting force was 245.5 ± 88.2 N/mm measured from the stable force zone.

5.2.2. Smoothed-particle hydrodynamics (SPH) formulation

Serrated chips were also formed using Smoothed-particle hydrodynamics (SPH) formulation implementing the Johnson-Cook material model with damage criteria.

5.2.2.1. Energy Balance

The energy balance typical of simulations performed with Smoothed-particle hydrodynamics (SPH) formulation is shown in Figure 5.8. The total energy was composed of internal energy stored in the deformed workpiece and kinetic energy of the moving tool and workpiece. In this case, the total energy of the system was almost equivalent to the external work. The sliding and hourglass energies were negligible, confirming that neither hourglass deformation nor penetration occurred. The energy ratio

was 1.0 throughout the simulation, which established the results are valid with respect to the energy balance.

5.2.2.2 Deformation of the Workpiece

Similar to the 2D Lagrangian element formulation method, excessive deformation was occurred in the workpiece at the tool tip for smoothed-particle hydrodynamics (SPH) formulation (Fig. 5.9a). Fig. 5.9b depicts that excessive deformation is occurred in the workpiece at the tool tip. Large amount of deformation is also occurred at the PDZ.

5.2.2.3. Strain Distribution

The strain distribution in the workpiece model is shown in Fig. 5.10a. Fig. 5.10b depicts the contours of strain distribution in the workpiece model. The maximum strain (1.6) was generated in the workpiece ahead of the tool tip. The strain value decreased along the cutting line from the tool tip in the X-direction. Numerically predicted depth of deformed zone and length of the primary deformation zone (from tool tip to chip root) using the SPH formulation, were 24 µm and 380 µm respectively.

5.2.2.4. Stress Distribution

The stress distribution in the workpiece model is shown in Fig. 5.11a. The contours of stress distribution in the workpiece model are shown in Fig. 5.11b. It was observed that the maximum predicted stress was generated in the PDZ of the workpiece. The model predicted the maximum stress as 1736 MPa at the tool tip.

5.2.2.5. Temperature Distribution

Fig. 5.12a represents the temperature profile in the model. The temperature distribution contours in the workpiece ahead of the tool tip are shown in Fig. 5.12b. It was observed that the maximum temperature was generated in the material at the tool tip and also in the secondary deformation zone (SDZ). The maximum predicted temperature was 892 K occurred during machining of Ti-6Al-4V alloy at 63.5 m/min cutting speed and 0.25 mm/rev feed rate.

5.2.2.6. Cutting Force Prediction

Fig. 5.13 depicts the variation of cutting force per unit thickness with time during machining of Ti-6Al-4V alloy at 63.5 m/min of cutting speed and 0.25 mm/rev of feed rate using SPH formulation. The force varied in a long range due to the formation of segmented chips. The predicted average cutting force is 307.9 ± 93.2 N/mm measured from the stable force zone.

5.2.3. Machining at higher cutting speed

The model developed using the 2D Lagrangian element formulation was used to simulate the machining of Ti-6Al-4V alloy at higher cutting speed. In this case the cutting speed was 1500 RPM or 120 m/min. It was predicted that the maximum strain in the material ahead of the tool tip was 1.80 and the temperature at the tool tip was 1288 K or 1015 ˚C for the cutting condition of 120 m/min of cutting speed and 0.25 mm/rev of feed rate. The predicted average shear band frequency or the distance between two shear

bands and the average cutting force measured from the stable force zone, are 128.4 ± 8.2 μm and 238.1 ± 95.2 N/mm respectively.

5.2.4. Effect of Friction

The friction between the tool and the workipiece is an important issue during machining. In this case, different friction values ($\mu = 0.0$, $\mu = 0.3$, $\mu = 0.6$ and $\mu = 0.99$) were assigned into the numerical model and the effect of friction was observed. It was observed that the temperature at the tool tip depended on the friction value. The predicted temperature at the tool tip was 1020 K (747 ˚C) for zero friction value. However, the predicted temperature for high coefficient value (0.99) was 1255 K (982 ˚C) at the tool tip (Fig. 5.14).

It was also observed that the strain at the tool tip also varied with increasing the COF value. The strains at the tool tip were 1.40, 1.48, 1.65 and 1.80 for the friction values of 0.0, 0.30, 0.60 and 0.99. The strain at the tool tip increased with the friction value assigned at the contact between tool and workpiece (Fig. 5.15). From the strain value, the surface roughness value of the machined surface can also be predicted using the Fig. 4.33.

FIGURES- CHAPTER 5
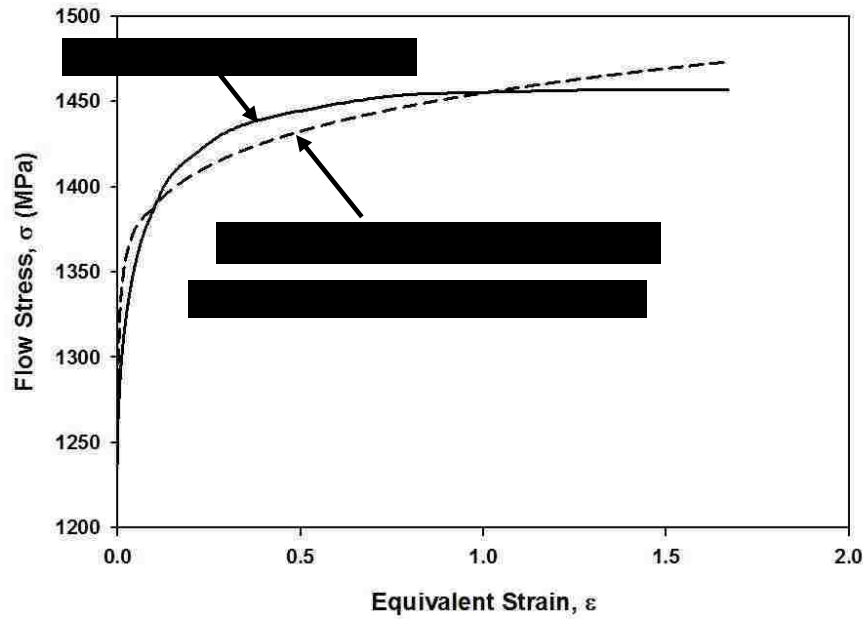
Fig. 5.1. Experimental stress-strain curve fitted with power law curve where the R^2 value

is 0.95.
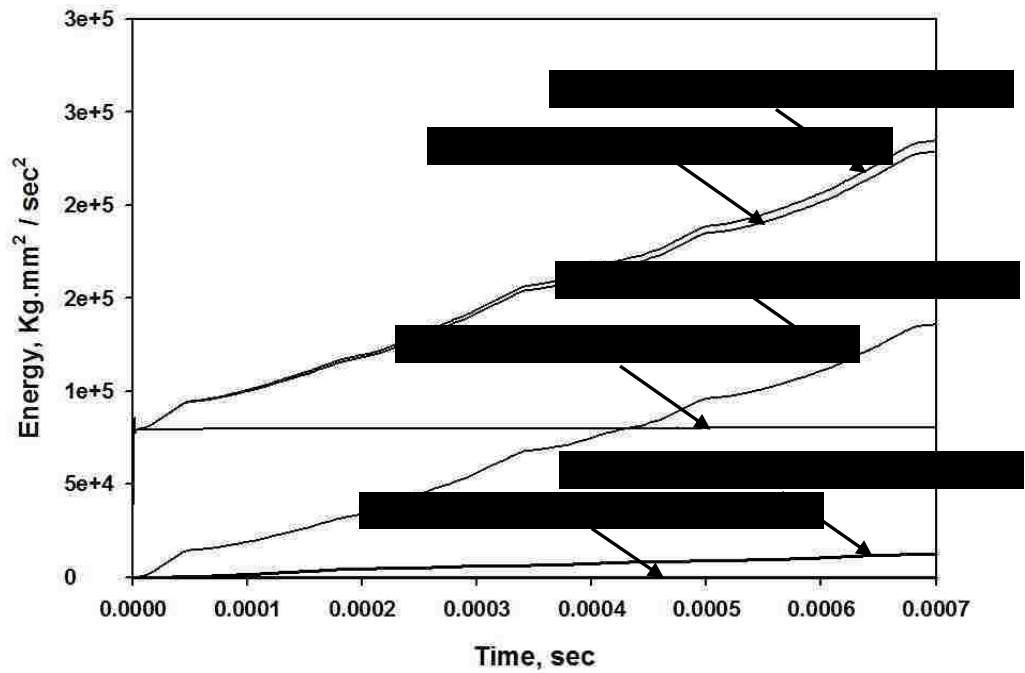
Fig. 5.2. Energy balance of serrated chip formation simulation using 2D Lagrangian

element formulation.
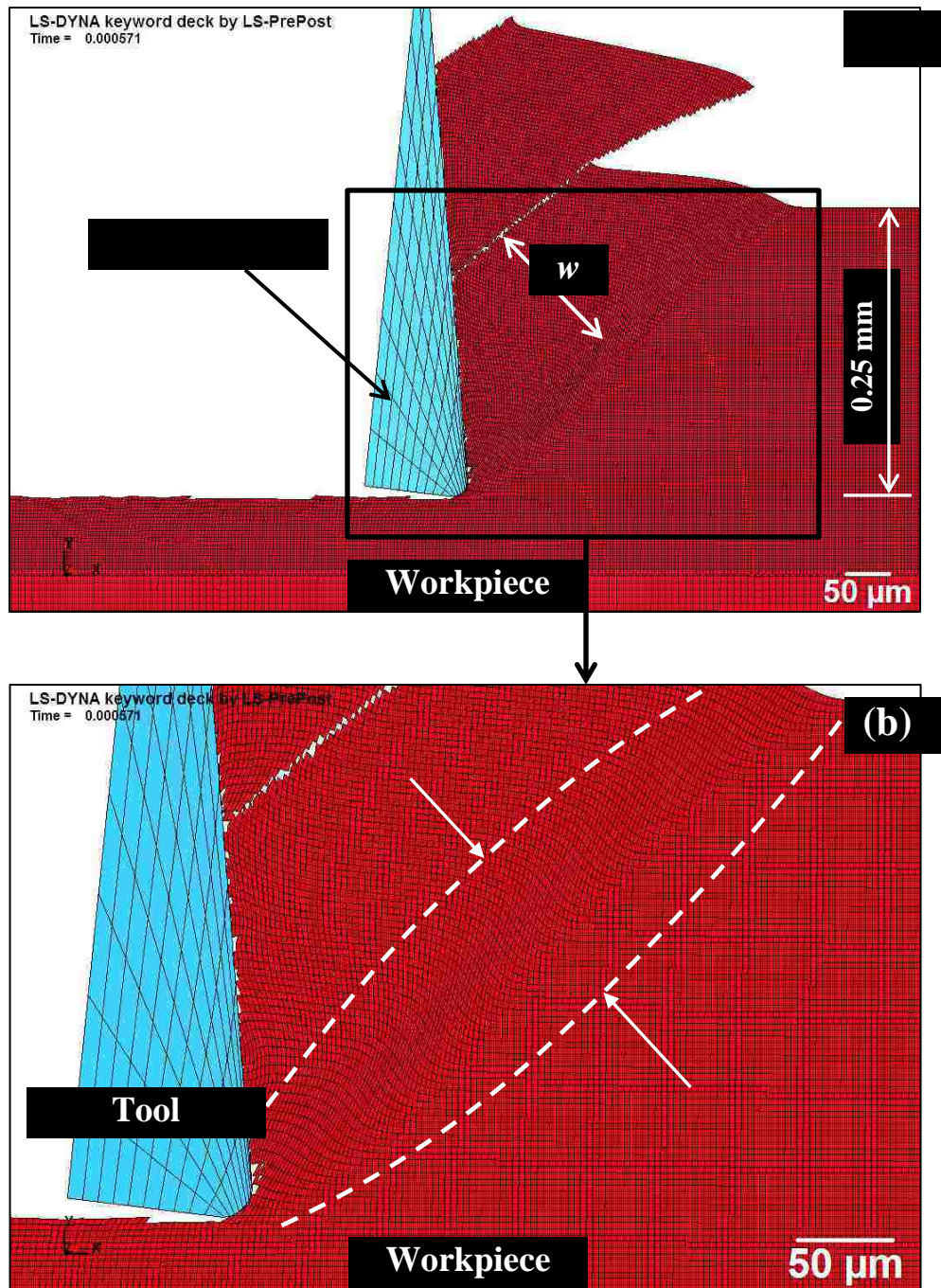
Fig. 5.3. (a) Serrated chips formation in simulated orthogonal cutting using Johnson-Cook material model, where w is the width of the chip which is equal to the shear band frequency, (b) Close view of PDZ.
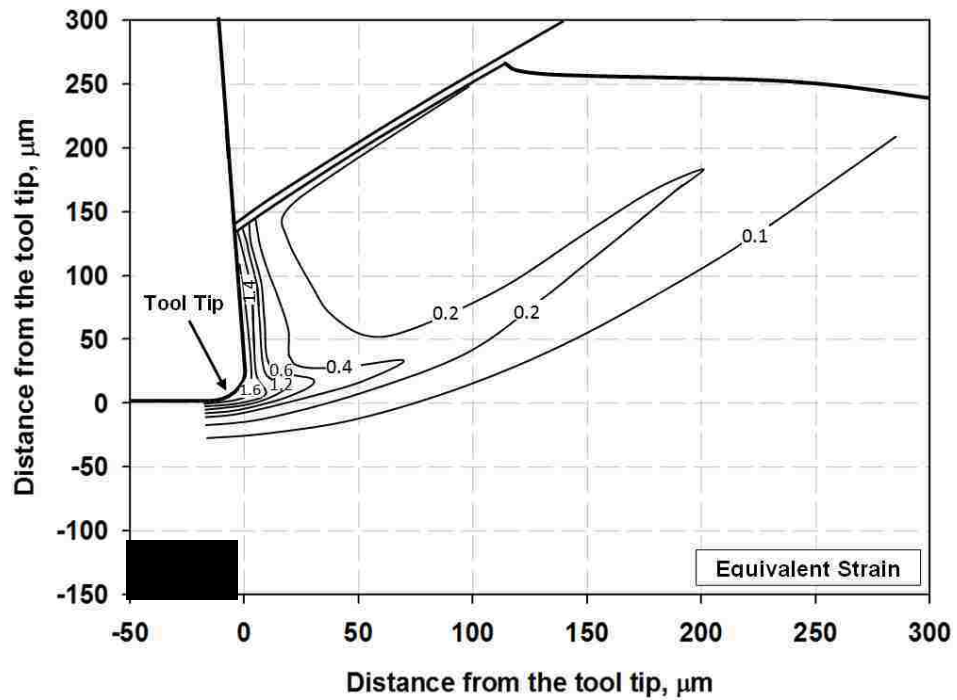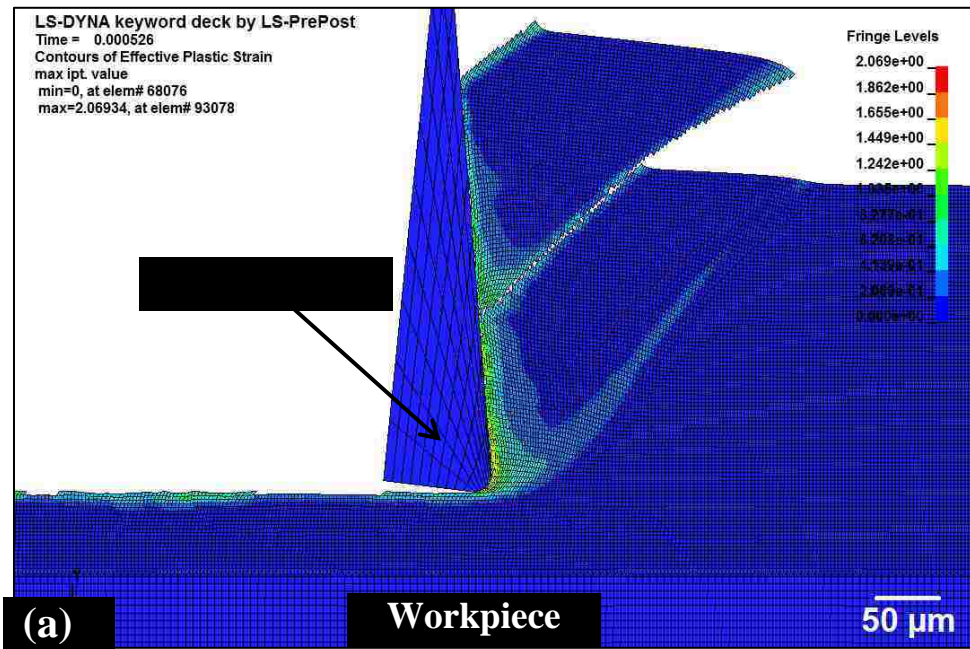
Fig. 5.4. (a) Strain distribution diagram, (b) Schematic strain distribution diagram in the material ahead of the tool tip for the cutting condition of 63 m/min of cutting speed and 0.25 mm/rev of feed rate.
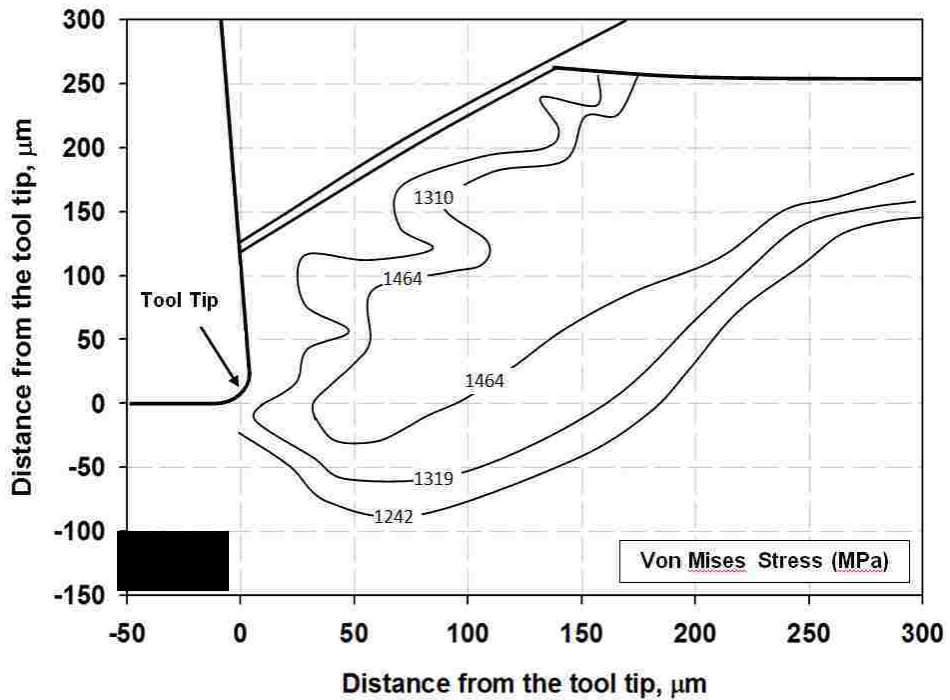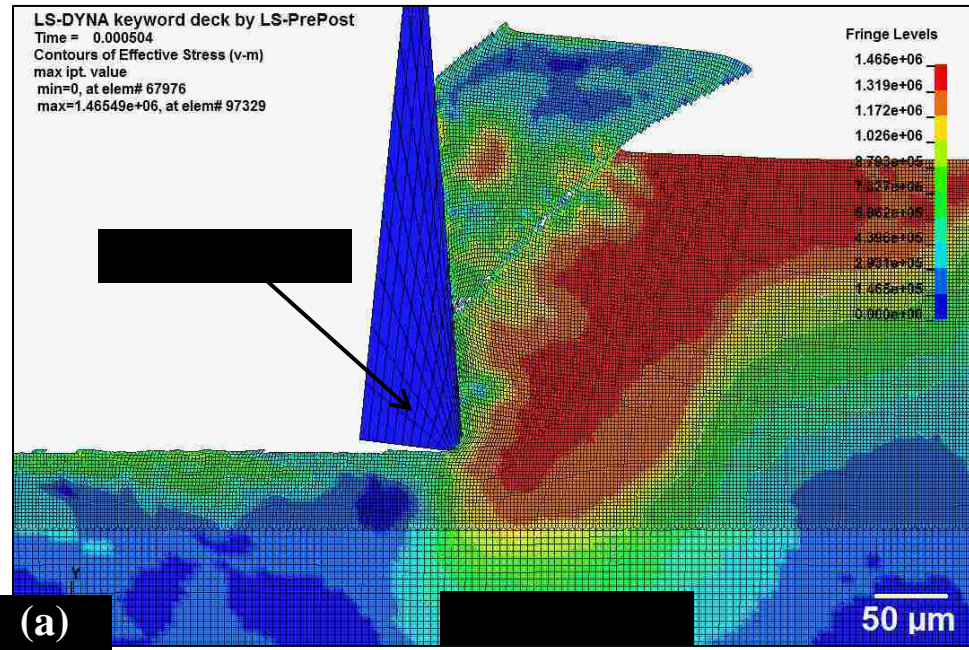
Fig. 5.5. (a) Stress distribution diagram (in units of Kg/mm/s^2), (b) Schematic stress distribution diagram in the material ahead of the tool tip for the cutting condition of 63 m/min of cutting speed and 0.25 mm/rev of feed rate.
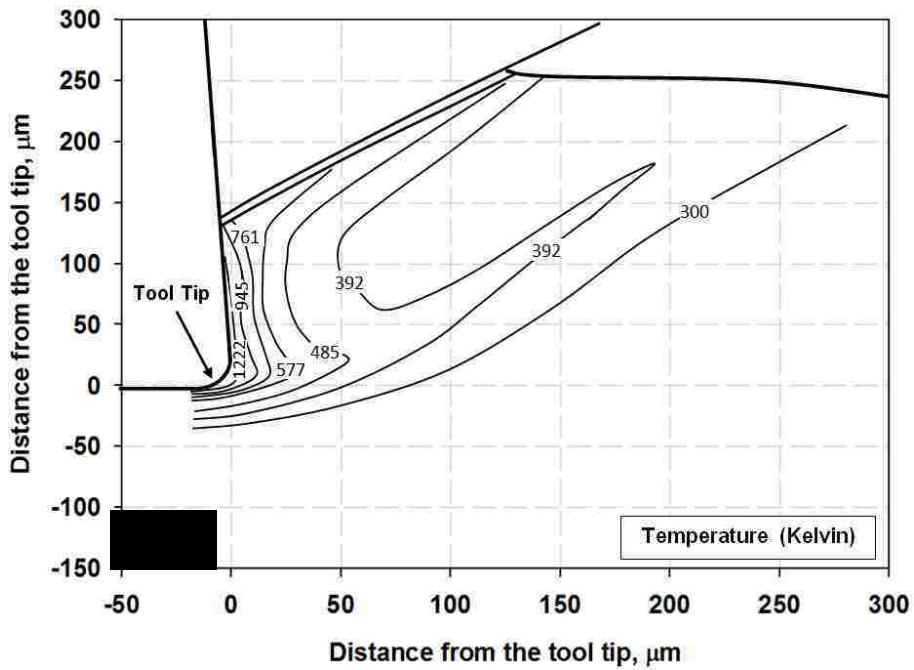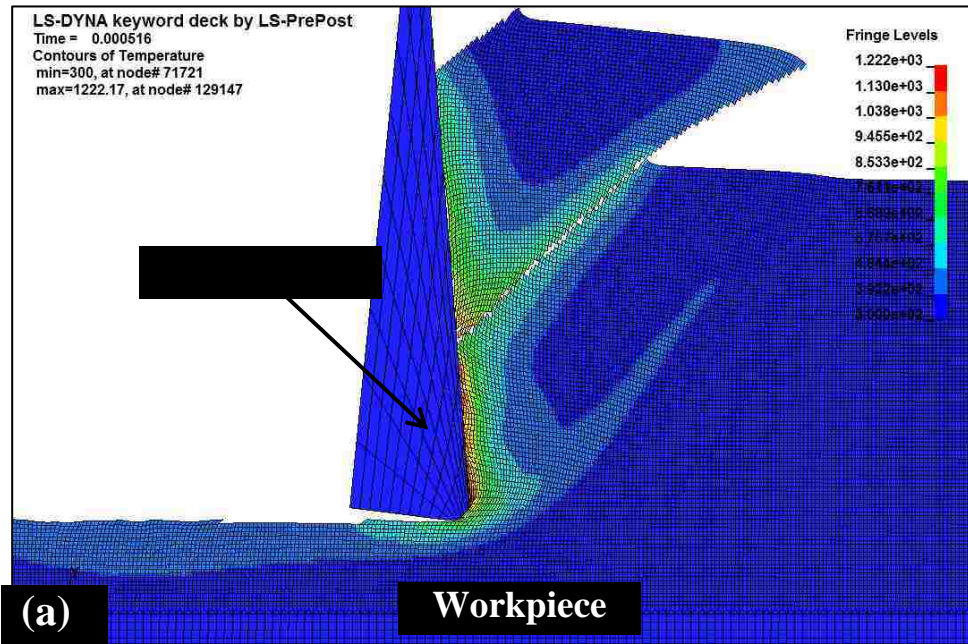
Fig. 5.6. (a) Temperature distribution diagram (in unit of Kelvin), (b) Schematic temperature distribution diagram in the material ahead of the tool tip for the cutting condition of 63 m/min of cutting speed and 0.25 mm/rev of feed rate.
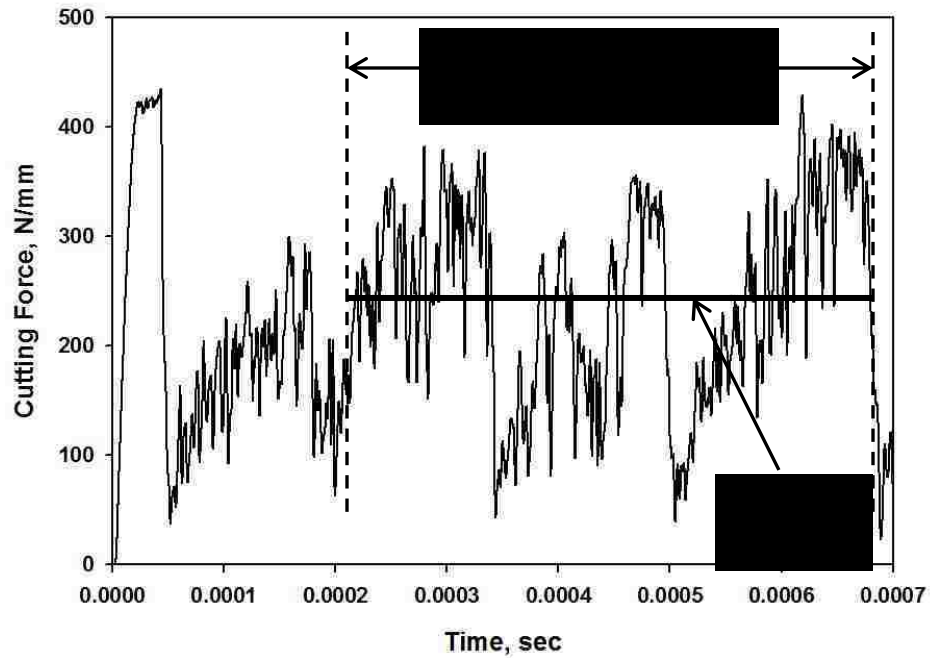
Fig. 5.7. Variation of cutting force per unit thickness with time for the cutting condition

of 63 m/min of cutting speed and 0.25 mm/rev of feed rate.
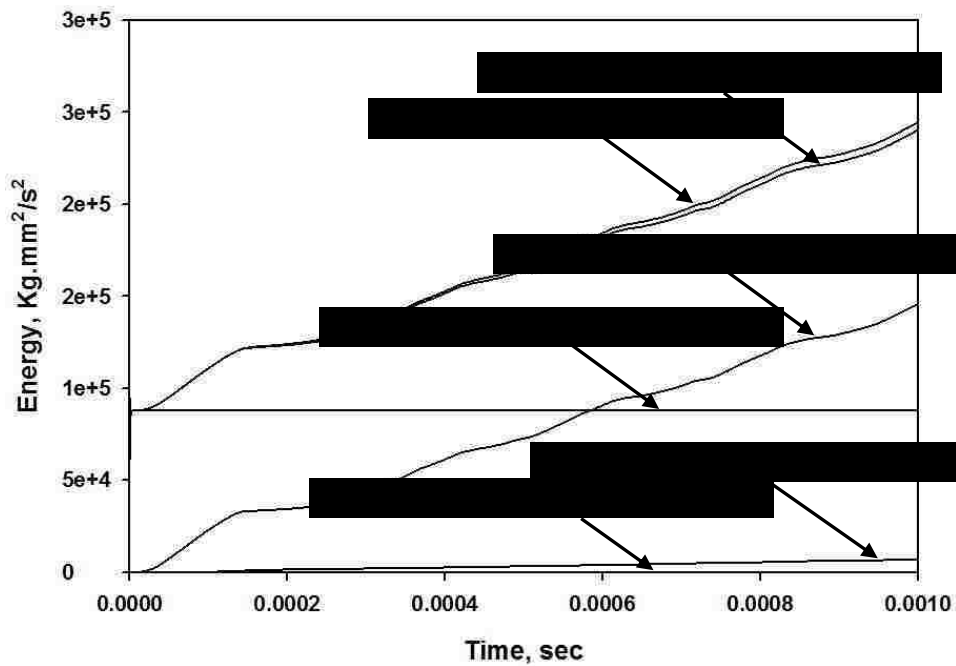
Fig. 5.8. Energy balance of serrated chip formation simulation using Smoothed-particle

hydrodynamics (SPH) formulation.
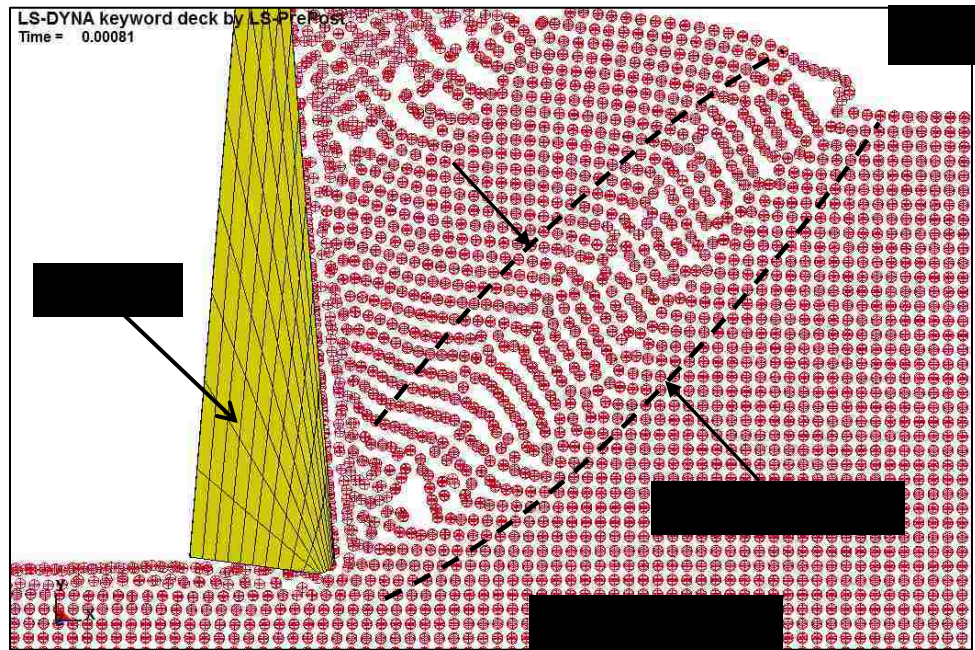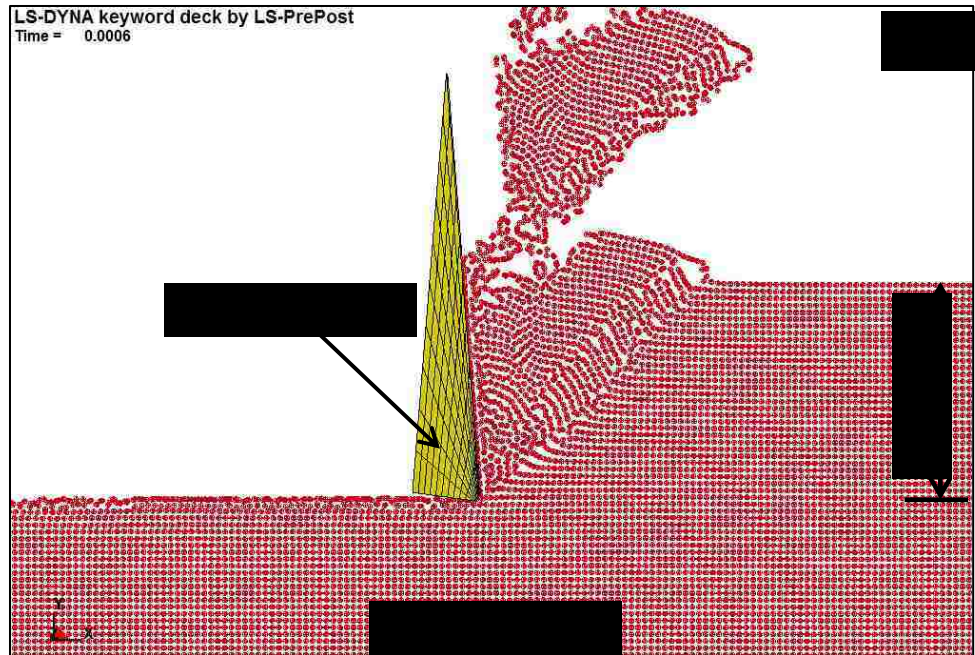
Fig. 5.9. (a) Serrated chips formation in simulated orthogonal cutting using Smoothed-particle hydrodynamics (SPH) formulation with Johnson-Cook material model, (b) Close view of PDZ.
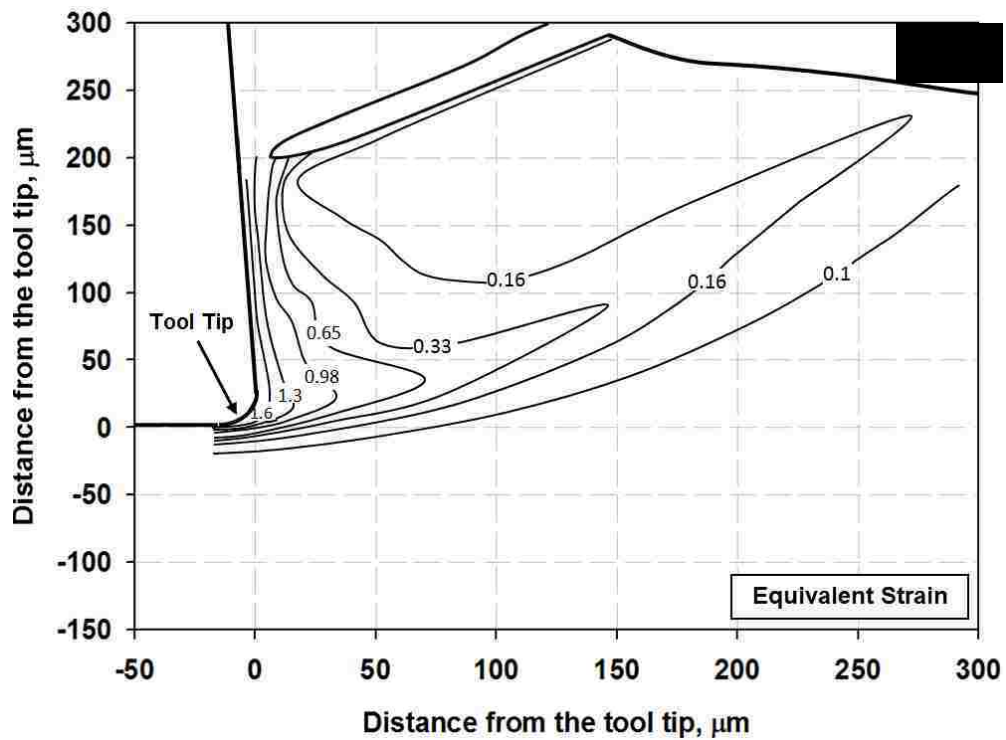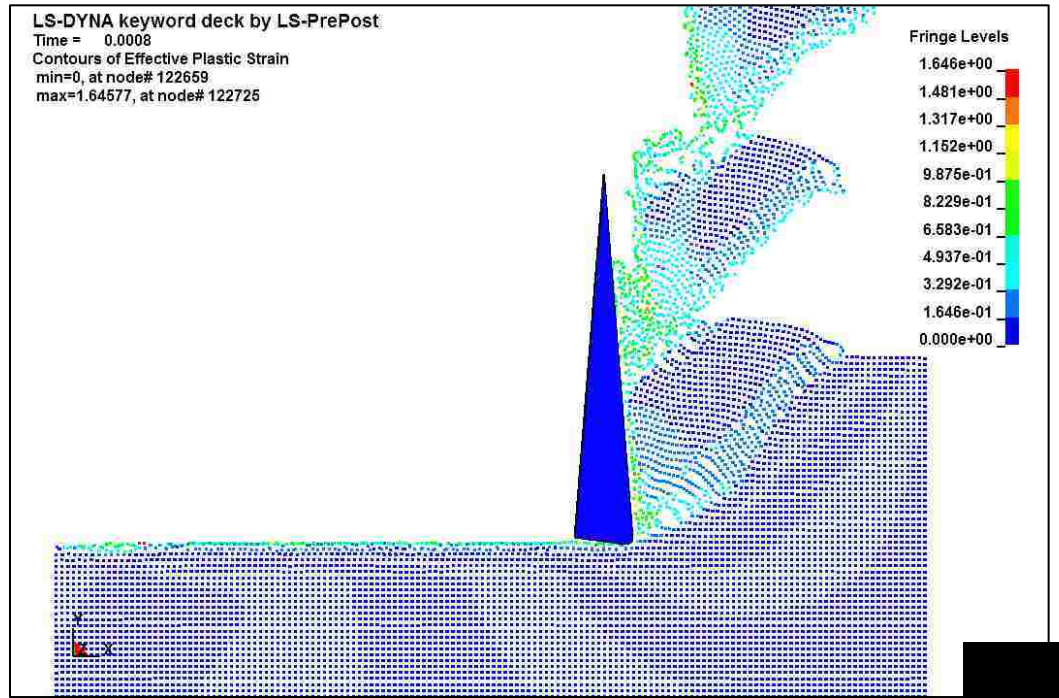
Fig. 5.10. (a) Strain distribution diagram, (b) Schematic strain distribution diagram in the material ahead of the tool tip for the cutting condition of 63 m/min of cutting speed and 0.25 mm/rev of feed rate using the SPH formulation.
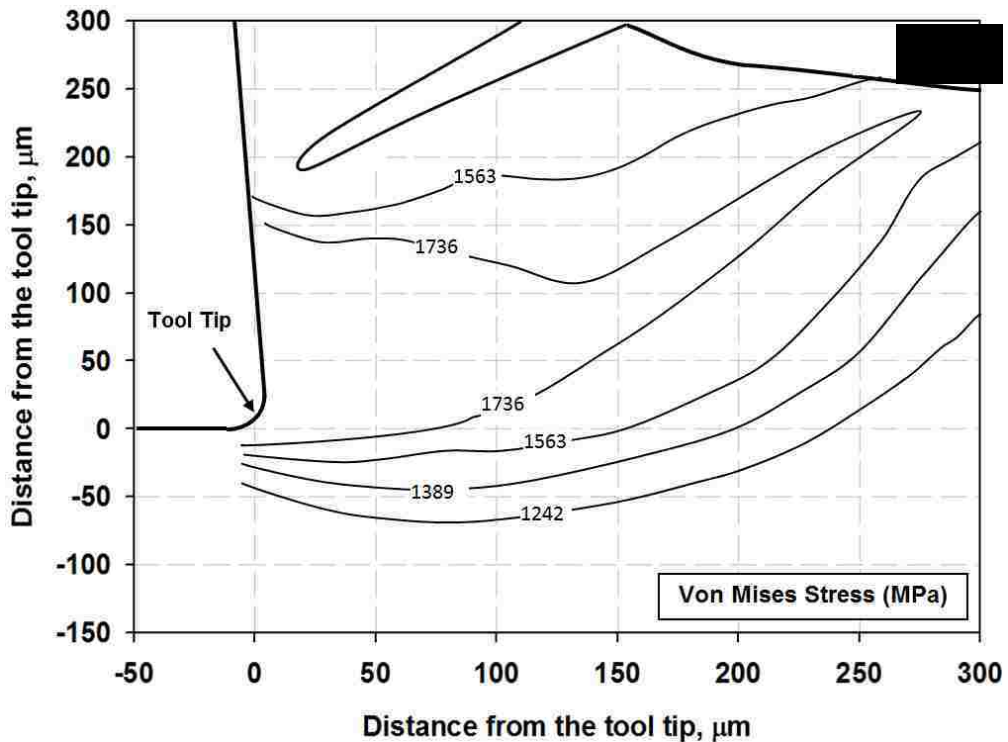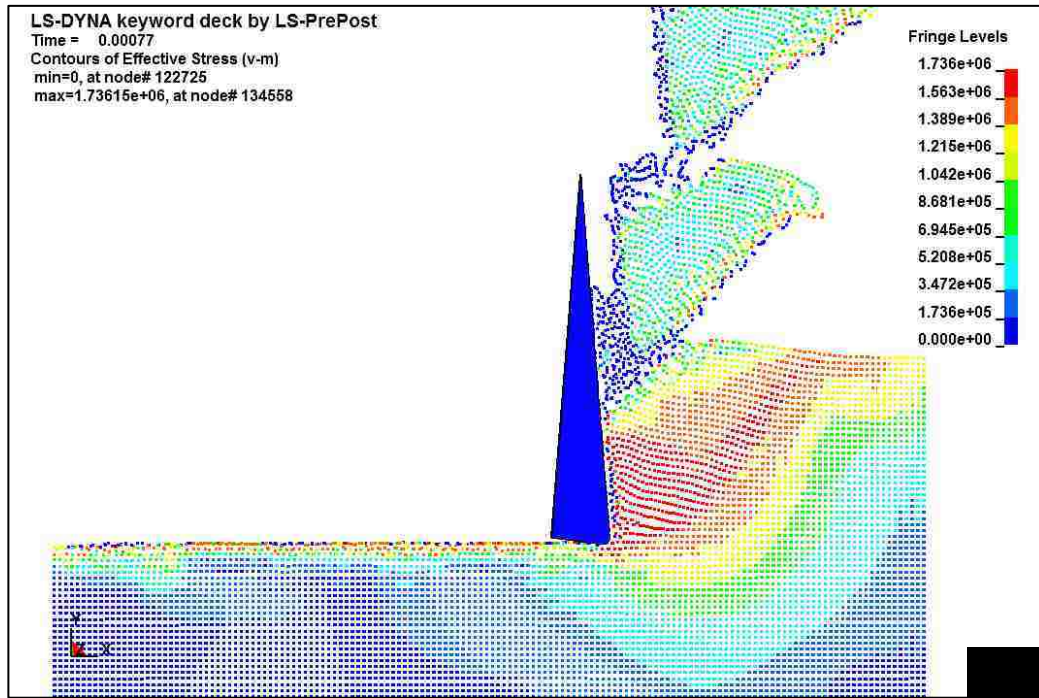
Fig. 5.11. (a) Stress distribution diagram (in unit of Kg/mm/s^2), (b) Schematic stress distribution diagram in the material ahead of the tool tip for the cutting condition of 63 m/min of cutting speed and 0.25 mm/rev of feed rate using the SPH formulation.
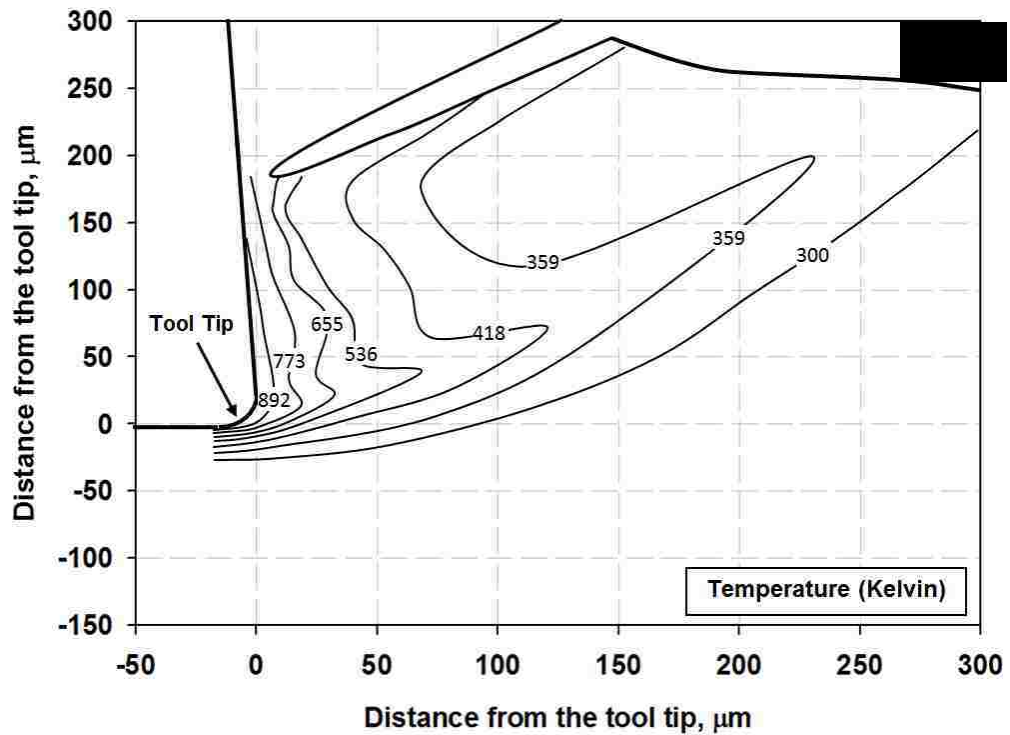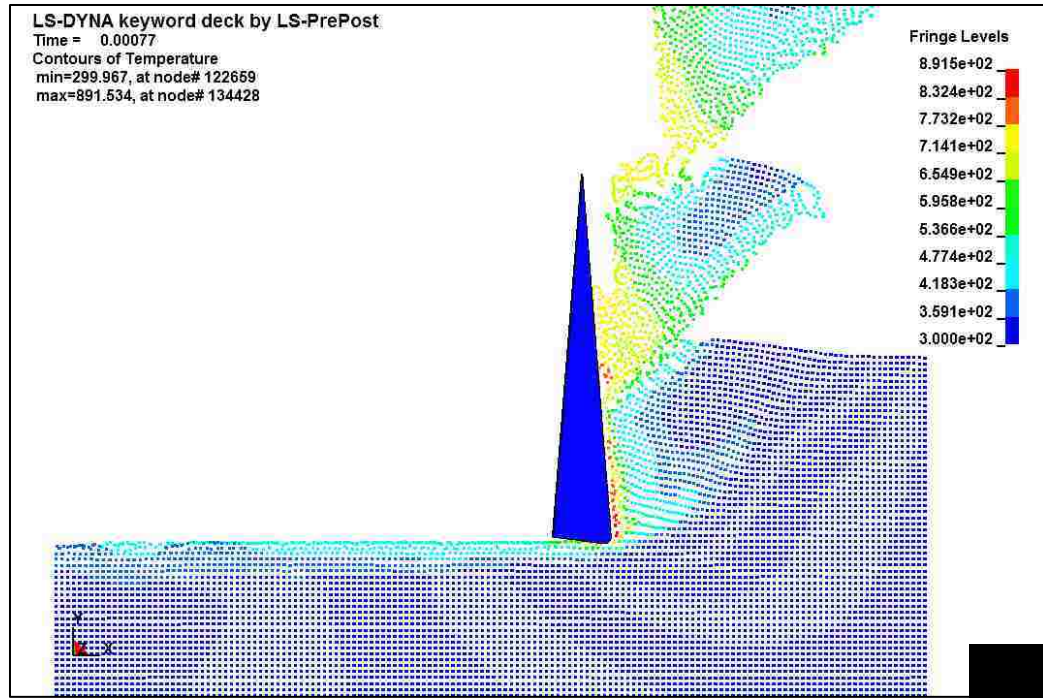
Fig. 5.12. (a) Temperature distribution diagram (in unit of Kelvin), (b) Schematic temperature distribution diagram for the cutting condition of 63 m/min of cutting speed and 0.25 mm/rev of feed rate using the SPH formulation.
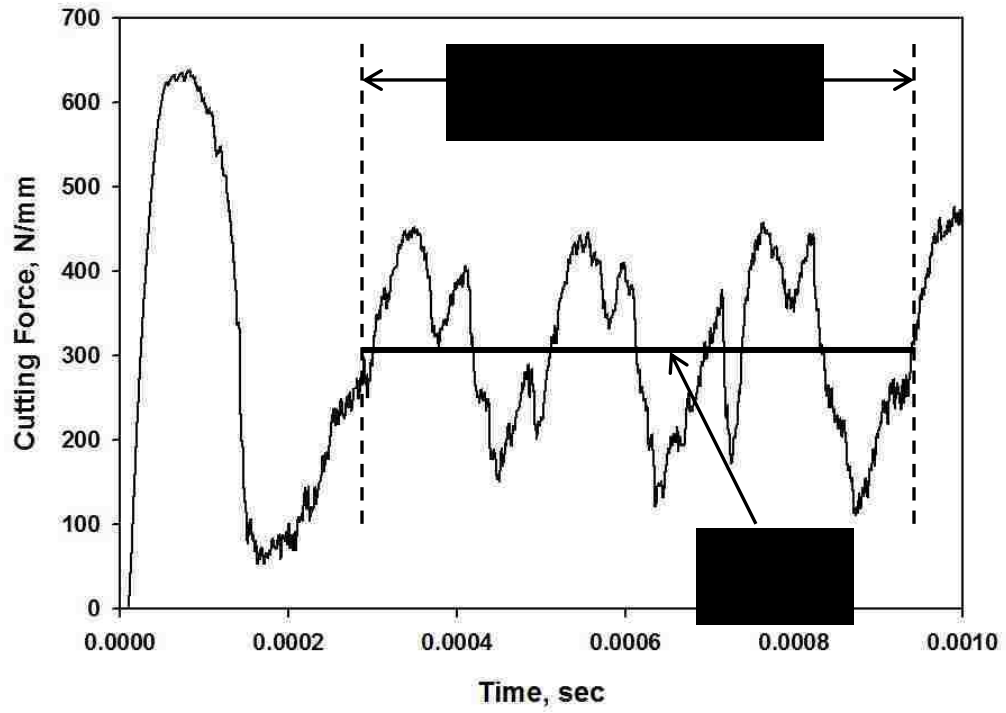
Fig. 5.13. Variation of cutting force per unit thickness with time for the cutting condition of 63 m/min of cutting speed and 0.25 mm/rev of feed rate using the SPH formulation.
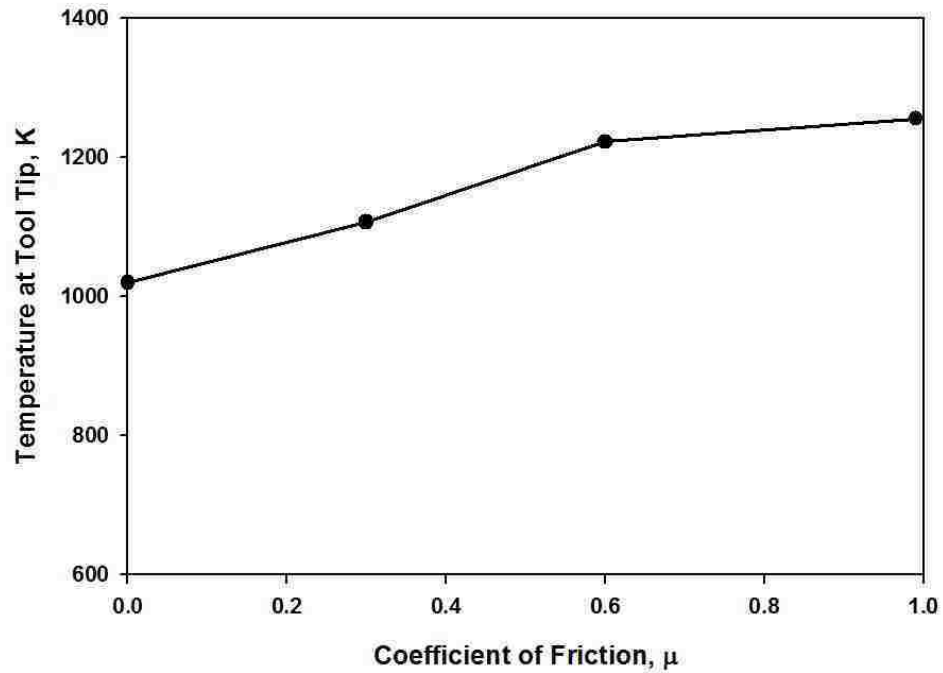
Fig. 5.14. Diagram showing the effect of friction on the temperature at the tool tip.
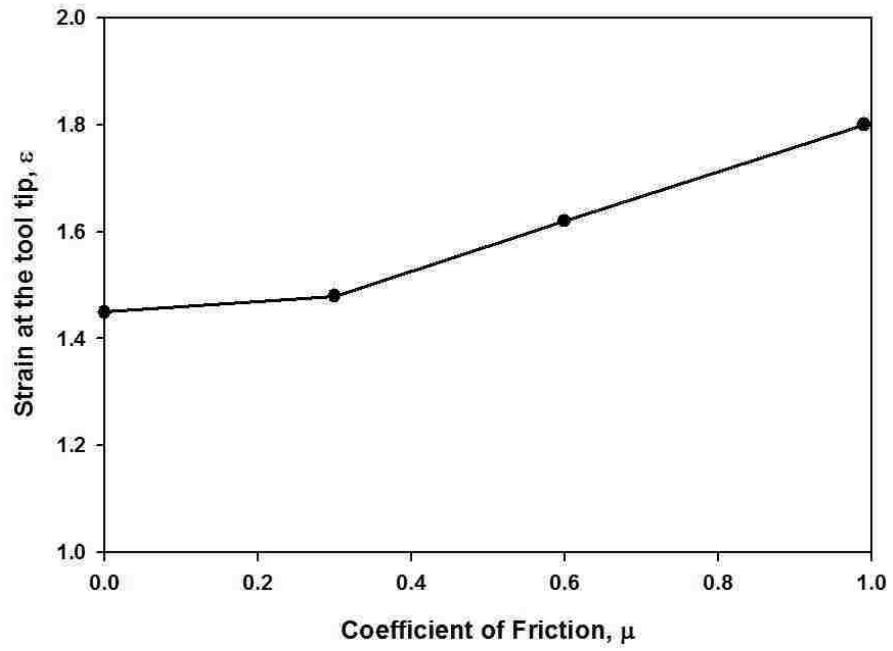
Fig. 5.15. Diagram showing the effect of friction on the strain at the tool tip.

CHAPTER 6: Discussion

6.1. Introduction

Orthogonal cutting of Ti-6Al-4V alloy, which produced serrated chips, was studied by machining the alloy under different cutting condition to assess the effects of machining parameters such as the feed rate and cutting speed. The effect of feed rate and cutting speed on the machining forces, chip morphology, subsurface deformation zone, the surface quality and temperature at the tool tip, is discussed in this chapter. The comparison between experimental results and the numerical results is also presented in this chapter.

6.2 Cutting and Thrust Force Measurements

Cutting and thrust forces were measured during orthogonal cutting of the Ti-6Al-4V alloy at different cutting conditions. It was found that the cutting force and thrust forces varied with the cutting conditions (Fig. 4.5). It was observed as noted in section 4.2.3, that the cutting force per unit depth of cut, ranged from approximately 157 N/mm to 388 N/mm. It was reported in the literature that the cutting force for the cutting condition of 43.2 m/min and 0.10 mm/rev feed rate was 175 N/mm [183]. However, the measured cutting force under the same cutting condition was 160 N/mm which was approximately equal to the reported value. This showed that the force responses are within the acceptable range.

Fig. 4.5a illustrates that the cutting and thrust forces increased with an increase in feed rate. Cutting force increased almost linearly with the feed rate. With the increase in feed, material removal rate ($Q = V_c fd$, where V_c is the cutting speed, f is the feed rate and d is the depth of cut), and hence the rate of plastic deformation, increases resulting in increase in the cutting force [184]. However, the temperature was increased with the feed rate. The effect of temperature was less to reduce the forces.

The variation of cutting force and thrust force with the cutting speed is illustrated in Fig. 4.5b. Observations indicate that the cutting and thrust forces decrease with the cutting speed. Machining at higher speed generates higher temperature at the tool tip compared to the machining at lower speed. Due to the increment of temperature at the tool tip, the forces required for removing metal and forming chip are also decreased [185,186].

During machining of the Ti-6Al-4V alloy the force responses fluctuated in magnitude. It was suggested that the fluctuation was occurred due to the cyclic generation of the shear bands in the chips during machining [15]. Vibration in tool and lathe also influenced the fluctuation.

6.3 Surface Quality of the Machined Surface

Surface profilometer, WYKO images and corresponding SEM images of the machined surface for different feed rates (Fig. 4.29(a-d)) and different cutting speeds (Fig. 4.30 (a-d)) confirmed that the surface quality depended on the cutting conditions. It was observed that the temperature at the tool tip increased with increasing the feed rate

and cutting speed (Fig. 4.65). Due to the increment of temperature, the depth of deformed zone and the maximum strain generated at the machined surface or the strain gradient increased. Surface roughness was observed to increase with feed rate and cutting speeds due to the strain gradient and the depth of deformed zone. A linear relationship was found between the surface roughness and the depth of deformed zone. However, the surface roughness was also increased linearly with the shear band frequency.

For low feed such as 0.10 mm/rev, the temperature at the tool tip was 900 K (627 ˚C), the depth of deformed zone was 30 μm, maximum strain below the machined surface is 1.1 and the surface roughness is 210 nm. However for high feed such as 0.25 mm/rev, the temperature at the tool tip was 1125 K (852 ˚C), the depth of deformed zone was about 52 μm, maximum strain below the machined surface was 1.5 and the surface roughness is 440 nm. High temperature increased the depth of deformed zone and strain gradient or strain below the machined surface. These factors influenced the surface roughness or decreased the surface quality.

The importance of the surface roughness value depends on the application of the machined products. If the acceptable limit of the surface roughness is 500 nm, in that case, all the cutting conditions can be applied. However, in case of productivity, the most suitable cutting condition would be of 63.5 m/min cutting speed and 0.25 mm/rev feed rate due to the low cutting force, low specific cutting energy and high productivity.

6.4. Chip Morphology and Adiabatic Shear Band Formation

Figures 4.13 and 4.14 confirmed that the serrated chips were formed during machining of Ti-6Al-4V alloy under the different cutting conditions used in this research. According to Eq. 2.22, the criteria for catastrophic slip can be written as:

$$0 \leq \frac{\frac{\delta\sigma}{\delta\varepsilon}}{-\frac{\delta\sigma}{\delta T}\frac{dT}{d\varepsilon}} \leq 1 \tag{2.22}$$

In Eq. 2.22, if the ratio between the strain hardening and thermal softening is in between zero and 1, the material will shear catastrophically and shear band will be formed.

For the cutting conditions of 63.5 m/min and 0.25 mm/rev, the average work hardening rate $\left(\frac{\delta\sigma}{\delta\varepsilon}\right)$ for the flow stress between 1400 MPa and 1440 MPa was 223 MPa obtained from Fig. 4.53b. The corresponding $d\varepsilon$, $\delta\sigma$ and δT values were 0.16, -40 MPa and 83 K obtained from Figures 4.35, 4.43 and 4.58 respectively (value difference from (50 μm, 0 μm) to (100 μm, 0 μm)). The calculated value of the ratio between the strain hardening and thermal softening or, $(\frac{\frac{\delta\sigma}{\delta\varepsilon}}{-\frac{\delta\sigma}{\delta T}\frac{dT}{d\varepsilon}})$ was 0.89 which satisfied the formation of adiabatic shear band criterion. Adiabatic shear bands were formed as the thermal softening predominated over the strain hardening. Similar procedure was applied for the other cuttings conditions and it was found that the criterion was satisfied shown in Table 6.1. However, the SEM image of the shear band (Fig. 4.12) also confirmed that the serrated chips were formed due to the formation of adiabatic shear bands. The ratio

between the strain hardening and thermal softening for aluminum and copper were also determined (discussed in Appendix D) and the values were greater than 1. For this reason, the shear band was absent in aluminum and copper in that cutting conditions.

Table 6.1. Important properties of different metals [40-45]**.**

Machining Conditions	$\dfrac{\dfrac{\delta\sigma}{\delta\varepsilon}}{-\dfrac{\delta\sigma}{\delta T}\dfrac{dT}{d\varepsilon}}$	SB formation criteria satisfied or unsatisfied
0.10 feed rate & 43.2 m/min	0.96	Satisfied
0.15 feed rate & 43.2 m/min	0.91	Satisfied
0.20 feed rate & 43.2 m/min	0.86	Satisfied
0.25 feed rate & 43.2 m/min	0.71	Satisfied
0.25 feed rate & 14.4 m/min	0.87	Satisfied
0.25 feed rate & 29.6 m/min	0.77	Satisfied
0.25 feed rate & 43.2 m/min	0.71	Satisfied
0.25 feed rate & 63.5 m/min	0.89	Satisfied

Semiatin and Rao [75], suggested the flow localization parameter for the formation of adiabatic shear band. The flow localization parameter can be defined as [76]:

$$\beta = -\frac{\sqrt{3}}{m}\left[\frac{n}{\gamma} + \frac{0.9\left(\frac{\delta\tau}{\delta T}\right)}{\rho c\left(1+1.328\sqrt{\frac{k\gamma}{Vf}}\right)}\left(n+1-\frac{0.664\sqrt{\frac{k\gamma}{Vf}}}{1+1.328\sqrt{\frac{k\gamma}{Vf}}}\right)\right] \tag{6.1}$$

where, m is the strain rate sensitivity, c is the heat capacity and k is the thermal diffusivity. The flow localization parameter depends on the cutting speed and feed rate. For the formation of shear localization in the Ti-6Al-4V alloy, the critical value of chip load which is defined by (feed × cutting speed) or Vf is 0.004 m^2/min [76].

In this research, the chip load values for the cutting conditions such as cutting speed cutting speed 43.2 m/min and feed rate 0.10 mm/rev, 43.2 m/min and feed rate 0.15 mm/rev, cutting speed 43.2 m/min and feed rate 0.20 mm/rev, cutting speed 43.2 m/min and feed rate 0.25 mm/rev, cutting speed 29.6 m/min and feed rate 0.25 mm/rev, and cutting speed 63.5 m/min and feed rate 0.25 mm/rev were 0.0043 m^2/min, 0.0065 m^2/min, 0.0086 m^2/min, 0.0108 m^2/min, 0.0074 m^2/min and 0.0159 m^2/min respectively. All these values were higher than the critical chip load value (0.004 m^2/min) and shear localizations were observed. However, shear localization was also observed for the cutting condition of 43.2 m/min cutting speed and 0.10 mm/rev feed rate which had the chip load value 0.0036 m^2/min (<0.004 m^2/min). Shear localization was observed in this cutting condition as the chip load value was close to the critical value.

Chip thickness (Fig. 4.15), shear band frequency or the average distance between the center-line of two consecutive shear bands (Fig. 4.17) and shear band width (Fig. 4.22) varied with the machining parameters such as feed rate and cutting speed. As the cutting speed and the feed rate increased the maximum temperature at the tool tip also increased (Fig. 4.65). Due to the large thermal gradient, the chip thickness as well as the shear band frequency and the shear band width increased with the feed rate and cutting speed [102]. However, the obtained values were identical with the literature [104].

6.5. Study of Plastic Deformation by Stress-Strain Estimation

The effect of feed rate and cutting speed on the stress-strain curve was also studied. It was found that the value of saturation stress increased with the cutting speed (Fig. 4.52) or the strain rate ($\dot{\varepsilon} = V_c/L$, where L is the length of deformed zone). As Ti-6Al-4V alloy is a strain rate sensitive material [33], the saturation stress increases with increasing the strain rate. The value of strain rate sensitivity, c, of Ti-6Al-4V alloy is low (c = 0.012) and in this case the cutting speed varied within a short range or the strain rate varied form 800 s^{-1} to 3525 s^{-1}. For these reasons the saturation stress varied within a short range from 1442 MPa to 1457 MPa for the cutting speed from 14.6 m/min to 63.5 m/min respectively.

It was also found that the saturation stress varied within a short range (from 1440 MPa to 1452 MPa) for different feed rates (Fig. 4.51). In this case, the material was deformed at a constant speed. A close observation of the stress-strain curves for different feed rate suggested that the deformation behaviour of Ti-6Al-4V alloy was independent of feed rate. However, it is also suggested in the literature that the saturation stress or the deformation behaviour is independent of feed rate during metal cutting [187].

6.6. Temperature at the Tool Tip

A large portion of the work done during the plastic deformation of the workpiece is transformed into heat to produce a temperature increase (ΔT) in the work material. The temperature distribution diagram in the material ahead of the tool tip for different cutting conditions (Figures 4.58-4.64) revealed that the temperature at the tool tip varied with the

207

cutting parameters such as cutting speed and feed rate. Material removal rate or the plastic deformation of the workpiece increased with the feed rate and cutting speed and for this reason the temperature gradient or tool tip temperature also increased. However, the temperature at the tool tip for Ti-6Al-4V alloy for machining at 43.2 m/min cutting speed and 0.25 mm/rev feed rate was higher (1125 K or 852 ˚C) compared to the temperature (517 K or 244 ˚C) for aluminum 1100 for machining at 36 m/min cutting speed and 0.30 mm/rev feed rate [28]. The temperature distribution diagrams also illustrate that the temperature gradients are steep and the heat-affected zone is small due to the low thermal conductivity of the Ti-6Al-4V alloy (Table. 2.1).

However, the experimentally measured temperatures (Fig. 4.66) at the tool tip were lower than the calculated value due to the low thermal conductivity of the carbide tool and moreover the thermocouple was placed approximately 1 mm away from the tool edge. Transferred material was observed at the tool edge due to adhesion. It was confirmed using EDS (Fig. 4.72) that the transferred material was the workpiece material (Ti-6Al-4V alloy). The amount of transferred material was increased with an increase in the cutting speed (Fig. 4.73) due to the temperature increment.

6.7. Temperature and Hardness of the Shear Band

The temperature within the shear band was greater than the $(\alpha + \beta)/\beta$ transformation temperature (995±15 ˚C) [6], which indicated that transformed type adiabatic shear bands were formed during machining of Ti-6Al-4V alloy. However, for the cutting conditions of 43.2 m/min and 0.10 mm/rev feed rate, and 14.4 m/min and 0.25 mm/rev feed rate, the temperature within the shear were 1023 K (800 ˚C) and

1248 K (975 ˚C) respectively. Deformed shear band is formed and the shear strain value within the shear band was lower for these cutting conditions. The shear strain values were 6.5 and 8.5 for the cutting conditions of 43.2 m/min and 0.10 mm/rev feed rate, and 14.4 m/min and 0.25 mm/rev feed rate respectively. However, for the rest of the cutting conditions the temperature within the shear band was higher than the transformation temperature. As a result transformed shear band was formed and the shear strain within the shear band was higher (Fig. 4.23). However, for the phase transformation within the shear band, cracks were observed in the shear band. This crack was formed due to the volume mismatch. Volume mismatch occurred as the β phase (b.c.c. structure) transformed into α' matensite (h.c.p. structure) due to rapid cooling. The hardness of the crack tip was also measured and the value was high due to the plastic zone formation ahead of the crack tip.

Fig. 4.69 shows that the hardness value of the shear band was lower than the surrounding deformed grains. It was reported in the literature that the hardness of the shear band was up to $\sim$ 10 % lower than the adjacent deformed matrix for transformed shear band. In this case, the hardness of the shear band was 3.6 % lower than the adjacent deformed matrix which indicated the shear band formed during machining of Ti-6Al-4V alloy at the cutting speed of 63.5 m/min and feed rate of 0.25 mm/rev was 'transformed' shear band.

6.8. Comparison between Experimental and Numerical Results

An accurate model for orthogonal machining should be able to predict the strain, stress and temperature distributions in the material ahead of the tool tip, and the magnitudes of cutting forces accurately. In this research, the Johnson-Cook material model was used to represent the workpiece, where the most of the parameters of the Johnson-Cook material model were obtained from the experimental results. Although the chips were not separated or failed during experimental machining of Ti-6Al-4V alloy, failure criteria were used in numerical modeling to obtain the serrated chips under this research. However, cracks were observed at the end of the shear bands during chip formation (Fig. 4.12b).

For 2D Lagrangian element formulation the mesh size of the workpiece was small (3 µm × 3 µm). However for smoothed particle hydrodynamics (SPH) formulation, the distance between the two particles were 8 µm. The metal cutting simulation using 2D Lagrangian element formulation with mesh size of 8 µm × 8 µm was also performed and it was confirmed that the results were not affected by this mesh size. For the SPH formulation the initial number of neighbors per particles was also varied from 100 to 200 and confirmed that the results were not affected by this initial number of neighbors per particles.

The comparisons between the experimental and numerical results are discussed below.

6.8.1. Strain Distribution

Both the Lagrangian element formulation (Fig. 5.3) and Smoothed-particle hydrodynamics (SPH) formulations (Fig. 5.9) predicted the serrated chips during orthogonal cutting of Ti-6Al-4V alloy. Both the models predicted the maximum strain as 1.65 at the tool tip (Fig. 5.4 and Fig. 5.10) for the machining conditions of cutting speed of 63.5 m/min and feed rate of 0.25 mm/rev, which was identical with the experimental strain at the tool tip (Fig. 4.35). The strains decreased along the cutting line form the tool tip in the X-direction for both (experimental and numerical) cases. Experimentally obtained length of the primary deformation zone (from tool tip to chip root) was 400 μm while the numerically predicted length was 375 μm for both models. In the mid-section of the primary shear plane (175μm, 125μm), experimentally determined strain was 0.25 while the numerically predicted strain values were 0.17 and 0.20 for Lagrangian element formulation and SPH formulations respectively. The experimental depth of the deformed zone below the machined surface was 40 μm, where the predicted values were 35 μm and 25 μm for Lagrangian element formulation and SPH formulation respectively. However, both numerical strain distributions showed good overall correlation with the experimental strain distributions.

6.8.2. Stress Distribution

The experimental stress distributions (Fig. 4.43) showed that the maximum stress was 1457 MPa, generated at the primary deformation zone. The predicted maximum stress using the Lagrangian element formulation method was 1464 MPa generated at the PDZ (Fig. 5.5) which was close to the experimental result. Numerical stress distributions

in the material ahead of the tool tip using the Lagrangian element formulation method were observed to be somewhat similar to the experimental findings. At the point (150 µm, 0 µm), the experimental stress was 1350 MPa while the numerically predicted value was 1340 MPa. However, the SPH formulation predicted much higher stress (1736 MPa) at the PDZ (Fig. 5.11) compared to the experimental results.

6.8.3. Temperature Distribution

The Experimental temperature distributions showed that the maximum temperature was 1217 K, generated at the tool tip and the secondary deformation zone (Fig. 4.58). The Lagrangian element formulation predicted the maximum temperature as 1222 K at the tool tip and SDZ (Fig. 5.6), which was in a very good agreement to the experimental value. At the point (25 µm, 0 µm), the experimental temperature was 470 K while the predicted value was 495 K. However the SPH formulation predicted much lower temperature (892 K) at the tool tip and SDZ (Fig. 5.12) compared to the experimental results.

6.8.4. Cutting Force

The experimental average cutting force for the machining of Ti-6Al-4V alloy at 63.5 m/min of cutting speed and 0.25 mm/rev of feed rate was 280.6 ± 8.1 N/mm (Fig. 4.5). The predicted average cutting forces were 245.5 ± 88.2 N/mm and 307.9 ± 93.2 N/mm using the Lagrangian element formulation (Fig. 5.7) and SPH (Fig. 5.13) formulations respectively. It was found that both the predicted the cutting forces were comparable to the experimental results.

The above discussion on the comparison between experimental and numerical results suggests that the both models predict the strain, stress and temperature distributions, and cutting force close to the experimental results. However, the predicted results are more accurate for the Lagrangian element formulation method. For this reason, this model can be used to predict the cutting force as well as the temperature, stress and strain distributions in the material ahead of the tool tip for different cutting conditions. However, the model did not predict the deformation behaviour at the shear band accurately

The Lagrangian element formulation method was also used to analyze the effect of friction at the contact between tool and the workpiece on the temperature at the tool tip. The temperature at the tool tip increases with increasing the friction value (Fig. 5.14) and due to the increment of temperature at the tool tip, the strain at the tool tip was also increased with the friction.

From this both experimental and numerical work the mechanism of chip formation during machining of Ti-6Al-4V alloy is clarified. The effect of feed rate and cutting speed on the surface quality is also clarified. The numerical model can predict the stress, strain and temperature distributions in the material ahead of the tool tip similar to the experimental results. Using the numerical model the effect of friction was analyzed. However, this model can also be used to obtain the optimum cutting conditions for the machining of Ti-6Al-4V alloy.

CHAPTER 7. CONCLUSIONS

7.1. Conclusions

The present research studied on the effect of machining parameters on the deformation microstructure and surface morphology of Ti-6Al-4V alloy during dry orthogonal cutting tests. The main conclusions drawn from this study are:

1. During machining of Ti-6Al-4V alloy at different feed rates and cutting speeds serrated chips are formed due to the adiabatic shear band formation.

2. Shear band frequency or the average distance between the center-line of two consecutive shear bands, shear band width and chip thickness increased with feed rate and cutting speed. The temperature generated during machining increased with increasing the feed rate and cutting speed, and amplified the shear band frequency and shear band width.

3. The cutting and thrust forces were increased with the feed rate due to the increment of material removal rate. However, the cutting and thrust forces were decreased with increasing the cutting speed due to the increment of temperature.

4. The depth of deformed zone below the machined surface increased with an increase in the feed rate and cutting speed due to the increment of temperature and this has led to the increment of surface roughness.

5. The distributions of equivalent strain and Local flow stress in the material ahead of the tool tip were determined in a machined Ti-6Al-4V alloy at different cutting speeds and feed rates. The maximum equivalent strain and flow stress generated

in the material at the tool tip were varied with the cutting conditions. The strain in the material ahead of the tool tip increased with the feed rate and cutting speed.

6. Flow curves that showed the relationship between the flow stresses and the equivalent strains were obtained for different cutting conditions. It was found that the saturation stress was independent of the feed rate. However, that saturation stress increased with the cutting speed due to the strain rate sensitivity of this alloy.

7. The temperature increment due to plastic deformation in the material ahead of the tool tip was determined using the equivalent flow stress and the equivalent strain relationship. The temperature ahead of the tool tip was increased with the cutting speed and feed rate due to the increment of material removal rate or plastic deformation of the material.

8. The temperature within the shear band was 1508.5 K or 1235.5 ˚C, which is higher than the $(\alpha + \beta)/\beta$ transus temperature (995±15 ˚C) and transformed adiabatic shear band is formed. However, the hardness of the shear band was lower compared to the surrounding deformed zone and indicated the transformed shear band.

9. To represent the experimental work, numerical models were developed using 2D Lagrangian element formulation and Smoothed-particle hydrodynamics (SPH) formulation implementing Johnson-Cook material model with the Johnson-Cook damage criteria. The parameters used in the JC material model were determined form the experimental flow curves.

10. Both 2D Lagrangian element formulation and Smoothed-particle hydrodynamics (SPH) formulation predicted the serrated chips formations. Both models also predicted the strain, stress and temperature distributions, and cutting force close to the experimental results. However, the Lagrangian element formulation predicted all the distributions and force more accurately compared to SPH formulation.

11. The Lagrangian element formulation was used to predict the effect of friction at the tool-workpiece contact. It was found that the temperature at the tool tip increased with an increase in the friction value. However, due to the increment of temperature, strain at the tool tip was also increased with friction. This result suggests that a better quality tool has to be developed that would reduce the friction and temperature as well as increase the tool life and productivity.

The Lagrangian element formulation can be used to predict the cutting force as well as the temperature, stress and strain distributions in the material ahead of the tool tip for different cutting conditions and that would help to reduce the production cost and time. However, the model did not predict the deformation behaviour at the shear band accurately.

7.2. Suggestions for Future Work

The future work that may be performed to carry this research work further would be to machine the Ti-6Al-4V alloy with coolant and to understand the effect of coolant on the deformation of the workpiece, chip morphology and the surface quality. Machining of Ti-6Al-4V alloy can be done at very high cutting speed to understand the effect of high cutting speed. However, TEM analysis can be performed to investigate the shear band

zone more deeply. Different coated tool can be used to find out a suitable coated tool for machining Ti-6Al-4V alloy that can resist the thermal stress and have the characteristic of chemical inertness.

For numerical analysis, a suitable material model that can take into account the phase transformation phenomena or that can represent the machining operation more accurately, can be develop. Microstructural modelling obtained using the microstructure of the Ti-6Al-4V alloy can also be developed to understand the deformation behaviour during machining operation more clearly. The grain deformation can be observed more accurately form the microstructure based modeling.

REFERENCES

[1] ME Merchant. Mechanics of the metal cutting process. I. Orthogonal cutting and a type 2 chip, J.Appl.Phys. 16 (1945) 267-275.

[2] EH Lee, BW Shaffer. Theory of plasticity applied to problem of machining, American Society of Mechanical Engineers, Journal of Applied Mechanics ASME Transactions. 19 (1952) 234-239.

[3] Stevenson MG, Oxley PLB. An experimental investigation of the influence of speed and scale on the strain-rate in a zone of intense plastic deformation, 184 (1969) 561-76 plate.

[4] S Ramalingam, AC Bell. A scanning electron microscope stage for the observation of chip formation, Rev.Sci.Instrum. 44 (1973) 573-576.

[5] JF Kahles, M Field, D Eylon, FH Froes. Machining of titanium alloys, J.Met. 37 (1985) 27-35.

[6] R Komanduri. Some clarifications on the mechanics of chip formation when machining titanium alloys, Wear. 76 (1982) 15-34.

[7] RF Recht. Catastrophic thermoplastic shear, Journal Of Applied Mechanics. (1964) 189-193.

[8] SP Timothy, IM Hutchings. The structure of adiabatic shear bands in a titanium alloy, Acta Metallurgica. 33 (1985) 667-676.

[9] T Belytschko, WK Liu, B Moran. Nonlinear Finite Elements for Continua and Structures, John Wiley & Sons Ltd. (2000).

[10] J Limido, C Espinosa, M Salaun, JL Lacome, A new approach of high speed cutting modelling: SPH method, Journal De Physique. IV : JP. 134 (2006) 1195-1200.

[11] D Umbrello. Finite element simulation of conventional and high speed machining of Ti6Al4V alloy, J.Mater.Process.Technol. 196 (2008) 79-87.

[12] M Sima, T Özel. Modified material constitutive models for serrated chip formation simulations and experimental validation in machining of titanium alloy Ti-6Al-4V, Int.J.Mach.Tools Manuf. 50 (2010) 943-960.

[13] J Limido, C Espinosa, M Salaün, JL Lacome. SPH method applied to high speed cutting modelling, Int.J.Mech.Sci. 49 (2007) 898-908.

[14] DJ Benson, S Okazawa. Simulations of high-speed machining using a multi-material finite element formulation, NUMIFORM, Material Processing and Design: Modeling, Simulation and Applications. (2004) 1341-1346.

[15] MC Shaw. Metal cutting principles, Oxford University Press. (1984) 5-8, 10-46, 168-201.

[16] DA Stephanenson, JS Agapiou. Metal cutting theory and practice, Marcel Dekker, INC. (1997) 17-20, 28-33, 371-416, 459-478, 551-697.

[17] EJA Armarego, RH Brown. The Machining of Metals. (1969).

[18] ME Merchant. Mechanics of the metal cutting process. II. Plasticity conditions in orthogonal cutting, J.Appl.Phys. 16 (1945) 318-324.

[19] V Piispanen. Theory of formation of metal chips, J.Appl.Phys. 19 (1948) 876-881.

[20] H Zhang, AT Alpas. Quantitative evaluation of plastic strain gradients generated during orthogonal cutting of an aluminum alloy, Materials Science and Engineering A. 332 (2002) 249-254.

[21] H Ni, AT Alpas. Sub-micrometer structures generated during dry machining of copper, Materials Science and Engineering A. 361 (2003) 338-349.

[22] ASM Handbook, ASM Metals Handbook, Vol.16, Machining. (1989) 7-18.

[23] JC Lemaire, WA Backofen. Adiabatic instability in the orthogonal cutting of steel, Metallurgical Transactions. 3 (1972) 481-485.

[24] R Komanduri, T Schroeder, J Hazra, BF Von Turkovich, DG Flom. On the catastrophic shear instability in high-speed machining of an AISI 4340 steel. J ENG IND TRANS ASME. V 104 (1982) 121-131.

[25] HA Grebe, H- Pak, MA Meyers. Adiabatic shear localization in titanium and Ti-6 pct Al-4 pct V alloy, Metallurgical Transactions A. 16 (1985) 761-775.

[26] BM Manyindo, PLB Oxley. Modelling the catastrophic shear type of chip when machining stainless steel. Proceedings of the Institution of Mechanical Engineers.Part C.Mechanical engineering science. 200 (1986) 349-358.

[27] S Ramalingam, JT Black. An electron microscopy study of chip formation, Metallurgical Transactions. 4 (1973) 1103-1112.

[28] H Ni, M Elmadagli, AT Alpas. Mechanical properties and microstructures of 1100 aluminum subjected to dry machining, Materials Science and Engineering A. 385 (2004) 267-278.

[29] JH Dautzenberg, JH Zaat. Quantitative determination of deformation by sliding wear, Wear. 23 (1973) 9-19.

[30] EG Thomsen, CT Yang, S Kobayashi. Mechanics of Plastic Deformation in Metal Processing, The Macmillan Co., New York,. (1965).

[31] M Elmadagli, AT Alpas. Metallographic analysis of the deformation microstructure of copper subjected to orthogonal cutting, Materials Science and Engineering A. 355 (2003) 249-259.

[32] D Tabor. A simple theory of static and dynamic hardness, Proceedings of the Royal Society of London, Series A, Mathematical and Physical Science. 192 (1948) 247-274.

[33] GE Dieter. Mechanical Metallurgy, SI Metric Ed. (1988) 87, 301-304.

[34] R Hill, EH Lee, SJ Tupper. The Theory of Wedge Indentation of Ductile Material, Proceedings of the Royal Society of London. Series A, Mathematical and Physical Sciences. 188 (1947) 273-289.

[35] DM Marsh. Plastic Flow in Glass, Proceedings of the Royal Society of London. Series A, Mathematical and Physical Sciences. 279 (1964) 420-435.

[36] E Voce. The relationship between stress and strain for homogeneous deformation, J. Inst. Met. 74 (1948) 537–562.

[37] H Fujii, K Takahashi, Y Yamashita. Application of titanium and its alloys for automobile parts, Nippon Steel Technical Report. (2003) 70-75.

[38] JR Myers, HB Bomberger, FH Froes. Corrosion behavior and use of titanium and its alloys. J.Met. 36 (1984) 50-59.

[39] EW Collings. The physical metallurgy of titanium alloys, ASM Series in Metal Processing. (1984) 1-9, 39-50.

[40] J Mathew Donachie Jr. Titanium a Technical Guide, ASM International, 2nd Edition. (2000) 13-24.

[41] GG Ye, SF Xue, W Ma, MQ Jiang, Z Ling, XH Tong, et al. Cutting AISI 1045 steel at very high speeds, Int.J.Mach.Tools Manuf. 56 (2012) 1-9.

[42] M Rogante. Wear characterisation and tool performance of sintered carbide inserts during automatic machining of AISI 1045 steel, J.Mater.Process.Technol. 209 (2009) 4776-4783.

[43] JG Kaufman. Properties of aluminum alloys: Tensile creep and fatigue data at high and low temperatures, ASM International. (1999) 11-15.

[44] ASM Handbook, Properties and Selection: Non Ferrous Alloys and Special Purpose Materials, ASM Metal Handbook,. 2 (1989) 759-761.

[45] JR Davis. Copper and copper alloys, ASM International Handbook. (2001) 35-47.

[46] G Lutjering, JC Williams. Titanium, Engineering Materials and Processes, 2nd Ed. (2007) 16-36.

[47] MC Shaw, SO Dirke, PA Smith, NH Cook, EG Loewen, CT Yang. Machining titanium, MIT Rep., (Contract AF 33 (600) 22674. (1954).

[48] NH Cook. Chip formation in machining titanium, In Proc. Symp. On Machining and Grinding Titanium, Watertown Arsenal, Watertown, MA, US Army Ordnance Corps. (1953) 1-7.

[49] OW Boston, RM Caddell, LV Colwell, RE McKee, KF Packer, PR Visser. Machining titanium, Final Rep. (Production Engineering Department, University of Michigan) (US Army Contract 20-018-ORD-11918). (1955).

[50] R Komanduri, BF Von Turkovich. New observations on the mechanism of chip formation when machining titanium alloys, Wear. 69 (1981) 179-188.

[51] HC Child, AF Dalton. Machining of titanium alloy, ISI Special Report. 94 (1968) 139-142.

[52] N Zlatin. Modern Mach.Shop. 42 (1970) 139-144.

[53] N Narutaki, A Murakoshi, S Motonishi, H Takeyama. Study on Machining of Titanium Alloys, CIRP Ann.Manuf.Technol. 32 (1983) 65-69.

[54] RM Freeman. PhD Thesis, University of Birmingham, UK. (1974).

[55] S Motonishi, Y Hara, S Isoda, H Itoh, Y Tsumori, Y Terada. Kobelco Tech Rev. 2 (1987) 28-31.

[56] W Konig. Applied Research on the Machinability of Titanium and Its Alloys, Proceedings of the Forty-seventh Meeting of AGARD, AGARD Structural and Material. CP256 (1979) 1-10.

[57] A Ginting, M Nouari. Surface integrity of dry machined titanium alloys, Int.J.Mach.Tools Manuf. 49 (2009) 325-332.

[58] S Jeelani, K Ramakrishnan. Surface damage in machining titanium 6Al-2Sn-4Zr-2Mo alloy, J.Mater.Sci. 20 (1985) 3245-3252.

[59] CH Che-Haron, A Jawaid. The effect of machining on surface integrity of titanium alloy Ti-6% Al-4% v, J.Mater.Process.Technol. 166 (2005) 188-192.

[60] CH Che-Haron. Tool life and surface integrity in turning titanium alloy, J.Mater.Process.Technol. 118 (2001) 231-237.

[61] AKMN Amin, AF Ismail, MK Nor Khairusshima. Effectiveness of uncoated WC-Co and PCD inserts in end milling of titanium alloy-Ti-6Al-4V, J.Mater.Process.Technol. 192-193 (2007) 147-158.

[62] X Yang, CR Liu. Machining titanium and its alloys, Mach.Sci.Technol. 3 (1999) 107-139.

[63] JDP Velásquez, A Tidu, B Bolle, P Chevrier, J- Fundenberger. Sub-surface and surface analysis of high speed machined Ti-6Al-4V alloy, Materials Science and Engineering A. 527 (2010) 2572-2578.

[64] M Field. Seminar on Advances in machine tools for production trends, The Pennsylvania State University. (1969).

[65] GA Ibrahim, CH Che Haron, JA Ghani. The effect of dry machining on surface integrity of titanium alloy Ti-6A1-4V ELI, Journal of Applied Sciences. 9 (2009) 121-127.

[66] A Ramesh, SN Melkote, LF Allard, L Riester, TR Watkins. Analysis of white layers formed in hard turning of AISI 52100 steel, Materials Science and Engineering A. 390 (2005) 88-97.

[67] J Barry, G Byrne, D Lennon. Observations on chip formation and acoustic emission in machining Ti-6Al-4V alloy, Int.J.Mach.Tools Manuf. 41 (2001) 1055-1070.

[68] NH Cook, I Finnie, MC Shaw. Discontinuous chip formation, Trans.ASME. 76 (1954) 153-162.

[69] K Nakayama, M Arai, T Kanda. Machining Characteristics of Hard Materials, CIRP Ann.Manuf.Technol. 37 (1988) 89-92.

[70] MA Elbestawi, AK Srivastava, TI El-Wardany. A model for chip formation during machining of hardened steel, CIRP Ann.Manuf.Technol. 45 (1996) 71-76.

[71] A Vyas, MC Shaw. Mechanics of saw-tooth chip formation in metal cutting, J.Manuf.Sci.Eng.Trans.ASME. 121 (1999) 163-172.

[72] G Poulachon, AL Moisan. Hard turning: Chip formation mechanisms and metallurgical aspects, J.Manuf.Sci.Eng.Trans.ASME. 122 (2000) 406-412.

[73] S Pratibha. Deformation state of aluminum-6% silicon alloy (319 Al) subjected to orthogonal cutting at differebt speeds and feed rates, MASc Thesis, University of Windsor, Windsor, ON, Canada. (2009).

[74] J Hua, R Shivpuri. Prediction of chip morphology and segmentation during the machining of titanium alloys, J.Mater.Process.Technol. 150 (2004) 124-133.

[75] SL Semiatin, SB Rao. Shear localization during metal cutting, Materials Science and Engineering. 61 (1983) 185-192.

[76] JQ Xie, AE Bayoumi, HM Zbib. A study on shear banding in chip formation of orthogonal machining, Int.J.Mach.Tools Manuf. 36 (1996) 835-847.

[77] JQ Xie, AE Bayoumi, HM Zbib. Analytical and experimental study of shear localization in chip formation in orthogonal machining, Journal of Materials Engineering and Performance. 4 (1995) 32-39.

[78] JQ Xie, AE Bayoumi, HM Zbib, Characterization of chip formation and shear banding in orthogonal machining using finite element analysis, American Society of Mechanical Engineers, Applied Mechanics Division, AMD. 183 (1994) 285-301.

[79] ZB Hou, R Komanduri. Modeling of thermomechanical shear instability in machining, Int.J.Mech.Sci. 39 (1997) 1273-1314.

[80] A Gente, H- Hoffmeister. Chip formation in machining Ti6AI4V at extremely high cutting speeds, CIRP Ann.Manuf.Technol. 50 (2001) 49-52.

[81] JD Puerta Velásquez, B Bolle, P Chevrier, G Geandier, A Tidu. Metallurgical study on chips obtained by high speed machining of a Ti-6 wt.%Al-4 wt.%V alloy, Materials Science and Engineering A. 452-453 (2007) 469-474.

[82] M Cotterell, G Byrne. Dynamics of chip formation during orthogonal cutting of titanium alloy Ti-6Al-4V, CIRP Ann.Manuf.Technol. 57 (2008) 93-96.

[83] J Barry, G Byrne. The mechanisms of chip formation in machining hardened steels, J.Manuf.Sci.Eng.Trans.ASME. 124 (2002) 528-535.

[84] C Zener, JH Hollomon. Effect of strain rate upon plastic flow of steel, J.Appl.Phys. 15 (1944) 22-32.

[85] SP Timothy. The structure of adiabatic shear bands in metals: A critical review, Acta Metallurgica. 35 (1987) 301-306.

[86] SL Semiatin, JJ Jonas. Formability and workability of metals - Plastic instability and flow localization, Am.Soc.Metals. (1984) 225-243.

[87] J Peirs, P Verleysen, J Degrieck, F Coghe. The use of hat-shaped specimens to study the high strain rate shear behaviour of Ti-6Al-4V, Int.J.Impact Eng. 37 (2010) 703-714.

[88] S Liao, J Duffy. Adiabatic shear bands in a TI-6Al-4V titanium alloy, J.Mech.Phys.Solids. 46 (1998) 2201-2231.

[89] SL Semiatin, GD Lahoti. Deformation and unstable flow in hot forging of Ti-6Al-2Sn-4Zr-2Mo-0. 1Si, Metallurgical Transactions A (Physical Metallurgy and Materials Science). 12 A (1981) 1705-1717.

[90] RS Culver. Metallurgical Effects at High Strain Rates, Plenum Press, New York. (1973) 519-530.

[91] AE Bayoumi, JQ Xie. Some metallurgical aspects of chip formation in cutting Ti-6wt.%Al-4wt.%V alloy, Materials Science and Engineering A. 190 (1995) 173-180.

[92] R Komanduri, Z- Hou. On thermoplastic shear instability in the machining of a titanium alloy (Ti-6Al-4V), Metall Mat Trans A Phys Metall Mat Sci. 33 (2002) 2995-3010.

[93] ME Backman, SA Finnegan. Metallurgical Effects at High Strain Rates, Plenum Press, New York. (1973) 531-535.

[94] DM Turley, ED Doyle, S Ramalingam. Calculation of shear strains in chip formation in titanium, Materials Science and Engineering. 55 (1982) 45-48.

[95] PW Leech. Observations of adiabatic shear band formation in 7039 aluminum alloy, Metallurgical Transactions A. 16 (1985) 1900-1903.

[96] S Nemat-Nasser, W- Guo, VF Nesterenko, SS Indrakanti, Y- Gu. Dynamic response of conventional and hot isostatically pressed Ti-6Al-4V alloys: Experiments and modeling, Mech.Mater. 33 (2001) 425-439.

[97] A Molinari, C Musquar, G Sutter. Adiabatic shear banding in high speed machining of Ti-6Al-4V: Experiments and modeling, Int.J.Plast. 18 (2002) 443-459.

[98] AR Shahan, AK Taheri. Adiabatic shear bands in titanium and titanium alloys: a critical review, Materials and Design. 14 (1993) 243-250.

[99] MA Meyers, CL Wittman. Effect of metallurgical parameters on shear band formation in low-carbon (approx. 0.20 wt pct) steels, Metallurgical transactions.A, Physical metallurgy and materials science. 21 A (1990) 3153-3164.

[100] MA Meyers. Dynamic behavior of materials, J.Wiley. (1994) 448-487.

[101] Y Me-Bar, D Shechtman. On the adiabatic shear of Ti6Al4V ballistic targets, Materials Science and Engineering. 58 (1983) 181-188.

[102] AR Machado, J Wallbank. Machining of titanium and its alloys. A review, Proceedings of the Institution of Mechanical Engineers.Part B.Management and engineering manufacture. 204 (1990) 53-60.

[103] TW Wright, H Ockendon. Research note: A scaling law for the effect of inertia on the formation of adiabatic shear bands, Int.J.Plast. 12 (1996) 927-934.

[104] ZP Wan, YE Zhu, HW Liu, Y Tang. Microstructure evolution of adiabatic shear bands and mechanisms of saw-tooth chip formation in machining Ti6Al4V, Materials Science and Engineering A. 531 (2012) 155-163.

[105] PA Dearnley, AN Grearson. Evaluation of principal wear mechanisms of cemented carbides and ceramics used for machining titanium alloy IMI 318. Materials Science and Technology. 2 (1986) 47-58.

[106] PD Hartung, BM Kramer, BF von Turkovich. Tool Wear in Titanium Machining, CIRP Ann.Manuf.Technol. 31 (1982) 75-80.

[107] SK Bhattacharyya, IR Pashya, R Ezugwu, AR Machado. Eighth CBECIMT (Engineering and Materials Science Brazilian Conference) UNICAMP, Campinas, SP, Brazil, Dec 12-15. (1988) 271.

[108] F Nabhani. Wear mechanisms of ultra-hard cutting tools materials, J.Mater.Process.Technol. 115 (2001) 402-412.

[109] P- Arrazola, A Garay, L- Iriarte, M Armendia, S Marya, F Le Maître. Machinability of titanium alloys (Ti6Al4V and Ti555.3), J.Mater.Process.Technol. 209 (2009) 2223-2230.

[110] F Yang, G Meng, J Zhao, X Ai. Fabrication of WC Matrix Composite Tool Material and Its Cutting Performance in Machining Titanium Alloys, Tsinghua Science and Technology. 14 (2009) 75-78.

[111] L Olovsson, M Soulli, I Do. LS-DYNA-ALE Capabilities, Fluid-structure Interactin   Modeling   Tutorial
, Livermore Software Technology Corporation (LSTC). (2003).

[112] LS-Dyna theoretical manual, Livermore Software Technology Corporation, Livermore, CA. (1998).

[113] B Van Leer. Towards the ultimate conservative difference scheme. IV. A new approach to numerical convection, Journal of Computational Physics. 23 (1977) 276-299.

[114] B van Leer. Towards the ultimate conservative difference scheme. II. Monotonicity and conservation combined in a second-order scheme, Journal of Computational Physics. 14 (1974) 361-370.

[115] BE Klamecki. Incipient chip formation in metal cutting - A three dimension finite element analysis, Ph.D. Dissertation, University of Illinois, Urbana-Champaign, IL. (1973).

[116] E Usui, T Shirakashi, Mechanics of machining - from 'descriptive' to 'Predictive' theory, American Society of Mechanical Engineers, Production Engineering Division (Publication) PED. 7 (1982) 13-35.

[117] K Iwata, K Osakada, Y Terasaka. Process modeling of orthogonal cutting by the rigid-plastic finite element method, J Eng Mater Technol Trans ASME. 106 (1984) 132-138.

[118] JS Strenkowski, JT Carroll III. Finite element model of orthogonal metal cutting, Journal of engineering for industry. 107 (1985) 349-354.

[119] JT Carroll III, JS Strenkowski. Finite element models of orthogonal cutting with application to single point diamond turning, Int.J.Mech.Sci. 30 (1988) 899-920.

[120] AJM Shin, S Chandrasekar, HTY Yang. Finite element simulation of metal cutting process with strain-rate and temperature effects, Trans.ASME, Fundam.Issues Machining. (1990) 11-24.

[121] E Ceretti, P Fallböhmer, WT Wu, T Altan. Application of 2D FEM to chip formation in orthogonal cutting, J.Mater.Process.Technol. 59 (1996) 169-180.

[122] AJ Shih, HTY Yang. Experimental and finite element predictions of residual stresses due to orthogonal metal cutting, Int J Numer Methods Eng. 36 (1993) 1487-1507.

[123] AJ Shih. Finite element simulation of orthogonal metal cutting, Journal of engineering for industry. 117 (1995) 84-93.

[124] AJ Shih. Finite element analysis of orthogonal metal cutting mechanics, Int.J.Mach.Tools Manuf. 36 (1996) 255-273.

[125] Von Turkovich BF. Shear stress in metal cutting, J Eng Ind Trans ASME. 92 Ser B (1970) 151-157.

[126] Z- Lin, Y- Yarng. Three-dimensional cutting process analysis with different cutting velocities, J.Mater.Process.Technol. 70 (1997) 22-33.

[127] Z- Lin, S- Lo. A study of deformation of the machined workpiece and tool under different low cutting velocities with an elastic cutting tool, Int.J.Mech.Sci. 40 (1998) 663-681.

[128] S- Lo. An analysis of cutting under different rake angles using the finite element method, J.Mater.Process.Technol. 105 (2000) 143-151.

[129] C Shet, X Deng. Finite element analysis of the orthogonal metal cutting process, J.Mater.Process.Technol. 105 (2000) 95-109.

[130] TD Marusich, M Ortiz. Modelling and simulation of high-speed machining, Int J Numer Methods Eng. 38 (1995) 3675-3694.

[131] E Ceretti, C Lazzaroni, L Menegardo, T Altan. Turning simulations using a three-dimensional FEM code, J.Mater.Process.Technol. 98 (2000) 99-103.

[132] M Vaz Jr., DRJ Owen. Aspects of ductile fracture and adaptive mesh refinement in damaged elasto-plastic materials, Int J Numer Methods Eng. 50 (2000) 29-54.

[133] K Komvopoulos, SA Erpenbeck. Finite element modeling of orthogonal metal cutting, Journal of engineering for industry. 113 (1991) 253-267.

[134] B Zhang, A Bagchi. Finite element simulation of chip formation and comparison with machining experiment, Journal of engineering for industry. 116 (1994) 289-297.

[135] Z- Lin, S- Lo. Ultra-precision orthogonal cutting simulation for oxygen-free high-conductivity copper, J.Mater.Process.Technol. 65 (1997) 281-291.

[136] T Obikawa, E Usui. Computational machining of titanium alloy - finite element modeling and a few results, J.Manuf.Sci.Eng.Trans.ASME. 118 (1996) 208-215.

[137] R Shivpuri, J Hua, P Mittal, AK Srivastava, GD Lahoti. Microstructure-mechanics interactions in modeling chip segmentation during titanium machining, CIRP Ann.Manuf.Technol. 51 (2002) 71-74.

[138] J Hua, R Shivpuri. Prediction of chip morphology and segmentation during the machining of titanium alloys, J.Mater.Process.Technol. 150 (2004) 124-133.

[139] T Özel, S Yildiz, J Ciurana. Influence of material models on serrated chip formation in simulation of machining Ti-6Al-4V titanium alloy, 12th CIRP Proceedings of Conference on Modelling of Machining Operations. (2009) 123-131.

[140] YB Guo, DW Yen. A FEM study on mechanisms of discontinuous chip formation in hard machining, J.Mater.Process.Technol. 155-156 (2004) 1350-1356.

[141] T Özel, M Sima, AK Srivastava, Finite element simulation of high speed machining Ti-6Ai-4V alloy using modified material models, Transactions of the North American Manufacturing Research Institution of SME. 38 (2010) 49-56.

[142] T Özel, M Sima, AK Srivastava, B Kaftanoglu. Investigations on the effects of multi-layered coated inserts in machining Ti-6Al-4V alloy with experiments and finite element simulations, CIRP Ann.Manuf.Technol. 59 (2010) 77-82.

[143] M Calamaz, D Coupard, F Girot. A new material model for 2D numerical simulation of serrated chip formation when machining titanium alloy Ti-6Al-4V, Int.J.Mach.Tools Manuf. 48 (2008) 275-288.

[144] M Calamaz, D Coupard, M Nouari, F Girot. Numerical analysis of chip formation and shear localisation processes in machining the Ti-6Al-4V titanium alloy, Int J Adv Manuf Technol. (2010) 1-9.

[145] Y Karpat. Temperature dependent flow softening of titanium alloy Ti6Al4V: An investigation using finite element simulation of machining, J.Mater.Process.Technol. 211 (2011) 737-749.

[146] JQ Xie, AE Bayoumi, HM Zbib. FEA modeling and simulation of shear localized chip formation in metal cutting, Int.J.Mach.Tools Manuf. 38 (1998) 1067-1087.

[147] E Ceretti, M Lucchi, T Altan. FEM simulation of orthogonal cutting: serrated chip formation, J.Mater.Process.Technol. 95 (1999) 17-26.

[148] S- Rhim, S- Oh. Prediction of serrated chip formation in metal cutting process with new flow stress model for AISI 1045 steel, J.Mater.Process.Technol. 171 (2006) 417-422.

[149] A Raczy, M Elmadagli, WJ Altenhof, AT Alpas. An Eulerian finite-element model for determination of deformation state of a copper subjected to orthogonal cutting, Metall Mat Trans A Phys Metall Mat Sci. 35 A (2004) 2393-2400.

[150] M Souli, A Ouahsine, L Lewin. ALE formulation for fluid-structure interaction problems, Comput.Methods Appl.Mech.Eng. 190 (2000) 659-675.

[151] SS Akarca, X Song, WJ Altenhof, AT Alpas. Deformation behaviour of aluminium during machining: Modelling by Eulerian and smoothed-particle hydrodynamics methods, Proceedings of the Institution of Mechanical Engineers, Part L: Journal of Materials: Design and Applications. 222 (2008) 209-221.

[152] JS Strenkowski, KJ Moon. Finite element prediction of chip geometry and tool/workpiece temperature distributions in orthogonal metal cutting, Journal of Engineering for Industry. 112 (1990) 313-318.

[153] DJ Benson, S Okazawa. Contact in a multi-material Eulerian finite element formulation, Comput.Methods Appl.Mech.Eng. 193 (2004) 4277-4298.

[154] B David J. An efficient, accurate, simple ale method for nonlinear finite element programs, Comput.Methods Appl.Mech.Eng. 72 (1989) 305-350.

[155] MR Movahhedy, MS Gadala, Y Altintas. Simulation of chip formation in orthogonal metal cutting process: an ALE finite element approach, Mach.Sci.Technol. 4 (2000) 15-42.

[156] M Movahhedy, MS Gadala, Y Altintas. Simulation of the orthogonal metal cutting process using an arbitrary Lagrangian-Eulerian finite-element method, J.Mater.Process.Technol. 103 (2000) 267-275.

[157] L Olovsson, L Nilsson, K Simonsson. ALE formulation for the solution of two-dimensional metal cutting problems, Computers and Structures. 72 (1999) 497-507.

[158] MNA Nasr, E- Ng, MA Elbestawi. Modelling the effects of tool-edge radius on residual stresses when orthogonal cutting AISI 316L, Int.J.Mach.Tools Manuf. 47 (2007) 401-411.

[159] H Miguélez, R Zaera, A Rusinek, A Moufki, A Molinari, Numerical modelling of orthogonal cutting: Influence of cutting conditions and separation criterion, Journal De Physique. IV : JP. 134 (2006) 417-422.

[160] O Pantalé, J- Bacaria, O Dalverny, R Rakotomalala, S Caperaa. 2D and 3D numerical models of metal cutting with damage effects, Comput.Methods Appl.Mech.Eng. 193 (2004) 4383-4399.

[161] JL Lacome. Smoothed particle hydrodynamics (SPH): A new feature in LS-DYNA, 7th International LS-DYNA Users Conference. (2002) 29-34.

[162] P Cleary, M Prakash, J Ha, M Sinnott, T Nguyen, J Grandfield. Modeling of cast systems using smoothed-particle hydrodynamics, JOM. 56 (2004) 67-70.

[163] GR Liu, MB Liu. Smoothed Particle Hydrodynamics - a meshfree particle method, World Scientific Pub.Co. ISBN 981 (2003) 238-456 1.

[164] J Bonet, S Kulasegaram. Correction and stabilization of smooth particle hydrodynamics methods with applications in metal forming simulations, Int J Numer Methods Eng. 47 (2000) 1189-1214.

[165] M Buyuk, CDS Kan, NE Bedewi, A Durmus, S Utku. Moving beyond the finite elements, a comparison between the finite element methods and meshless methods for a ballistic impact simulation, Proceedings of the 8th International LS-DYNA User's Conference. (2004) 81-96.

[166] SS Akarca, WJ Altenhof, AT Alpas. A Smoothed-Particle Hydrodynamics Model for Machining of 1100 Aluminum, 10th International LS-DYNA User Conference, Metal Forming (3). (2008) 12.1-12.8.

[167] M Calamaz, J Limido, M Nouari, C Espinosa, D Coupard, M Salaün, et al. Toward a better understanding of tool wear effect through a comparison between experiments and SPH numerical modelling of machining hard materials, International Journal of Refractory Metals and Hard Materials. 27 (2009) 595-604.

[168] E Bagci. 3-D numerical analysis of orthogonal cutting process via mesh-free method, International Journal of Physical Sciences. 6 (2011) 1267-1282.

[169] J Limido. Metal cutting modelling SPH approach, International journal of machining and machinability of materials. 9 (2011) 177-196.

[170] LS-Dyna Keyword User's Manual Livermore Software Technology Corporation, Livermore, CA. 1 (1998).

[171] GR Johnson, WH Cook. A constitutive model and data for metals subjected to large strains, high strain rates and high temperatures, Proceedings of the Seventh International Symposium on Ballistics. (1983) 541-547.

[172] RC Batra, MVS Ravinsankar. Three-dimensional numerical simulation of the Kalthoff experiment, Int.J.Fract. 105 (2000) 161-186.

[173] HW Meyer Jr., DS Kleponis. Modeling the high strain rate behavior of titanium undergoing ballistic impact and penetration, Int.J.Impact Eng. 26 (2001) 509-521.

[174] W- Lee, C- Lin. High-temperature deformation behaviour of Ti6A14V alloy evaluated by high strain-rate compression tests, J.Mater.Process.Technol. 75 (1998) 127-136.

[175] YB Guo, Q Wen, KA Woodbury. Dynamic material behavior modeling using internal state variable plasticity and its application in hard machining simulations, J.Manuf.Sci.Eng.Trans.ASME. 128 (2006) 749-759.

[176] G Chern. Development of a new and simple quick-stop device for the study on chip formation, Int.J.Mach.Tools Manuf. 45 (2005) 789-794.

[177] FP Bowden, D Tabor. The Friction and Lubrication of Solids, Part II, Oxford University Press, London. (2004) 12, 321-349.

[178] Y Sun, W Zeng, Y Han, Y Zhao, G Wang, MS Dargusch, et al. Modeling the correlation between microstructure and the properties of the Ti–6Al–4V alloy based on an artificial neural network, Materials Science and Engineering: A. 528 (2011) 8757-8764.

[179] W- Lee, C- Lin. Plastic deformation and fracture behaviour of Ti-6Al-4V alloy loaded with high strain rate under various temperatures, Materials Science and Engineering A. 241 (1998) 48-59.

[180] S Sun, M Brandt, MS Dargusch. The effect of a laser beam on chip formation during machining of Ti6Al4V alloy, Metall Mat Trans A Phys Metall Mat Sci. 41 (2010) 1573-1581.

[181] DR Lesuer. Experimental investigations of material models for Ti-6Al-4V titanium and 2024-T3 aluminum, Final Report, U.S. Department of Transportation Federal Aviation Administration. (2000) DOT/FAA/AR-00/25.

[182] DJ Steinberg. Equation of state and strength properties of selected materials, Equation of State and Strength Properties of Selected Materials. (1996).

[183] M Cotterell, G Byrne. Characterisation of chip formation during orthogonal cutting of titanium alloy Ti-6Al-4V, CIRP Journal of Manufacturing Science and Technology. 1 (2008) 81-85.

[184] KVBS Kalyan Kumar, SK Choudhury. Investigation of tool wear and cutting force in cryogenic machining using design of experiments, J.Mater.Process.Technol. 203 (2008) 95-101.

[185] H Saglam, S Yaldiz, F Unsacar. The effect of tool geometry and cutting speed on main cutting force and tool tip temperature, Mater Des. 28 (2007) 101-111.

[186] N Fang, Q Wu. A comparative study of the cutting forces in high speed machining of Ti–6Al–4V and Inconel 718 with a round cutting edge tool, J.Mater.Process.Technol. 209 (2009) 4385-4389.

[187] X Song. Experimental studies and numerical simulations of continuous and discontinuous chip formation during orthogonal cutting, MASc Thesis, University of Windsor, Windsor, ON, Canada. (2005).

APPENDIX A

Deformation Angle (θ) Measurement at Each Point Using "TableCurve 2D" Software

Fig. A.1. depicts the microstructure below the machined surface. The β-phase grans are deformed along the cutting direction. ABO is a flow line that is drawn by using the β-phase grans as a marker.
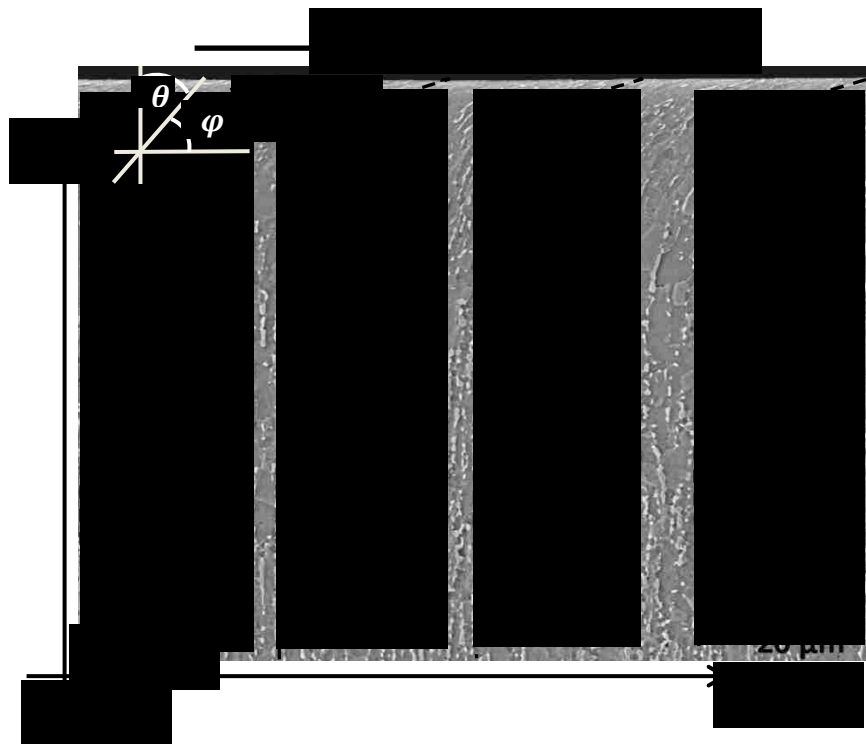
Fig. A.1. SEM image of the microstructure below the machined surface (Cutting speed 63.5 m/min and feed rate 0.25 mm/rev). Here ABO is a flow line drawn by using the β-phase grans as a marker. φ and θ are the shear and deformation angle respectively.

The equation for the ABO flow line was determined using the curve fitting software named "TableCurve 2D" where the R^2 value was 0.95. The equation is:

$$y = \frac{25 + 116100\,x + 1068570\,x^2 + 80228.66\,x^3}{1 + 24360.8\,x + 11469.9\,x^2 + 584.43\,x^3} \tag{A.1}$$

The value of dy/dx or $tan\,\varphi$ was determined using analytical software named 'MAPLE 12' from the Eq. A.1 as:

$$\frac{dy}{dx} = tan\,\varphi$$

$$= \frac{116100 + 2137140\,x + 2.40 \times 10^5\,x^2}{1 + 24360.8\,x + 11469.9\,x^2 + 584.43\,x^3}$$

$$- \frac{(25 + 1161000x + 1068570x^2 + 80228.6x^3)(24360.8 + 22939.8x + 1753.3x^2)}{(1 + 24360.8\,x + 11469.9\,x^2 + 584.43\,x^3)^2}$$

$$\tag{A.2}$$

Form the Eq. A.2, the value of shear angle, φ, at point of the flow line was determined and the deformation angle was determined as: $\theta = 90 - \varphi$.

APPENDIX B

Sample LS-DYNA Input File for Ti-6Al-4V Alloy Using Lagrangian Element

Formulation

```
*KEYWORD
$ UNITS: micrometer, kilograms and seconds
*TITLE
Ti-6Al-4V Alloy Using Lagrangian Element Formulation
*CONTROL_HOURGLASS
$#   ihq      qh
      6 0.100000
*CONTROL_SOLUTION
$#  soln    nlq   isnan   lcint
      2      0      0     100
*CONTROL_TERMINATION
$# endtim  endcyc  dtmin  endeng  endmas
 7.3000E-4      0  0.000   0.000   0.000
*CONTROL_THERMAL_SOLVER
$# atype   ptype  solver  cgtol    gpt  eqheat   fwork    sbc
      1      0      1   0.000      0   0.000 1.000000   0.000
*CONTROL_THERMAL_TIMESTEP
$#   ts     tip    its    tmin    tmax   dtemp    tscp    lcts
      0 0.500000 1.0000E-7  0.000   0.000   0.000   0.000      0
*CONTROL_TIMESTEP
$# dtinit  tssfac   isdo   tslimt   dt2ms   lctm
   0.000 0.900000      0   0.000   0.000      0
*DATABASE_GLSTAT
1.0000E-7      0      0      1
*DATABASE_MATSUM
1.0000E-7      0      0      1
*DATABASE_RBDOUT
1.0000E-7      0      0      1
*DATABASE_RCFORC
1.0000E-7      0      0      1
*DATABASE_TPRINT
1.0000E-7      0      0      1
*DATABASE_BINARY_D3PLOT
$#   dt    lcdt    beam    npltc   psetid
 1.0000E-7      0      0      0      0
*DATABASE_BINARY_D3THDT
$#   dt    lcdt    beam    npltc   psetid
 1.0000E-7      0      0      0      0

*DATABASE_EXTENT_BINARY
$# neiph   neips   maxint  strflg  sigflg  epsflg  rltflg  engflg
      0      0      3      1      1      1      1      1
$# cmpflg  ieverp  beamip  dcomp   shge    stssz   n3thdt  ialemat
      0      0      0      1      1      1      2      1
$# nintsld pkp_sen  sclp   unused  msscl   therm  intout  nodout
      0      0 1.000000      0      0
*BOUNDARY_PRESCRIBED_MOTION_RIGID
$#   pid    dof     vad    lcid     sf     vid    death   birth
      2      1      0      1 1.000000      01.0000E+28   0.000
*BOUNDARY_SPC_SET
$#  nsid    cid    dofx    dofy    dofz    dofrx   dofry   dofrz
      1      0      1      1      1      1      1      1
*SET_NODE_LIST_TITLE
NODESET(SPC) 1
$#   sid    da1     da2     da3     da4
      1   0.000   0.000   0.000   0.000
$#  nid1   nid2    nid3    nid4    nid5    nid6    nid7    nid8
```

```
   104116   104192   104268   104344   104420   104496   104572   104648
………… (Cont'd)

*BOUNDARY_SPC_SET
$#   nsid      cid     dofx     dofy     dofz    dofrx    dofry    dofrz
        2        0        0        0        1        1        1        0
*SET_NODE_LIST_TITLE
NODESET(SPC) 2
$#    sid      da1      da2      da3      da4
        2    0.000    0.000    0.000    0.000
$#   nid1     nid2     nid3     nid4     nid5     nid6     nid7     nid8
   104116   104117   104118   104119   104120   104121   104122   104123
………… (Cont'd)


*CONTACT_2D_AUTOMATIC_SINGLE_SURFACE_ID
$#    cid                                          title
        2
$#   sids     sidm    sfact     freq       fs       fd       dc    membs
        3        0 1.000000       50 0.600000 0.600000 1000.0000        6
$# tbirth   tdeath      sos      som      nds      ndm      cof     init
   0.0001.0000E+20 1.000000 1.000000        0        0        0        0
*SET_PART_LIST_TITLE
WP
$#    sid      da1      da2      da3      da4
        3    0.000    0.000    0.000    0.000
$#   pid1     pid2     pid3     pid4     pid5     pid6     pid7     pid8
        1        0        0        0        0        0        0        0
*CONTACT_2D_AUTOMATIC_SURFACE_TO_SURFACE_ID
$#    cid                                          title
        2
$#   sids     sidm    sfact     freq       fs       fd       dc    membs
        3        4 1.000000       50 0.600000 0.600000 10.000000        6
$# tbirth   tdeath      sos      som      nds      ndm      cof     init
   0.0001.0000E+20 1.000000 1.000000        0        0        0        0
*SET_PART_LIST_TITLE
Tool
$#    sid      da1      da2      da3      da4
        4    0.000    0.000    0.000    0.000
$#   pid1     pid2     pid3     pid4     pid5     pid6     pid7     pid8
        2        0        0        0        0        0        0        0
*PART
$# title
WP
$#    pid    secid      mid    eosid     hgid     grav   adpopt     tmid
        1        1        4        1        0        0        0        1
*SECTION_SHELL_TITLE
WP
$#  secid   elform     shrf      nip    propt   qr/irid    icomp    setyp
        1       13 1.000000        3        1        0        0        1
$#     t1       t2       t3       t4     nloc    marea     idof   edgset
 1.100000 1.100000 1.100000 1.100000    0.000    0.000    0.000        0
*MAT_JOHNSON_COOK_TITLE
WP
$#    mid       ro        g        e       pr      dtf       vp
        4 4.4300E-6 5.5000E+7 1.1000E+8 0.330000    0.000    0.000
$#      a        b        n        c        m       tm       tr     epso
 1.2400E+6 2.2000E+5 0.260000 0.012300 1.010000 1933.0000 296.00000 1.000000
$#     cp       pc    spall       it       d1       d2       d3       d4
 5.6800E+8    0.000 1.000000 1.000000 -0.090000 0.500001 0.480000 0.014000
$#     d5
 2.500000
*EOS_GRUNEISEN
$#  eosid        c       s1       s2       s3    gamao        a       e0
        1 5.1300E+6 1.028000    0.000    0.000 1.230000 0.500000    0.000
$#     v0
 1.000000
*PART
$# title
$#    pid    secid      mid    eosid     hgid     grav   adpopt     tmid
        2        2        2        0        0        0        0        2
```

235

```
*SECTION_SHELL_TITLE
Tool
$#   secid  elform   shrf   nip   propt  qr/irid  icomp   setyp
       2     13 1.000000     3      1       0       0       1
$#     t1      t2      t3      t4    nloc   marea    idof   edgset
 1.110000 1.110000 1.110000 1.110000   0.000   0.000   0.000       0
*MAT_RIGID_TITLE
Tool
$#    mid      ro       e      pr       n   couple       m    alias
       2 7.1000E-6 2.1000E+8 0.330000   0.000   0.000   0.000
$#    cmo    con1    con2
 1.000000       5       7
$# lco or a1     a2      a3      v1      v2      v3
   0.000   0.000   0.000   0.000   0.000   0.000
*MAT_ADD_EROSION
$#    mid    excl  mxpres   mneps  effeps  voleps   numfip     ncs
       4   0.000   0.000   0.000 1.660000   0.000 1.000000 1.000000
$# mnpres   sigp1   sigvm   mxeps   epssh   sigth  impulse  failtm
   0.000   0.000   0.000 1.660000 2.000000   0.000 4.200000 1.000000
*MAT_THERMAL_ISOTROPIC_TITLE
Workpiece
$#   tmid     tro   tgrlc  tgmult    tlat    hlat
       1 4.4300E-6   0.000   0.000   0.000   0.000
$#     hc      tc
 5.2600E+8 6700.0000
*MAT_THERMAL_ISOTROPIC_TITLE
Tool
$#   tmid     tro   tgrlc  tgmult    tlat    hlat
       2 7.1000E-6   0.000   0.000   0.000   0.000
$#     hc      tc
 5.2600E+8 27200.000
*INITIAL_TEMPERATURE_SET
$#   nsid    temp     loc
       0 300.00000       0
*DEFINE_CURVE_TITLE
Velocity
$#   lcid    sidr     sfa     sfo    offa    offo
       1       0 1.000000 1.000000   0.000   0.000
$#          a1              o1
        0.000    1060.0000000
      0.1000000    1060.0000000
*ELEMENT_SHELL
$#  eid  pid    n1    n2    n3    n4    n5    n6    n7    n8
 67976    2 71709 71710 71721 71720     0     0     0     0
 67977    2 71710 71711 71722 71721     0     0     0     0
………… (Cont'd)

*NODE
$#  nid        x          y          z    tc    rc
 71709   -0.0028500    0.2161320      0.000     0     0
………… (Cont'd)

*END
```

236

APPENDIX C

Sample LS-DYNA Input File for Ti-6Al-4V Alloy Using Smoothed-particle hydrodynamics (SPH)

```
*KEYWORD
$ UNITS: micrometer, kilograms and seconds
*TITLE
Ti-6Al-4V Alloy Using Smoothed-particle hydrodynamics (SPH)
*CONTROL_ENERGY
$#   hgen    rwen   slnten   rylen
      2       2       1       1
*CONTROL_HOURGLASS
$#   ihq     qh
      1  0.100000
*CONTROL_SOLUTION
$#   soln    nlq   isnan   lcint
      2       0      0      100
*CONTROL_SPH
$#   ncbs   boxid    dt    idim  memory   form   start    maxv
      2       0  0.100000    0    150      0   0.0001.0000E+15
$#   cont   deriv
      0       0
*CONTROL_TERMINATION
$#  endtim  endcyc  dtmin  endeng  endmas
  0.002000    0    0.000   0.000   0.000
*CONTROL_THERMAL_SOLVER
$#  atype   ptype  solver  cgtol    gpt  eqheat  fwork    sbc
      1       0      1    0.000      0   0.000 1.000000  0.000
*CONTROL_THERMAL_TIMESTEP
$#   ts     tip    its    tmin    tmax   dtemp    tscp    lcts
      0  0.500000 1.0000E-7 0.000  0.000   0.000   0.000    0
*CONTROL_TIMESTEP
$#  dtinit  tssfac  isdo  tslimt   dt2ms   lctm   erode   ms1st
   0.000  0.150000    0   0.000    0.000     0      0       0
$#  dt2msf  dt2mslc  imscl
   0.000      0       0
*DATABASE_GLSTAT
1.0000E-7     0      0      1
*DATABASE_MATSUM
1.0000E-7     0      0      1
*DATABASE_NODFOR
1.0000E-7     0      0      1
*DATABASE_RBDOUT
1.0000E-7     0      0      1
*DATABASE_RCFORC
1.0000E-7     0      0      1
*DATABASE_TPRINT
1.0000E-7     0      0      1
*DATABASE_BINARY_D3PLOT
$#   dt     lcdt   beam   npltc  psetid
 1.0000E-7    0      0      0      0
$#  ioopt
      0
*DATABASE_BINARY_D3THDT
$#   dt     lcdt   beam   npltc  psetid
 1.0000E-4    0      0      0      0
*DATABASE_EXTENT_BINARY
$#  neiph   neips  maxint  strflg  sigflg  epsflg  rltflg  engflg
      0       0      3      1      1      1      1      1
$#  cmpflg  ieverp  beamip  dcomp   shge   stssz  n3thdt  ialemat
      0       0      0      1      1      1      2      1
```

```
$# nintsld  pkp_sen  sclp   unused  msscl   therm  intout  nodout
      0       0 1.000000    0      0      0
*BOUNDARY_PRESCRIBED_MOTION_RIGID
$#   pid    dof    vad    lcid    sf    vid   death   birth
      4      1      0      1 1.000000    01.0000E+28   0.000
*BOUNDARY_SPC_SET
$#   nsid   cid   dofx   dofy   dofz   dofrx  dofry  dofrz
      1      0     1      1     1      1      1      1
*SET_NODE_LIST_TITLE
NODESET(SPC) 1
$#   sid    da1    da2    da3    da4
      1    0.000  0.000  0.000  0.000
$#   nid1   nid2   nid3   nid4   nid5   nid6   nid7   nid8
   122659 122660 122789 122790 122919 122920 123049 123050
………… (Cont'd)


*BOUNDARY_SPC_SET
$#   nsid   cid   dofx   dofy   dofz   dofrx  dofry  dofrz
      2      0     0      0     1      1      1      0
*SET_NODE_LIST_TITLE
NODESET(SPC) 2
$#   sid    da1    da2    da3    da4
      2    0.000  0.000  0.000  0.000
$#   nid1   nid2   nid3   nid4   nid5   nid6   nid7   nid8
   122659 122660 122661 122662 122663 122664 122665 122666
………… (Cont'd)
*CONTACT_AUTOMATIC_NODES_TO_SURFACE_ID
$#   cid                                        title
      1
$#   ssid   msid   sstyp  mstyp  sboxid  mboxid   spr    mpr
      3      4      4      3     0      0      0      0
$#    fs     fd     dc     vc    vdc   penchk   bt     dt
 0.600000 0.600000 100.00000   0.000 20.000000   0   0.0001.0000E+20
$#   sfs    sfm    sst    mst   sfst   sfmt    fsf    vsf
 10.000000 10.000000   0.000   0.000 1.000000 1.000000 1.000000 1.000000
*SET_NODE_LIST
$#   sid    da1    da2    da3    da4
      3    0.000  0.000  0.000  0.000
$#   nid1   nid2   nid3   nid4   nid5   nid6   nid7   nid8
   122659 122660 122661 122662 122663 122664 122665 122666
………… (Cont'd)


*PART
$# title
SphNode
$#   pid    secid   mid   eosid   hgid   grav  adpopt   tmid
      1      5      1      1     0      0      0      1
*SECTION_SPH_TITLE
Wp
$#   secid   cslh    hmin   hmax   sphini  death   start
      5 1.200000 0.200000 2.000000   0.0001.0000E+20   0.000
*MAT_JOHNSON_COOK_TITLE
WP
$#   mid     ro      g      e     pr    dtf    vp
      1 4.4300E-6 5.5000E+7 1.1000E+8 0.330000   0.000   0.000
$#    a      b      n      c      m     tm     tr    epso
 1.2400E+6 2.2000E+5 0.260000 0.019700 0.577000 1933.0000 296.00000 1.000000
$#    cp     pc    spall    it     d1     d2     d3     d4
 5.6800E+8   0.000 2.000000   0.000 -0.090000 0.500001 0.480000 0.014000
$#    d5
 2.500000
*EOS_GRUNEISEN
$#   eosid    c     s1     s2     s3   gamao    a     e0
      1 5.1300E+6 1.028000   0.000   0.000 1.230000 0.800000   0.000
$#    v0
 1.000000
*PART
$# title
```

```
$#    pid    secid    mid   eosid    hgid    grav   adpopt    tmid
       4       4       2       0       0       0       0       2
*SECTION_SOLID_TITLE
Tool solid
$#  secid   elform    aet
       4       1       0
*MAT_RIGID_TITLE
Tool
$#    mid     ro      e      pr      n   couple     m    alias
       2 7.100E-6 2.1000E+8 0.330000  0.000   0.000   0.000
$#   cmo    con1    con2
 1.000000       5       7
$# lco or a1    a2      a3      v1      v2      v3
   0.000   0.000   0.000   0.000   0.000   0.000
*MAT_THERMAL_ISOTROPIC_TITLE
WP
$#   tmid     tro    tgrlc   tgmult    tlat    hlat
       1 4.4300E-6   0.000   0.000   0.000   0.000
$#    hc      tc
 5.2600E+8 6700.0000
*MAT_THERMAL_ISOTROPIC_TITLE
WP
$#   tmid     tro    tgrlc   tgmult    tlat    hlat
       2 7.1000E-6   0.000   0.000   0.000   0.000
$#    hc      tc
 5.2600E+8 27200.000
*INITIAL_TEMPERATURE_SET
$#  nsid    temp    loc
       0 300.00000       0
*DEFINE_CURVE_TITLE
Vel
$#   lcid    sidr     sfa     sfo     offa    offo   dattyp
       1       0 1.000000 1.000000   0.000   0.000       0
$#         a1              o1
       0.000    1000.0000000
   0.0020000    1000.0000000
*ELEMENT_SOLID
$#  eid    pid    n1     n2     n3     n4     n5     n6     n7     n8
 142159      4 142159 142160 142171 142170 142280 142281 142282 142283
………… (Cont'd)
*ELEMENT_SPH
$#  nid    pid     mass
 122659      1 1.1340800e-012
………… (Cont'd)
*NODE
$#  nid          x          y          z     tc    rc
 122659    0.0040000    0.0040000    0.0020000      0      0
………… (Cont'd)
*END
```

APPENDIX D

Shear Band Formation Criteria for Aluminum and Copper

Aluminum [28]**:**

For the cutting conditions of 36 m/min and 0.30 mm/rev, the average work hardening rate $\left(\frac{\delta\sigma}{\delta\varepsilon}\right)$ for the flow stress between 260.35 MPa and 254.15 MPa was 27 MPa. The corresponding $d\varepsilon, \delta T$ and $\delta\sigma$ values were 0.42, 43 K and -6.2 MPa. The calculated value of the ratio between the strain hardening and thermal softening or, $\left(\dfrac{\frac{\delta\sigma}{\delta\varepsilon}}{-\frac{\delta\sigma}{\delta T}\frac{dT}{d\varepsilon}}\right)$ was 1.82 which did not satisfy the adiabatic shear band criterion.

Copper [31]**:**

For the cutting conditions of 36 m/min and 0.25 mm/rev, the average work hardening rate $\left(\frac{\delta\sigma}{\delta\varepsilon}\right)$ for the flow stress between 320.8 MPa and 315.2 MPa was 41 MPa. The corresponding $d\varepsilon, \delta T$ and $\delta\sigma$ values were 0.4, 20 K and -5.6 MPa. The calculated value of the ratio between the strain hardening and thermal softening or, $\left(\dfrac{\frac{\delta\sigma}{\delta\varepsilon}}{-\frac{\delta\sigma}{\delta T}\frac{dT}{d\varepsilon}}\right)$ was 2.9, which did not satisfy the adiabatic shear band criterion.

APPENDIX E

<u>DVD with all the Input Files</u>

A DVD that contains all the input files for the simulation is attached with this thesis.

VITA AUCTORIS

NAME:	Md. Aquidul Islam
PLACE OF BIRTH:	Rangpur, Bangladesh
YEAR OF BIRTH:	1987
EDUCATION:	Bangladesh University of Engineering and Technology (BUET), Bangladesh. Dept. of Materials & Metallurgical Engineering (MME) B.Sc. Engg. (MME) December 2004 – October 2009
	University of Windsor, Windsor, ON. Dept. of Mechanical, Automotive and Materials Eng. M.A.Sc. in Engineering Materials May 2010 – April 2012

Publications

- Md. A. Islam, W. J. Altenhof and A. T. Alpas, "Determination of Deformation State of Ti-6Al-4V alloy Subjected to Orthogonal Cutting Using Experimental and Numerical Methods", Accepted for 1st International Conference on Virtual Machining Process Technology (VPMT 2012), Montreal, Canada.

- Md. A. Islam, S. Bhowmick and A. T. Alpas, "Metallographic analysis of the deformation microstructure of Ti-6Al-4V alloy subjected to orthogonal cutting", Proceedings of the 23rd CANCAM-2011, Vancouver, Canada, TA4.2, pp-503-506.